

JONAS HUND

# Characterisation and modelling of PC/ABS blends



Jonas Hund

## **Characterisation and modelling of PC/ABS blends**

**Schriftenreihe des Instituts für Mechanik  
Karlsruher Institut für Technologie (KIT)**

**Band 8**

Herausgeber:

Prof. Dr.-Ing. habil. Peter Betsch

Prof. Dr.-Ing. habil. Thomas Seelig

Eine Übersicht aller bisher in dieser Schriftenreihe erschienenen Bände  
finden Sie am Ende des Buches.

# Characterisation and modelling of PC/ABS blends

by  
Jonas Hund

Karlsruher Institut für Technologie  
Institut für Mechanik

Characterisation and modelling of PC/ABS blends

Zur Erlangung des akademischen Grades eines Doktor-Ingenieurs  
von der KIT-Fakultät für Bauingenieur-, Geo- und Umweltwissenschaften  
des Karlsruher Instituts für Technologie (KIT) genehmigte Dissertation

von Jonas Hund, M.Sc.

Tag der mündlichen Prüfung: 16. Juli 2021  
Hauptreferent : Prof. Dr.-Ing. habil. Peter Betsch  
Korreferent : Prof. Dr.-Ing. habil. Thomas Böhlke  
Korreferent : Prof. Dr.Ing. Arild Holm Clausen

## Impressum



Karlsruher Institut für Technologie (KIT)  
KIT Scientific Publishing  
Straße am Forum 2  
D-76131 Karlsruhe

KIT Scientific Publishing is a registered trademark  
of Karlsruhe Institute of Technology.

Reprint using the book cover is not allowed.

[www.ksp.kit.edu](http://www.ksp.kit.edu)



*This document – excluding parts marked otherwise, the cover, pictures and graphs –  
is licensed under a Creative Commons Attribution-Share Alike 4.0 International License  
(CC BY-SA 4.0): <https://creativecommons.org/licenses/by-sa/4.0/deed.en>*



*The cover page is licensed under a Creative Commons  
Attribution-No Derivatives 4.0 International License (CC BY-ND 4.0):  
<https://creativecommons.org/licenses/by-nd/4.0/deed.en>*

Print on Demand 2022 – Gedruckt auf FSC-zertifiziertem Papier

ISSN 2363-4936

ISBN 978-3-7315-1157-1

DOI 10.5445/KSP/1000141093







# Abstract

Blends of polycarbonate (PC) and the rubber-toughened polymer acrylonitrile butadiene styrene (ABS) are a class of engineering plastics that feature a beneficial fracture toughness. This makes them a popular choice for commercial applications such as personal protective equipment and consumer electronics. The key blend parameters determining the material behaviour and microstructure are the PC/ABS ratio and the rubber content in ABS. The interrelationship between blend composition and fracture toughness is non-monotonic with the complex blend microstructure also having an impact. Although extensive experimental studies investigating the mechanical response have been conducted, the underlying micromechanisms are not yet fully understood and accounted for in constitutive models. In this thesis, a comprehensive approach to investigating PC/ABS blends is presented.

Three commercial PC/ABS blends of different compositions are experimentally investigated in uniaxial tensile tests and fracture tests using digital image correlation to gauge the surface strain fields. One characteristic feature of PC/ABS blends is their pronounced plastic dilatancy. As such, the blend composition with the greatest ABS content exhibits the most pronounced plastic dilatancy. Regarding yield stress, strength, and specific work, a higher PC content is found to be beneficial.

In a modelling approach regarding PC/ABS in a homogenised sense, three plastically dilatant material models are fitted from uniaxial tensile tests and subsequently compared regarding their ability to capture the materials' fracture behaviour. In that regard, the purely phenomenological Raghava and Drucker-Prager yield surfaces prove to be superior to the Green model that features an evolving porosity. The Drucker-Prager and the Raghava model are capable of reproducing the experimentally observed plastic zone surrounding a notch in PC-rich blend compositions, yet overestimate the peak load. Thus, these models do not sufficiently take into account the materials' susceptibility to notches and higher stress triaxialities.

The objective of this work is to improve the understanding of the composition-dependent deformation and particularly the failure behaviour. For this purpose, a three-dimensional unit cell approach is applied, in which the PC and ABS phases are modelled, and the PC/ABS ratio and rubber content in ABS are systematically varied. Special emphasis is put on the constitutive modelling of the ABS phase where the rubber volume fraction is considered in a continuum micromechanical approach and applied to different material models. As part of this study, a novel constitutive model is introduced that combines the deformation mechanisms of shear yielding and distributed crazing. While this model represents an improvement over preceding micromechanical models, the Raghava model

still proves superior regarding the global unit cell response with respect to the macroscopic deformation and failure behaviour. Therefore, the unit cell modelling approach highlights discrepancies in the current material modelling and geometrical representation of the phases particularly regarding failure behaviour emphasising the need for further research. However, the unit cell models are found to qualitatively capture the non-monotonic dependence of fracture toughness on composition underlining the impact of the rubber content in ABS on the overall blend behaviour.

# Kurzfassung

Mischungen aus Polycarbonat (PC) und dem gummi-modifizierten Acrylnitril-Butadien-Styrol (ABS) gehören zur Klasse der Ingenieurkunststoffe und finden aufgrund ihrer vorteilhaften Schlagzähigkeit in vielerlei Hinsicht Verwendung. Ihre wichtigsten Kenngrößen zur Bestimmung des Materialverhaltens sowie der Mikrostruktur sind das Verhältnis von PC zu ABS sowie der Gummigehalt im ABS. Die Wechselbeziehung zwischen Mischungszusammensetzung und Schlagzähigkeit ist jedoch nicht monoton, wobei auch die mitunter komplexe Mikrostruktur eine Rolle spielt. Obwohl zahlreiche experimentelle Forschungsanstrengungen unternommen wurden, besteht immer noch Unklarheit über die dabei involvierten Deformationsmechanismen sowie deren Berücksichtigung in Materialmodellen.

In der vorliegenden Arbeit werden drei kommerziell verfügbare PC/ABS Mischungen unterschiedlicher Zusammensetzungen in uniaxialen Zugversuchen sowie Bruchversuchen unter der Verwendung optischer Verzerrungsmessung charakterisiert. Eine der charakteristischen Eigenschaften von PC/ABS Mischungen ist eine ausgeprägte plastische Dilatanz. Von den drei untersuchten Materialien zeigt dasjenige mit dem höchsten Anteil von ABS die stärkste plastische Volumenzunahme. Hinsichtlich der Fließspannung, der Festigkeit sowie der spezifischen Arbeit ist hingegen ein größerer PC-Anteil von Vorteil.

In einem homogenisierten Modellierungsansatz werden drei plastisch dilatante Materialmodelle anhand der Daten aus den uniaxialen Zugversuchen kalibriert und hinsichtlich ihrer Eignung, das Versagensverhalten von PC/ABS abzubilden, verglichen. Die rein phänomenologischen Drucker-Prager und Raghava Fließflächen stellen sich dabei dem Green'schen Modell, das eine Evolution der Porosität berücksichtigt, als überlegen heraus. Das Drucker-Prager und das Raghava Modell eignen sich dazu, die experimentell beobachtete Entwicklung der plastischen Zone rund um eine Kerbe wiederzugeben, überschätzen jedoch die Maximallast. Die Kerbempfindlichkeit sowie der Einfluss höherer Spannungs-dreiachsigkeiten auf das Materialverhalten wird von diesen Materialmodellen folglich nicht korrekt berücksichtigt.

Ziel der vorliegenden Arbeit ist es, die Abhängigkeit des Deformations- sowie des Versagensverhaltens von der Zusammensetzung besser zu verstehen. Zu diesem Zweck werden in dreidimensionalen Einheitszellen, die PC und ABS Phasen modelliert und das PC/ABS Verhältnis sowie der Gummigehalt im ABS systematisch variiert. Ein besonderes Augenmerk wird dabei auf die konstitutive Modellierung des ABS gelegt, indem der Gummianteil kontinuumsmechanisch mittels Homogenisierung in unterschiedlichen

Materialmodellen berücksichtigt wird. Als Teil dieser Studie wird ein neuartiges Materialmodell eingeführt, das die Deformationsmechanismen des verteilten Crazings sowie Scherfließens in kombinierter Weise berücksichtigt. Während dieses Modell eine Verbesserung vorhergehender mikromechanischer konstitutiver Modelle hinsichtlich der Modellierung des makroskopischen Deformations- und Versagensverhaltens darstellt, erweist sich das Raghava Modell insgesamt als überlegen. Dadurch zeigt der Modellierungsansatz mit Einheitszellen Schwachstellen in den aktuellen konstitutiven Modellen sowie der geometrischen Repräsentation der Materialphasen auf. Insbesondere hinsichtlich des Versagensverhaltens besteht weiterer Forschungsbedarf. Die Modellierung mit Einheitszellen erweist sich jedoch als dazu geeignet, die nicht monotone Abhängigkeit der Schlagzähigkeit von der Zusammensetzung qualitativ wiederzugeben und die besondere Bedeutung des Gummigehaltes im ABS für das Materialverhalten der Mischungen zu betonen.

# Acknowledgements

First and foremost, I would like to thank my supervisor Prof. Thomas Seelig for your great patience in teaching me the particularities of polymer blends regarding both their characterisation and modelling. Thank you for giving me the opportunity to undertake this scientific venture, always having an open door to discuss the latest developments, as well as providing ample inspiration and fresh ideas.

I would also like to thank Prof. Peter Betsch for guiding me through the final administrative steps and being the main examiner of my thesis. My thanks also go to Prof. Thomas Böhlke for initially proposing me for the position of a doctoral researcher at the Institute of Mechanics and acting as an examiner of my thesis. I would also like to express special thanks to Prof. Arild Holm Clausen for his commitment as an examiner of the thesis.

Arriving at the institute as a stranger, I was immediately welcomed by Alexander Janz as his new office mate. Despite the awkward first impression I must have left, you not only endured the occasional odour of garlic but also befriended me such that we did not only share an office but also countless jokes and to this day undertake unforgettable challenges on our bikes. When it was time for Alexander to move on, I came to know Timo Ströhle a former student, turned office mate, turned friend. I am deeply grateful for your high yet calming spirits, diverse discussions about mechanics and life, your select taste in music, many bags of tea, and the select occasions you let me introduce you to the road bike life. My special thanks also go to Julian Bauer. Thank you for your patience in improving my Python skills and advising me on professional life but also for the countless discussions, food for thought, and corrections to my manuscript, all while being a good friend to whom I can ask and discuss anything. I would also like to thank Marlon Franke for being a friend from the first occasion we met as colleagues and for welcoming me into his office on countless occasions to discuss everything non-work related and share a laugh.

Concerning the experimental work, I had the pleasure of working together with Florian Schrammer. Thank you for spending countless hours preparing specimens for their destruction, letting me undertake my first steps in material testing, and providing a helping hand before anything could go wrong, while always maintaining your calm and patience.

Many thanks also go to all the other members of the Institute of Mechanics for making this a fun place to be and work. Thank you for laughing along with my jokes and shenanigans, not judging me for their sometimes silly and embarrassing nature. I am deeply grateful for the comfortable atmosphere that you created but even more so, for the occasions to stuff my mouth with delicacies that you brought along.

Thanks also to Catherine Harriman and Christian Leppin for giving much appreciated professional advice, sharing experiences, and proofreading parts of the manuscript.

Special thanks go to Emma for caring for my physical and mental wellbeing, supporting me day in, day out, and picking me up on all the occasions I needed it. I could not have done this without your patience, understanding, and love.

Last but not least I would also like to thank my bike and stationary bike trainer for allowing me to dissipate mental stress into physical exertion. You were always there for me, not complaining about the sometimes rigorous workouts I treated you to.

# Contents

<b>Abstract</b> . . . . .	<b>i</b>
<b>Kurzfassung</b> . . . . .	<b>iii</b>
<b>Acknowledgements</b> . . . . .	<b>v</b>
<b>1. Introduction</b> . . . . .	<b>1</b>
1.1. Motivation . . . . .	1
1.2. Objectives of this work . . . . .	3
1.3. Outline . . . . .	3
<b>2. Continuum mechanics and the finite element method</b> . . . . .	<b>7</b>
2.1. Continuum mechanics . . . . .	8
2.1.1. Kinematics . . . . .	8
2.1.2. The concept of stress . . . . .	12
2.1.3. Time derivatives of kinematic quantities . . . . .	14
2.1.4. Strain rate measures . . . . .	15
2.1.5. Concept of objectivity . . . . .	16
2.1.6. Objective stress rates . . . . .	17
2.2. Balance relations of mechanics . . . . .	18
2.2.1. Balance of mass . . . . .	20
2.2.2. Balance of linear momentum . . . . .	21
2.2.3. Balance of rotational momentum . . . . .	22
2.3. The initial boundary value problem (IBVP) . . . . .	24
2.4. The finite element method (FEM) . . . . .	24
2.4.1. The weak form . . . . .	25
2.4.2. Discretisation of the weak form . . . . .	27
2.4.3. Discretisation in time . . . . .	28
<b>3. PC/ABS blends</b> . . . . .	<b>31</b>
3.1. Polycarbonate (PC) . . . . .	31
3.1.1. Amorphous thermoplastic polymers . . . . .	31
3.1.2. Mechanical response . . . . .	32
3.1.3. Mechanisms of plastic deformation . . . . .	34
3.2. Acrylonitrile-butadiene-styrene (ABS) . . . . .	37
3.2.1. Rubber-toughened polymer blends . . . . .	37

3.2.2.	Mechanisms of plastic deformation . . . . .	38
3.2.3.	The uniaxial stress-strain response . . . . .	39
3.3.	PC/ABS blends . . . . .	40
3.4.	Morphology of PC/ABS blends . . . . .	42
3.4.1.	Sea-island morphologies . . . . .	42
3.5.	Mechanical behaviour of PC/ABS blends . . . . .	44
<b>4.</b>	<b>PC/ABS blends investigated in this work . . . . .</b>	<b>49</b>
4.1.	Materials . . . . .	49
4.1.1.	Micrographs . . . . .	49
4.1.2.	Sample preparation . . . . .	50
4.2.	Blend compositions . . . . .	50
4.3.	Blend morphologies . . . . .	51
4.3.1.	Morphology at the surface . . . . .	51
4.3.2.	Morphology of the skin layer . . . . .	52
4.3.3.	Morphology of the core region . . . . .	53
4.3.4.	Remarks on the morphology . . . . .	54
<b>5.</b>	<b>Experimental testing setup . . . . .</b>	<b>57</b>
5.1.	Mechanical testing . . . . .	57
5.1.1.	Uniaxial tensile tests . . . . .	57
5.1.2.	Fracture tests . . . . .	58
5.1.3.	Specimen manufacturing . . . . .	58
5.2.	Digital image correlation (DIC) . . . . .	60
5.2.1.	Fundamentals of DIC . . . . .	61
5.2.2.	Computation of the true stress and volume strain response . . . . .	62
5.2.3.	DIC analysis in the through-thickness direction . . . . .	63
5.2.4.	Analysis . . . . .	65
<b>6.</b>	<b>The impact of blend composition on the material response . . . . .</b>	<b>67</b>
6.1.	Deformation behaviour - uniaxial tensile tests . . . . .	67
6.1.1.	Nominal strain rate $\dot{\epsilon} = 0.1 \text{ s}^{-1}$ . . . . .	67
6.1.2.	Nominal strain rate $\dot{\epsilon} = 0.01 \text{ s}^{-1}$ . . . . .	72
6.2.	Failure behaviour - SENT tests . . . . .	76
6.2.1.	Plastic zone formation at notch . . . . .	76
6.2.2.	Force-displacement response . . . . .	77
6.2.3.	Specific work of fracture . . . . .	79
6.3.	Discussion . . . . .	79
6.3.1.	Deformation behaviour - uniaxial tensile tests . . . . .	79
6.3.2.	Failure behaviour - SENT tests . . . . .	85
6.4.	Conclusions . . . . .	87
<b>7.</b>	<b>The impact of the specimen orientation on the material response . . . . .</b>	<b>89</b>
7.1.	Study outline . . . . .	89



7.2.	Results . . . . .	89
7.2.1.	Deformation behaviour - uniaxial tensile tests . . . . .	90
7.2.2.	Failure behaviour - SENT tests . . . . .	92
7.3.	Discussion and conclusions . . . . .	95
<b>8.</b>	<b>Constitutive modelling . . . . .</b>	<b>99</b>
8.1.	Constitutive models to a phenomenological modelling approach . . . . .	99
8.1.1.	Viscoplastic framework . . . . .	100
8.1.2.	Three yield surfaces to model plastic dilatancy . . . . .	102
8.2.	Constitutive models for PC . . . . .	102
8.2.1.	$J_2$ -plasticity model . . . . .	103
8.2.2.	Boyce model . . . . .	103
8.3.	Continuum micromechanical modelling of ABS . . . . .	105
8.3.1.	Overall elastic material response . . . . .	106
8.3.2.	Microstructural considerations and scaling relations . . . . .	106
8.3.3.	Distributed crazing model . . . . .	107
8.3.4.	Continuum micromechanical Raghava model . . . . .	109
8.3.5.	Combined model for shear yielding and distributed crazing . . . . .	109
<b>9.</b>	<b>Macroscopic modelling approach . . . . .</b>	<b>113</b>
9.1.	Constitutive modelling . . . . .	113
9.2.	Parameter calibration . . . . .	113
9.2.1.	Comparison of the initial yield loci . . . . .	115
9.3.	Numerical studies . . . . .	117
9.3.1.	SENT fracture tests . . . . .	117
9.3.2.	Plastic zone formation at a notch . . . . .	118
9.3.3.	Simulation of fracture behaviour . . . . .	124
9.4.	Conclusions . . . . .	128
<b>10.</b>	<b>Unit cell modelling approach . . . . .</b>	<b>131</b>
10.1.	Unit cell models . . . . .	131
10.2.	Blend morphology and unit cell geometry . . . . .	132
10.3.	Finite element modelling . . . . .	134
10.3.1.	Meshing and local failure . . . . .	134
10.3.2.	Boundary conditions and load cases . . . . .	134
10.4.	Impact of the key microstructural parameters . . . . .	137
10.4.1.	Constitutive modelling . . . . .	137
10.4.2.	Material parameter calibration . . . . .	138
10.4.3.	Calibrated phase material behaviour . . . . .	140
10.4.4.	Results - uniaxial tension . . . . .	140
10.4.5.	Results - specific work of fracture . . . . .	149
10.4.6.	Loading with $\langle \eta_\epsilon \rangle = 1$ . . . . .	154
10.4.7.	Conclusions . . . . .	158

10.5. Impact of plastic deformation mechanisms . . . . .	159
10.5.1. $J_2$ -DC model calibration . . . . .	159
10.5.2. Numerical study - deformation behaviour . . . . .	161
10.5.3. Results - PC/ABS ( $J_2/J_2$ -DC) . . . . .	162
10.5.4. Results - PC/ABS (Boyce/ $J_2$ -DC) . . . . .	166
10.5.5. Conclusions . . . . .	167
10.6. Conclusions . . . . .	169
<b>11. Conclusions and outlook . . . . .</b>	<b>171</b>
11.1. Conclusions . . . . .	171
11.2. Outlook . . . . .	174
<b>A. Appendix to Chapter 6 . . . . .</b>	<b>175</b>
A.1. Tables to the uniaxial tensile tests . . . . .	175
A.2. Tables to the SENT fracture tests . . . . .	176
<b>B. Appendix to Chapter 7 . . . . .</b>	<b>177</b>
B.1. Tables to the uniaxial tensile tests . . . . .	177
B.2. Tables to the SENT fracture tests . . . . .	177
<b>C. Appendix to Chapter 9 . . . . .</b>	<b>179</b>
C.1. Material parameters to the constitutive models . . . . .	179
<b>D. Appendix to Chapter 10 . . . . .</b>	<b>181</b>
D.1. Material parameters to the constitutive models . . . . .	181
D.2. Implementation details . . . . .	182
D.2.1. Time scaling in simulations of viscous materials . . . . .	182
D.2.2. Coordinate systems in Abaqus VUMAT user subroutines . . . . .	182
D.2.3. The $J_2$ -plasticity model in Abaqus/Explicit . . . . .	183
<b>Publications and talks . . . . .</b>	<b>185</b>
<b>Nomenclature . . . . .</b>	<b>187</b>
<b>Bibliography . . . . .</b>	<b>195</b>
<b>List of figures . . . . .</b>	<b>205</b>
<b>List of tables . . . . .</b>	<b>215</b>

# 1. Introduction

Synthetic polymers are the youngest class of materials that surround us, having only been introduced throughout the 20th century. Yet, their production volume has outpaced that of steel and aluminium, mainly due to their popularity as packaging materials and in the construction sector [34]. Continuous efforts in research and development have made them popular engineering materials as well. These so-called engineering plastics, mainly used in the automotive and electronics industries, exhibit various desirable mechanical, thermal, and electrical properties.

One of the beneficial traits of polymers is their variability. Bespoke materials can be developed to meet the requirements of particular applications. In general, their strength is about 10 % and their elastic stiffness is about 0.1 % of that of metals. In contrast, pure polymers feature a far lower density than metals. Furthermore, compared to metals, they are also far superior electrical and thermal isolators. However, if needed these characteristics can easily be modified by adding fillers [34].

Another way of creating polymer materials with desired properties is blending several polymers together. This can be done to improve the processability, lowering the costs, or improve the resistance to environmental impact and other mechanical characteristics. One polymer blend that achieves all these goals is the class of PC/ABS blends, mixtures of the glassy thermoplastic polycarbonate (PC) and acrylonitrile-butadiene-styrene (ABS).

## 1.1. Motivation

PC/ABS blends are commercially available in a great variety of compositions. Since the ABS phase is itself a mixture of the glassy thermoplastic styrene-acrylonitrile (SAN) and finely dispersed rubber (butadiene) particles, PC/ABS is referred to as a ternary blend. The commercial grades essentially differ by their composition (e.g., amount of PC, amount of rubber in ABS) and – consequently – their deformation and failure behaviours [23, 41, 59, 60, 76, 86, 103, 106, 114].

Pure PC, a glassy amorphous thermoplastic, is stiff and ductile, but in the presence of notches exhibits brittle failure. The main mechanical benefits of blending PC and ABS are an improved notch resistance and fracture toughness. The increase in toughness is achieved by preventing localisation of the damage and ultimately failure in the material. Introducing a multitude of damage initiation sites in the form of rubber particles enables

a distribution of the energy dissipation during failure. This is reflected in an improved toughness. A distinctive feature of PC/ABS blends is, that for certain compositions, the fracture toughness can be higher than that of both constituents which is referred to as the synergistic effect [43, 41, 42, 25, 114, 76]. Yet, this effect seems not universal and contradictory findings are reported in the literature [103, 66, 48]. But in general, the fracture behaviour of PC/ABS blends is found to be highly nonlinear with composition. These contradictory findings and a missing consensus about the underlying reasons emphasise that more experimental work and modelling is needed to better understand the failure behaviour of PC/ABS blends.

Regarding the deformation behaviour, one characteristic feature of PC/ABS blends is a macroscopic plastic dilatancy which is known to originate from various micromechanisms such as rubber particle cavitation, plastic void growth, crazing, and debonding at the interface between PC and ABS [42, 60, 17, 59]. Despite a variety of investigations into the deformation behaviour of PC/ABS blends, their plastic dilatancy is rarely reported in the literature [35, 54]. Since PC is plastically incompressible, the overall dilation originates from the ABS phase. Yet, the contributions of the individual micromechanisms are not fully clear and a systematic investigation into the dependence of the dilation behaviour on composition has not been done.

The different responses of PC/ABS blends to mechanical stress are accompanied and partly caused by a complex microstructure that depends on their composition as well as the manufacturing conditions [75, 74, 6, 114, 76, 58, 106, 32]. The phase-topology of PC/ABS blends rich in one of the two main constituents is that of a matrix-particle structure [75, 74, 114, 32, 106, 42]. For more equal volume fractions of PC and ABS, PC/ABS blends exhibit an interpenetrating phase morphology [57, 106, 74]. Since parts from PC/ABS are commonly manufactured through injection moulding, the direction of melt flow and high cooling rates often result in an anisotropic microstructure [74, 75, 114, 6]. The microstructure of PC/ABS blends as well as its dependence on composition and manufacturing have been analysed in many experimental studies. Yet, investigations on the consequences such as a possibly anisotropic deformation and fracture behaviour so far are rare.

In contrast to many fracture mechanical experimental studies on PC/ABS blends, theoretical investigations concerning the constitutive modelling of their mechanical behaviour are rare. For instance, the large-strain rate-dependent behaviour under uniaxial tension has been fitted by a phenomenological one-dimensional model in Fang et al. [35]. The plastically incompressible response under compressive loading was described by a rate-dependent  $J_2$  plasticity model in Wang et al. [112]. Qualitative micromechanical studies concerning the influence of the blend composition on the macroscopic response were carried out in works by Seelig and Van der Giessen [92, 93]. For practical applications involving structural finite element (FE) simulations, efficient macroscopic models are needed which quantitatively capture the material behaviour under complex loading states up to failure. Additionally, micromechanical approaches can help to further understand the local deformation and failure behaviour of PC/ABS blends and their dependence on composition. A better understanding of the micromechanisms involved could enable the

future development of bespoke materials and prediction of an ideal composition for a specific use case.

## 1.2. Objectives of this work

The work presented is dedicated to a better understanding of the composition-dependent material behaviour of PC/ABS blends from both an experimental and a theoretical modelling perspective on different scales.

The subject of this work concerns three commercial PC/ABS blends of different compositions provided in the form of injection-moulded raw materials. In two experimental studies, the three PC/ABS blends are investigated with the goal of gaining further insights into their composition- and orientation-dependent deformation and fracture behaviour. Emphasis is put on the plastic dilatancy and possible consequences of an anisotropic morphology in injection-moulded specimens.

In a modelling effort on the macroscale, for each PC/ABS material three plastically dilatant material models are calibrated from uniaxial tension with special emphasis on the volume strain response. Subsequently, the models are analysed regarding their abilities to reproduce the material response in complex loading situations. The objective thereby is to satisfy the need for an efficient macroscopic constitutive description of the material response that requires little calibration effort.

To systematically analyse the impact of the PC/ABS ratio and the rubber content in ABS on the deformation and failure behaviour of PC/ABS blends, a three-dimensional unit cell approach is presented. The primary objective is an improved understanding of the impact of the key blend parameters on the mechanical blend response and the micromechanical damage mechanisms involved in fracture.

## 1.3. Outline

Introduced in Chapter 2 are the fundamental continuum mechanical concepts as well as the finite element method (FEM), which is the tool used throughout this work to solve the initial boundary value problem (IBVP) posed by continuum mechanics. Starting with the kinematics of the continuum body, the concept of stress and the mechanical balance relations lead to the formulation of the IBVP. Subsequently, the weak formulation of the IBVP is deduced which is then discretised in space and time to enable solutions with the FEM.

The microstructure and behaviour of PC/ABS blends are complex and depend on many factors such as the composition and the material properties of the main constituents.

Therefore, Chapter 3 starts with an introduction to thermoplastics, the mechanical response of glassy polymers such as PC, and the concept of rubber toughening with an emphasis on the material behaviour of ABS. Afterwards, the composition-dependent behaviour and microstructure of PC/ABS blends are discussed based on experimental findings from the literature.

In Chapter 4, the three commercial PC/ABS blends that are the subject of further experimental investigations throughout this work are introduced. From micrographs, their morphology is analysed and through a novel application of a machine learning algorithm their composition is determined.

Chapter 5 describes in detail the experimental setup and methods, spanning the topics of specimen geometries, the method of digital image correlation (DIC), and the testing machine used to conduct the experimental work. Furthermore, limitations of the measuring hardware and possible implications on the experimental results are discussed.

In Chapter 6, an extensive study of the large-strain deformation and fracture behaviour of the three PC/ABS blends is presented. Experimental data gathered in uniaxial tensile tests and fracture experiments on single-edge-notch-tension (SENT) specimens is discussed regarding the impact of blend composition on the material response. Besides the uniaxial true stress-strain behaviour, particular emphasis is put on the volume strain response and the evolution of the plastic zone in the SENT fracture tests.

In a follow-up study, presented in Chapter 7, an impact of the anisotropic microstructure of the blends on the macroscopic deformation and failure behaviour is investigated. Both uniaxial tensile tests and fracture tests are conducted using specimens with a different orientation relative to the direction of melt flow during manufacturing than in the preceding study.

Laying the foundations for the modelling approaches presented later in the work, in Chapter 8 constitutive models are introduced to capture the specifics of the material response of PC, ABS, and PC/ABS blends. To deal with heterogeneous microstructures in a continuum mechanical sense, the Mori-Tanaka homogenisation approach is applied to material models aiming at capturing the material behaviour of ABS. To improve the micromechanics-based material modelling of ABS, a material model considering the deformation mechanisms of distributed crazing and shear yielding in a continuum micromechanical approach is presented.

A homogenised modelling approach to PC/ABS blends is introduced in Chapter 9. Three different plastically dilatant material models are compared to each other regarding their applicability to PC/ABS blends. The models are calibrated from the data of the uniaxial tensile tests, also taking into account the volume strain response. The models' abilities to capture the behaviour of PC/ABS in more complex loading situations are assessed in simulations of SENT fracture tests.

To take into account the complex microstructure of PC/ABS blends, in Chapter 10 a three-dimensional unit cell approach is presented. The PC/ABS ratio and rubber content

in ABS are varied in a systematic manner with the aim to better understand the impact of these two blend parameters on the fracture toughness of PC/ABS blends. Also, the impact of considering different plastic deformation mechanisms through more elaborate material modelling is investigated. The before mentioned novel constitutive model is introduced in the ABS phase. A critical review discusses its improvements and shortcomings in comparison to the existing models as well as the capabilities of the whole unit cell approach.

In Chapter 11, the most important implications of the work presented are summarised and conclusions are drawn. With an outlook on possible future investigations, this work comes to a close.





## 2. Continuum mechanics and the finite element method

---

*In the following chapter, the basic concepts of continuum mechanics and the finite element method are introduced since both are the fundamental tools to mathematically describe and subsequently overcome the challenges posed by material characterisation and modelling. A more comprehensive treatment of the concepts and methods presented can be found in the literature, e.g. Bertram [12], Bonet and Wood [13], Bower [14], Haupt [49], Holzapfel [55], De Souza Neto, Peric, and Owen [29], and Wriggers [115].*

---

### Notation

Scalar values are denoted by italicised Greek or Latin lowercase letters such as  $\alpha$  or  $f$ . Lowercase bold letters denote tensors of first order or vectors. The dyadic product between two tensors of first order  $\mathbf{a}$  and  $\mathbf{b}$  yields a tensor of second order  $\mathbf{A}$  and is specified by

$$\mathbf{A} = \mathbf{a} \otimes \mathbf{b} \quad \text{or} \quad A_{ij} = a_i b_j \quad (2.1)$$

in symbolic or index notation, respectively. In index notation, the Einstein summation convention is used. The second-order tensor  $\mathbf{C} = \mathbf{A} \cdot \mathbf{B}$  represents a single contraction between the two second-order tensors  $\mathbf{A}$  and  $\mathbf{B}$  which in index notation reads

$$C_{ij} = A_{ik} B_{kj} . \quad (2.2)$$

A single contraction between two tensors, hereafter is denoted by a single dot “ $\cdot$ ”. The single contraction of a tensor of second order  $\mathbf{A}$  with itself is denoted by

$$\mathbf{A}^2 = \mathbf{A} \cdot \mathbf{A} . \quad (2.3)$$

The colon “ $:$ ” denotes a double contraction between two tensors. The result of the double contraction  $\mathbf{A} : \mathbf{B}$  yields a scalar and is specified in index notation by

$$\alpha = A_{ij} B_{ij} . \quad (2.4)$$

The Frobenius norm of a tensor  $\mathbf{A}$  is denoted by  $\|\mathbf{A}\|$  and is given by

$$\|\mathbf{A}\| = \sqrt{\mathbf{A}:\mathbf{A}}. \quad (2.5)$$

The dyadic product between two tensors of second rank  $\mathbf{A}$  and  $\mathbf{B}$  yields a fourth-order tensor  $\mathbb{E} = \mathbf{A} \otimes \mathbf{B}$  which in index notation reads

$$E_{ijkl} = A_{ij}B_{kl}. \quad (2.6)$$

## 2.1. Continuum mechanics

This section introduces the equations which describe the motion and deformation of material bodies subjected to mechanical loads. Within the context of solid continuum mechanics, the material body  $\mathcal{B}$  of continuously distributed matter in space is regarded as a set  $\mathcal{B} = \{\mathcal{P}\}$  with material points  $\mathcal{P}$ . Considering the free body principle, this material body is separated from its surroundings creating the two disjoint sections of the outside world and the material body itself. Interactions between the material body and the outside world are described via balance relations.

### 2.1.1. Kinematics

To describe the deformation of  $\mathcal{B}$ , different configurations are introduced, i.e. different spatial distributions of the material points  $\mathcal{P}$  at fixed times  $t$ . Thereby, the reference configuration is fixed at will for the designation of the material points such that a particle in the reference configuration can be addressed through its material or reference coordinates  $\mathbf{X} = \mathbf{R}(\mathcal{P})$ , where  $\mathbf{R}$  is a one-to-one mapping between the material points and the reference coordinates. Hence, a material point  $\mathcal{P}$  may be identified in terms of its reference coordinates  $\mathbf{X}$  by

$$\mathcal{P} = \mathbf{R}^{-1}(\mathbf{X}) . \quad (2.7)$$

The time-dependent current configuration  $\chi_t$  maps a material point to its current position in space at time  $t$  and is given by

$$\mathbf{x} = \chi_t(\mathcal{P}, t) , \quad (2.8)$$

where  $\mathbf{x}$  are the spatial coordinates. In this work, both the reference coordinates  $\mathbf{X}$  and the spatial coordinates  $\mathbf{x}$  are defined with respect to the same Cartesian basis  $\{\mathbf{e}_i\}$  of the Euclidean point space  $\mathbb{E}^3$ .

While it is technically not necessary that the material body ever occupied the reference configuration, it is assumed here that the special current configuration at the time  $t = 0$

serves as the reference or initial configuration  $\chi_{t_0} = \mathbf{R}$ . By inserting Eq. (2.7) into Eq. (2.8), the current positions of all material points for all fixed times  $t$  can be specified by

$$\mathbf{x} = \chi_t(\chi_{t_0}^{-1}(\mathbf{X}), t) = \chi(\mathbf{X}, t), \quad (2.9)$$

where  $\chi$  denotes the motion of the material body  $\mathcal{B}$ . The motion  $\chi$  is assumed to be uniquely invertible such that the inverse motion exists and is specified by

$$\mathbf{X} = \chi^{-1}(\mathbf{x}, t). \quad (2.10)$$

The motion  $\chi(\mathbf{X}, t)$  is a so-called material representation which means it characterises a physical property with respect to the material coordinates  $\mathbf{X}$ . The inverse motion, in contrast, is a so-called spatial representation since it denotes a function defined with respect to the spatial coordinates  $\mathbf{x}$ . Therefore, in general the following two representations or descriptions of a physical quantity  $w = f(\mathcal{P}, t)$  exist in every particle  $\mathcal{P}$ , depending on whether  $\mathcal{P}$  is substituted by its current or reference position:

- Material (Lagrangian) representation:

$$\hat{f} : (\mathbf{X}, t) \mapsto w = \hat{f}(\mathbf{X}, t) = f(\mathbf{R}^{-1}(\mathbf{X}), t) \quad (2.11)$$

- Spatial (Eulerian) representation:

$$\bar{f} : (\mathbf{x}, t) \mapsto w = \bar{f}(\mathbf{x}, t) = f(\chi_t^{-1}(\mathbf{x}), t) \quad (2.12)$$

In the material description, the same fixed particle is tracked over time. In contrast, the spatial representation describes what happens over time at a fixed location in space  $\mathbf{x}$ .

## Deformation gradient

The difference between the current location  $\mathbf{x}$  of a material point and its initial position  $\mathbf{X}$  is referred to as the displacement  $\mathbf{u} = \mathbf{x} - \mathbf{X}$  given in its material representation by

$$\mathbf{u}(\mathbf{X}, t) = \chi(\mathbf{X}, t) - \mathbf{X}. \quad (2.13)$$

The motion  $\chi$  relates the positions of individual material points in the reference configuration  $\mathbf{X}$  and spatial configuration  $\mathbf{x}$ . To similarly relate the shape and deformation of line and volume elements, the behaviour of the motion in the neighbourhood of a point is specified by the deformation gradient  $\mathbf{F}$ . It represents a linear mapping between the two tangent spaces  $\mathbb{T}_{\mathbf{X}}$  and  $\mathbb{T}_{\mathbf{x}}$  formed by  $\mathbf{X}$  and  $\mathbf{x}$ , respectively, and is given by

$$\begin{aligned} \mathbf{F} : \mathbb{T}_{\mathbf{X}} &\longrightarrow \mathbb{T}_{\mathbf{x}} \\ d\mathbf{X} &\longmapsto d\mathbf{x} = \mathbf{F} \cdot d\mathbf{X}. \end{aligned} \quad (2.14)$$

The deformation gradient  $\mathbf{F}$  is key in continuum mechanics in its role as a measure of deformation. It is given by

$$\mathbf{F} = \frac{\partial \boldsymbol{\chi}(\mathbf{X}, t)}{\partial \mathbf{X}} = \frac{\partial \mathbf{x}}{\partial \mathbf{X}}. \quad (2.15)$$

Thus,  $\mathbf{F}$  is the material gradient of the motion. The material gradient refers to the derivative of a quantity, in this case the motion, given in its material representation with respect to the reference or material coordinates  $\mathbf{X}$ . Based on Eq. (2.15), the mapping for line elements ( $d\mathbf{x}$ ,  $d\mathbf{X}$ ), analogous transformations can be derived for surface elements ( $d\mathbf{a}$ ,  $d\mathbf{A}$ ) and volume elements ( $dv$ ,  $dV$ ). A surface element  $d\mathbf{a} = \mathbf{n} da$  with its unit normal  $\mathbf{n}$  in the current configuration is specified by

$$d\mathbf{a} = \det(\mathbf{F}) \mathbf{F}^{-T} \cdot d\mathbf{A}, \quad (2.16)$$

where  $d\mathbf{A}$  is the corresponding surface element with its unit normal  $\mathbf{N}$  in the reference configuration. Equation (2.16) is referred to as Nanson's formula. The change in volume from the reference configuration to the current configuration is specified by

$$dv = \det(\mathbf{F}) dV. \quad (2.17)$$

From Eq. (2.17) it follows that the determinant  $\det(\mathbf{F}) =: J$  is the volume ratio of the deformation. Since  $\mathbf{F}$  is invertible,  $\det(\mathbf{F})$  must be non-zero at all times. Furthermore from a physical perspective,  $\det(\mathbf{F}) > 0$  is required to prevent negative volumes, i.e. self-penetration of matter. A volume-preserving or isochoric deformation is characterised by  $J = 1$  for all times  $t$ .

As with every tensor of second order, the deformation gradient can be decomposed into symmetric and orthogonal parts and thus be represented as the single contraction of these parts. The orthogonal<sup>1</sup> part  $\mathbf{R}$  is the rotation. The symmetric<sup>2</sup> part then represents the stretch of the deformation. It is not unique since the complete deformation can either be represented through a stretch  $\mathbf{U}$  followed by the rotation  $\mathbf{R}$  or vice versa when the rotation of the material body is succeeded by the stretch  $\mathbf{V}$ . Thus, the two polar decompositions

$$\mathbf{F} = \mathbf{R} \cdot \mathbf{U} \quad \text{and} \quad \mathbf{F} = \mathbf{V} \cdot \mathbf{R} \quad (2.18)$$

exist. Owing to its position relative to  $\mathbf{R}$  in Eq. (2.18),  $\mathbf{U}$  is referred to as the right stretch tensor. It is defined in the reference configuration, whereas the left stretch tensor  $\mathbf{V}$  is defined in the spatial configuration.

<sup>1</sup> A second-order tensor  $\mathbf{A}$  is orthogonal if  $\mathbf{A}^T \cdot \mathbf{A} = \mathbf{1}$ , where  $\mathbf{1}$  denotes the second-order identity tensor.

<sup>2</sup> A second-order tensor  $\mathbf{A}$  is symmetric if  $\mathbf{A} = \mathbf{A}^T$ .

The eigenvalues of  $\mathbf{U}$  and  $\mathbf{V}$  are equal and called principal stretches  $\lambda_a$ . Hence, the spectral decomposition of  $\mathbf{U}$  and  $\mathbf{V}$  yields

$$\mathbf{U} = \sum_{a=1}^3 \lambda_a \mathbf{N}_a \otimes \mathbf{N}_a, \quad (2.19)$$

$$\mathbf{V} = \sum_{a=1}^3 \lambda_a \mathbf{n}_a \otimes \mathbf{n}_a. \quad (2.20)$$

The eigenvectors  $\mathbf{N}_a$  and  $\mathbf{n}_a$  are referred to as the principal material or spatial directions, respectively. The principal directions are related to each other via the rotation  $\mathbf{R}$  as specified by

$$\mathbf{n}_a = \mathbf{R} \cdot \mathbf{N}_a. \quad (2.21)$$

### Strain measures

The deformation gradient characterises all changes the material elements undergo over the course of a deformation and includes both rigid-body motion and distortion of the material body. The motivation for strain measures is to provide comparable measures of the distortion or strain of the material body as a deviation from rigid-body motion. As a consequence, strain measures have to be free of rotational parts and are therefore symmetric tensors. The right Cauchy-Green tensor  $\mathbf{C} \in \text{Sym}^+$  refers to the stretch at a material point in the reference configuration and is given by

$$\mathbf{C} = \mathbf{F}^T \cdot \mathbf{F} = \mathbf{U}^2 = \sum_{a=1}^3 \lambda_a^2 \mathbf{N}_a \otimes \mathbf{N}_a. \quad (2.22)$$

The left Cauchy-Green tensor  $\mathbf{B} \in \text{Sym}^+$  refers to the stretch at a material point in the current configuration and is specified by

$$\mathbf{B} = \mathbf{F} \cdot \mathbf{F}^T = \mathbf{V}^2 = \sum_{a=1}^3 \lambda_a^2 \mathbf{n}_a \otimes \mathbf{n}_a. \quad (2.23)$$

Neither of the two Cauchy-Green tensors includes information about the rotation, just like the left and right stretch tensors. Hence, they are eligible starting points for the computation of strain tensors. In order to provide meaningful measures to describe the distortion, a strain measure should vanish in a strain free configuration that is the initial configuration. The following two strain measures meet this requirement and represent changes in length and angle of material line elements:

- The Green-Lagrange strain tensor  $\mathbf{E}$  operates in the reference configuration and is given by

$$\mathbf{E} = \frac{1}{2} (\mathbf{C} - \mathbf{1}), \quad (2.24)$$

where  $\mathbf{1}$  denotes the second-order identity tensor.

- The Euler-Almansi strain tensor

$$\mathbf{A} = \frac{1}{2} (\mathbf{1} - \mathbf{B}^{-1}) \quad (2.25)$$

operates in the current configuration.

The Euler-Almansi strain tensor is the result of the push-forward operation<sup>3</sup> applied to the Green-Lagrange strain tensor as given by

$$\mathbf{A} = \mathbf{F}^{-T} \cdot \mathbf{E} \cdot \mathbf{F}^{-1} . \quad (2.26)$$

Seth [96] introduced a generalised strain measure as a function of  $k \in \mathbb{R} \setminus 0$  which reads as

$$\mathbf{E}^k = \frac{1}{k} (\mathbf{U}^k - \mathbf{1}) \quad (2.27)$$

in material (Lagrangian) description and

$$\mathbf{e}^k = \frac{1}{k} (\mathbf{V}^k - \mathbf{1}) \quad (2.28)$$

in spatial (Eulerian) description. In the case of  $k = 0$ , the Hencky strain tensor is specified by

$$\mathbf{E}^H = \frac{1}{2} \ln(\mathbf{C}) = \ln(\mathbf{U}) \quad \text{or} \quad \mathbf{e}^H = \frac{1}{2} \ln(\mathbf{B}) = \ln(\mathbf{V}) , \quad (2.29)$$

respectively. Since the Hencky strain tensor is particularly useful in nonlinear constitutive theories, it is the primary measure of strain used in this work.

### 2.1.2. The concept of stress

The concept of stress is based on the traction vector  $\mathbf{t} = \mathbf{t}(\mathbf{x}, t)$ . Besides  $\mathbf{x}$  and  $t$ , it is only dependent on the outer normal vector  $\mathbf{n}$  of the surface of a body or free-cut body part. On the whole surface, the infinitesimal surface force  $d\mathbf{f}_o$  is related to the stress vector  $\mathbf{t}$  in the spatial configuration through  $d\mathbf{f}_o = \mathbf{t} da$ . The traction vector  $\mathbf{t}$  at a point  $\mathbf{x}$  on the boundary surface of a body is the linear map between a second rank tensor  $\boldsymbol{\sigma}$  and the outer normal  $\mathbf{n}$  in what is referred to as the Cauchy principle

$$\mathbf{t} = \boldsymbol{\sigma} \cdot \mathbf{n} , \quad (2.30)$$

where  $\boldsymbol{\sigma}$  denotes the symmetric Cauchy stress tensor. Its components describe the effects of the surface force acting upon on a material surface element in the spatial configuration.

<sup>3</sup> The transformation of a tensor field operating in the reference configuration to obtain its representation with respect to the current configuration.

In a similar fashion, the infinitesimal surface force  $d\mathbf{f}_o$  (acting in the current configuration) can be related to a traction vector  $\mathbf{T}$  and a material surface element  $dA$  with corresponding outer normal  $\mathbf{N}$  in the material configuration through  $d\mathbf{f}_o = \mathbf{T} dA$ . Analogous to Eq. (2.30), the 1st Piola-Kirchhoff stress tensor  $\mathbf{P}$  is specified by

$$\mathbf{T} = \mathbf{P} \cdot \mathbf{N} . \quad (2.31)$$

The 1st Piola-Kirchhoff stress tensor describes the effects of the surface forces on a material line element in the material configuration and, in general, is not symmetric. Because of  $d\mathbf{f}_o = \mathbf{t} da = \mathbf{T} dA$ , the Cauchy stress tensor  $\boldsymbol{\sigma}$  and the 1st Piola-Kirchhoff stress tensor  $\mathbf{P}$  are linked by

$$\mathbf{P} = J\boldsymbol{\sigma} \cdot \mathbf{F}^{-T} \quad \text{or} \quad \boldsymbol{\sigma} = J^{-1}\mathbf{P} \cdot \mathbf{F}^T , \quad (2.32)$$

respectively. Like every second-order tensor, stress tensors can be decomposed into a hydrostatic and a deviatoric part. From a continuum mechanical point of view, the split in hydrostatic and deviatoric parts separates components of a tensor describing the volume change from those associated with shape change. Considering the Cauchy stress tensor  $\boldsymbol{\sigma}$ , this decomposition reads as

$$\boldsymbol{\sigma} = \boldsymbol{\sigma}' + \sigma_m \mathbf{1} , \quad (2.33)$$

where  $\boldsymbol{\sigma}'$  denotes the stress deviator and the hydrostatic stress  $\sigma_m$  is given by

$$\sigma_m = \frac{1}{3} \text{tr}(\boldsymbol{\sigma}) . \quad (2.34)$$

The trace of the Cauchy stress is also one of the three principal invariants of the Cauchy stress tensor.

The principal invariants of a second-order tensor behave invariant with respect to a change of basis or coordinate system, hence their name. They appear as coefficients in the characteristic polynomial to the homogeneous algebraic system of equations which in the case of the Cauchy stress read as

$$(\boldsymbol{\sigma} - \sigma_a \mathbf{1}) \cdot \mathbf{n}_a = \mathbf{0} , \quad a = 1, 2, 3 \quad (2.35)$$

with the eigenvalues or principal stresses  $\sigma_a$  and the eigenvectors  $\mathbf{n}_a$ , also referred to as the principal axes. The principal axes define an orthogonal basis in which the off-diagonal components of  $\boldsymbol{\sigma}$ , the shear stresses, vanish. For solutions of Eq. (2.35) to exist, it is required that  $\det(\boldsymbol{\sigma} - \sigma_a \mathbf{1}) = 0$ . This yields the characteristic polynomial for the principal stresses

$$\sigma_a^3 - I_1 \sigma_a^2 + I_2 \sigma_a - I_3 = 0 , \quad a = 1, 2, 3 \quad (2.36)$$

with the principal invariants of the Cauchy stress  $\boldsymbol{\sigma}$  given by

$$I_1 = \text{tr}(\boldsymbol{\sigma}) , \quad (2.37)$$

$$I_2 = \frac{1}{2} [\text{tr}(\boldsymbol{\sigma})^2 - \text{tr}(\boldsymbol{\sigma}^2)] , \quad (2.38)$$

$$I_3 = \det(\boldsymbol{\sigma}) , \quad (2.39)$$

where  $\boldsymbol{\sigma}^2 = \boldsymbol{\sigma} \cdot \boldsymbol{\sigma}$ .

In similar fashion, the principal invariants  $J_a$  of the stress deviator  $\boldsymbol{\sigma}'$  can be calculated and are given by

$$J_1 = \text{tr}(\boldsymbol{\sigma}') = 0, \quad (2.40)$$

$$J_2 = \frac{1}{2} \text{tr}((\boldsymbol{\sigma}')^2) = \frac{1}{2} \boldsymbol{\sigma}' : \boldsymbol{\sigma}', \quad (2.41)$$

$$J_3 = \det(\boldsymbol{\sigma}'). \quad (2.42)$$

The first invariant  $J_1$  reiterates the characteristic feature of deviatoric tensors being trace free. The second invariant of the deviatoric stress  $J_2$  is important in this work as part of an eponymous material model (Sec. 8.2.1).

### 2.1.3. Time derivatives of kinematic quantities

Since a deformation may not only be time-dependent but also nonlinear in its temporal evolution, the rate of changes of the kinematic fields is required for its description. The material derivative, i.e. the total derivative with respect to time of the motion  $\boldsymbol{x}$  or  $\boldsymbol{\chi}$ , respectively, is the velocity field  $\boldsymbol{v}$  specified by

$$\boldsymbol{v} = \dot{\boldsymbol{x}} = \frac{d}{dt} \boldsymbol{\chi}(\mathcal{P}, t). \quad (2.43)$$

Thus, its material representation  $\hat{\boldsymbol{v}}$  is given by

$$\hat{\boldsymbol{v}} = \frac{\partial}{\partial t} \boldsymbol{\chi}(\boldsymbol{X}, t). \quad (2.44)$$

Its spatial representation  $\bar{\boldsymbol{v}}$  is obtained by substituting  $\boldsymbol{X} = \boldsymbol{\chi}^{-1}(\boldsymbol{x}, t)$

$$\bar{\boldsymbol{v}} = \hat{\boldsymbol{v}}(\boldsymbol{\chi}^{-1}(\boldsymbol{x}, t), t). \quad (2.45)$$

Since the reference coordinates  $\boldsymbol{X}$  are time-independent, for the material or Lagrangian representation  $\hat{f}(\boldsymbol{X})$  of a physical quantity  $w$ , the material derivative becomes the partial derivative

$$\dot{w}(t) = \frac{\partial}{\partial t} \hat{f}(\boldsymbol{X}, t). \quad (2.46)$$

In the case of the spatial or Eulerian representation  $\bar{f}(\boldsymbol{x}, t)$  of  $w$ , the material derivative as a result of applying the chain rule is given by

$$\dot{w}(t) = \frac{\partial}{\partial t} \bar{f}(\boldsymbol{x}, t) + \{\text{grad}(\bar{f}(\boldsymbol{x}, t))\} \cdot \bar{\boldsymbol{v}}(\boldsymbol{x}, t), \quad (2.47)$$



where  $\text{grad}(\cdot)$  is the spatial gradient operator denoting a differentiation with respect to  $\mathbf{x}$ . The acceleration  $\mathbf{a}$  is the material derivative of the velocity field  $\mathbf{v}$ . Its material representation is given by

$$\hat{\mathbf{a}}(\mathbf{X}, t) = \frac{\partial}{\partial t} \hat{\mathbf{v}}(\mathbf{X}, t) = \frac{\partial^2}{\partial t^2} \chi(\mathbf{X}, t) . \quad (2.48)$$

From Eq. (2.47), the spatial representation of the acceleration follows as

$$\bar{\mathbf{a}}(\mathbf{x}, t) = \frac{\partial}{\partial t} \bar{\mathbf{v}}(\mathbf{x}, t) + \{\text{grad}(\bar{\mathbf{v}}(\mathbf{x}, t))\} \cdot \bar{\mathbf{v}}(\mathbf{x}, t) . \quad (2.49)$$

The deformation gradient  $\mathbf{F}$  (Eq. (2.15)) describes the change of material line elements  $d\mathbf{x}$ . The corresponding property describing the rate at which these changes take place in

$$\frac{d}{dt} (d\mathbf{x}) = \mathbf{L} \cdot d\mathbf{x} \quad (2.50)$$

is the spatial velocity gradient

$$\mathbf{L}(\mathbf{x}, t) = \text{grad}(\bar{\mathbf{v}}(\mathbf{x}, t)) . \quad (2.51)$$

The velocity gradient in its material representation describes the rate of change of the deformation gradient itself and is given by

$$\dot{\mathbf{F}} = \text{Grad}(\hat{\mathbf{v}}(\mathbf{X}, t)) , \quad (2.52)$$

where  $\text{Grad}(\cdot)$  is the material gradient operator denoting a differentiation with respect to  $\mathbf{X}$ . The material velocity gradient  $\dot{\mathbf{F}}$  and the spatial velocity gradient  $\mathbf{L}$  are related to each other by  $\dot{\mathbf{F}} = \mathbf{L} \cdot \mathbf{F}$ . Likewise to the deformation gradient  $\mathbf{F}$ , the velocity gradient  $\mathbf{L}$  comprises the stretch as well as the rotation of the deformation. But unlike the former, it is split into the corresponding parts additively. The changes in stretch and rotation are represented by the symmetric and skew parts, respectively, such that the decomposition of  $\mathbf{L}$  is given by

$$\mathbf{L} = \text{sym}(\mathbf{L}) + \text{skw}(\mathbf{L}) = \frac{1}{2} (\mathbf{L} + \mathbf{L}^T) + \frac{1}{2} (\mathbf{L} - \mathbf{L}^T) = \mathbf{D} + \mathbf{W} . \quad (2.53)$$

The symmetric part  $\mathbf{D} = \frac{1}{2} (\mathbf{L} + \mathbf{L}^T)$  is called the rate of deformation or strain rate tensor. The skew part  $\mathbf{W} = \frac{1}{2} (\mathbf{L} - \mathbf{L}^T)$  is referred to as the spin tensor.

#### 2.1.4. Strain rate measures

The rate of deformation  $\mathbf{D} = \mathbf{D}(\mathbf{x}, t)$  is a tensor field operating in the current configuration and as such is a spatial representation. The material representation of the strain rate tensor is called the Green strain rate tensor

$$\dot{\mathbf{E}}(\mathbf{X}, t) = \frac{1}{2} (\dot{\mathbf{F}}^T \cdot \mathbf{F} + \mathbf{F}^T \cdot \dot{\mathbf{F}}) . \quad (2.54)$$

It is the result of the pull-back operation<sup>4</sup> applied to the spatial strain rate tensor  $\mathbf{D}$  as given by

$$\dot{\mathbf{E}} = \mathbf{F}^T \cdot \mathbf{D} \cdot \mathbf{F}. \quad (2.55)$$

Hence, the relation between the material and spatial representations of the strain rate tensors  $\dot{\mathbf{E}}$  and  $\mathbf{D}$  is similar to the relation between the Green-Lagrange strain tensor  $\mathbf{E}$  and the Almansi-Euler strain tensor  $\mathbf{A}$  (Eq. (2.26)).

### 2.1.5. Concept of objectivity

Mathematical representations of physical processes must consider that these processes are independent of a change of observer. This is reflected by the concept of objectivity for tensor fields describing physical quantities, kinematics, strain, and stress. The concept of objectivity imposes requirements on the transformation behaviour under a change of observer.

The position  $\mathbf{x}^*$  from the view of a second observer of the same point in space  $\mathbf{x}$  is given by the Euclidean transformation

$$\mathbf{x}^* = \mathbf{c}(t) + \mathbf{Q}(t) \cdot \mathbf{x}, \quad (2.56)$$

where the vector  $\mathbf{c}$  is a translation and  $\mathbf{Q}$  is a proper orthogonal rotation ( $\det(\mathbf{Q}) = +1$ ) and both are time-dependent. A second-order tensor  $\mathbf{A}$ , a vector  $\mathbf{a}$ , and a scalar  $\alpha$  fulfil the requirement of objectivity, if they transform according to

$$\mathbf{A}^* = \mathbf{Q} \cdot \mathbf{A} \cdot \mathbf{Q}^T, \quad (2.57)$$

$$\mathbf{a}^* = \mathbf{Q} \cdot \mathbf{a}, \quad (2.58)$$

$$\alpha^* = \alpha. \quad (2.59)$$

A change of observer, as described by Eq. (2.56), may equally be seen as a description of a rigid-body motion applied to the current configuration. As such, the transformation rules for tensor fields regarding the Euclidean transformation must also hold in the case of rigid-body motions superimposed on the material body  $\mathcal{B}$ . Since rigid-body motion must not impact the deformation and stress state, the quantities describing these must also satisfy Eq. (2.57).

The deformation gradient  $\mathbf{F}$  is an objective quantity, although it transforms according to

$$\mathbf{F}^* = \mathbf{Q} \cdot \mathbf{F}, \quad (2.60)$$

the reason being that one of its indices describes material coordinates  $\mathbf{X}$ . For the same reason, the right stretch tensor  $\mathbf{U}$  remains unaltered in the case of a change of observer.

---

<sup>4</sup> The transformation of a tensor field operating in the current configuration to obtain its representation with respect to the reference configuration.

Since the spatial velocity gradient  $\mathbf{L}$  does not transform according to Eq. (2.57), it is not objective due to the spin tensor  $\mathbf{W}$  being affected by rigid-body motions. The rate of deformation tensor  $\mathbf{D}$  is objective, however.

### 2.1.6. Objective stress rates

While the Cauchy stress tensor  $\boldsymbol{\sigma}^* = \mathbf{Q} \cdot \boldsymbol{\sigma} \cdot \mathbf{Q}^T$  is an objective quantity, its time derivative given by

$$\dot{\boldsymbol{\sigma}}^* = \dot{\mathbf{Q}} \cdot \boldsymbol{\sigma} \cdot \mathbf{Q}^T + \mathbf{Q} \cdot \dot{\boldsymbol{\sigma}} \cdot \mathbf{Q}^T + \mathbf{Q} \cdot \boldsymbol{\sigma} \cdot \dot{\mathbf{Q}}^T \quad (2.61)$$

is not. In general, material time derivatives of objective tensors are not objective. However, time-dependent processes that require a formulation in rate form need objective stress rates. These objective rates are modified material time derivatives that fulfil the requirement of objectivity.

A possible definition of an objective stress rate can be obtained by substituting the material time derivative of the rotation  $\dot{\mathbf{Q}}$  specified by

$$\dot{\mathbf{Q}} = \mathbf{W}^* \cdot \mathbf{Q} - \mathbf{Q} \cdot \mathbf{W} \quad (2.62)$$

into Eq. (2.61). In doing so, one obtains the Jaumann-Zaremba rate of Cauchy stress

$$\overset{\nabla}{\boldsymbol{\sigma}} = \dot{\boldsymbol{\sigma}} - \mathbf{W} \cdot \boldsymbol{\sigma} + \boldsymbol{\sigma} \cdot \mathbf{W}, \quad (2.63)$$

for which the objectivity requirement for second-order tensor fields holds.

Another approach to obtain objective stress rates is given in the form of the Lie time derivative that begins with the pull-back operation of the spatial stress tensor field to the reference configuration, then takes the material time derivative, and afterwards performs the push-forward operation on the result. The objective stress rate obtained using the Lie time derivative is called the Oldroyd stress rate, and for the Cauchy stress  $\boldsymbol{\sigma}$  is specified by

$$\begin{aligned} \mathcal{L}(\boldsymbol{\sigma}) &= \mathbf{F} \cdot \left[ \frac{d(\mathbf{F}^{-1} \cdot \boldsymbol{\sigma} \cdot \mathbf{F}^{-T})}{dt} \right] \cdot \mathbf{F}^T \\ &= \mathbf{F} \cdot \left( \dot{\mathbf{F}}^{-1} \cdot \boldsymbol{\sigma} \cdot \mathbf{F}^{-T} + \mathbf{F}^{-1} \cdot \dot{\boldsymbol{\sigma}} \cdot \mathbf{F}^{-T} + \mathbf{F}^{-1} \cdot \boldsymbol{\sigma} \cdot \dot{\mathbf{F}}^{-T} \right) \cdot \mathbf{F}^T. \end{aligned} \quad (2.64)$$

Substituting with  $\dot{\mathbf{F}}^{-1} = -\mathbf{F}^{-1} \cdot \mathbf{L}$  and  $\dot{\mathbf{F}}^{-T} = -\mathbf{L}^T \cdot \mathbf{F}^{-T}$  yields

$$\mathcal{L}(\boldsymbol{\sigma}) = \dot{\boldsymbol{\sigma}} - \mathbf{L} \cdot \boldsymbol{\sigma} - \boldsymbol{\sigma} \cdot \mathbf{L}^T. \quad (2.65)$$

The Jaumann-Zaremba stress rate (Eq. (2.63)) is indeed a special case of the Oldroyd stress rate (Eq. (2.65)) with the rate of deformation tensor  $\mathbf{D}$  assumed to vanish. Another

important special case of the Oldroyd stress rate is obtained when setting  $\mathbf{F} = \mathbf{R}$ . This is referred to as the Green-Naghdi stress rate  $\dot{\boldsymbol{\sigma}}$  as specified by

$$\dot{\boldsymbol{\sigma}} = \dot{\boldsymbol{\sigma}} - \dot{\mathbf{R}} \cdot \mathbf{R}^T \cdot \boldsymbol{\sigma} + \boldsymbol{\sigma} \cdot \dot{\mathbf{R}} \cdot \mathbf{R}^T. \quad (2.66)$$

In the case of rigid-body rotation ( $\mathbf{W} = \dot{\mathbf{R}} \cdot \mathbf{R}^T$ ), the Jaumann-Zaremba and the Green-Naghdi stress rate coincide. It should be noted that if the material body is not subjected to finite shear and finite rotations, both rates are approximately equal.

## 2.2. Balance relations of mechanics

As a result of the free-body principle, the material body  $\mathcal{B}$  and the surrounding world are defined as two disjoint sections. Whereas kinematics just describes the geometry of motion, the field of kinetics relates the motion with its reasons from the outside world. Interactions between the outside world and the material body are described in balance relations that must be satisfied for the material body as a whole, as well as for each particle. From a mechanical standpoint, those relations make up the balance of mass, linear momentum, and rotational momentum.

### Reynolds transport theorem

The Reynolds transport theorem as well as the general balance relation for an arbitrary scalar and vector-valued physical quantity  $\psi$  and  $\boldsymbol{\psi}$ , respectively, are introduced with the purpose of gaining a better understanding of the balance relations of actual physical quantities. The Reynolds transport theorem states that the material derivative in of a volume specific physical quantity  $\psi = \psi(\mathbf{x}, t)$  in a volume  $V(t)$  is given as a sum of a local and a convective part as specified by

$$\frac{d}{dt} \iiint_{V(t)} \psi \, dv = \iiint_{V(t)} \frac{\partial \psi}{\partial t} \, dv + \iint_{\partial V(t)} \boldsymbol{\psi} \mathbf{v} \cdot \mathbf{n} \, da, \quad (2.67)$$

where  $\mathbf{v} = \bar{\mathbf{v}}(\mathbf{x}, t)$  denotes the spatial velocity field and  $\mathbf{n}$  is the unit outward normal. On the right-hand side of Eq. (2.67), the local part is given by the volume integral of the time derivative of  $\psi$ . The convective part is specified by the transport of  $\psi$  through the volume's current surface  $\partial V(t)$ . It is given by the area integral over  $\partial V(t)$  of the surface element's velocity in normal direction multiplied with the local value of  $\psi$ .

In the realm of continuum mechanics, the volume  $V(t)$  is the volume occupied by the material body  $\mathcal{B}$ , a closed system, at time  $t$ . The divergence or Gauß theorem in terms of the vector-valued quantity  $\boldsymbol{\psi} \mathbf{v}$  is given by

$$\iint_{\partial V(t)} \boldsymbol{\psi} \mathbf{v} \cdot \mathbf{n} \, da = \iiint_{V(t)} \operatorname{div}(\boldsymbol{\psi} \mathbf{v}) \, dv. \quad (2.68)$$

By means of the divergence theorem (Eq. (2.68)), the term describing the convective flow can be transformed such that Eq. (2.67) can be rewritten as

$$\frac{d}{dt} \iiint_{V(t)} \psi \, dv = \iiint_{V(t)} \frac{\partial \psi}{\partial t} + \operatorname{div}(\psi \mathbf{v}) \, dv. \quad (2.69)$$

Assuming a vector-valued quantity  $\boldsymbol{\psi} = \boldsymbol{\psi}(\mathbf{x}, t)$ , Eq. (2.69) reads

$$\frac{d}{dt} \iiint_{V(t)} \boldsymbol{\psi} \, dv = \iiint_{V(t)} \frac{\partial \boldsymbol{\psi}}{\partial t} + \operatorname{div}(\boldsymbol{\psi} \otimes \mathbf{v}) \, dv, \quad (2.70)$$

where the divergence theorem formulated in terms of the second rank tensor field  $\boldsymbol{\psi} \otimes \mathbf{v}$  as specified by

$$\iint_{\partial V(t)} (\boldsymbol{\psi} \otimes \mathbf{v}) \cdot \mathbf{n} \, da = \iiint_{V(t)} \operatorname{div}(\boldsymbol{\psi} \otimes \mathbf{v}) \, dv \quad (2.71)$$

has been used to obtain the last addend under the integral of the right-hand side of Eq. (2.70).

## General balance relation

The general balance relation describes the rate of change of an extensive physical quantity  $\psi$  in the material body's volume  $V(t)$  but relates it to three causes:

- the production  $p_\psi$  within the material body,
- the supply  $s_\psi$  inside the material body, and
- the (non-convective) flow  $\mathbf{q}_\psi$  over the volume's surface.

Therefore, the so-called global form (with respect to the whole volume of the material body) of the general balance relation for  $\psi$  reads as

$$\frac{d}{dt} \iiint_{V(t)} \psi \, dv = \iiint_{V(t)} p_\psi + s_\psi \, dv + \iint_{\partial V(t)} \mathbf{q}_\psi \cdot \mathbf{n} \, da. \quad (2.72)$$

Applying the divergence theorem (Eq. (2.68)) to the last addend of the right-hand side of Eq. (2.72) and transforming the left-hand side according to the Reynolds transport theorem (Eq. (2.69)) yields the alternative form of the global balance relation as specified by

$$\iiint_{V(t)} \frac{\partial \psi}{\partial t} + \operatorname{div}(\psi \mathbf{v}) \, dv = \iiint_{V(t)} p_\psi + s_\psi \, dv + \iiint_{V(t)} \operatorname{div}(\mathbf{q}_\psi) \, dv. \quad (2.73)$$

With the requirement that it must be satisfied also for arbitrary subvolumes, the local form of the general balance relation is given by

$$\frac{\partial \psi}{\partial t} + \operatorname{div}(\psi \mathbf{v}) = p_\psi + s_\psi + \operatorname{div}(\mathbf{q}_\psi). \quad (2.74)$$

With regard to a vector-valued quantity  $\boldsymbol{\psi}$ , the global balance relation in its global form is given by

$$\iiint_{V(t)} \frac{\partial \psi}{\partial t} + \operatorname{div}(\psi \mathbf{v}) \, dv = \iiint_{V(t)} \mathbf{p}_\psi + \mathbf{s}_\psi \, dv + \iint_{\partial V(t)} \mathbf{Q}_\psi \cdot \mathbf{n} \, da, \quad (2.75)$$

where  $\mathbf{Q}_\psi$  denotes the second-order tensor of non-convective flow. The corresponding local form of the balance relation of  $\boldsymbol{\psi}$  reads

$$\frac{\partial \boldsymbol{\psi}}{\partial t} + \operatorname{div}(\boldsymbol{\psi} \otimes \mathbf{v}) = \mathbf{p}_\psi + \mathbf{s}_\psi + \operatorname{div}(\mathbf{Q}_\psi). \quad (2.76)$$

Balance relations with vanishing production, i.e.  $p_\psi = 0$ , are called conservation laws. In continuum mechanics, all balance relations are conservation laws. It must be noted though that all relations previously introduced only hold under the assumption of continuously differentiable fields  $\psi$  and  $\mathbf{q}_\psi$ , i.e. no discontinuity surfaces within the material body's volume.

### 2.2.1. Balance of mass

Every particle in the closed system that is the material body  $\mathcal{B}$  has a volumetric mass density  $\rho(\mathbf{x}, t)$  such that the mass of the material body is given by

$$m(t) = \iiint_{V(t)} \rho(\mathbf{x}, t) \, dv = \iiint_{V_0} \rho_0(\mathbf{X}) \, dV, \quad (2.77)$$

where  $\rho_0$  denotes the mass density in the reference configuration,  $V(t)$  is the volume that  $\mathcal{B}$  occupies in the current configuration, and  $V_0$  denotes the volume of  $\mathcal{B}$  in the reference configuration. Within the context of continuum mechanics and the closed system that  $\mathcal{B}$  is, no mass is added or subtracted. Consequently, there is neither a supply nor a flow of mass across the boundaries  $\partial V(t)$ . Also, mass is a conserved quantity. Hence, there is no production of mass within the material volume.

Therefore, the global form of the balance of volumetric mass density reads as

$$\dot{m} = \frac{d}{dt} \iiint_{V(t)} \rho(\mathbf{x}, t) \, dv = \frac{\partial}{\partial t} \iiint_{V_0} \rho_0(\mathbf{X}) \, dV = 0 \quad (2.78)$$

and states that mass is conserved. Substituting  $dV$  with Eq. (2.17) and requiring that Eq. (2.77) holds for all partial volumes, yields the continuity equation as given by

$$\rho(\mathbf{x}, t)J = \rho_0(\mathbf{X}), \quad (2.79)$$

where  $J = \det(\mathbf{F})$ . Under the assumption that mass is a conserved quantity, Eq. (2.74) for  $\psi = \rho$  yields the local form of the conservation of mass

$$\frac{\partial \rho}{\partial t} + \operatorname{div}(\rho \mathbf{v}) = 0 \quad \text{or} \quad \dot{\rho} + \rho \operatorname{div}(\mathbf{v}) = 0. \quad (2.80)$$

### 2.2.2. Balance of linear momentum

The linear momentum of the whole material body  $\mathcal{B}$  occupying the volume  $V(t)$  is characterised by the velocity field weighted with the mass density. As such it is a vector-valued quantity given by

$$\mathbf{I} = \iiint_{V(t)} \rho \mathbf{v} \, dv. \quad (2.81)$$

The linear momentum is impacted by the resultant force  $\mathbf{f}$ , which the free-cut material body is exposed to by its surroundings. It is given by

$$\mathbf{f} = \iiint_{V(t)} \rho \mathbf{b} \, dv + \iint_{\partial V(t)} \mathbf{t} \, da \quad (2.82)$$

and comprises forces distributed over the surface as well as the volume of the material body. The surface forces are a result of the Cauchy stress vector  $\mathbf{t}$  acting on  $\partial V(t)$ . The volume force density per unit mass  $\mathbf{b}$ , e.g. in form of gravity loading, is acting on all material points with volume mass density  $\rho$  that are part of  $\mathcal{B}$ .

As a generalisation of Newton's first law, the sum of all forces  $\mathbf{f}$  is equal to the temporal change of the linear momentum  $\dot{\mathbf{I}}$ , such that the global form of the balance of linear momentum is given by

$$\frac{d}{dt} \iiint_{V(t)} \rho \mathbf{v} \, dv = \iiint_{V(t)} \rho \mathbf{b} \, dv + \iint_{\partial V(t)} \mathbf{t} \, da. \quad (2.83)$$

In regards to the general balance relation (Eq. (2.75)), the volume forces can be identified as the supply  $\mathbf{s}_\psi = \rho \mathbf{b}$  and from Cauchy's principle (Eq. (2.30)) follows that the Cauchy stress represents the second rank tensor  $\mathbf{Q}_\psi$  of the non-convective flow. Since the linear momentum is a conserved quantity, no production needs to be considered.

To obtain the local form of the balance of linear momentum, the left-hand side of Eq. (2.83) can be transformed, evaluating the Reynolds theorem (Eq. (2.70)) for  $\psi = \rho \mathbf{v}$ . Additionally applying Cauchy's principle (Eq. (2.30)) and the divergence theorem (Eq. (2.71)) to the

second addend of the right-hand side of Eq. (2.83) yields the alternative formulation of the global form of the balance of linear momentum as specified by

$$\iiint_{V(t)} \rho \dot{\mathbf{v}} \, dv = \iiint_{V(t)} \rho \mathbf{b} \, dv + \iiint_{V(t)} \operatorname{div}(\boldsymbol{\sigma}) \, dv. \quad (2.84)$$

Requiring that Eq. (2.84) must also be satisfied for all partial volumes eventually yields the local form of the balance of linear momentum, also called Cauchy's first equation of motion

$$\rho \dot{\mathbf{v}} = \rho \mathbf{b} + \operatorname{div}(\boldsymbol{\sigma}). \quad (2.85)$$

In the special case of static systems, the acceleration vanishes ( $\dot{\mathbf{v}} = \mathbf{o}$ ) and Eq. (2.85) becomes

$$\rho \mathbf{b} + \operatorname{div}(\boldsymbol{\sigma}) = \mathbf{o}. \quad (2.86)$$

Equation (2.86) is referred to as Cauchy's equation of equilibrium.

### 2.2.3. Balance of rotational momentum

The rotational or angular momentum  $\mathbf{H}$  differs from the linear momentum  $\mathbf{I}$  in that it is always given relative to a point in space  $\mathbf{c}$ , fixed at will. As such, the vector-valued balanced quantity per unit volume in the current configuration is expressed through  $\boldsymbol{\psi} = \mathbf{r} \times \mathbf{v} \rho$ , where  $\mathbf{r} = (\mathbf{x} - \mathbf{c})$  denotes the position vector. The global angular momentum is therefore given by

$$\mathbf{H} = \iiint_{V(t)} \mathbf{r} \times \mathbf{v} \rho \, dv. \quad (2.87)$$

As is the linear momentum, the angular momentum is subject to change due to external forces, inducing a torque on the reference point  $\mathbf{c}$ . The vector of the resultant torque  $\mathbf{M}$  sums up the impact of the surface and volume forces in terms of their torque on  $\mathbf{c}$  as given by

$$\mathbf{M} = \iiint_{V(t)} \mathbf{r} \times \mathbf{b} \rho \, dv + \iint_{\partial V(t)} \mathbf{r} \times \mathbf{t} \, da. \quad (2.88)$$

Analogous to the linear momentum in the sense of a generalisation of Newton's first law, the rate of change of the angular momentum equals the resultant torque. Thus, the global form of the balance of angular momentum reads

$$\frac{d}{dt} \iiint_{V(t)} \mathbf{r} \times \mathbf{v} \rho \, dv = \iiint_{V(t)} \mathbf{r} \times \mathbf{b} \rho \, dv + \iint_{\partial V(t)} \mathbf{r} \times \mathbf{t} \, da. \quad (2.89)$$



By means of Cauchy's principle and the divergence theorem, the part of the resultant torque caused by the surface traction  $\mathbf{t}$  can be transformed as specified by

$$\iint_{\partial V(t)} \mathbf{r} \times \mathbf{t} \, da = \iint_{\partial V(t)} \mathbf{r} \times \boldsymbol{\sigma} \cdot \mathbf{n} \, da = \iiint_{V(t)} (\mathbf{r} \times \operatorname{div}(\boldsymbol{\sigma}) + \boldsymbol{\epsilon} : \boldsymbol{\sigma}^T) \, dv, \quad (2.90)$$

where  $\boldsymbol{\epsilon} = \epsilon_{ijk} \mathbf{e}_i \otimes \mathbf{e}_j \otimes \mathbf{e}_k$  denotes the third order permutation or Levi-Civita tensor whose components  $\epsilon_{ijk}$  are given by

$$\epsilon_{ijk} = \begin{cases} 1 & \text{for even permutations } \{ijk\} = \{123, 231, 312\} \\ -1 & \text{for odd permutations } \{ijk\} = \{132, 213, 321\} \\ 0 & \text{otherwise.} \end{cases} \quad (2.91)$$

Further following the steps undertaken for the linear momentum, the left-hand side of Eq. (2.89) can be transformed by means of the Reynolds transport theorem (Eq. (2.70)), evaluated for  $\boldsymbol{\psi} = \mathbf{r} \times \boldsymbol{\nu} \rho$ . This yields the alternative form of the global form of the angular momentum balance as specified by

$$\iiint_{V(t)} \mathbf{r} \times \dot{\boldsymbol{\nu}} \rho \, dv = \iiint_{V(t)} \mathbf{r} \times \mathbf{b} \rho \, dv + \iiint_{V(t)} (\mathbf{r} \times \operatorname{div}(\boldsymbol{\sigma}) + \boldsymbol{\epsilon} : \boldsymbol{\sigma}^T) \, dv. \quad (2.92)$$

Using the fact that the volume is arbitrary and rearranging yields

$$\mathbf{r} \times (\dot{\boldsymbol{\nu}} \rho - \mathbf{b} \rho - \operatorname{div}(\boldsymbol{\sigma})) = \boldsymbol{\epsilon} : \boldsymbol{\sigma}^T. \quad (2.93)$$

Now taking into account Eq. (2.85), Cauchy's first equation of motion, gives

$$\boldsymbol{\epsilon} : \boldsymbol{\sigma}^T = \mathbf{0}. \quad (2.94)$$

Evaluation of Eq. (2.94) yields a vector of constraints for the six off-diagonal components of the Cauchy stress tensor as specified by

$$\begin{bmatrix} \epsilon_{123} \sigma_{32} + \epsilon_{132} \sigma_{23} \\ \epsilon_{231} \sigma_{13} + \epsilon_{213} \sigma_{31} \\ \epsilon_{312} \sigma_{21} + \epsilon_{321} \sigma_{12} \end{bmatrix} = \begin{bmatrix} \sigma_{32} - \sigma_{23} \\ \sigma_{13} - \sigma_{31} \\ \sigma_{21} - \sigma_{12} \end{bmatrix} = \mathbf{0}. \quad (2.95)$$

In order to satisfy Eqs. (2.95), the Cauchy stress tensor must be symmetric. Thus, the local implication of the balance of rotational momentum is

$$\boldsymbol{\sigma} = \boldsymbol{\sigma}^T \quad (2.96)$$

also referred to as Cauchy's second equation of motion.

### 2.3. The initial boundary value problem (IBVP)

Cauchy's first equation of motion (Eq. (2.85)) in combination with a constitutive model, which links the stress tensor with the kinematic properties of the continuum body, leads to the formulation of IBVPs. In order to acquire a solution, appropriately defined initial and boundary conditions are required. Initial conditions define the position and velocity distribution of the whole material body in the initial configuration at time  $t = t_0$  as specified by

$$\mathbf{u}(\mathbf{x}, t_0) = \mathbf{u}_0(\mathbf{X}), \quad (2.97)$$

$$\dot{\mathbf{u}}(\mathbf{x}, t_0) = \dot{\mathbf{u}}_0(\mathbf{X}) \quad (2.98)$$

for all material points  $\mathcal{P}$  of the material body  $\mathcal{B}$ . The surface of the material body constitutes the domain boundary  $\partial V$  on which either the traction vector on  $\partial V_t$  or the motion have to be prescribed on  $\partial V_u$  such that

$$\partial V(t) = \partial V_u \cup \partial V_t, \quad \partial V_u \cap \partial V_t = \emptyset. \quad (2.99)$$

Constraining the motion by setting the displacement  $\bar{\mathbf{u}}$  on  $\partial V_u$  is called a geometric or Dirichlet boundary condition. Stipulation of the traction vector  $\bar{\mathbf{t}}$  on  $\partial V_t$  is referred to as a dynamic or Neumann boundary condition.

Apart from the constitutive law provided by a material model, appropriately reproducing the relation between stress and strain for the very material regarded, the strong form of the IBVP of continuum mechanics is then given by the set of equations

$$\operatorname{div}(\boldsymbol{\sigma}) + \rho \mathbf{b} = \rho \ddot{\mathbf{u}}, \quad (2.100a)$$

$$\mathbf{u} = \bar{\mathbf{u}} \quad \text{on } \partial V_u, \quad (2.100b)$$

$$\mathbf{t} = \bar{\mathbf{t}} \quad \text{on } \partial V_t, \quad (2.100c)$$

$$\mathbf{u}(\mathbf{x}, t_0) = \mathbf{u}_0(\mathbf{X}), \quad (2.100d)$$

$$\dot{\mathbf{u}}(\mathbf{x}, t_0) = \dot{\mathbf{u}}_0(\mathbf{X}). \quad (2.100e)$$

The solution of Eqs. (2.100) is not trivial and analytical solutions can only be obtained for a selected number of problems. However, approximate methods such as the finite element method (FEM) provide solution strategies for complex geometries of  $\mathcal{B}$  and  $V(t)$ .

### 2.4. The finite element method (FEM)

The FEM is the main tool in this work to compute the material response in simulations featuring complex problem geometries and loadings. Equations (2.100) can be formulated in a so-called weak form. The weak form of the IBVP is the starting point to an approximate solution with the finite element method (FEM). It can be shown that the FEM solution of

the weak form is the optimal solution regarding the potential energy of the problem in the manifold of possible solutions provided by the ansatz used. Inserting an approximate solution  $\mathbf{u}_h$  into the linear momentum balance (Eq. (2.100a)) yields

$$\operatorname{div}(\boldsymbol{\sigma}(\mathbf{u}_h)) + \rho \mathbf{b} - \rho \ddot{\mathbf{u}}_h = R, \quad (2.101)$$

where  $R$  denotes the residual, referring to a deviation from the equilibrium state.

### 2.4.1. The weak form

The weak form of the problem is constructed in a way that the residual vanishes for any suitable approximate solution. It requires the exact satisfaction of the balance only in a “weak” sense, namely just for points on  $\partial V_u$ . In order to obtain the weak form of the balance of linear momentum, the strong form of the problem is first multiplied with an arbitrary test function  $\delta \mathbf{u} = \{\delta \mathbf{u} \mid \delta \mathbf{u} = \mathbf{o} \text{ on } \partial V_u\}$ . Subsequent rearranging and integration over the whole current spatial domain  $V(t)$  yields

$$\iiint_{V(t)} \operatorname{div}(\boldsymbol{\sigma}) \cdot \delta \mathbf{u} \, dv + \iiint_{V(t)} \rho (\mathbf{b} - \ddot{\mathbf{u}}) \cdot \delta \mathbf{u} \, dv = 0. \quad (2.102)$$

The integrand of the first term in Eq. (2.102) can be transformed by reversely applying the product rule as specified by

$$\operatorname{div}(\boldsymbol{\sigma}) \cdot \delta \mathbf{u} = \operatorname{div}(\boldsymbol{\sigma} \cdot \delta \mathbf{u}) - \boldsymbol{\sigma} : \operatorname{grad}(\delta \mathbf{u}). \quad (2.103)$$

Subsequently applying the divergence theorem (Eq. (2.68)) and Cauchy’s principle (Eq. (2.30)), as well as introducing the boundary conditions in form of the traction vector and using that  $\delta \mathbf{u} = \mathbf{o}$  on  $\partial V_u$ , Eq. (2.102) becomes the weak form of the balance of linear momentum

$$G(\mathbf{x}, \delta \mathbf{u}) = \iiint_{V(t)} \boldsymbol{\sigma} : \operatorname{grad}(\delta \mathbf{u}) - \rho (\mathbf{b} - \ddot{\mathbf{u}}) \cdot \delta \mathbf{u} \, dv - \iint_{\partial V_t} \bar{\mathbf{t}} \cdot \delta \mathbf{u} \, da = 0. \quad (2.104)$$

$G(\mathbf{x}, \delta \mathbf{u})$  is nonlinear with respect to both the geometry of  $\mathcal{B}$  and the material model, which presents additional challenges in the solving process.

Equation (2.104) can also be derived using the principle of virtual work. In that sense, the test function  $\delta \mathbf{u}$  represents a virtual displacement. After rearranging Eq. (2.104), the individual contributions to the virtual work  $\delta W$  can then be identified as the internal

virtual work  $\delta W^{\text{int}}$ , the virtual work of the applied forces or external virtual work  $\delta W^{\text{ext}}$ , and the virtual work of the inertial forces  $\delta W^{\text{kin}}$  as specified by

$$\delta W^{\text{int}} = \iiint_{V(t)} \boldsymbol{\sigma} : \text{sym}(\text{grad}(\delta \mathbf{u})) \, dv, \quad (2.105)$$

$$\delta W^{\text{ext}} = \iiint_{V(t)} \rho \mathbf{b} \cdot \delta \mathbf{u} \, dv + \iint_{\partial V_t} \bar{\mathbf{t}} \cdot \delta \mathbf{u} \, da, \quad (2.106)$$

$$\delta W^{\text{kin}} = \iiint_{V(t)} \rho \ddot{\mathbf{u}} \cdot \delta \mathbf{u} \, dv, \quad (2.107)$$

where in Eq. (2.105) the symmetry of  $\boldsymbol{\sigma}$  has been exploited. It should be noted that the weak form is analytically exact and any deviation from equilibrium is the consequence of introducing approximate solutions.

#### 2.4.1.1. Discretisation in space

While the weak form reduces the requirements a solution must satisfy, it does not facilitate obtaining these for arbitrary shapes of the material body and thus integration domains. The finite element method represents a divide-and-conquer strategy to that challenge. In what is referred to as spatial discretisation, the geometry of the continuous body is subdivided into  $n_{\text{el}}$  finite elements that in their union approximate the volume of the material body in the reference configuration as given by

$$V_0 \approx V_0^{\text{h}} = \bigcup_{e=1}^{n_{\text{el}}} V_0^e. \quad (2.108)$$

Thereby, the elements in terms of their individual volumes  $V_0^e \subset V_0^{\text{h}}$  have to be continuous in the volume  $V_0^{\text{h}}$  yet disjoint, since an overlapping is not allowed.

In the finite element method, an interpolation function of a chosen order is used to approximate the field variables of interest. Here, this is the displacement  $\mathbf{u}$ , for which the approximation within an element reads

$$\mathbf{u} \approx \mathbf{u}_{\text{el}}^{\text{h}} = \sum_{i=1}^n N_i(\mathbf{X}) \mathbf{u}_i, \quad (2.109)$$

where  $\mathbf{u}_i$  are the  $n$  nodal displacements or degrees of freedom, and  $N_i(\mathbf{X})$  denotes the shape functions. In what is referred to as the isoparametric concept, the same ansatz functions are used for both the approximation of the kinematic properties and the geometry. The isoparametric concept allows for an easy mapping from a reference element  $\Omega_{\square}$  to both the reference and the current configuration, making it well suited for nonlinear

problems. Therefore, the approximations for the nodal positions in an element in the reference and current configuration are given by

$$\mathbf{X}_{\text{el}}^{\text{h}} = \sum_{i=1}^n N_i(\boldsymbol{\xi}) \mathbf{X}_i, \quad (2.110)$$

$$\mathbf{x}_{\text{el}}^{\text{h}} = \sum_{i=1}^n N_i(\boldsymbol{\xi}) \mathbf{x}_i, \quad (2.111)$$

where the shape functions  $N_i(\boldsymbol{\xi})$  are functions of the reference coordinates  $\boldsymbol{\xi}$  that are defined in the reference element  $\Omega_{\square}$ . Analogous to the description of motion for the continuum body by the configuration  $\boldsymbol{\chi}$  and the deformation gradient  $\mathbf{F}$ , similar unique point to point mappings from the reference element to the element in the initial and current configuration are used.

### 2.4.2. Discretisation of the weak form

As a consequence of the discretisation of the material body, the volume and surface integrals of the weak form in Eq. (2.104) become an assembly of the integrals of over all finite element volumes. Thereby, the same ansatz used for the kinematic properties is also applied to the virtual displacement  $\delta \mathbf{u}$  which gives

$$\delta \mathbf{u}_{\text{el}}^{\text{h}} = \sum_{i=1}^n N_i(\boldsymbol{\xi}) \delta \mathbf{u}_i, \quad (2.112)$$

$$\text{sym}\left(\text{grad}\left(\delta \mathbf{u}_{\text{el}}^{\text{h}}\right)\right) = \sum_{i=1}^n \mathbf{B}_{0i} \cdot \delta \mathbf{u}_i, \quad (2.113)$$

where  $\mathbf{B}_{0i}$  are matrices specifying the symmetric part of the spatial gradient of the shape functions  $N_i$ , independently of the displacement field. The individual parts of the weak form as specified in Eqs. (2.105), (2.106), and (2.107) can then be reformulated in a discretised manner and assembled as specified by

$$\begin{aligned} \iiint_{V(t)} \boldsymbol{\sigma} : \text{sym}(\text{grad}(\delta \mathbf{u})) \, dv &= \bigcup_{e=1}^{n_{\text{el}}} \sum_{i=1}^n \delta \mathbf{u}_i^T \cdot \iiint_{V^e(t)} \mathbf{B}_{0i}^T \cdot \boldsymbol{\sigma}^e \, dv^e \\ &= \bigcup_{e=1}^{n_{\text{el}}} \sum_{i=1}^n \delta \mathbf{u}_i^T \cdot \mathbf{f}_i^{\text{int}} = \delta \mathbf{u}^T \cdot \mathbf{f}^{\text{int}}, \end{aligned} \quad (2.114)$$

$$\begin{aligned}
 \iiint_{V(t)} \rho \mathbf{b} \cdot \delta \mathbf{u} \, dv + \iint_{\partial V_t} \bar{\mathbf{t}} \cdot \delta \mathbf{u} \, da &= \bigcup_{e=1}^{n_{el}} \sum_{i=1}^n \delta \mathbf{u}_i^T \cdot \iiint_{V^e(t)} N_i \rho \mathbf{b} \, dv^e \\
 &\quad + \bigcup_{r=1}^{n_\Gamma} \sum_{i=1}^m \delta \mathbf{u}_i^T \cdot \iint_{\partial V_t^r} N_i \bar{\mathbf{t}} \, da^r \\
 &= \delta \mathbf{u}^T \cdot \mathbf{f}^{\text{ext}}, \tag{2.115}
 \end{aligned}$$

$$\begin{aligned}
 \iiint_{V(t)} \rho \ddot{\mathbf{u}} \cdot \delta \mathbf{u} \, dv &= \bigcup_{e=1}^{n_{el}} \sum_{i=1}^n \sum_{j=1}^n \delta \mathbf{u}_i^T \cdot \left[ \iiint_{V^e(t)} N_i \rho^e N_j \, dv^e \right] \mathbf{1} \cdot \ddot{\mathbf{u}} \\
 &= \bigcup_{e=1}^{n_{el}} \sum_{i=1}^n \sum_{j=1}^n \delta \mathbf{u}_i^T \cdot \mathbf{M} \cdot \ddot{\mathbf{u}} = \delta \mathbf{u}^T \cdot \mathbf{M} \cdot \ddot{\mathbf{u}}, \tag{2.116}
 \end{aligned}$$

where  $\bigcup$  denotes the assembly operator,  $\mathbf{M}$  is the mass matrix,  $\mathbf{f}^{\text{int}}$  is the vector of the internal forces,  $\mathbf{f}^{\text{ext}}$  denotes the applied external forces in their entirety, and  $n_\Gamma$  is the number of elements on the traction surface of the discretised material body. Equations (2.114), (2.115), and (2.116) can be combined to rewrite the weak form (Eq. (2.104)) in its discrete version

$$\delta \mathbf{u}^T \cdot [\mathbf{M} \cdot \ddot{\mathbf{u}} + \mathbf{f}^{\text{int}} - \mathbf{f}^{\text{ext}}] = 0. \tag{2.117}$$

Since the virtual displacement  $\delta \mathbf{u}$  is arbitrary, Eq. (2.117) leads to the system of nonlinear ordinary differential equations

$$\mathbf{M} \cdot \ddot{\mathbf{u}} + \mathbf{f}^{\text{int}} - \mathbf{f}^{\text{ext}} = \mathbf{o}. \tag{2.118}$$

### 2.4.3. Discretisation in time

With regard to static problems ( $\ddot{\mathbf{u}} = 0$ ), Eq. (2.118) represents a system of nonlinear algebraic equations independent of time. However, if an inelastic constitutive behaviour such as viscoplasticity is considered, the material response depends on the temporal evolution of the deformation. In this case, the system of ordinary partial differential equations given by Eq. (2.118) also has to be discretised in time to reflect that. The discretisation in time is carried out by introducing discrete times  $t_n$  at which Eq. (2.118) has to be solved. In the case of an isochronic discretisation, the time differences between to subsequent moments  $t_{n+1}$  and  $t_n$  is given by the constant time increment or step size  $\Delta t = t_{n+1} - t_n$ . The time-discrete set of equations at time  $t_{n+1}$  reads

$$\mathbf{M} \cdot \ddot{\mathbf{u}}_{n+1} + \mathbf{f}_{n+1}^{\text{int}} - \mathbf{f}_{n+1}^{\text{ext}} = \mathbf{o}, \tag{2.119}$$

where the properties  $(\cdot)_{n+1}$  have to be computed at time  $t_{n+1}$ . To perform the task of time integration, two different strategies are available referred to as implicit and explicit integration schemes.

### Implicit time integration

In implicit time integration schemes, the quantities at time  $t_{n+1}$  depend on their history, i.e. of quantities at  $t_n$ , as well as still unknown quantities at times  $t_{n+\alpha}$ . Therefore, implicit time integration schemes require the solution of a nonlinear system of algebraic equations in every time step. Oftentimes, a linearisation of the system's equation in combination with the Newton-Raphson method is used. The advantage of implicit methods is that they are unconditionally stable and therefore not restricted regarding the size of the time step  $\Delta t$ .

### Explicit time integration

In explicit time integration schemes, the solution at time  $t_{n+1}$  is computed only using known quantities at time  $t_n$ . Therefore, they represent an extrapolation of the current state of the system. The central difference rule is commonly used to integrate the equations of motion explicitly through time and is also implemented in Abaqus/Explicit [28], the finite element analysis (FEA) software used throughout this work. Applying this scheme to express the unknown displacement  $\mathbf{u}_{n+1}$  at time  $t_{n+1}$  yields

$$\mathbf{u}_{n+1} = \mathbf{u}_n + \Delta t \dot{\mathbf{u}}_{n+1/2}, \quad (2.120)$$

where the unknown velocity  $\dot{\mathbf{u}}_{n+1/2}$  at time  $t_{n+1/2} = t_n + 1/2(t_n + \Delta t)$  can also be expressed by means of the central difference scheme as

$$\dot{\mathbf{u}}_{n+1/2} = \dot{\mathbf{u}}_{n-1/2} + \Delta t \ddot{\mathbf{u}}_n. \quad (2.121)$$

Applying the central difference scheme to  $\mathbf{u}_n$  and rearranging yields

$$\dot{\mathbf{u}}_{n-1/2} = \frac{\mathbf{u}_n - \mathbf{u}_{n-1}}{\Delta t}. \quad (2.122)$$

Inserting Eq. (2.122) into Eq. (2.121) and subsequently using the result in Eq. (2.120) gives an explicit expression for the unknown displacement  $\mathbf{u}_{n+1}$  as specified by

$$\mathbf{u}_{n+1} = 2\mathbf{u}_n - \mathbf{u}_{n-1} + (\Delta t)^2 \ddot{\mathbf{u}}_n, \quad (2.123)$$

where  $\ddot{\mathbf{u}}_n$  is the solution of Eq. (2.118) from the previous time step as given by

$$\ddot{\mathbf{u}}_n = \mathbf{M}^{-1} \cdot \left( \mathbf{f}_n^{\text{ext}} - \mathbf{f}_n^{\text{int}} \right). \quad (2.124)$$

For certain quadrature rules in conjunction with appropriate shape functions, the mass matrix  $\mathbf{M}$  becomes a diagonal or lumped matrix such that solving for the accelerations is greatly facilitated since the matrix inversion is trivial in that case. The solver of Abaqus/Explicit uses a diagonal or lumped mass matrix making it efficient and fast. But the central difference scheme only integrates constant accelerations  $\ddot{\mathbf{u}}$  exactly. As a result,

the time steps should be so small that accelerations are approximately constant during an increment. Thus, this explicit time integration scheme, and explicit time integration schemes in general, are restricted regarding the maximum step size  $\Delta t$ . The critical step size of a discrete problem can be estimated using the Courant criterion which reads

$$\Delta t_{\min} = \frac{l_{\min}}{c_d}, \quad (2.125)$$

where  $l_{\min}$  is the smallest characteristic length of an element in the model and  $c_d$  denotes the speed of a dilatational wave through the material body. Since  $c_d$  is commonly computed with the elastic modulus  $E$  as specified by

$$c_d = \sqrt{\frac{E}{\rho}}, \quad (2.126)$$

to consider nonlinear effects, the minimum step size obtained through Eq. (2.125) should be reduced by a factor of between 0.2 and 0.9 [115].



## 3. PC/ABS blends

---

*This chapter provides fundamental information about the materials in the scope of this work: blends of polycarbonate (PC) and acrylonitrile butadiene styrene (ABS). Blends are materials consisting of several components with macroscopically distinguishable behaviour and characteristics. Starting with PC, the two main constituents are introduced with special emphasis on the mechanisms of plastic deformation. The mechanical response and morphology of PC/ABS blends, with special emphasis on their composition dependence, is also presented.*

---

### 3.1. Polycarbonate (PC)

#### 3.1.1. Amorphous thermoplastic polymers

PC is a neat amorphous thermoplastic. Like all polymeric materials, thermoplastics are macromolecular materials. They consist of macromolecular chains consisting of identical constitutional repeat units and are synthesised from one or several types of small molecules termed monomers. There may be multiple residuals of the monomer (monomeric or structural unit) in one repeat unit.

Polymers containing only one structural unit are homopolymers, those with more than one structural unit are copolymers. The chain length, i.e. the number of structural units forming a chain, is expressed through the degree of polymerisation (DP). The number-averaged degree of polymerisation  $X_n$  in a polymer is given through relating the number-average molecular weight  $M_n$  to the molecular weight  $M_0$  of a single repeat unit:

$$X_n = \frac{M_n}{M_0}. \quad (3.1)$$

The variation in the chain length is represented through the molecular weight distribution which depends on the process conditions during synthesis. The molecular weight distribution can impact the manufacturing process as well as the thermal and mechanical properties. A higher count of long polymer chains, for instance, leads to a higher viscosity of the melt flow and increases the material's strength [34].

Polymers consisting of the same repeat units can still feature different arrangements of monomer residues along the backbone of the chain which is described with the term configuration. Depending on the configuration, constitutional repeat unit, and processing conditions, thermoplastics can feature an amorphous or semicrystalline microstructure. That is, if the rate of crystallisation is too slow, a glass is formed before a significant proportion of the material has crystallised [50].

Another important aspect of the constitution is the architecture describing the branching and linking between the macromolecular chains of a polymer. The occurrence and frequency of chemical links between the macromolecular chains determine the mechanical response of different classes of polymers. Thermoplastic polymers don't feature any chemical links in between their chains. Their coiled macromolecules are only physically linked to each other through entanglements (Fig. 3.1). Since the arrangement of the macromolecules of amorphous thermoplastics like PC in their solid state resembles that of their molten state, their microstructure is also referred to as that of a supercooled liquid. But compared to the liquid state, the mobility of the coiled and entangled macromolecules is drastically reduced in this glassy state. The free volume necessary to enable macromolecular motion with the chain segments rotating at their links is missing. Only at elevated temperatures, exceeding the material-specific glass transition temperature, the free volume in the material exceeds the threshold necessary ( $\approx 2.5\%$  [34]) for the macromolecules to change their conformation. Thus, the glass transition temperature or rather glass transition temperature range is characterised through an increasing specific volume as well as drastic loss in stiffness. However, this transition to the rubbery state is not associated with a phase change and is fully reversible.

Parts made from thermoplastics are commonly injection-moulded or extruded. Depending on the flow direction of the liquid, the glassy material's response may be anisotropic if the macromolecular chains are oriented and then frozen through rapid cooling. An orientation and alignment of the macromolecules can also be achieved through mechanical straining, after which the materials retain their new shape. Thereby, the limit stretch that can be achieved is a function of entanglement density since the entanglements stay intact and restrict the macromolecules' ability to align and eventually stretch.

Yet, when the material is heated above its glass transition temperature, it reverts to its original shape. This is called the shape memory effect and is caused by the recoiling of the polymer chains between the still-present entanglements. This process is driven by the macromolecular chains' aspiration to reach the random state of maximum entropy.

### 3.1.2. Mechanical response

The intramolecular interactions within the macromolecular chains are covalent bonds. They are about two decades stronger than the intermolecular interactions based on the Van der Waals forces. Therefore, the elastic behaviour at room temperature is determined mainly by the intermolecular interactions while the intramolecular interactions can be

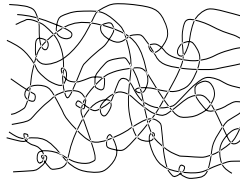


**Figure 3.1.:** Network of entangled macromolecules of a thermoplastic.

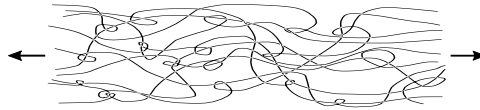


**Figure 3.2.:** Deformed network of entangled macromolecules of a thermoplastic.

considered virtually rigid. A small deformation of the material creates a non-equilibrium state that is retained upon unloading since equilibrium is energetically preferred. Therefore, the materials' response at room temperature is almost linear elastic and independent of the loading rate. Depending on material-specific factors such as loading rate, triaxiality of the stress state, temperature, and specimen geometry, glassy polymers fail either in a brittle or ductile manner. While PC exhibits a ductile failure behaviour also under uniaxial tension, other thermoplastics always fail in a brittle manner when subjected to tensile loadings, e.g. styrene-acrylonitrile resin (SAN). Only under compressive loading can these thermoplastics eventually exhibit a ductile material response.

If brittle fracture can be suppressed, then upon larger deformations thermoplastics exhibit a distinct yield stress in the form of a stress peak that marks the beginning of plastic deformation (Fig. 3.3). This yield stress features a dependence on both the loading rate and the temperature. Thereby, an increased loading rate or a lower temperature causes an elevated yield stress [38].

Past their yield stress, thermoplastics typically exhibit an intrinsic strain softening that under uniaxial tension is not the result of a reduction of the cross section [38]. This softening is followed by a progressive rehardening up to large strains, over the course of which the macromolecular chains are aligned (Fig. 3.2). Thus, this is also referred to as orientation hardening [15]. Once the limit stretch of the macromolecular network is reached the deformation becomes elastic again since the covalent bonds of the chain molecules themselves are stretched and eventually fail through rupture. The stress-strain response of PC at different strain rates subjected to uniaxial tension is shown in Fig. 3.3.

Technically, this perceived “plastic” behaviour in the glassy state is a nonlinear viscoelastic material response since it is reversible owing to the shape memory effect.

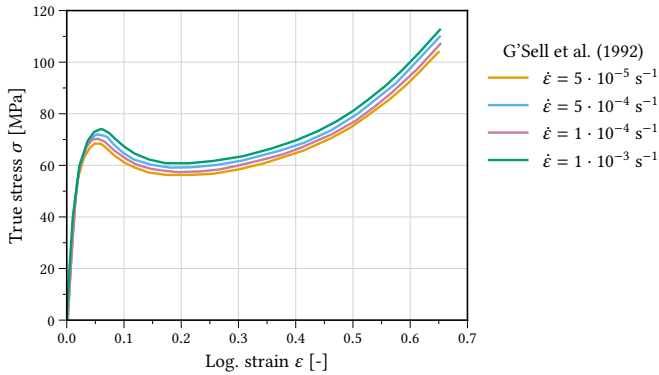


Figure 3.3.: Uniaxial stress-strain response of PC for different nominal strain rates [38].

### 3.1.3. Mechanisms of plastic deformation

#### Shear yielding

The ductile failure of thermoplastics is related to the evolution of shear bands [1]. The intrinsic softening in thermoplastics causes a localisation of the plastic deformation. However, the rehardening enables the plastic deformation to propagate through the material into regions of less deformed material. The whole deformation process upon the intrinsic softening in thermoplastic polymers is virtually isochoric, i.e. thermoplastics behave plastically incompressible. Thus, this deformation can only stem from the volume-preserving deformation mechanism shear. The characteristic process zones are thereby shear bands. They are observed in various scales depending on the material and originate at some local material inhomogeneity. In uniaxial tensile tests, shear yielding leads to necking as the plastic deformation propagates through the specimen (Fig. 3.4). The necking mechanism starts with a shear band developing at a constant angle across the specimen (Fig. 3.4a). With ongoing deformation, the first shear band propagates and a second complementary shear band nucleates (Fig. 3.4b). The complementary shear band grows, widens, and interacts with the initial shear band causing the initially sheared specimen to align again with the tensile direction (Fig. 3.4c). When the shear bands have propagated through all remaining areas, the yielded region in between them continues to propagate as a stable neck (Fig. 3.4d).

#### Crazing

A craze is a crack that is still bridged by thin fibrils of highly oriented and aligned macromolecular polymer chains. Unlike a true crack, a craze can still bear loading and develops only under a tensile stress [63]. The orientation of a craze is characterised by the plane it is growing in. In isotropic polymers, this plane is normal to the maximum

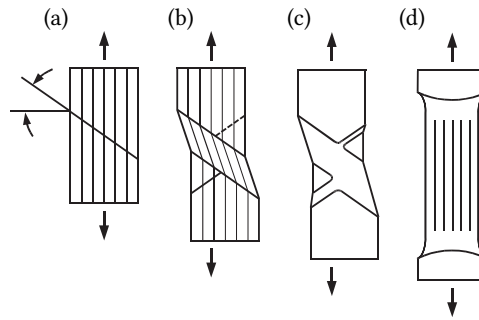


**Figure 3.4.:** Schematic illustration of the stages of the necking process in a PC specimen under uniaxial tension (adapted from Stokes and Bushko [102]).

principal stress [50]. In glassy polymers featuring an orientation, the craze planes are occurring perpendicular to the main principal strain [7]. Similarly, the craze planes might reflect the flow directions from the manufacturing process and thus be curved instead of planar [63].

Crazes originate at material imperfections and can reach lengths (in the craze plane) of a few centimetres with a thickness (in the out-of-plane direction) of several micrometres. Since the refractive index of crazes differs from that of the transparent amorphous surrounding material, they scatter light and appear white. This phenomenon is referred to as stress whitening. The process of crazing can be divided into three stages: craze initiation, craze widening and propagation, and craze breakdown.

A craze is usually initiated at an inhomogeneity or a surface notch of the material. Around it, the stress state is characterised by a high hydrostatic stress leading to the formation of voids. This means that crazing is related to an increase in volume. In PC, the critical hydrostatic stress for craze initiation is about 90 MPa [83].

In between the voids, the material undergoes plastic deformation until the fibrils emerge forming an interpenetrating structure with the voids. The craze widening relies on polymer chains being drawn into the fibrils from the surrounding bulk material. Within the fibrils, the macromolecules are further aligned and eventually stretched. In the “active zone” at the fibril base, disentanglements of two polymer chains as well as chain scission take place, irreversibly changing the material’s microstructure. Thus, the process of crazing is more prevalent in thermoplastics with a low entanglement density since the drawing of the material from the surrounding is facilitated [50].

An interface convolution mechanism, referred to as the meniscus instability, is responsible for the craze propagation [3]. Along the craze tip, voids form and coalesce with the free volume in the craze as illustrated in Fig. 3.5a. This leads to fingers of void volume reaching into the bulk material or vice versa when regarded from the craze’s through-thickness direction as shown in Fig. 3.5b. The next step could then be described as raising the hand without the fingertips spawning new fibrils (Fig. 3.5c). The craze tip in the meantime has

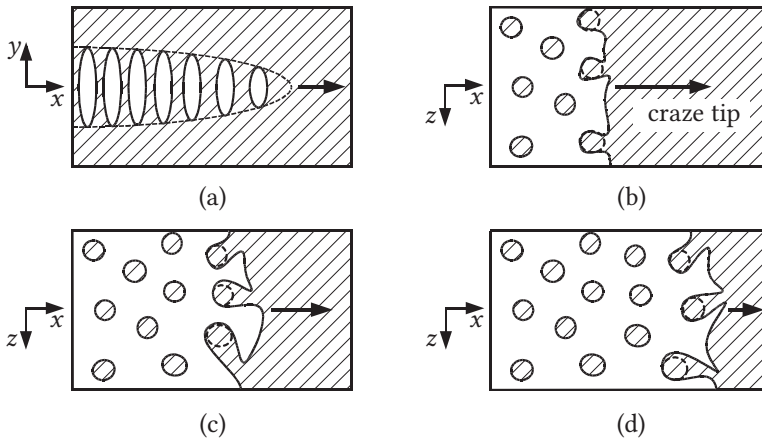


**Figure 3.5.:** Schematic visualisation of the craze propagation through the meniscus instability process (adapted from Stokes [101]).

propagated and the process repeats itself (Fig. 3.5d). The same mechanism can be observed in the fibrillar break-up of a mastic when peeling adhesive tape or labels [3].

When the polymer chains forming the fibrils reach their limit stretch, they eventually break down. The rupture of the fibrils upon a critical craze opening displacement turns the craze into an actual crack. Thus in glassy thermoplastics, crazing is the precursor of brittle failure [108]. In PC, high triaxiality stress states promote crazing over shear yielding resulting in brittle failure [98].

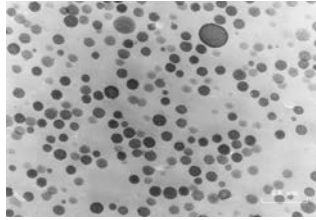


**Figure 3.6.:** Micrograph of an ABS blend with homogeneous rubber particles [40].

## 3.2. Acrylonitrile-butadiene-styrene (ABS)

ABS is synthesised from the three monomers styrol, butadiene, and acrylonitrile (AN), making ABS a terpolymer. Regarding its morphology, ABS is a binary polymer blend consisting of a co-polymeric styrene-acrylonitrile (SAN) matrix which contains finely dispersed butadiene (rubber) particles as shown in Fig. 3.6.

Since heterogeneous blends of thermoplastics exhibit as many glass transition temperatures as phases, ABS features two glass transition temperatures [34]. Subjected to tensile loadings, the amorphous glassy thermoplastic SAN fails in a brittle manner. Through the addition of rubber particles to form ABS, this brittle failure can be suppressed, resulting in a uniaxial tensile response similar to that of PC (Fig. 3.8).

### 3.2.1. Rubber-toughened polymer blends

The addition of rubber particles to SAN greatly increases the fracture toughness. Thus, ABS belongs to the class of rubber-toughened materials. The concept of rubber-toughening embodies blending a brittle polymer such as a glassy thermoplastic with rubber particles to create a tough material. Rubber-toughened polymer blends in general contain a volume fraction of 5–40 % sub-micron sized rubber particles. A rubber-toughened polymer exhibits an increased fracture toughness and improved notch resistance over the neat (matrix) material. Regarding ABS, the optimum rubber volume fraction in terms of maximising the fracture energy is in the range of 20 – 30 % [11, 100, 106].

The brittleness of neat thermoplastics such as PC in the presence of sharp notches is due to these materials' inability to dissipate energy over an extended volume. As a consequence, they fail due to localised mechanisms such as crazing. Added rubber particles enable energy dissipation throughout a larger part of the material volume at many sites. Therefore, they cause a tougher material response and increase fracture toughness.

Blend parameters such as the matrix properties (i.e. AN content, number-average molecular weight), rubber particle volume fraction, and particle size as well as shape impact the deformation and fracture behaviour of the blend. The rubber particle size and shape in particular depend on the polymerisation technique. Mass polymerisation yields rubber

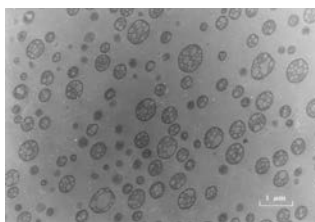


**Figure 3.7.:** Micrograph of an ABS blend featuring rubber particles with SAN subinclusions (“salami” structure) [40].

particles that feature glassy SAN subinclusions giving them a heterogeneous morphology that is also referred to as “salami” structure (Fig. 3.7). However, emulsion polymerisation leads to finely dispersed homogeneous rubber particles.

### 3.2.2. Mechanisms of plastic deformation

The deformation mechanisms enabling the energy dissipation throughout increased portions of the material volume in rubber-toughened blends are:

- rubber particle cavitation
- matrix shear yielding, and
- distributed crazing.

Matrix shear yielding and distributed crazing are the main mechanisms of inelastic deformation and energy dissipation in ABS. Yet the occurrence and amount of rubber particle cavitation play a key role since the prevalence of one mechanism over the other depends on it as well as other parameters such as the particle diameter.

The rubber particles cavitate upon relatively low hydrostatic stress inside the particle. Thus, this process precedes the other inelastic deformation mechanisms and is regarded as fundamental in promoting the delocalisation of inelastic deformation. Since the stress state inside particles cannot be experimentally determined, the overall macroscopic hydrostatic stress at which cavitation occurs is used as a measure instead. It is reported to be in the range of 8 – 20 MPa [72]. Thereby, heterogeneous particles with SAN subinclusions as shown in Fig. 3.7 exhibit a higher cavitation resistance than homogeneous ones [61].

In highly triaxial stress states, shear yielding in the matrix phase of a rubber-toughened polymer is assumed to take place after rubber particle cavitation that effectively lowers the stress triaxiality [61].

The process of distributed crazing represents another deformation mechanism that can effectively reduce the hydrostatic stress in the matrix material. Due to different thermal expansion coefficients, the rubber particles can cause a tensile stress on the surrounding matrix material in the equatorial plane of the particle after cooling [34]. External tensile



stress in one direction increases the local hydrostatic stress facilitating the creation of a void. Eventually, a craze forms in the equatorial plane of the rubber particle [34].

Different factors such as the blend morphology, the macroscopic loading conditions, and the local stress lead to conditions that favour either shear yielding or distributed crazing. In this competition of the two processes regarding inelastic deformation, smaller homogeneous rubber particles promote matrix shear yielding [31]. Also, at relatively low loading rates, the material is more likely to exhibit shear yielding, while high deformation speeds favour distributed crazing [11]. As a consequence of this dependence on multiple factors, different studies have reached different conclusions regarding whether eventually matrix shear yielding [40, 100, 62, 17] or distributed crazing [11] contributes more to increasing the fracture toughness.

Macroscopically, the zone of plastic deformation in ABS is characterised by stress whitening. The plastic zone is found to be elongated and as wide as the notch it originates from [51].

### 3.2.3. The uniaxial stress-strain response

On a macroscopic scale, ABS blends exhibit a similar stress-strain response to uniaxial tension as PC. That is, the yield curves for PC and ABS are approximately self-similar (Figs. 3.3 and 3.8). Both feature a softening upon yield as well as progressive rehardening for large strains (Fig. 3.8). Yet, the strain rate effect on the yield stress is more pronounced for ABS (Figs. 3.3 and 3.8). Also, in contrast to PC, ABS blends exhibit a pronounced plastic dilatancy since both rubber particle cavitation and in particular distributed crazing increase the overall material volume (Fig. 3.8).

The rubber content in ABS impacts both the yield stress and the extent of plastic dilatancy in ABS blends. Neat SAN fails at virtually zero plastic deformation in a brittle manner due to crazing. Nevertheless, SAN exhibits a failure stress greater than that of neat PC [93, 76, 69]. Increasing the rubber content decreases the yield stress and elastic modulus of ABS [60, 106]. Consequently, ABS grades with a higher rubber content feature significantly lower yield stresses than PC (Figs. 3.3 and 3.8) for an identical nominal strain rate of  $\dot{\epsilon} = 0.001\text{s}^{-1}$  [76]. Ishikawa [60] found that for an ABS blend with a rubber mass fraction of 40 %, the yield stress roughly amounts to half of that of an ABS blend with a rubber mass fraction of 15 %. The amount of plastic volume strain on the other hand increases with the rubber content in ABS.

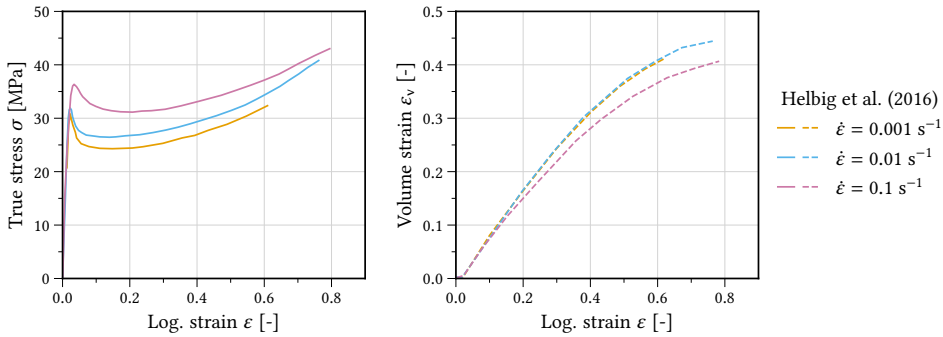


**Figure 3.8.:** Uniaxial stress-strain response and volume strain response of ABS for different nominal strain rates [52].

### 3.3. PC/ABS blends

PC/ABS is a popular engineering plastic used in many applications in the automotive and electronics industries. Commercial PC/ABS grades are available in various compositions, to meet the requirements of their applications. Two benefits of blending PC and ABS are an improved fracture toughness and notch insensitivity. The fracture toughness is commonly evaluated in experiments on notched specimens where the impact strength is measured. For instance, in the Izod test setup, a pivoting hammer breaks a specimen and the difference in potential energy prior to and after the impact determines the energy absorbed by the specimen. The fracture toughness is then the absorbed energy expressed per unit cross section at the notch. Neat PC can be successfully rubber-toughened through adding rubber particles [111, 24]. However, adding ABS to PC instead of rubber also lowers the viscosity of the melt flow and therefore improves the blend's processability significantly [42, 114, 118]. Simultaneously, the beneficial thermal properties of PC are retained as well [76, 114].

PC/ABS blends of certain compositions exhibit better properties compared with their neat constituents with regard to the neat constituents' respective advantageous characteristics. This is referred to as the "synergistic effect" and is observed, for instance, when regarding fracture toughness [43, 41, 42, 25, 114, 76] or melt flow viscosity [116, 86]. Yet the findings in the literature are contradictory regarding the extent of the effect as well as the compositions and processing conditions for which to expect significant improvements (Figs. 3.9 and 3.10). That is, other studies on the composition dependence of the mechanical response do not report any synergistic range and find the opposite to be true [103, 66, 48] (Fig. 3.11). This is due to the many parameters eventually determining the material behaviour of PC/ABS blends. Yet regarding the mechanical behaviour, the most significant blend parameters are the PC/ABS ratio and the rubber content in ABS. These two parameters are also of utmost importance for the morphology of PC/ABS blends.

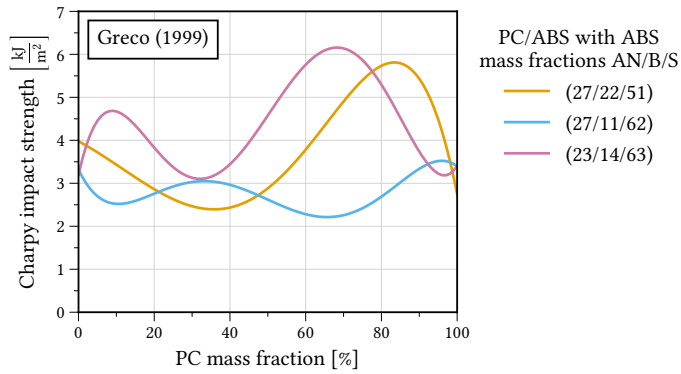


**Figure 3.9.:** Impact strength of PC/ABS blends in Izod test setup made with ABS grades of different compositions (given as mass fractions of acrylonitrile (AN), butadiene (B), and styrene (S), adapted from Greco [42]).

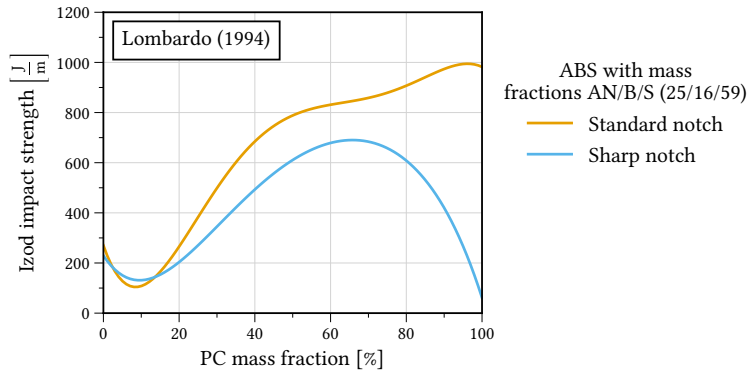


**Figure 3.10.:** Standard notch and sharp notch Izod impact strength of PC/ABS blends made with an ABS grade featuring a composition (mass fractions) of AN/B/S (25/16/59) (adapted from Lombardo, Keskkula, and Paul [76]).

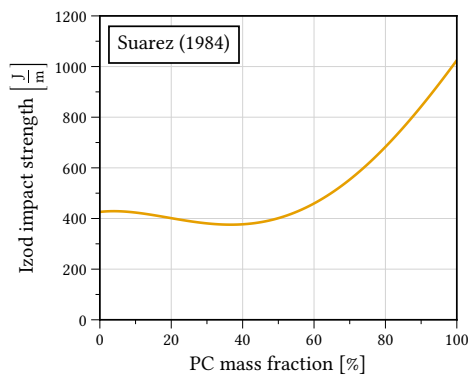


**Figure 3.11.:** Izod impact strength of PC/ABS blends (adapted from Suarez, Barlow, and Paul [103]).

### 3.4. Morphology of PC/ABS blends

Since PC/ABS blends contain the neat glassy polymer PC and the binary rubber-toughened polymer blend ABS they are ternary polymer blends. They feature a hierarchical microstructure because the ABS phase contains another phase in the form of rubber particles (Sec. 3.2). However, the phase morphology of PC/ABS blends is shaped by the two immiscible phases PC and ABS and mainly depends on the PC/ABS ratio [42]. Blends rich in one of the two main constituents PC or ABS exhibit a phase-matrix morphology that is also referred to as a sea-island structure [122]. With regard to PC-rich compositions that were cooled at a low rate, a sea-island structure formed by a PC matrix with dispersed spherical ABS particles is common [114, 76, 75, 74] (Fig. 3.12).

In the case of more equal PC/ABS fractions, morphologies with two continuous interpenetrating phases form. This is the case for ABS mass fractions of about 45 % to 55 % [57, 74]. Apart from the mere composition, the processing parameters such as temperature, molecular characteristics, and manufacturing methods have an impact on the blend morphology.

That is, morphologies often exhibit a distinct anisotropy from the direction of melt flow during injection moulding. Injection-moulded parts from blends of immiscible components exhibit a morphology gradient from the part's surface to its core [75, 74, 122]. The surface is formed by an instantaneously frozen layer whereas the so-called skin layer and the core region solidify later in the process. With increasing distance from the mould, the cooling rate decreases, giving the melt more time to relax and approach the energetically favourable equilibrium state. Yet, in injection-moulded sheet-like structures, the morphology in the core usually features an orientation reflecting the melt flow [75, 74, 122].

#### 3.4.1. Sea-island morphologies

Sea-island or matrix-inclusion microstructures are common in PC/ABS blends rich in one of the two main constituents. In these morphologies, the component occupying the most space usually forms the matrix. Yet a transition zone regarding the PC/ABS ratio exists whereby both constituents can also be present as continuous phases.

##### PC-rich blends

PC-rich blend compositions with a PC matrix and dispersed ABS domains are found up to ABS mass fractions of about 40 % [57, 6]. Thereby, the ABS phase can be present in the form of spherical particles with dispersed rubber subinclusions (Fig. 3.12). For higher ABS contents, larger domains can emerge through the coalescence of several particles [6, 74].

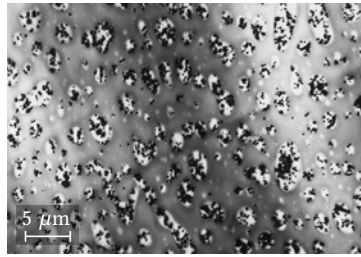


**Figure 3.12.:** Micrograph of a PC/ABS (70/30) blend with homogeneous rubber particles [114].

The morphology of injection-moulded sheets features different structures in the through-thickness direction [74, 6]. The surface layer most clearly exhibits an anisotropic morphology from the direction of melt flow [74, 6]. The high cooling rate at the surface layer directly in contact with the mould freezes the material in place, resulting in morphologies that are shaped by shear and elongation forces [6]. Consequently, even injection-moulded plaques with an ABS mass fraction as low as 10 % may exhibit a bead-and-string morphology near the surface [75, 74]. In an extensive study on the subject, Lee, Hiltner, and Baer [74] found that a blend with a mass fraction of 30 % ABS featured a continuous ABS phase near the specimen surface. With increasing distance from the surface, the material has more time to relax during solidification. In PC-rich blends, dispersed ABS particles in a PC matrix form. The particles coalesce for higher ABS mass fractions of up to 40 % [74]. Yet micrographs of the centre of injection-moulded specimen may feature a microstructure showing the direction of the melt flow [114, 75, 74, 6, 113].

Blends containing a PC mass fraction of 60 % always feature a continuous PC phase but the ABS may not always form dispersed domains [32, 74]. In PC-rich blends with an ABS mass fraction of approximately 40 %, the mixing time and temperature of the melt, the processing conditions, and the cooling rate are all parameters that influence whether the ABS phase is dispersed or continuous [21, 6].

### ABS-rich blends

ABS-rich blends with mass fractions of 60 % ABS or more feature an ABS matrix with interspersed PC domains [74, 32, 106]. Particularly in PC/ABS (40/60), the role of ABS as a matrix is promoted by its lower viscosity in comparison to PC. When mixing a melt consisting of two components of different viscosities, the component with the lower viscosity encapsulating the component with the higher viscosity reduces the rate of energy dissipation [57]. In injection-moulded plaques of PC/ABS (40/60), the PC domains near the surface appear elongated in the direction of the melt flow as well as sheet-like and densely arrayed, while in the regions further away from the mould their shape is more spherical and without a clear orientation [74]. This reflects the lower cooling rate that enables relaxation of the melt flow which is hindered by the high cooling rate near the

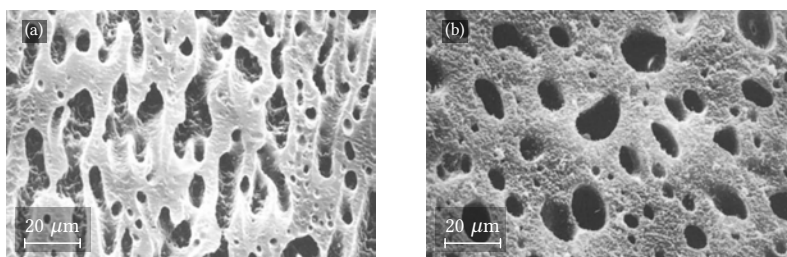


**Figure 3.13.**: Micrographs from Dong, Greco, and Orsello [32] of (a) PC/ABS (60/40) etched by an aqueous acid solution to remove the semi-continuous ABS phase and (b) PC/ABS (40/60) etched by an aqueous NaOH solution to remove the PC particles.

mould surface. With a decreasing PC content, the particles become smaller and more finely dispersed [74]. The tendency of PC in an ABS matrix to form spherical particles without an orientation is greater than that of ABS particles in a PC matrix (Fig. 3.13). This is a consequence of the higher viscosity of PC. Since the shear and elongational forces stretch the PC domains in the melt to a lesser extent, relaxation to a spherical shape is facilitated [74]. Moreover, the melt viscosity as a whole decreases with a decreasing PC content [37, 42, 86]. Consequently, the shear in the melt decreases too.

### 3.5. Mechanical behaviour of PC/ABS blends

Similar to their morphology, the mechanical behaviour of PC/ABS blends also depends on their composition, mainly in terms of PC/ABS ratio and the rubber content in ABS.

#### Young's modulus and yield stress

Young's modulus and yield stress of PC/ABS blends increase with increasing PC content if the ABS contains enough rubber. That is because neat SAN exhibits a higher Young's modulus and yield stress than PC [93, 76, 69]. The threshold rubber mass fraction, upwards from which PC exhibits a higher Young's modulus than ABS, seems to be lower than 16 % [76]. With an increasing rubber content, the elastic modulus only decreases further. In the case of a rubber mass fraction of 50 %, the elastic modulus of ABS decreases to roughly a quarter of that of PC [76]. Consequently, for an ABS with a rubber mass fraction of 16 %, Lombardo, Keskkula, and Paul [76] found that the elastic modulus only slightly increases with increasing PC content whereas the elastic modulus quadruples for an ABS with mass fraction of 50 % rubber over the whole range of PC mass fractions from 0 % to 100 %.

With regard to the yield stress, a rubber mass fraction of 10 % in ABS already causes the yield stress of ABS to be lower than that of PC [106]. The yield stress of ABS with a mass

fraction of 16 % rubber was found to amount to only about two thirds of that of PC [76]. Increasing the mass fraction in ABS to 50 % reduces the yield stress of ABS to only a sixth of that of PC [76]. As a consequence, the yield stress in PC/ABS blends from two given PC and ABS grades increases with an increasing PC content of the blends, if the rubber mass fraction in ABS exceeds 10 %.

The trends of both Young's modulus and yield stress can often be predicted for given PC and ABS grades with the rule of mixing without exhibiting significant synergistic effects [76, 69, 67, 86, 23, 103, 5]. However, significant antagonistic effects are reported for certain grades of ABS as well [86, 23].

### **Large-strain deformation behaviour**

Adding ABS mass fractions greater than 40 % to PC results in a stark decrease in elongation at break under uniaxial tension for the blend compared to neat PC [5, 42, 69, 86, 103]. For some PC and ABS material combinations, the smallest elongation at break is found for intermediate compositions with interpenetrating phases [69, 86, 42, 23], whereas sometimes compositions featuring an ABS mass fraction of about 30 % yield the smallest value [103, 69, 23]. Different studies investigated the elongation at break for PC/ABS blends comparing ABS grades with different rubber and acrylonitrile (AN) contents [23, 69, 86]. Thereby, the rubber content alone was not decisive, but the AN content having a great impact on the phase adhesion also played an important role. According to Huang and Wang [56], the maximum adhesion between PC and ABS is found for an AN mass fraction in ABS between 25 % and 30 %. Less cohesion of the phases seems to shift the minimum elongation at break towards the co-continuous PC/ABS (50/50) composition [86]. Findings in the case of PC-rich blends are contradictory as well. For particular ABS grades, synergistic effects are reported [69]. However, significantly antagonistic effects seem to be more frequent [69, 86, 5, 42].

### **Composition-dependent failure behaviour**

Similar to the elongation at break, the fracture toughness of PC/ABS blends is highly composition-dependent. Thereby, this dependence of fracture toughness on composition is found to be starkly non-monotonic [42, 23, 5, 76, 103] (Figs. 3.9, 3.10, and 3.11). In ABS grades that feature an identical favourable AN content in their SAN phase but differ in their rubber content, the latter seems decisive as to whether a synergistic or an antagonistic effect in the fracture toughness is observed for PC-rich compositions [76, 42]. That is, the rubber content in ABS has a bigger influence on fracture toughness than the PC/ABS ratio in this case. Likewise, for a favourable rubber content an optimum ABS mass fraction maximising the fracture toughness can be found in the range of between 5 and 40 % [76, 42].

However, a sufficiently sharp notch seems a prerequisite to observe a synergistic effect at all (Fig. 3.10) regardless of the shape and size of the rubber particles in the ABS phase of the blends [76, 58]. Nigam, Nigam, and Mathur [86] found solely antagonistic effects regarding the fracture toughness using standard Izod tests for two different grades of ABS in PC/ABS blends. Similar behaviour in standard notched Izod tests was observed by Suarez, Barlow, and Paul [103] (Fig. 3.11). These findings resemble those of Lombardo, Keskkula, and Paul [76] for the standard notch (Fig. 3.10). Thus, they might be ascribed to a notch not sharp enough to trigger the synergistic effect.

Balakrishnan and Neelakantan [5] found a stark synergistic effect regarding fracture toughness for a large composition range only if a compatibiliser was used to improve phase adhesion. Zhao et al. [121] also concluded that using a compatibiliser improves not only the phase interface but also fracture toughness by reducing the domain size of the dispersed phase in PC-rich blends. Furthermore, the low fracture toughness obtained with certain ABS grades can be ascribed to the presence of impurities in the form of metal salts in these ABS materials that cause the PC to degrade [74, 5].

However, given sufficient phase adhesion and amount of rubber in ABS, PC-rich blend compositions seem likely to exhibit beneficial synergistic fracture toughness [42, 76, 5]. ABS-rich blends in general seem to yield less favourable fracture toughness when being compared to PC-rich compositions of the same PC and ABS grades [42, 76, 5, 121, 103, 86].

## Conclusions

Despite the contradictory nature of the aforementioned investigations in the literature with regard to the composition-dependent fracture toughness of PC/ABS blends, the following conclusions can be drawn.

- The elastic properties and yield stress of PC/ABS blends can be sufficiently well predicted using the rule of mixing. In contrast, properties such as the elongation at break and particularly fracture toughness exhibit a stark non-monotonic dependence on blend composition.
- In the presence of sharp notches, PC-rich PC/ABS blends can exhibit significantly better fracture toughness than neat PC.
- Whether or to what extent the fracture toughness is improved, depends to a large part on the rubber and acrylonitrile content in ABS. For a favourable combination of PC and ABS, an optimum PC/ABS ratio can be found.
- However, the interface properties and impurities in ABS that degrade PC also have an impact. Compatibilisation of the PC and ABS phases can improve the fracture toughness through improved interface adhesion and reduced domain size of the dispersed phase.



- On the other hand, given appropriate ABS grades, beneficial blend properties do not require any form of compatibilisation [106, 41]. It is rather the amount of AN in SAN which seems key to ensure good interface properties which commercial blends make use of [42, 19, 33, 56].



## 4. PC/ABS blends investigated in this work

---

*This chapter introduces the three different commercial PC/ABS blends that are the subject of all experimental studies underlying this work. The morphologies of the injection-moulded specimen materials are analysed by means of micrographs. Through a novel application of a machine learning algorithm to polymer blends, the composition of the three PC/ABS blends is determined from the micrographs.*

---

### 4.1. Materials

Subject to all investigations in this work were three commercial PC/ABS blends manufactured by Covestro AG: *Bayblend T45*, *Bayblend T65* and *Bayblend T85*. The materials were provided in the form of rectangular injection-moulded sheets measuring 148 mm in length, 105 mm in width, and  $3.22 \pm 0.01$  mm in thickness (Fig. 5.3). Each sheet featured a clearly marked far and gate end with the latter stretching over approximately 101 mm along the sheet's width (Fig. 5.3).

#### 4.1.1. Micrographs

As a consequence of the specimen materials being manufactured through injection moulding, they were hypothesised to feature a layered microstructure as well as an orientation depending on the direction of the melt flow. To investigate the materials' microstructure, micrographs were acquired through transmission electron microscopy (TEM). To investigate the skin-core morphology gradient of the materials' morphologies, images of the surface, the skin layer, and the specimen core were captured. All micrographs were generated from cuts parallel to the injection flow. The sample preparation and image acquisition were carried out by *Neue Materialien Bayreuth GmbH*.

### 4.1.2. Sample preparation

Small cuboids were cut from the centre of the injection-moulded plates. Using a ultramicrotome outfitted with a cryo unit, ultra-thin sections measuring 50 nm in thickness were cut from these cuboids using a diamond knife in a nitrogen atmosphere. The specimen and the knife were cooled to  $-140^{\circ}\text{C}$  and  $-30^{\circ}\text{C}$ , respectively. The cutting plane was the trough-thickness plane orthogonal to the direction of material flow during manufacturing. The obtained samples were stained using osmium tetroxide ( $\text{OsO}_4$ ) and subsequently ruthenium tetroxide ( $\text{RuO}_4$ ) to enhance the contrast between phases in the TEM images. Osmium tetroxide makes the rubbery component of the ABS appear black, whereas staining with  $\text{RuO}_4$  dyes the PC phase grey in TEM images [6]. Thus, ABS appears light grey, PC is dark grey, and rubber is black in TEM micrographs of PC/ABS blends (Sec. 4.3.3).

## 4.2. Blend compositions

The exact composition of the three blends was uncertain, since the manufacturer's specification sheets do not specify the PC/ABS ratios. According to Seidler and Grellmann [95], *Bayblend T45* features a PC mass fraction of 45 % whereas the mass fraction of PC in *Bayblend T65* is 60 % and *Bayblend T85* contains a PC mass fraction of 70 %. To validate that the materials provided for this thesis featured the same compositions, the micrographs were used to determine the phase volume fractions of the blends based on area fractions, assuming the principle of Delesse [30]. From the thus obtained phase volume fractions the mass fractions were deduced.

To ascertain the phase volume fractions of the three materials, the pixel classification software *ilastik* [10] was employed. The *ilastik* algorithm is based on a neural network that was trained on sections of micrographs for each material. The calibrated classification model was then applied to other micrographs of the same material and magnification to determine the PC/ABS volume ratios. Using the mass densities  $\rho_{\text{PC/ABS}}$  for the PC/ABS blends from the manufacturer's specification sheets in conjunction with the mass density of a commercial general-purpose PC from the same manufacturer (*Makrolon 2407*,  $\rho_{\text{PC}} = 1200\text{ kg/m}^3$ ), the mass density of the ABS phase  $\rho_{\text{ABS}}$  in each blend was estimated (Tab. 4.1). Combining these results with the phase volume fractions, the latter could be converted into mass fractions. Thereby, the above mentioned compositions in terms of PC mass fractions could be confirmed (Tab. 4.1).

*Bayblend T45* is hereafter referred to as PC/ABS (45/55), *Bayblend T65* as PC/ABS (60/40), and *Bayblend T85* as PC/ABS (70/30), respectively.

Material	$\rho_{PC/ABS}$ $\left[\frac{\text{kg}}{\text{m}^3}\right]$	$\rho_{ABS}$ $\left[\frac{\text{kg}}{\text{m}^3}\right]$	Volume fractions (PC/ABS) [%] from micrographs	Mass fractions (PC/ABS) [%] from micrographs	Mass fractions (PC/ABS) [%] from [95]
<i>Bayblend T45</i>	1100	1030	(41.3/58.7)	(45.0/55.0)	(45/55)
<i>Bayblend T65</i>	1130	1040	(55.9/44.1)	(59.4/40.6)	(60/40)
<i>Bayblend T85</i>	1140	1020	(66.6/33.4)	(70.1/29.9)	(70/30)

**Table 4.1.:** PC/ABS volume fractions, overall blend mass density and estimated mass density of the ABS phase for all three PC/ABS blends investigated.

## 4.3. Blend morphologies

### 4.3.1. Morphology at the surface

The first up to ten micrometres into the specimen volume are commonly termed the surface when referring to the different sections of an injection-moulded part's morphology [6, 122]. The melt flow in this region is almost instantaneously frozen when coming into contact with the mould. The shear and elongational forces in the melt flow in this section are very high such that immiscible blends usually exhibit a lamellar structure [6, 122].

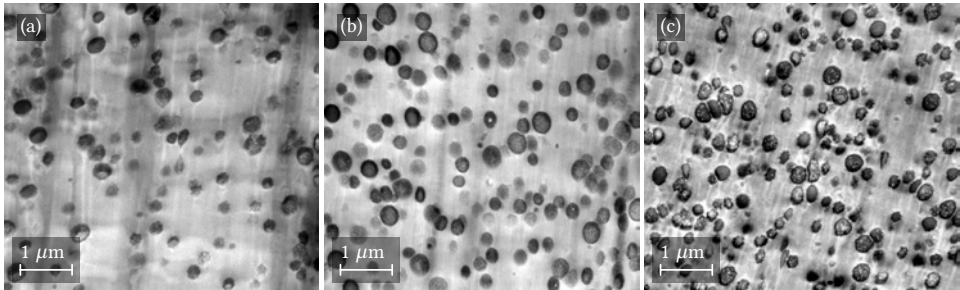


**Figure 4.1.:** The morphology at the surface of (a) PC/ABS (70/30), (b) PC/ABS (60/40), and (c) PC/ABS (45/55).

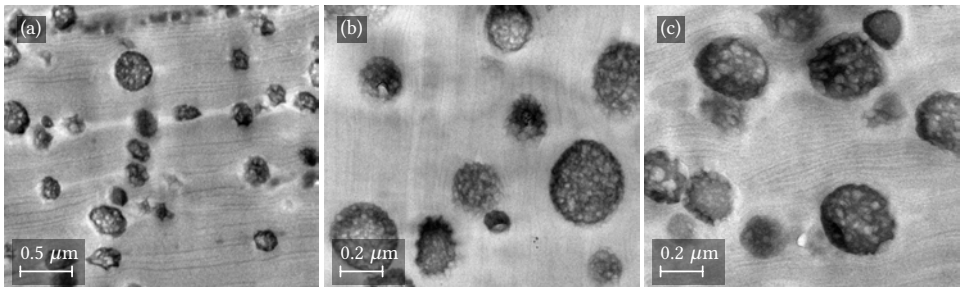


**Figure 4.2.:** Detail of the morphology at the surface of (a) PC/ABS (70/30), (b) PC/ABS (60/40), and (c) PC/ABS (45/55).

All three materials exhibited an obviously oriented lamellar structure of PC and SAN with the rubber particles included like droplets (Fig. 4.1). The very fine lamellae of PC and ABS in the surface layer measured only several micrometres in thickness (Fig. 4.2). Using a higher magnification, the arrangement of rubber particles with diameters up to about 300 nm resembled a finely grained wooden surface with knotholes (Fig. 4.2).

The rubber particles of all three materials exhibited a heterogeneous microstructure with SAN subinclusions (salami type, see Sec. 3.2.1). Due to the higher ABS content, the amount of rubber in the PC/ABS (45/55) blend was visibly increased over the two PC-rich compositions (Fig. 4.1). The increased SAN content in PC/ABS (45/55) compared with the other blends, showed frequent thicker strings connecting the rubber particles in the flow direction.

### 4.3.2. Morphology of the skin layer

The cross section in close proximity to the mould next to the surface is referred to as the skin layer. In the skin layer, the shear in the melt flow is maximal [105]. Depending on the blend properties, the skin layer may reach between 100 and several hundred micrometres into the material volume [36]. With regard to PC/ABS (60/40), Bärwinkel et al. [6] found a thickness of the skin layer of about 150  $\mu\text{m}$ . During manufacturing, the cooling rate in the skin layer is still very high, not allowing the phases to reach an equilibrium structure.

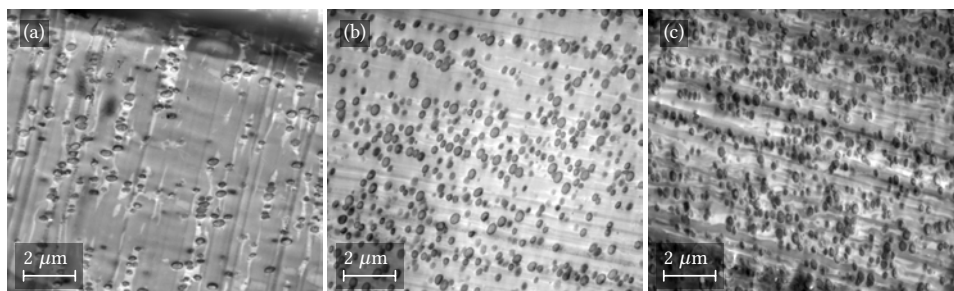


**Figure 4.3.:** The morphology in the skin layer of (a) PC/ABS (70/30), (b) PC/ABS (60/40), and (c) PC/ABS (45/55).

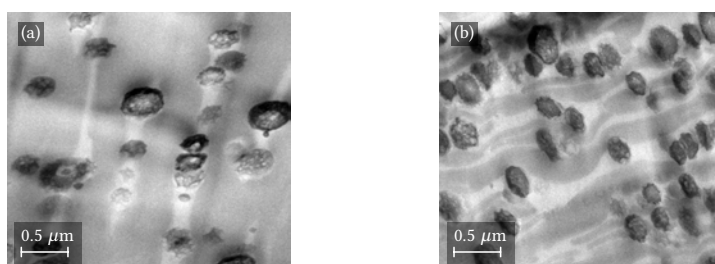


**Figure 4.4.:** Detail of the morphology in the skin layer of (a) PC/ABS (70/30) and (b) PC/ABS (45/55).

Owing to the maximum shear in the melt flow, the PC/ABS blends exhibited a highly oriented bead-and-string structure in the skin layer (Fig. 4.3). Instead of the nano-lamellar structure that was prevalent in the surface layer, clearly separated homogeneous PC and SAN phases were found, indicating a lower cooling rate allowing for some relaxation and coalescence (Fig. 4.4). Also, the rubber particles reintegrated into the SAN phase. The increased ABS content of the PC/ABS (45/55) blend compared with the PC-rich blends, PC/ABS (70/30) in particular, became apparent in this region as well (compare Figs. 4.4 and 4.2).

### 4.3.3. Morphology of the core region

The core region makes up the biggest part of the material volume. In the core region, the lower shear forces in the melt flow and the lower cooling rate in comparison to the skin layer allow the material to relax and approach the energetically favourable equilibrium state during solidification. Thereby, the formerly separated domains may not only relax but also coalesce [122].

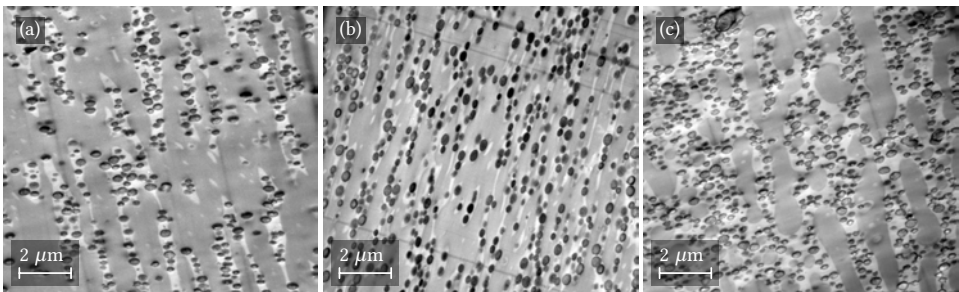


**Figure 4.5.:** The morphology in the core region of (a) PC/ABS (70/30), (b) PC/ABS (60/40), and (c) PC/ABS (45/55).

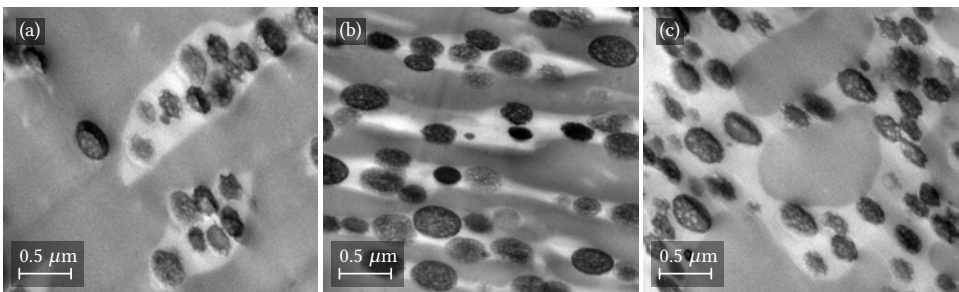


**Figure 4.6.:** Detail of the morphology in the skin layer of (a) PC/ABS (70/30), (b) PC/ABS (60/40), and (c) PC/ABS (45/55).

Therefore, PC/ABS (70/30) exhibited a sea-island structure as depicted in Fig. 4.5a. However, despite the lower cooling rate, the ABS domains remained oriented with the melt

flow direction and retained pointy ends parallel to flow (Figs. 4.5a and 4.6a). Compared with the skin region, the ABS domains increased in both length and width indicating coalescence (Figs. 4.5a) and 4.3a).

The morphology of the PC/ABS (60/40) blend in the core region featured a more pronounced orientation than the PC/ABS (70/30) blend. The ABS phase in this case was beginning to form a second interpenetrating phase permeating the PC with rubber-filled strings as shown in Fig. 4.5b. Nonetheless, the ABS domains did not seem entirely continuous, thus forming a semi-continuous phase. In contrast to PC/ABS (70/30), the ABS domains were slimmer, seldomly wider than two rubber particles (Figs. 4.5b and 4.6b).

The core region of the PC/ABS (45/55) blend featured a co-continuous microstructure slightly oriented by injection moulding (Fig. 4.5c). The size of individual phase domains was found to be bigger than in the PC-rich blends (Fig. 4.5c). Also, the phase boundaries between PC and ABS exhibited softer, more rounded shapes. This may be attributed to the high volume fraction of the lower viscosity ABS phase, reducing the shear forces in the melt flow and allowing the phase domains to more easily coalesce and relax during solidification.

#### 4.3.4. Remarks on the morphology

Regarding the dependence on composition, the morphologies of the three investigated PC/ABS blends were in line with other findings in the literature. Sea-island or matrix-particle structures are typical for PC/ABS (70/30) blends [76, 114, 32, 106, 74]. Also, the observation of a semi-continuous ABS phase in injection-moulded parts made from PC/ABS (60/40) blends is common [74, 32]. The exact composition of PC/ABS (45/55) is not commonly published. On the basis of similar PC/ABS ratios, the comparison with PC/ABS (50/50) seems appropriate. In this regard, the observation of a co-continuous microstructure is in line with other findings from the literature [106, 74, 32, 76].

Since Seidler and Grellmann [95] investigated materials of similar composition from the same manufacturer, it is remarkable that the structure and size distribution of the rubber particles reported strongly deviates from what was found in this study. All three materials underlying this work exhibited salami-type rubber particles with SAN subinclusions, whereas the materials analysed by Seidler and Grellmann [95] featured homogeneous rubber particles. The mean rubber particle size  $\bar{d}$ <sup>1</sup> between the materials in this study did not differ significantly (Tab. 4.2). However, the particle sizes reported by Seidler and Grellmann [95] were significantly smaller yet featured a less uniform distribution.

---

<sup>1</sup> The 95 % confidence interval (CI) to the mean  $\bar{d}$  is given by

$$CI = \bar{d} \pm 1.959 \frac{s_n}{\sqrt{n}}, \quad (4.1)$$

where  $s_n$  denotes the standard deviation and  $n$  is the particle count.



---

Material	$\bar{d}$ (mean and 95 % CI) [nm]
PC/ABS (45/55)	$307 \pm 25$
PC/ABS (60/40)	$299 \pm 31$
PC/ABS (70/30)	$274 \pm 22$

**Table 4.2.:** Mean particle size  $\bar{d}$  with 95 % confidence interval (CI) for all three materials.

The size of the rubber particles in the three materials investigated was within the range of reported rubber particle diameters. Diameters of less than 100 nm and greater than 500 nm are both common in commercial ABS grades [85, 31]. In the context of heterogeneous rubber particles with SAN occlusions, bigger particle sizes of  $\bar{d} \approx 1 \mu\text{m}$  seem more common [85, 76].



## 5. Experimental testing setup

---

*This chapter describes the experimental methods and setup employed during the mechanical material characterisation underlying the studies presented in Chapters 6 and 7. The specimen geometries used in the uniaxial tensile tests and the fracture tests on single-edge-notch-tension (SENT) specimens are introduced. Detail is given on the testing machine and the optical deformation measurement system which is based on digital image correlation (DIC). Subsequently, background information on and a critical assessment of the analysis techniques to evaluate the true stress-strain behaviour is presented.*

---

### 5.1. Mechanical testing

The mechanical testing comprised of uniaxial tensile tests and fracture tests on single-edge-notch-tension (SENT) specimens conducted at room temperature. All tests were carried out using an Instron 1342 servo-hydraulic testing machine, upgraded with the digital controller FastTrack 8800, and an Instron load cell (serial No. 102045) calibrated up to forces of 10 kN. The device was controlled via the Instron WaveMatrix software (Version 1.5.302.0) which was also used to record the signals from the load cell as well as the traverse displacement.

The specimens were fixed using mechanical clamps that were tightened using a torque wrench. The clamping torque for PC/ABS (45/55) and PC/ABS (60/40) was set to 30 Nm for all tests. Due to the higher reaction forces, the clamping torque for all experiments on PC/ABS (70/30) was set to 40 Nm to avoid slippage. Prior to each experiment, the specimen's thickness was determined to an accuracy of 0.01 mm.

#### 5.1.1. Uniaxial tensile tests

The specimen geometry used in the uniaxial tensile tests is depicted in Fig. 5.1 and was used in previous works by Helbig et al. [51] and Naumann [84]. This specimen geometry was developed by Becker [8] and was found to provide a sufficiently homogeneous uniaxial stress state [8]. Furthermore, the neck width of 12 mm provided a large surface area for the optical deformation measurement via DIC excluding edge effects.

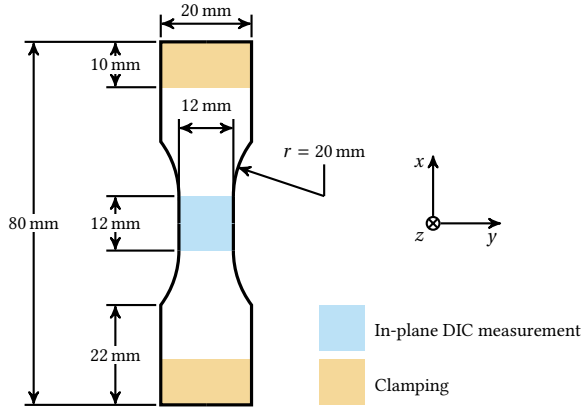


Figure 5.1.: Geometry of tensile test specimen (thickness  $t = (3.22 \pm 0.01)$  mm).

In all experiments, the nominal clamping length measured 10 mm on each end of the specimen (Fig. 5.1). The uniaxial tensile tests were carried out at two crosshead speeds,  $\dot{u} = 1.0$  mm/s and  $\dot{u} = 0.1$  mm/s. The two nominal strain rates,  $\dot{\epsilon} = 0.01$  s<sup>-1</sup> and  $\dot{\epsilon} = 0.1$  s<sup>-1</sup>, referred to in the following chapters, were defined as the approximate rates of overall specimen elongation divided by the gauge length of 12 mm (Fig. 5.1).

### 5.1.2. Fracture tests

The geometry of the SENT specimens is depicted in Fig. 5.2. The fracture tests were carried out using the same clamping mechanism and length as in the uniaxial tensile tests. In order to precisely clamp and align the specimens, a purpose-built guidance tool was used. The notch radius was 1 mm while the depth of the notch measured 4 mm. The SENT specimens were made from the same raw materials as the tensile specimens. The tests were performed at two different crosshead speeds,  $\dot{u} = 0.6$  mm/s and  $\dot{u} = 6.0$  mm/s.

### 5.1.3. Specimen manufacturing

All specimens were milled out of the raw materials introduced in Sec. 4.1. In a first step, workpieces measuring 20 mm in width and 80 mm in length were produced. These were either outfitted with a notch for the fracture tests or with a narrowing in the case of the uniaxial tensile tests. The cutter type and corresponding rotational speeds are listed in Tab. 5.1. Throughout the milling process, the tool as well as the process zone were cooled using a directed stream of compressed air in order to prevent thermal impact on the materials as good as possible.

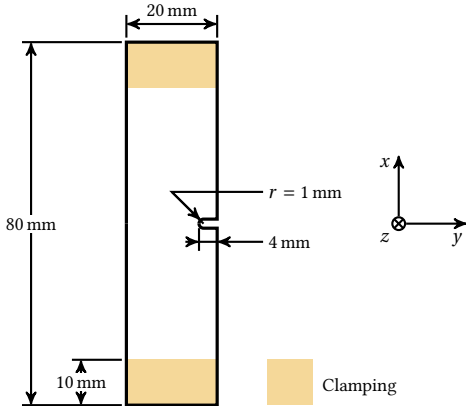


Figure 5.2.: Geometry of SENT fracture test specimen (thickness  $t = (3.22 \pm 0.01)$  mm).

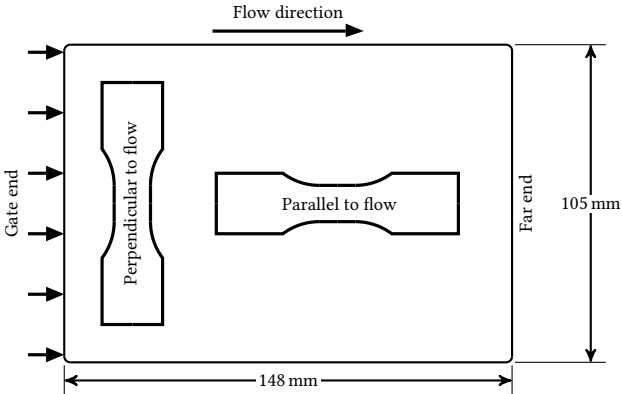


Figure 5.3.: Specimen orientations relative to material flow during injection moulding.

Step in manufacturing process	Mill diameter [mm]	No. of teeth [-]	Spindle speed [rpm]	Feed rate [mm/min]
Workpiece 20 mm x 80 mm	2	2	1400	50
Narrowing for uniaxial tensile test	40	6	220	30
Notch for SENT test	2	2	1400	50

Table 5.1.: Machining parameters for each stage of the specimen manufacturing process.

For the study presented in Chapter 6, all specimens were manufactured with their  $x$ -axis aligned along the direction of material flow in the injection moulding process (Fig. 5.3). For the study presented in Chapter 7, investigating whether the specimen orientation relative to the injection direction during manufacturing has an impact on the material response, a second batch of specimens was made. These specimens had their  $x$ -axis oriented orthogonally to the injection direction (Fig. 5.3). For clarity, the two different specimen orientations are referred to as “perpendicular to flow” and “parallel to flow”.

## 5.2. Digital image correlation (DIC)

To measure the local strain distribution on a specimen’s surface, a LIMESS Q-400 digital image correlation (DIC) system was used. Measuring displacements and deformations with DIC includes specimen preparation, image capture, and image evaluation, i.e. the actual step of digital image correlation and strain field computation.

With DIC, the deformations of surfaces can be tracked. Therefore, the part of the specimen surface where the strain field should be measured has to feature a random grey intensity pattern, commonly referred to as a speckle pattern (Sec. 5.2.1). To meet that requirement, all specimens in this work were first sprayed white and then speckled with black spray paint (Fig. 5.4).

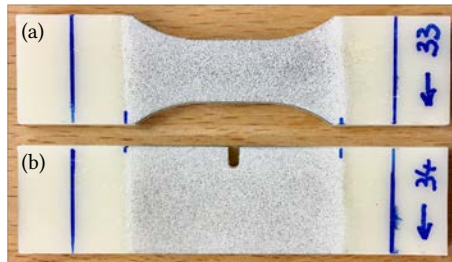


**Figure 5.4:** Example specimens showing speckle pattern for (a) the uniaxial tensile tests and (b) the SENT fracture tests.

The image capturing system featured one charge-coupled device (CCD) greyscale sensor (4:3 width to height ratio) with a resolution of 2 MP. Thus, two dimensional in-plane measurements were possible. To ensure precise measurements and avoid artefacts due to perspective distortion the specimen surface and the sensor planes were aligned. Attached to the sensor was a Nikon NIKKOR zoom lens (focal length: 28 – 105 mm, aperture: 1 : 3.5 – 4.5).

When using the whole sensor, the system’s maximum recording frequency is limited to 15 Hz. Adapting the recorded portion of the sensor to the actual region of interest (ROI) during the experiments allowed recording frequencies between 25 Hz and 30 Hz. The

camera's images as well as the experimental data recorded by the Instron 1342 testing machine were forwarded to a DANTEC TU-4XB timing hub. Triggered by the FastTrack 8800 controller, the timing hub also handled and synchronised the start of the image acquisition during an experiment. Once triggered, it forwarded the recorded images with synchronised force and displacement measurements to a computer to store them in a unified form. The data storage and setup of the DIC system were handled with the Istra4D software package (Version 4.3.0.1). In the Istra4D software package, the digital image correlation was carried out to determine the deformation. For the documentation, stress analysis, post processing, and visualisation of the results, two Python packages (expDoc & expAna) were developed.

### 5.2.1. Fundamentals of DIC

DIC tracks the displacement of a set of unique random intensity values throughout a series of subsequent images by comparison to the initial state. Firstly, the speckled ROI is selected in the reference image defining the initial state. In order to spatially resolve the displacement of points within the ROI, it is subdivided using virtual equidistant horizontal and vertical grids. Each intersection of these grids is treated as a centre point  $P(x_0, y_0)$  to a square subset of the ROI where  $x_0$  and  $y_0$  are the point's coordinates in the reference image (Fig. 5.5).

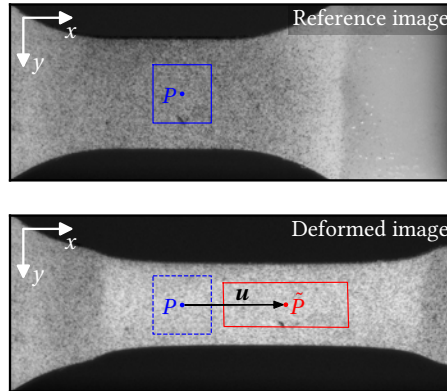


**Figure 5.5.:** Displacement and deformation of the reference square subset with centre point  $P(x_0, y_0)$ .

The task is now to spatially correlate  $P$  with its instance  $\tilde{P}(\tilde{x}_0, \tilde{y}_0)$  in the target image in order to calculate the grid point's displacement vector  $\mathbf{u} = (u, v)^T$  (Fig. 5.5). Since the target subset in general will not only move but also deform, an approach is needed to model this displacement transformation in proximity of the centre point, i.e. in all points part of the subset. Therefore, subset shape functions  $(\xi, \eta)$ , mapping the displacement in the  $x$  and  $y$  directions, respectively, are introduced. The requirement placed on appropriate

shape functions is that they are suited to describe the subset's shape change, i.e. accurately describe the target position of a point  $\tilde{Q}(\tilde{x}_i, \tilde{y}_i)$  of the subset. Using a first order Taylor expansion of the displacement vector as the subset shape functions, these allow for describing translation, rotation, scaling (normal strains), and shearing:

$$\xi(x_i, y_i) = u + \frac{\partial u}{\partial x}(x_i - x_0) + \frac{\partial u}{\partial y}(y_i - y_0), \quad (5.1)$$

$$\eta(x_i, y_i) = v + \frac{\partial v}{\partial x}(x_i - x_0) + \frac{\partial v}{\partial y}(y_i - y_0) \quad (5.2)$$

with reference coordinates  $x_i$  and  $y_i$  of the point  $Q$  in the reference image. Making use of the shape functions, the target coordinates of  $\tilde{Q}$  are then given by

$$\tilde{x}_i = x_i + \xi(x_i, y_i), \quad (5.3)$$

$$\tilde{y}_i = y_i + \eta(x_i, y_i). \quad (5.4)$$

In order to identify the reference subset's displacement and deformation in the target image, a cross-correlation criterion

$$C = f(u, v, \frac{\partial u}{\partial x}, \frac{\partial u}{\partial y}, \frac{\partial v}{\partial x}, \frac{\partial v}{\partial y}) \quad (5.5)$$

is used [91]. In an iterative process, the position and deformation of the subset in the target image is determined until a predefined convergence criterion is satisfied. The possibility of  $\tilde{Q}$  being located between pixels is treated by employing a sub-pixel interpolation scheme, also enabling the DIC method to provide sub-pixel precision. Thus, the positions and displacements as well as the local deformation gradient for each subset are computed and assigned to a grid point.

From the two-dimensional representation of the deformation gradient, the right Cauchy-Green tensor  $C$  (Eq. (2.22)) is computed as a starting point for the calculation of the in-plane strain field. Denoted by  $\epsilon$ , the logarithmic strain tensor (Eq. (2.29)) is used in the following chapters.

## 5.2.2. Computation of the true stress and volume strain response

Knowledge of the in-plane strain fields allowed for the determination of the true stress and volumetric strain response from the uniaxial tensile tests. Thereby, for a rectangular section of the specimen surface where DIC was performed (Fig. 5.1), the average strains in axial and transverse directions were computed. The section was selected based on the homogeneity of the in-plane strain fields in tensile and transverse directions such that edge effects were excluded. The true stress  $\sigma$  in the tensile direction is obtained by relating the reaction force  $F$  to the current specimen cross section  $A$  as specified by

$$\sigma = \frac{F}{A}. \quad (5.6)$$



In this work, the current cross section was calculated assuming an isotropic material behaviour, i.e. equal strains in the through-thickness and transverse in-plane directions. For a specimen orientation as shown in Fig. 5.1 where  $\varepsilon_{xx}$  represents the axial strain, this means  $\varepsilon_{zz} = \varepsilon_{yy}$ . The current specimen cross section can then be specified by

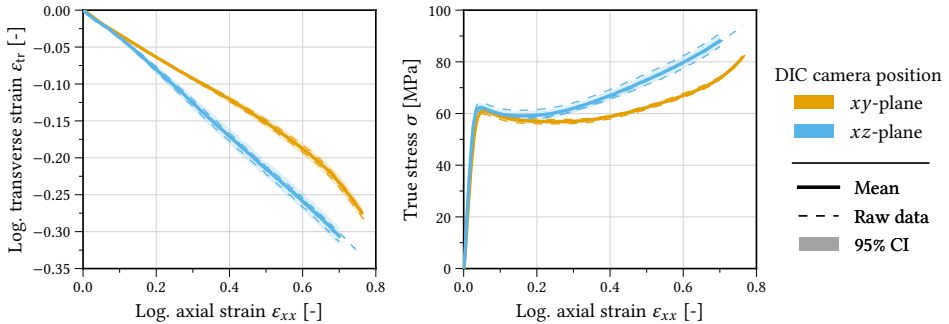
$$A = A_0 \exp(2 \varepsilon_{yy}), \quad (5.7)$$

where  $A_0$  denotes the initial cross section of the undeformed specimen. Still assuming an isotropic material, the volume strain is given by

$$\varepsilon_v = \text{tr}(\boldsymbol{\varepsilon}) = \varepsilon_{xx} + 2 \varepsilon_{yy}. \quad (5.8)$$

### 5.2.3. DIC analysis in the through-thickness direction

Apart from the DIC measurements “in-plane”, others measuring “through-thickness”, i.e. in the specimen’s  $xz$ -plane (Fig. 5.1), were carried out. The aim was to validate the assumption of equal transverse in-plane and through-thickness strains. The experiments for both camera positions were carried out using specimens made from PC/ABS (70/30) at a nominal strain rate of  $\dot{\varepsilon} = 0.1 \text{ s}^{-1}$ . The results were analysed as outlined in Sec. 5.2.4.



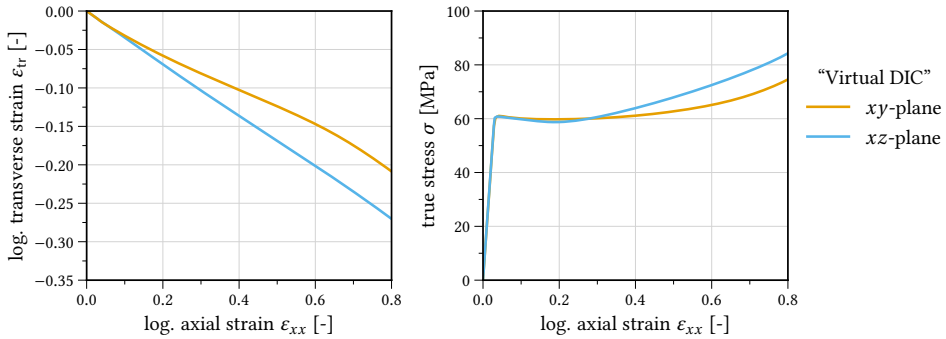
**Figure 5.6.:** Transverse strain  $\varepsilon_{tr}$  measured using DIC in the  $xy$ -plane and  $xz$ -plane of the specimen surface (Fig. 5.1) and corresponding true stress-strain curves.

Figure 5.6 reveals significant different transverse strain measurements for the different camera orientations. The transverse strain  $\varepsilon_{tr}$  observed in the through-thickness direction, i.e. in the  $xz$ -plane, had a significantly higher magnitude. The resulting greater decrease of the current specimen cross section calculated via Eq. (5.7) eventually yielded a higher true stress response (Fig. 5.6).

The results shown in Fig. 5.6 suggest that the assumption of equal through-thickness and in-plane transverse strains was not valid. However, limitations in the DIC setup could have had an impact on the results. Due to the system’s resolution, the through-thickness DIC results could only be based on a single-digit number of subsets in the transverse direction. This causes a high relative uncertainty of the measurements compared to the in-plane

measurements. Furthermore, the out-of-plane motion of the specimen surface away from the image plane due to necking must be considered. Since out-of-plane motion away from the image plane decreases the image magnification, it causes perceived negative normal strains in all directions [104]. This effect had an impact on the results since the measured transverse strains started to significantly diverge with the onset of necking.

Furthermore, the specimen geometry and possible edge effects prevalent in the  $xz$ -plane are other possible reasons for the observed differences. To dissect a possible impact of the measuring method from the apparent anisotropy in the material's response, the uniaxial tensile tests were simulated using Abaqus/Explicit. Therefore, one eighth of a tensile specimen (Fig. 5.1) was modelled and constrained accordingly. The constitutive model employed was the isotropic elastic-viscoplastic Raghava model calibrated from the in-plane DIC results (Sec. 9.2).



**Figure 5.7.:** Transverse logarithmic strains in the  $xy$ -plane and  $xz$ -plane of the specimen surface and corresponding true stress-strain curves from FE simulations.

Figure 5.7 shows the results for “virtual DIC” measurements on the simulated specimen that feature the same trends as the experimental results (Fig. 5.6). Since the material behaviour in the simulations was isotropic, this indicates an impact of the specimen geometry and edge effects on the through-thickness measurements resulting in a different stress triaxiality. Hence, the through-thickness measurement with the two-dimensional DIC setup in conjunction with the specimen geometry used, was not suited to determine a possible anisotropy in the material's deformation behaviour.

Without being able to certainly quantify a possibly anisotropic deformation behaviour, the assumption that the materials exhibit equal through-thickness and in-plane transverse strains was maintained throughout this work.

A quantitative analysis of the materials' volume strain behaviour using a three-dimensional DIC setup would be highly instructive since Hiermaier and Huberth [54] found an anisotropic transverse strain response for PC/ABS (60/40). However, Hiermaier and Huberth [54] also concluded that the assumption of isotropy has little impact on the true stress response.

### 5.2.4. Analysis

The analysis of the experimental data was based on three successful repetitions of each experiment with identical test parameters (sample size  $N = 3$ ). Results of each individual experiment were obtained as a series of  $(x, y)$  pairs. For the analysis, a reference series of  $\bar{x}$  values of equidistant spacing was defined for each sample of experiments and all results were mapped onto this reference  $\bar{x}$  series through interpolation. The sample mean was defined as a series of  $(\bar{x}, \bar{y})$  pairs where the  $\bar{y}$  values denote the arithmetic mean of the interpolated values  $\tilde{y}$  of each test in the sample

$$\bar{y} = \frac{1}{N} \sum_{j=1}^N \tilde{y}_j. \quad (5.9)$$

The sample standard deviation  $s_N$  for every  $(\bar{x}, \bar{y})$  pair was calculated through

$$s_N = \sqrt{\frac{1}{N} \sum_{j=1}^N (\tilde{y}_j - \bar{y})^2}. \quad (5.10)$$

Both the sample mean and the standard deviation were computed up to the first final failure occurring in the sample, unless stated otherwise. To more clearly assess the uncertainty as well as the significance of the sample, the 95 % confidence interval (CI) for the sample mean was calculated. The CI's boundaries in every  $(\bar{x}, \bar{y})$  pair are the upper and lower confidence limits

$$CL_{U/L} = \bar{y} \pm 1.959 s_{\bar{y}}, \quad (5.11)$$

where  $s_{\bar{y}}$  is the standard error of the sample mean given by

$$s_{\bar{y}} = \frac{s_N}{\sqrt{N}}. \quad (5.12)$$

However, variations in the specimens' widths as well as unavoidable differences in the clamping lengths were not accounted for in the analyses. Furthermore, uncertainties in the DIC process were assumed to have a similar impact on all experiments. Thus, the individual data sets obtained through DIC were assumed to be perfect, i.e. without an uncertainty attached to them.



## 6. The impact of blend composition on the material response

---

*This chapter presents an experimental investigation of the large-strain deformation and fracture behaviour of the three PC/ABS blends introduced in Chapter 4. With a focus on the effect of blend composition, uniaxial tensile tests and SENT fracture tests were conducted at two test speeds using the experimental setup presented in Chapter 5. Applying the methods introduced in Secs. 5.2.2 and 5.2.4, the true stress and volumetric strain response in uniaxial tensile tests as well as the evolution of the plastic zone in notched SENT specimens prior to and during fracture were determined.*

---

### 6.1. Deformation behaviour - uniaxial tensile tests

In this section, the deformation behaviour under uniaxial tension of the three PC/ABS blends introduced in Chapter 4 is presented and analysed in detail, beginning with the results for a nominal strain rate of  $\dot{\epsilon} = 0.1 \text{ s}^{-1}$ , the crosshead speed being  $\dot{u} = 1.0 \text{ mm/s}$ . Subsequently, the results for a nominal strain rate of  $\dot{\epsilon} = 0.01 \text{ s}^{-1}$  where the crosshead speed was  $\dot{u} = 0.1 \text{ mm/s}$  are shown. On the basis of the results for both strain rates, the strain rate dependency of the materials is discussed in Sec. 6.3.1.

#### 6.1.1. Nominal strain rate $\dot{\epsilon} = 0.1 \text{ s}^{-1}$

The force-displacement response at a crosshead speed of  $\dot{u} = 1.0 \text{ mm/s}$  of all three investigated materials is depicted in Fig. 6.1. Figures 6.2, 6.3, and 6.4 show the evolution of the logarithmic axial strain on the specimen surface corresponding with the raw experimental data annotated with (A), (B), and (C) in Fig. 6.1. All three figures illustrate in an early stage of the deformation ( $u = 2.5 \text{ mm}$ ) the formation and growth of the initial and complementary shear bands that precede the necking process, similarly to what can be found in neat PC (Sec. 3.1.3).

In the uniaxial tensile tests, the peak force  $F_{\max}$  was measured at the onset of plastic deformation for all three blends (Fig. 6.1). The peak force was found to increase with

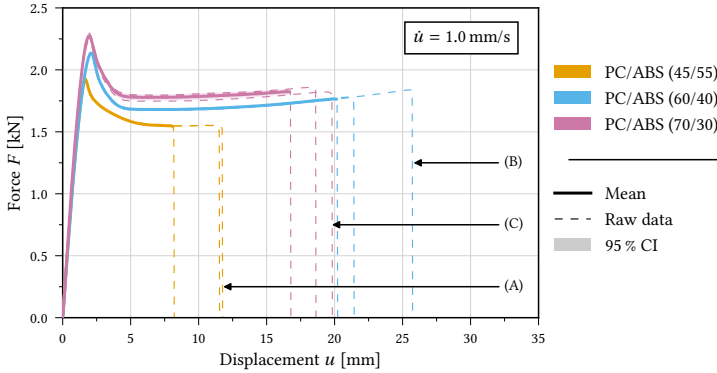


**Figure 6.1:** Force-displacement behaviour depending on PC/ABS composition at a crosshead speed of  $\dot{u} = 1.0 \text{ mm/s}$ ; the DIC strain fields belonging to experiments (A), (B), and (C) are shown in Figs. 6.2, 6.3, and 6.4.

the PC content of the blends (Fig. 6.1 and Tab. A.2). The total specimen elongation at break  $u_{\text{fail}}$  was significantly lower regarding PC/ABS (45/55) in comparison with the other two materials (Tab. A.2). The shatter in the failure displacement was considerable for all materials, though.

Figure 6.5 shows the stress-strain curves of the three PC/ABS blends at a strain rate of  $\dot{\epsilon} = 0.1 \text{ s}^{-1}$ . All three materials exhibited an almost linear elastic range ending with a distinct yield point (Figs. 6.5 and 6.6).

The elastic modulus  $E$  of PC/ABS (70/30) was found to be increased by roughly 6% over that of PC/ABS (60/40) and by about 7% over that of PC/ABS (45/55) (Tab. A.1). Thereby, the modulus  $E$  was defined as

$$E = \frac{\sigma(\epsilon_1 = 0.015) - \sigma(\epsilon_0 = 0.005)}{\epsilon_1 - \epsilon_0}. \quad (6.1)$$

The plastic range of the stress response for all three materials featured the characteristic strain softening followed by progressive strain rehardening up to failure. PC/ABS (70/30) exhibited a higher stress level in the plastic strain regime than the other two blends. Comparing the initial yield stress  $\sigma_0$ , defined as the peak stress value before the onset of softening, PC/ABS (70/30) exhibited a yield stress of  $\sigma_0 = (60.98 \pm 1.01) \text{ MPa}$ , whereas the yield stresses of PC/ABS (60/40) and PC/ABS (45/55) amounted to  $\sigma_0 = (58.15 \pm 0.14) \text{ MPa}$  and  $\sigma_0 = (51.46 \pm 0.24) \text{ MPa}$ , respectively (Tab. A.1).

Hence, the mean yield stress of PC/ABS (70/30) was increased by almost 19% over that of PC/ABS (45/55), and about 5% over that of PC/ABS (60/40). The amount of strain softening, defined as the ratio between the local minimum (plateau) stress in the plastic range  $\sigma_{\text{min}}$  and the initial yield stress  $\sigma_0$ , was found to be virtually identical in all three

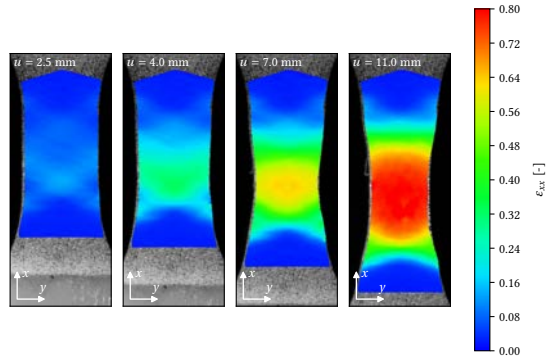


**Figure 6.2.:** Distribution of the axial strain  $\epsilon_{xx}$  on the specimen surface of PC/ABS (45/55) belonging to curve (A) in Fig. 6.1 at four values of the total specimen elongation  $u$ .

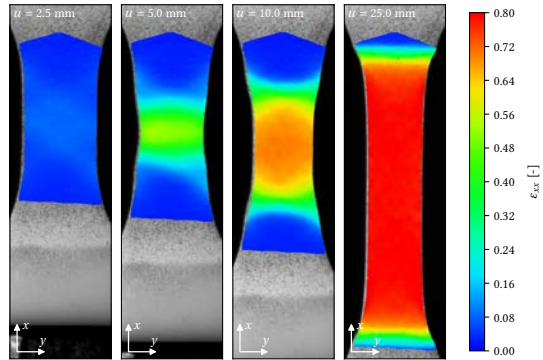


**Figure 6.3.:** Distribution of the axial strain  $\epsilon_{xx}$  on the specimen surface of PC/ABS (60/40) belonging to curve (B) in Fig. 6.1 at four values of the total specimen elongation  $u$ .

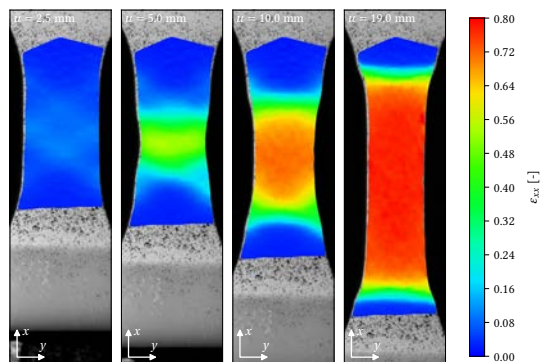


**Figure 6.4.:** Distribution of the axial strain  $\epsilon_{xx}$  on the specimen surface of PC/ABS (70/30) belonging to curve (C) in Fig. 6.1 at four values of the total specimen elongation  $u$ .

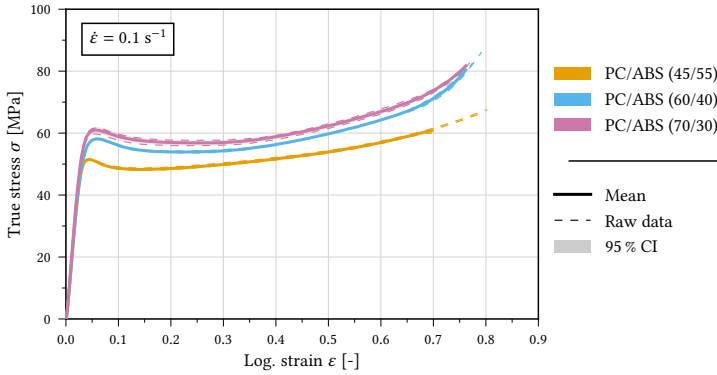


Figure 6.5.: True stress-strain behaviour depending on PC/ABS composition at a strain rate of  $\dot{\epsilon} = 0.1 \text{ s}^{-1}$ .

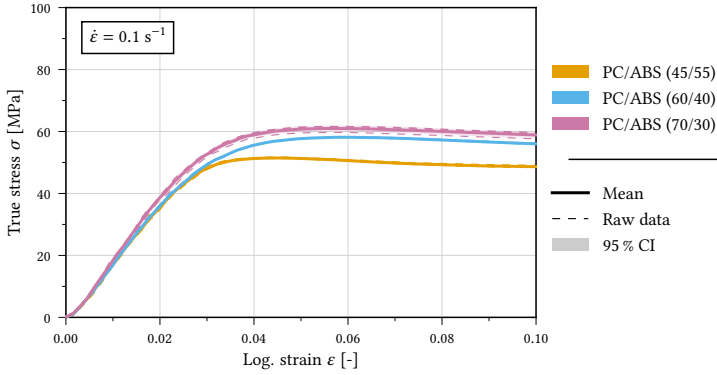


Figure 6.6.: True stress-strain behaviour of the three PC/ABS blends for a log. axial strain up to  $\epsilon = 0.1$  at a strain rate of  $\dot{\epsilon} = 0.1 \text{ s}^{-1}$ .

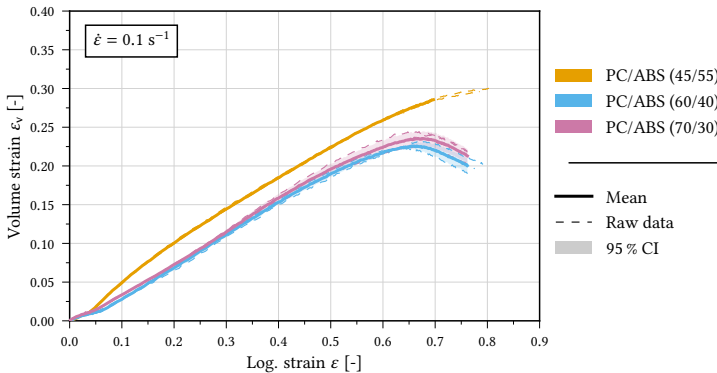


Figure 6.7.: Dilatation behaviour depending on PC/ABS composition at a strain rate of  $\dot{\epsilon} = 0.1 \text{ s}^{-1}$ .



materials with mean values of 0.93 regarding PC/ABS (60/40) and PC/ABS (70/30), and 0.94 for PC/ABS (45/55), respectively.

However, the difference between the corresponding strain values  $\varepsilon_0$  and  $\varepsilon_{\min}$  differs noticeably between the PC-rich blend compositions PC/ABS (70/30) ( $\varepsilon_0 - \varepsilon_{\min} = 0.194 \pm 0.008$ ) and PC/ABS (60/40) ( $\varepsilon_0 - \varepsilon_{\min} = 0.164 \pm 0.024$ ) in comparison with the ABS-rich blend composition PC/ABS (45/55) ( $\varepsilon_0 - \varepsilon_{\min} = 0.095 \pm 0.004$ ) (Tab. A.1). Thus, the rehardening set in significantly earlier in the case of PC/ABS (45/55) (Fig. 6.5). The overall amount of progressive rehardening at large strains was found to increase with the PC mass fraction and was thus somewhat more pronounced for the PC/ABS (70/30) and PC/ABS (60/40) blends (Fig. 6.5).

The raw test data in Fig. 6.5 indicates a larger amount of scatter in the failure strain  $\varepsilon_{\text{fail}}$  for PC/ABS (45/55) compared to PC/ABS (60/40) and PC/ABS (70/30) (Tab. A.3). However, the mean failure strains of the materials did not differ significantly (Tab. A.3). As well as the scatter in the failure strain increasing with the ABS mass fraction, the failure stress was also found to increase (Tab. A.3). The mean failure stresses of PC/ABS (70/30) and PC/ABS (60/40) were significantly higher than the failure stress found for PC/ABS (45/55). However, the difference in failure stress between PC/ABS (70/30) and PC/ABS (60/40) was within the uncertainty of the results (Tab. A.3).

The overall response of the three PC/ABS blends under uniaxial tension exhibited a pronounced plastic dilatancy, shown in Fig. 6.7. With the onset of plastic deformation at  $\varepsilon \approx 0.05$ , the different dilatancies of the three materials manifested themselves clearly. PC/ABS (45/55) exhibited a significantly larger dilation over both PC/ABS (60/40) and PC/ABS (70/30) (Fig. 6.7). Comparing the two PC-rich blends, PC/ABS (60/40) and PC/ABS (70/30), the difference in the overall volume increase was found to be within the uncertainty of the results. In all three materials, the growth in volume strain decreased again with axial strains larger than 0.6 (Fig. 6.7). In case of the two PC-rich blends, the overall dilation decreased significantly with strains larger than approximately 0.67 until final failure (Fig. 6.7). In the same range of axial strain, the stress-strain curves of both materials exhibited an even more distinct increase of the true stress lacking in the response of PC/ABS (45/55) (Fig. 6.5).

The in-plane Poisson's ratio  $\nu$  for all three materials is shown in Fig. 6.8. For small axial strains, and thus even smaller transverse strains, the results are heavily impacted by the finite resolution of the DIC system resulting in high uncertainties that could not be quantified. Therefore, only values for  $\varepsilon > 0.03$  are considered in the following analysis.

With the onset of plastic deformation, the Poisson's ratio in each material reached its maximum followed by a decline. Thereby, the drop was more pronounced and sharper in the case of PC/ABS (45/55) where the mean Poisson's ratio reached a minimum of  $\nu_{\min} = 0.24$  at  $\varepsilon_{\nu_{\min}} = 0.135$  (Tab. A.6). This drop was less pronounced for the other two materials, the minimum being  $\nu_{\min} = 0.31$  in the case of PC/ABS (60/40) and  $\nu_{\min} = 0.30$  for PC/ABS (70/30). Also, the decline for the PC-rich blends was less sharp such that they exhibited significantly greater values for  $\varepsilon_{\nu_{\min}}$  (Tab. A.6). Throughout the plastic

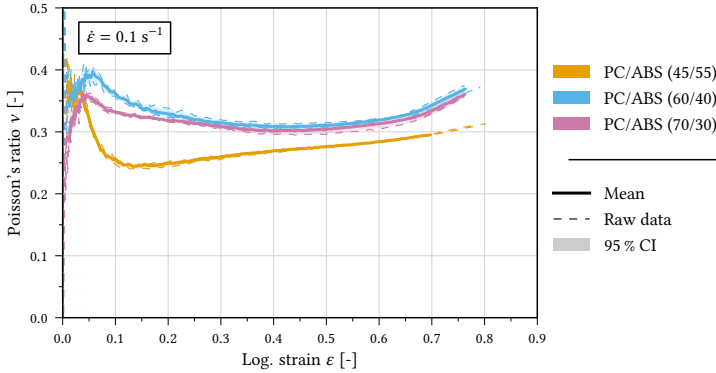


**Figure 6.8.:** Poisson's ratio depending on PC/ABS composition at a strain rate of  $\dot{\epsilon} = 0.1 \text{ s}^{-1}$ .

range, the Poisson's ratios for the two PC-rich blends were significantly higher than for PC/ABS (45/55) (Fig. 6.8). However, the dependence of the Poisson's ratio on the PC mass fraction in the range of strain softening (Fig. 6.5) appeared to be non-monotonic since PC/ABS (70/30) exhibited a smaller Poisson's ratio than PC/ABS (60/40) (Fig. 6.8).

### 6.1.2. Nominal strain rate $\dot{\epsilon} = 0.01 \text{ s}^{-1}$

Similar to the higher strain rate of  $\dot{\epsilon} = 0.1 \text{ s}^{-1}$ , the peak force was found to increase with PC content for the lower strain rate of  $\dot{\epsilon} = 0.01 \text{ s}^{-1}$ , the crosshead speed being  $\dot{u} = 0.1 \text{ mm/s}$  (Fig. 6.9 and Tab.A.4). On average, the fracture displacement increased for the lower crosshead speed compared to the higher crosshead speed for all three materials (Tables A.4 and A.2). Also, PC/ABS (45/55) again exhibited significantly lower specimen elongations at break than the two PC-rich blends (Tab. A.2). The DIC derived strain fields on the surface in tensile direction for different stages of the deformation for each material are depicted in Figs. 6.10, 6.11, and 6.12.

Figure 6.13 shows the stress-strain curves of the three PC/ABS materials at a strain rate of  $\dot{\epsilon} = 0.01 \text{ s}^{-1}$ . As was the case for the higher strain rate of  $\dot{\epsilon} = 0.1 \text{ s}^{-1}$ , the materials exhibited an almost linear elastic range up to a distinct yield point. The following large plastic range began with a softening upon yield and later featured a progressive rehardening (Fig. 6.13). Both the initial yield stress  $\sigma_0$  and the overall stress level were found to depend on the PC/ABS ratio and increased with the PC content of the blends (Fig. 6.13). Consequently, within the materials investigated, PC/ABS (70/30) exhibited the highest initial yield stress  $\sigma_0 = (62.43 \pm 0.35) \text{ MPa}$  which is an increase of 7.0 % over the mean obtained for PC/ABS (60/40) and 20.6 % regarding PC/ABS (45/55), respectively (Tab. A.5).

With regard to the mean extent of softening,  $\sigma_{\min}$  amounted to 91.6 % of  $\sigma_0$  for PC/ABS (45/55), 92.2 % for PC/ABS (60/40), and 90.4 % for PC/ABS (70/30) (Tab. A.5). The softening in PC/ABS (45/55) was found in a smaller range of the axial strain than in

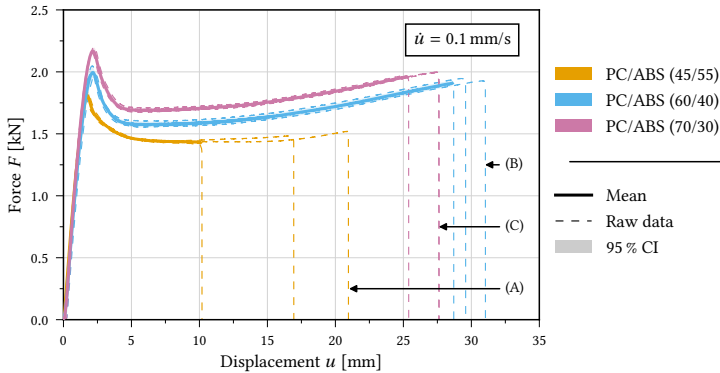


**Figure 6.9:** Force-displacement behaviour depending on PC/ABS composition at a crosshead speed of  $\dot{u} = 0.1 \text{ mm/s}$ ; the DIC strain fields belonging to experiments (A), (B), and (C) are shown in Figs. 6.10, 6.11, and 6.12.

the PC-rich blends PC/ABS (60/40) and PC/ABS (70/30) where the softening dragged on significantly longer (Fig. 6.13). Upon rehardening, the stress trends of PC/ABS (70/30) and PC/ABS (60/40) featured identical characteristics. After a gentle onset of rehardening, both materials exhibited two successive, almost linear, domains. The beginning of the latter was demarcated by a rather sharp and distinctive transition at an axial strain of  $\varepsilon \approx 0.65$  (Fig. 6.13), causing a sharp rise in stress until finale failure. In contrast, the rehardening in PC/ABS (45/55) was less pronounced. Only part of the raw data in Fig. 6.13 exhibits a sharp rise in true stress which is less distinct in comparison to the other two materials.

PC/ABS (45/55) featured the highest ABS mass fraction of the blends investigated and exhibited the biggest extent of volume strain also at a strain rate of  $\dot{\varepsilon} = 0.01 \text{ s}^{-1}$  (Fig. 6.14). The two PC-rich materials PC/ABS (60/40) and PC/ABS (70/30) showed a similar dilation behaviour which was less pronounced than that of PC/ABS (45/55). Regarding PC/ABS (60/40) and PC/ABS (70/30), the dilation curves in Fig. 6.14 exhibit a kink at an axial strain between  $\varepsilon = 0.6$  and  $\varepsilon = 0.7$ , where the almost linear increase of volume strain reverses to a nearly linear decline. This change concerning the dilation behaviour coincided with the before mentioned sharp rise in the stress response of both materials (Fig. 6.13).

Figure 6.15 shows the in-plane Poisson's ratio of the three investigated PC/ABS blends. With the onset of plastic deformation, the materials exhibited a local maximum in the Poisson's ratio that was more pronounced for PC/ABS (45/55) and PC/ABS (60/40) than in the case of PC/ABS (70/30) (Fig. 6.15). Overall, the Poisson's ratio of two the PC-rich blends was significantly higher than that of PC/ABS (45/55). Regarding only PC/ABS (60/40) and PC/ABS (70/30), the former exhibited a significantly higher peak and overall level up to an axial strain of about  $\varepsilon = 0.3$  (Fig. 6.15). For strains larger than that, both materials were found to behave similarly, exhibiting differences within the uncertainty of the results. PC/ABS (60/40) and PC/ABS (70/30) exhibited a slightly decreasing and afterwards all

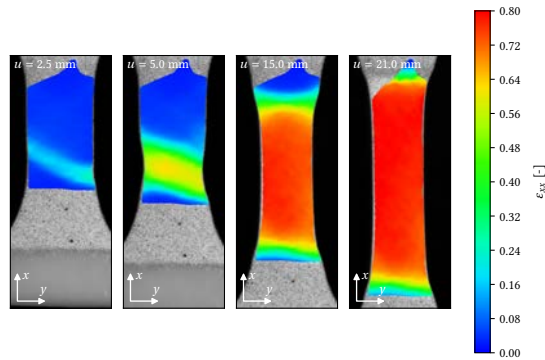


**Figure 6.10.:** Distribution of the axial strain  $\epsilon_{xx}$  on the specimen surface of PC/ABS (45/55) belonging to curve (A) in Fig. 6.9 at four values of the total specimen elongation  $u$ .

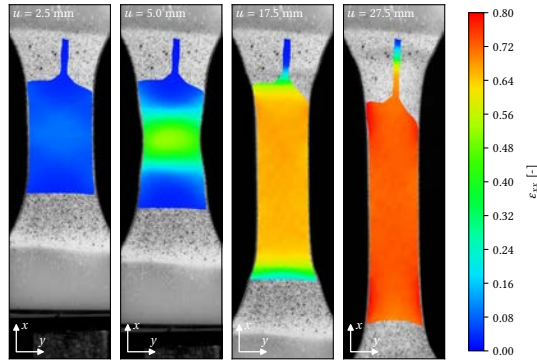


**Figure 6.11.:** Distribution of the axial strain  $\epsilon_{xx}$  on the specimen surface of PC/ABS (60/40) belonging to curve (B) in Fig. 6.9 at four values of the total specimen elongation  $u$ .

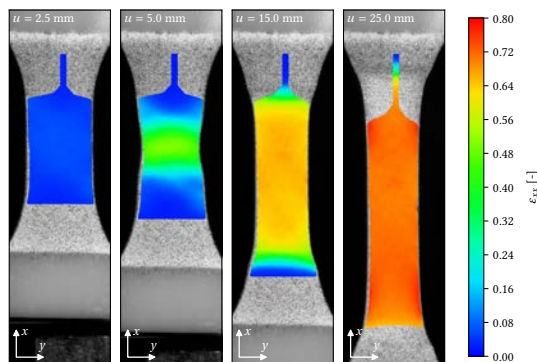


**Figure 6.12.:** Distribution of the axial strain  $\epsilon_{xx}$  on the specimen surface of PC/ABS (70/30) belonging to curve (C) in Fig. 6.9 at four values of the total specimen elongation  $u$ .

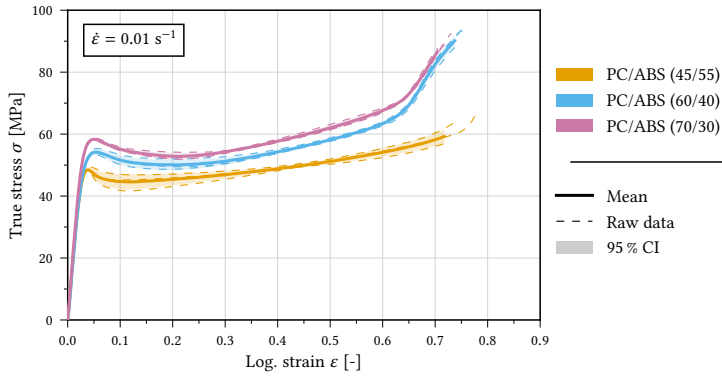


Figure 6.13.: True stress-strain behaviour depending on PC/ABS composition at a strain rate of  $\dot{\epsilon} = 0.01 \text{ s}^{-1}$ .

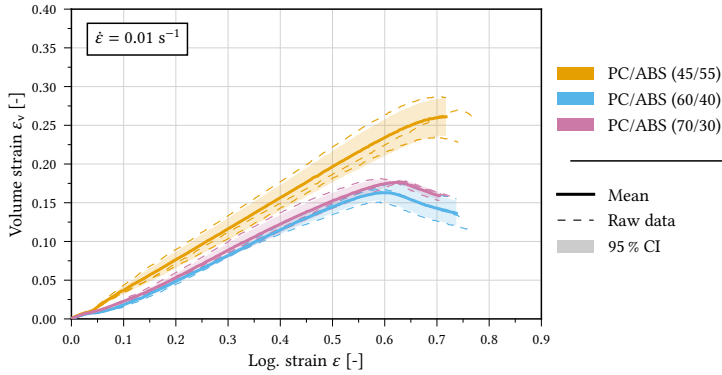


Figure 6.14.: Dilation behaviour depending on PC/ABS composition at a strain rate of  $\dot{\epsilon} = 0.01 \text{ s}^{-1}$ .

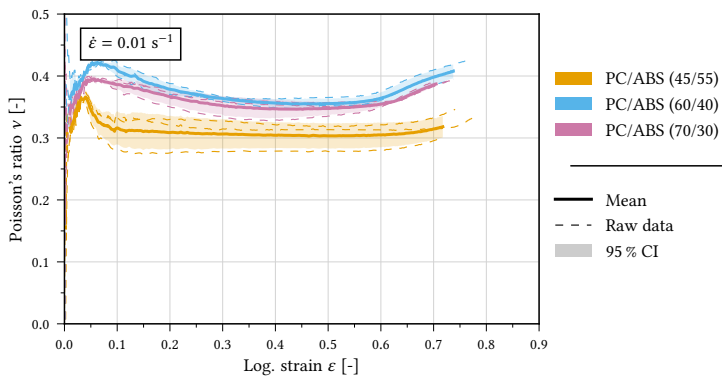


Figure 6.15.: Poisson's ratio depending on PC/ABS composition at a strain rate of  $\dot{\epsilon} = 0.01 \text{ s}^{-1}$ .

but constant Poisson's ratio for strains from  $\varepsilon = 0.4$  to  $\varepsilon = 0.6$ . Both materials' Poisson's ratios distinctively began to almost linearly increase again when the stress and volume strain responses also changed their trends (Figs. 6.15, 6.14, and 6.13).

## 6.2. Failure behaviour - SENT tests

To complement the insights into the large-strain deformation behaviour by means of uniaxial tensile tests, the failure behaviour was investigated in fracture tests using SENT specimens (Fig. 5.2). Apart from the force-displacement response, the evolution of the plastic deformation at the notch and the specific work of fracture were of particular interest.

### 6.2.1. Plastic zone formation at notch

Figures 6.16, 6.17, and 6.18 show contours of the logarithmic strain  $\varepsilon_{xx}$  in the tensile direction on the specimen surface for all three materials for a crosshead speed of  $\dot{u} = 0.6$  mm/s. Note, that in the region of large deformation in Figs. 6.16, 6.17, and 6.18, the depicted total strains are much larger than the elastic strains. Hence, they represent the plastic deformation at the notch for the corresponding value of the overall specimen elongation.

The plastic deformation was found to localise in an elongated zone ahead of the notch for all three investigated materials (Figs. 6.16, 6.17, and 6.18). Compared to PC/ABS (45/55), the plastic zone on the specimen surface of the PC-rich blends was bulkier and split up into two branches prior to as well as during crack propagation (Figs. 6.17 and 6.18). In addition, the size of the plastic zone shape in both PC/ABS (60/40) and PC/ABS (70/30) was notably smaller than in PC/ABS (45/55) for the same value of the overall specimen elongation.

Contour plots of the local strain field in the tensile direction of experiments conducted at a crosshead speed of  $\dot{u} = 0.6$  mm/s are shown in Fig. 6.19, 6.20, and 6.21. The differences in the displacements presented for the different deformation speeds arise from restrictions in the acquisition clock of the imaging system while maintaining a high enough resolution. Thus, the nearest corresponding stages of the deformation were chosen.

The general characteristics of the plastic zones for a crosshead speed of  $\dot{u} = 6.0$  mm/s were similar to those found for  $\dot{u} = 0.6$  mm/s in the sense that they were elongated ahead of the notch and of similar width (Figs. 6.16, 6.17, 6.18, 6.19, 6.20, and 6.21). Yet the plastic zone shape exhibited by PC/ABS (45/55) was not quite as elongated and its tip was less pointy (Figs. 6.16 and 6.19). The same applied to the branches of the PC-rich blends. Particularly for PC/ABS (60/40), the plastic zone shape appeared bulkier and the branching less distinct (Fig. 6.17 and 6.20). Regarding PC/ABS (70/30), for all depicted stages of the deformation at the higher test speed, the plastic zone shape was smaller than for corresponding loading situations at the lower test speed (Fig. 6.18 and 6.21).

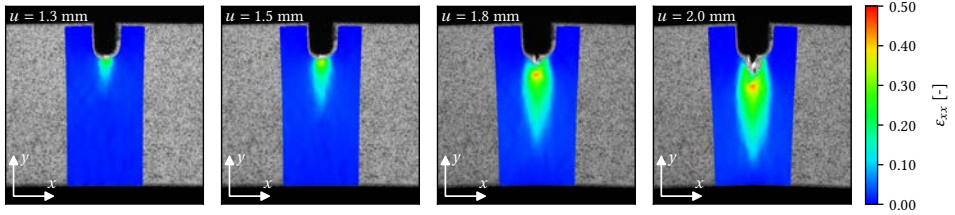


**Figure 6.16.:** Contours of the strain  $\epsilon_{xx}$  in tensile direction on SENT specimen for PC/ABS (45/55), four values of the overall specimen elongation  $u$ , and a crosshead speed of  $\dot{u} = 0.6$  mm/s.

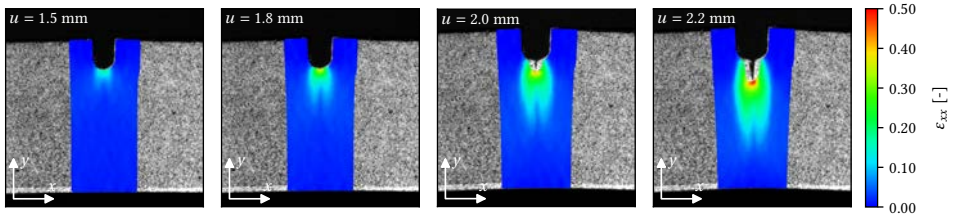


**Figure 6.17.:** Contours of the strain  $\epsilon_{xx}$  in tensile direction on SENT specimen for PC/ABS (60/40), four values of the overall specimen elongation  $u$ , and a crosshead speed of  $\dot{u} = 0.6$  mm/s.

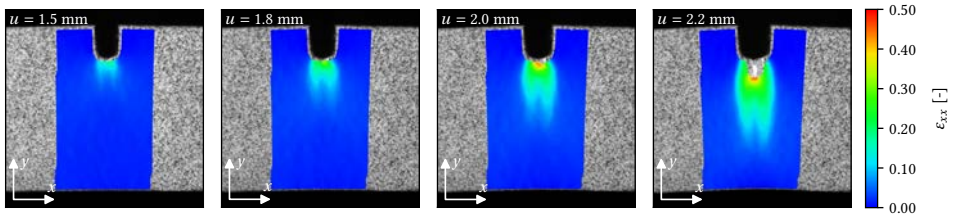


**Figure 6.18.:** Contours of the strain  $\epsilon_{xx}$  in tensile direction on SENT specimen for PC/ABS (70/30), four values of the overall specimen elongation  $u$ , and a crosshead speed of  $\dot{u} = 0.6$  mm/s.

### 6.2.2. Force-displacement response

The force-displacement curves shown in Figs. 6.22 and 6.23 for both displacement velocities feature a higher peak load with an increasing PC content of the blends. For the lower crosshead speed of  $\dot{u} = 0.6$  mm/s, the mean peak load  $F_{\max}$  for PC/ABS (70/30) was increased by 21.2% over that of PC/ABS (45/55) and by 8.4% over that of PC/ABS (60/40) (Tab. A.7). Also, the elastic response in the case of PC/ABS (70/30) was notably stiffer than what was found for PC/ABS (60/40) and PC/ABS (45/55) (Fig. 6.22). Regarding the higher test speed, the elastic responses of the PC-rich materials were similar (Fig. 6.23). The difference in stiffness between PC/ABS (60/40) and PC/ABS (70/30) in Fig. 6.23 is visibly smaller than the difference to PC/ABS (45/55). Yet, significant differences emerged with the onset of plastic deformation around a total specimen elongation of  $u = 1.0$  mm.

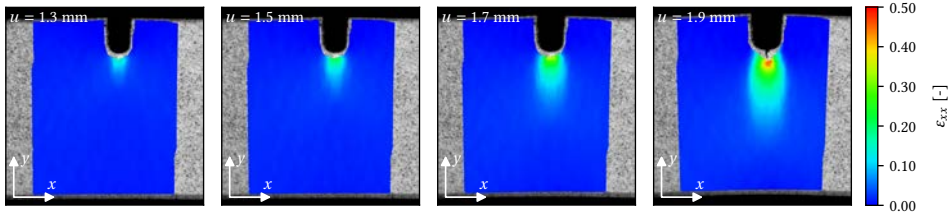


**Figure 6.19.:** Contours of the strain  $\varepsilon_{xx}$  in tensile direction on SENT specimen for PC/ABS (45/55), four values of the overall specimen elongation  $u$ , and a crosshead speed of  $\dot{u} = 6.0$  mm/s.

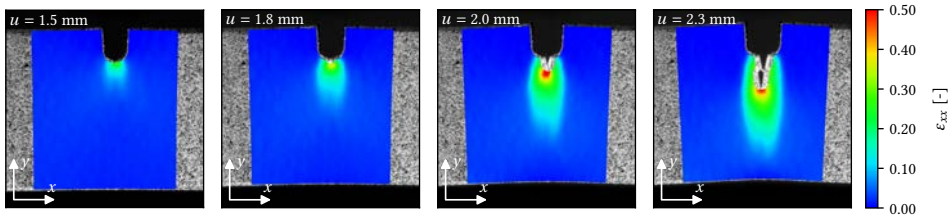


**Figure 6.20.:** Contours of the strain  $\varepsilon_{xx}$  in tensile direction on SENT specimen for PC/ABS (60/40), four values of the overall specimen elongation  $u$ , and a crosshead speed of  $\dot{u} = 6.0$  mm/s.

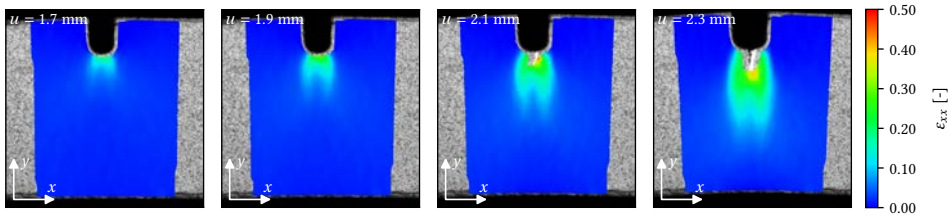


**Figure 6.21.:** Contours of the strain  $\varepsilon_{xx}$  in tensile direction on SENT specimen for PC/ABS (70/30), four values of the overall specimen elongation  $u$ , and a crosshead speed of  $\dot{u} = 6.0$  mm/s.

PC/ABS (70/30) exhibited a maximum force of  $F_{\max} = (2.51 \pm 0.10)$  kN which was an increase of  $(16.5 \pm 5.2)$  % over the peak value of PC/ABS (45/55). Since the raw data in Fig. 6.23 for PC/ABS (70/30) features a significant amount of scatter with regard to their maximum values, the increase of  $(4.33 \pm 5.76)$  % over PC/ABS (60/40) regarding the peak load was within the uncertainty of the results (Tab. A.7).

For a crosshead speed of  $\dot{u} = 0.6$  mm/s, the materials were found to feature an increasing overall elongation at complete specimen failure with an increasing PC content which was not the case for the test speed  $\dot{u} = 6.0$  mm/s (Figs. 6.22 and 6.23, Tab. A.7). For the higher test speed, the complete specimen failure of PC/ABS (70/30) featured a large amount of scatter. Regarding only the other two blends, it was found that the overall specimen elongation at failure  $u_{\text{fail}}$  was identical within the uncertainty of the results for



PC/ABS (60/40) (Tab. A.7). By contrast,  $u_{\text{fail}}$  in PC/ABS (45/55) in the case of  $\dot{u} = 6.0$  mm/s was increased by  $(17.5 \pm 4.4)$  % over  $u_{\text{fail}}$  at  $\dot{u} = 0.6$  mm/s (Tab. A.7).

The earlier onset of crack propagation in PC/ABS (45/55) at a specimen elongation of  $u = 1.5$  mm (Fig. 6.16) was also reflected in the force-displacement behaviour (Fig. 6.22). At this loading stage, the reaction force of PC/ABS (45/55) was beginning to decline whereas the peak loads of PC/ABS (60/40) and PC/ABS (70/30) had not been reached yet (Fig. 6.22).

### 6.2.3. Specific work of fracture

The increased fracture toughness of PC/ABS blends is one of their main advantages over neat thermoplastics and is highly dependent on blend composition (Sec. 3.3). Related to the fracture toughness determined in Izod or Charpy experiments, the total work  $W$  absorbed by the SENT specimens during experiments is derived as a comparable measure used in this work. The energy  $W$  absorbed by a specimen, i.e. the absolute work done on it, can be calculated by integrating the reaction force  $F$  over the traverse displacement  $u$  for the course of the loading history. Dividing  $W$  by the initial ligament cross section  $A_0$  yields the specific work of fracture  $w$  as specified by

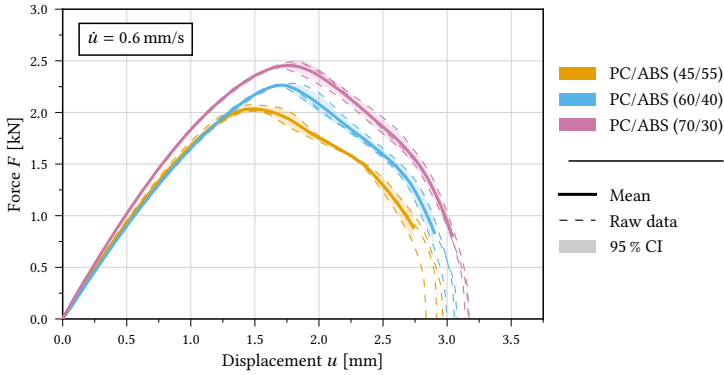
$$w = \frac{1}{A_0} \int_0^{u_{\text{fail}}} F \, du. \quad (6.2)$$

Figure 6.24 shows the results for the specific work of fracture for the SENT experiments for both crosshead speeds. The specific work of fracture was found to decrease with an increasing ABS mass fraction for both deformation velocities (Fig. 6.24). Mirroring the increase of the peak force in SENT experiments with the deformation speed, the specific work of fracture also increased (Fig. 6.24). But whereas for the lower crosshead speed of  $\dot{u} = 0.6$  mm/s the relation between  $w$  and the ABS mass fraction was found to be almost linear, a nonlinear relation was found for  $\dot{u} = 6.0$  mm/s. Therefore, in the case of a crosshead speed of  $\dot{u} = 6.0$  mm/s, PC/ABS (60/40) and PC/ABS (45/55) exhibited almost identical values of  $w$  (Fig. 6.24).

## 6.3. Discussion

### 6.3.1. Deformation behaviour - uniaxial tensile tests

Regarding the elastic range of the material response under uniaxial tension, the stiffness found for PC/ABS (70/30) was increased over the other two blends' elastic stiffnesses (Fig. 6.6 and Tab. A.1). The difference found between PC/ABS (60/40) and PC/ABS (45/55) is minor in comparison, however. In the literature, Young's modulus



**Figure 6.22.:** Force-displacement curves of SENT tests on PC/ABS (45/55), PC/ABS (60/40), and PC/ABS (70/30) at a crosshead speed of  $\dot{u} = 0.6 \text{ mm/s}$ .

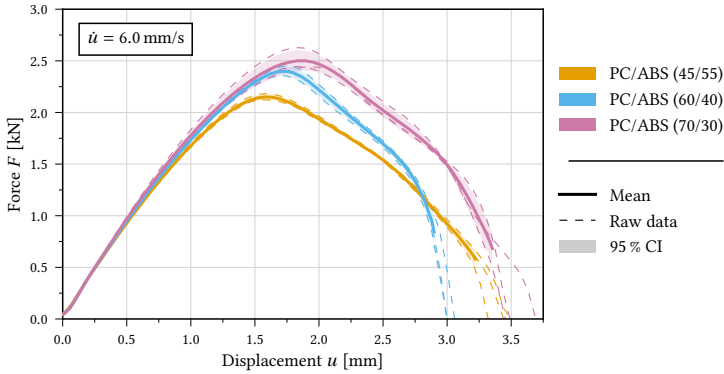


**Figure 6.23.:** Force-displacement curves of SENT tests on PC/ABS (45/55), PC/ABS (60/40), and PC/ABS (70/30) at a crosshead speed of  $\dot{u} = 6.0 \text{ mm/s}$ .

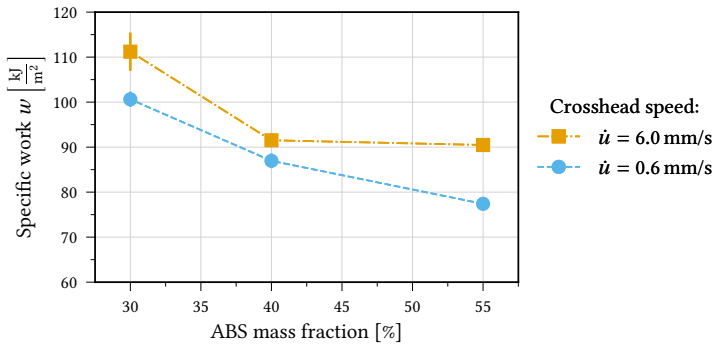


**Figure 6.24.:** Specific work of fracture  $w$  depending on composition for both crosshead speeds investigated.

of PC/ABS blends is found to be positively correlated with the PC content and the rubber content in ABS of the blends [106, 23, 103]. Yet, Tan et al. [106] found significant differences regarding the elastic modulus with an increasing PC content only for rubber mass fractions larger than 20%. Comparing two different ABS compositions and their impact on the stiffness of PC/ABS blends, Chiang and Hwung [23] found that the rubber content in ABS had a bigger impact than a variation of the PC/ABS ratio. Thus, different rubber contents might explain the similar apparent moduli found for PC/ABS (60/40) and PC/ABS (45/55). However, the salami structure of the rubber particles found in the blends investigated here prevented a precise assessment of the pure rubber volume fraction. Also, the rubber particle diameter in both blends did not differ significantly (Tab. 4.2). Therefore, vastly different tendencies regarding rubber particle cavitation decreasing the elastic stiffness are unlikely as well. However, other studies also found the elastic modulus of PC/ABS blends to not vary significantly over a large range of ABS mass fractions [48].

For the three materials and two strain rates considered, the yield stress and overall stress level of the uniaxial stress response was found to increase significantly with the PC content of the blends (Figs. 6.5 and 6.13). This finding corresponds with other experimental findings reported in the literature [106, 23, 86, 103, 48]. Consequently, PC/ABS (70/30) exhibited the highest yield stress and overall stress level for both strain rates (Figs. 6.5 and 6.13).

The three investigated PC/ABS blends also exhibited pronounced plastic dilatancy (Figs. 6.7 and 6.14). This plastic dilatancy stems from micromechanisms such as void growth and crazing in the ABS phase [17, 41, 60], and eventually interface debonding [59]. By contrast, neat PC behaves plastically incompressible (Sec. 3.1.3). Thus, the more pronounced dilation of PC/ABS (45/55) in comparison with PC/ABS (60/40) and PC/ABS (70/30) can be attributed to its higher ABS mass fraction. Consequently, the dilation found for neat ABS reported by Helbig et al. [51] is larger than that of all blends investigated in this work. The plastic dilatancy determined for PC/ABS (60/40) is comparable to that reported in other studies [54]. Due to the underlying assumption of identical in-plane and through-thickness strains, the greater dilation here has to be the result of a lower in-plane Poisson's ratio. The findings for the blends' Poisson's ratios confirm this. The blend with the highest ABS mass fraction exhibited a significantly lower Poisson's ratio than the other two blends (Figs. 6.8 and 6.15).

For both strain rates, PC/ABS (70/30) and PC/ABS (60/40) exhibited similar volume strain responses shown in Figs. 6.7 and 6.14. Regarding the mean volume strain, a slightly greater dilation for PC/ABS (70/30) in comparison to PC/ABS (60/40) was found (Figs. 6.7 and 6.14). Since ABS is the phase causing the plastic dilatancy in PC/ABS blends, this finding is somewhat surprising considering the higher ABS mass fraction of PC/ABS (60/40). Similarly, the Poisson's ratio  $\nu$  was found to be greater for PC/ABS (60/40) than for PC/ABS (70/30) (Figs. 6.8 and 6.15). However, a higher Poisson's ratio for PC/ABS (70/30) stemming from its higher PC mass fraction was expected. Dong, Greco, and Orsello [32] and Lee, Hiltner, and Baer [74] reported a change in the morphology between PC/ABS (60/40) and PC/ABS (70/30) that was also found for the blends investigated in this work (Sec. 4.3). The more pronounced orientation and rather co-continuous microstructure

might cause an anisotropy in the dilation behaviour of PC/ABS (60/40). Due to the DIC system used being restricted to in-plane measurements (Sec. 5.2), no definitive answer can be given. Therefore, as discussed in Sec. 5.2.3, the assumption of equal transverse in-plane and through-thickness strains was maintained throughout this work.

PC/ABS (60/40) and PC/ABS (70/30) exhibited a sharp increase in the slope of their hardening curves at an axial strain of approximately 0.65 for a strain rate of  $\dot{\epsilon} = 0.01 \text{ s}^{-1}$  (Fig. 6.13). Neat PC subjected to uniaxial tensile loading exhibits a similar behaviour that is referred to as locking [15] and is a result of cold drawing [5]. Cold drawing describes the development of a material orientation during necking. One consequence is the uniaxial orientation of the polymer chains and subsequent stretching of their covalent bonds [78]. Hence, the behaviour in this stage of the deformation is described as elastic [78]. This behaviour is barely observed for PC/ABS (45/55) (Fig. 6.13) as the addition of ABS is reported to harm this yielding process in PC [5]. Consequently, the presence of this distinct rehardening in PC/ABS (70/30) and PC/ABS (60/40) can be attributed to their higher PC mass fraction. The experimental data available also suggests that the cold drawing process is more stable for PC-rich blend compositions and lower deformation speeds (Figs. 6.2, 6.3, 6.4, and 6.1).

Coinciding with the change in the stress response attributed to locking, PC/ABS (60/40) and PC/ABS (70/30) exhibit a sharp decline in their volume strain response as well as an equally pronounced increase of their Poisson's ratios (Figs. 6.7, 6.14, 6.8, and 6.15). These findings further indicate a shift to a PC-dominated material behaviour and a change to microscopic deformation mechanisms that are not prevalent in the ABS-rich PC/ABS (45/55).

### 6.3.1.1. Impact of the strain rate

As is typical for thermoplastic polymers, PC/ABS blends exhibit a rate dependent behaviour with an increasing yield stress for an increasing strain rate (Figs. 6.25, 6.26, and 6.27). Increasing the strain rate by one magnitude resulted in an increase of the mean initial yield stress for PC/ABS (45/55) of about 6 % and approximately 7 % for PC/ABS (60/40), respectively (Tab. A.1 and Tab. A.5). The increase was less pronounced for PC/ABS (70/30), amounting to about 4 %.

The softening upon yield in all three materials was similarly pronounced for both strain rates (Figs. 6.25, 6.26, and 6.27). Regarding PC/ABS (45/55), the rehardening also occurred to a similar extent. However, the rehardening behaviour of PC/ABS (60/40) and PC/ABS (70/30) for a strain rate of  $\dot{\epsilon} = 0.01 \text{ s}^{-1}$  differed significantly from that found for a strain rate of  $\dot{\epsilon} = 0.01 \text{ s}^{-1}$  (Figs. 6.26 and 6.27). The rehardening in the case of the lower strain rate was more pronounced from its onset. Yet, the most remarkable difference was observed upon strains larger than  $\epsilon = 0.6$ . Despite the typical higher stress level of PC/ABS blends in the case of the higher strain rate for both PC-rich blends, the stress level for the lower strain rate of  $\dot{\epsilon} = 0.01 \text{ s}^{-1}$  exceeded that found for the higher strain rate of  $\dot{\epsilon} = 0.1 \text{ s}^{-1}$ .

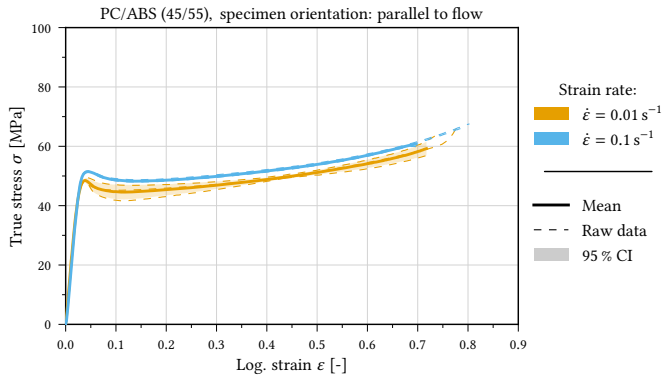


Figure 6.25.: Stress response of PC/ABS (45/55) to uniaxial tension for two values of the nominal strain rate  $\dot{\epsilon}$ .

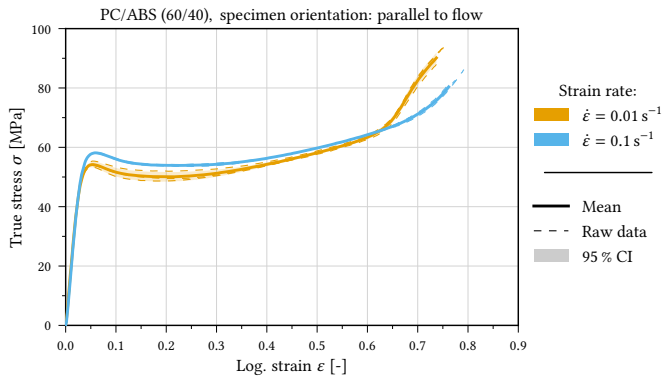


Figure 6.26.: Stress response of PC/ABS (60/40) to uniaxial tension for two values of the nominal strain rate  $\dot{\epsilon}$ .

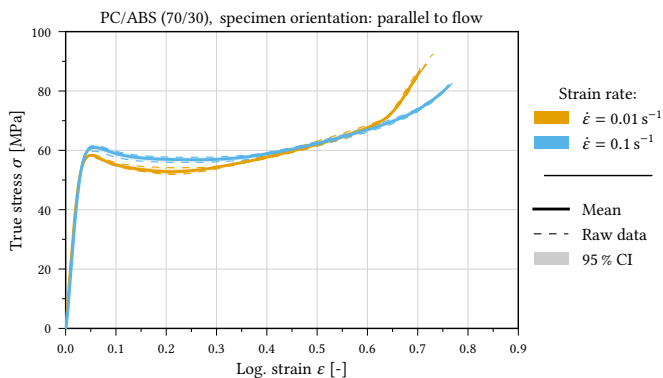
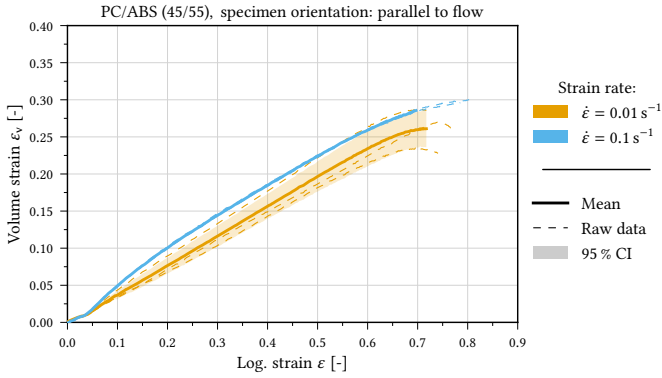
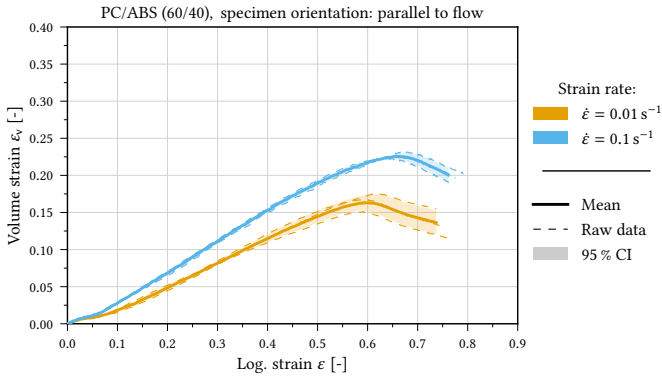


Figure 6.27.: Stress response of PC/ABS (70/30) to uniaxial tension for two values of the nominal strain rate  $\dot{\epsilon}$ .



**Figure 6.28.** Volume strain response of PC/ABS (45/55) in uniaxial tensile tests for two values of the nominal strain rate  $\dot{\epsilon}$ .



**Figure 6.29.** Volume strain response of PC/ABS (60/40) in uniaxial tensile tests for two values of the nominal strain rate  $\dot{\epsilon}$ .

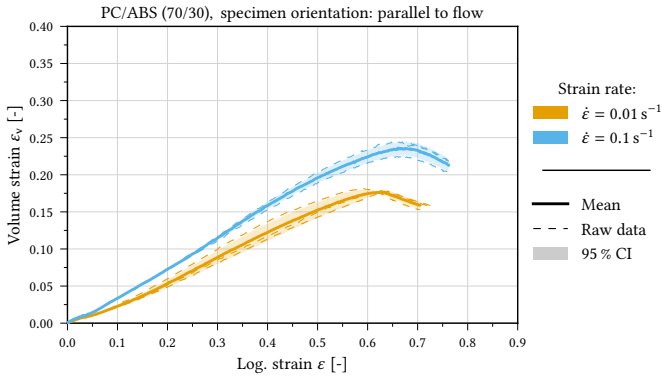


**Figure 6.30.** Volume strain response of PC/ABS (70/30) in uniaxial tensile tests for two values of the nominal strain rate  $\dot{\epsilon}$ .

This behaviour could be the result of a competition between shear yielding and distributed crazing. In ABS, lower strain rates favour the mechanism of shear yielding whereas crazing dominates for higher deformation speeds [65]. That said, the difference of only one magnitude in the different strain rates regarded here is rather small. Nonetheless, it seems as if the orientation hardening in the PC phase, of which the underlying plastic deformation mechanism is shear yielding, has a bigger impact for the lower strain rate of  $\dot{\epsilon} = 0.01 \text{ s}^{-1}$ . The lower volume strains for PC/ABS (60/40) and PC/ABS (70/30) over the whole course of the plastic deformation are another indicator that for the lower strain rate of  $\dot{\epsilon} = 0.01 \text{ s}^{-1}$  a bigger fraction of the plastic deformation can be attributed to shear yielding (Figs. 6.29 and 6.30). Obviously, the smaller cross section resulting from this behaviour contributed to the end result where the experiments carried out at a lower strain rate exhibited a higher failure stress. In the case of PC/ABS (45/55), which featured the biggest ABS mass fraction of the materials investigated, the differences regarding the volume strain were barely significant (Fig. 6.28). This observation further strengthens the argument that a higher PC content and the deformation mechanism of shear yielding are the reasons for the observed behaviour.

### 6.3.2. Failure behaviour - SENT tests

The elongated plastic zone shape ahead of the notch found in all SENT fracture experiments is typical for rubber-toughened polymers [51, 110]. Consequently, the blend featuring the highest fraction of the rubber-toughened ABS exhibited the most elongated and pointiest plastic zone shape (Fig. 6.16). With regard to the two PC-rich blend compositions, the plastic zone shape was found to be bulkier and split into two branches (Figs. 6.17 and 6.18). This indicates a through-thickness slip mechanism ahead of the notch which is also found in neat PC [79]. The smaller size of the plastic zone and delayed crack initiation in the PC-rich blends might be attributed to their higher yield strength (Figs. 6.5 and 6.13). Consequently, the peak load was found to increase with the PC content, too. The observed differences regarding the elastic response in the SENT tests at a crosshead speed of  $\dot{u} = 0.6 \text{ mm/s}$  mirror those found for the uniaxial tensile tests (Fig. 6.6 and Tab. A.1).

#### 6.3.2.1. Impact of the strain rate

Figures 6.31, 6.32, and 6.33 show the impact of the test speed on the force-displacement behaviour in SENT tests of the three blends investigated. The maximum reaction force increased by about 6 % for the higher test speed over the lower test speed in the case of PC/ABS (60/40) and PC/ABS (45/55) (Fig. 6.31, Fig. 6.32, and Tab. A.7). Considering PC/ABS (70/30), the increase of the crosshead speed by one magnitude did not have a significant impact on the peak force and its corresponding displacement (Fig. 6.33 and Tab. A.7). However, the fracture displacement was significantly increased for the higher test speed (Fig. 6.33 and Tab. A.7). A similar behaviour was found regarding PC/ABS (45/55).

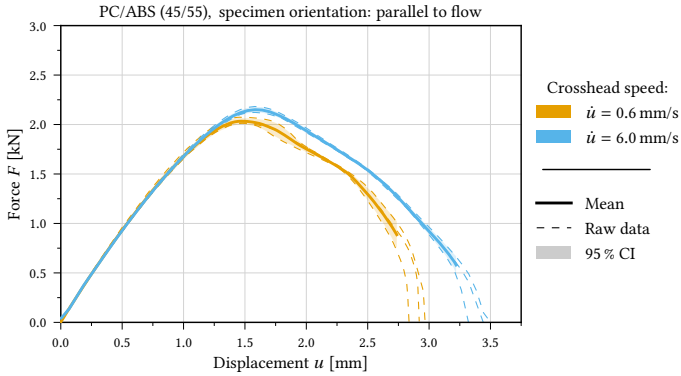


**Figure 6.31.:** Force-displacement curves of PC/ABS (45/55) from SENT fracture tests for two values of the test speed  $\dot{u}$ .

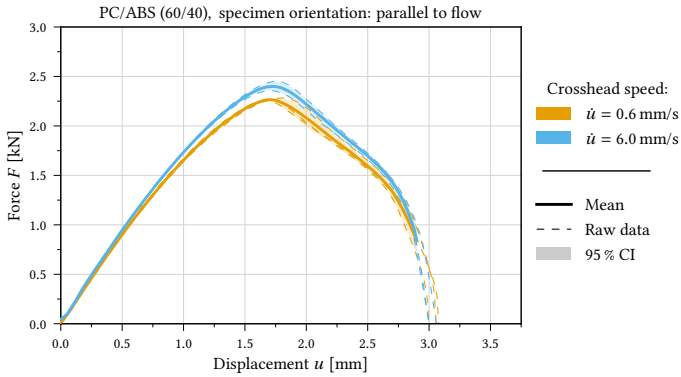


**Figure 6.32.:** Force-displacement curves of PC/ABS (60/40) from SENT fracture tests for two values of the test speed  $\dot{u}$ .

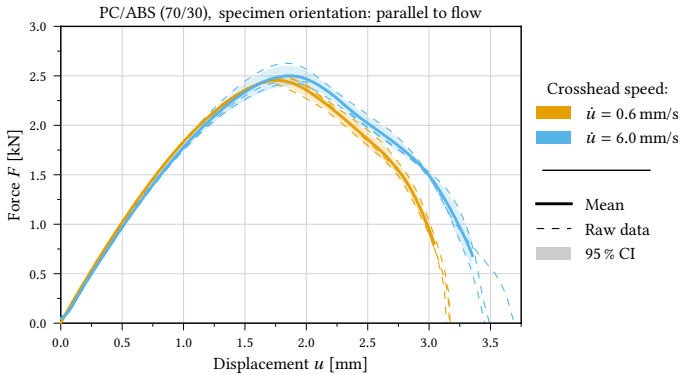


**Figure 6.33.:** Force-displacement curves of PC/ABS (70/30) from SENT fracture tests for two values of the test speed  $\dot{u}$ .



However, the total specimen elongation at failure of PC/ABS (60/40) was similar for both test speeds (Figs. 6.31, 6.32, and 6.33).

Overall, the impact of a tenfold increase in test speed on the peak force was either not pronounced or not significant. The reason could be a stronger increase of the temperature in the process zone at the higher deformation speed causing a local decrease in the yield stress and increase in failure strain. However, in a similar study involving SENT tests on PC/ABS materials, Inberg [59] also did not find a pronounced increase of the maximum measured temperature in plastic zones for the range of test speeds considered in this work.

The impact of an increased test speed on the specific work of fracture is shown in Fig. 6.24. The higher of the two crosshead speeds consistently resulted in a higher specific work of fracture for all three materials. Qualitatively, this finding is in good agreement with the results from Inberg [59].

#### 6.3.2.2. Dependency of the specific work of fracture on blend composition

The plastic zone, developing during plastic deformation and fracture, is also an indicator of the amount of energy dissipation and therefore is related to the fracture toughness of a material. Investigating the fracture toughness of PC/ABS blends, some studies found that it is highly non-monotonic in composition. Thereby, both the PC/ABS ratio and the rubber content in ABS are of great importance (Sec. 3.3). While the rubber content of the blends investigated was unknown, conclusions regarding the PC/ABS ratio can be drawn. For the three materials investigated, the specific work of fracture decreased with an increasing ABS mass fraction of the blend (Fig. 6.24). Regarding the same range of ABS mass fractions in the presence of a blunt notch, qualitatively similar behaviour regarding fracture toughness was found in other studies [76, 103, 114] (Figs. 3.10 and 3.11).

## 6.4. Conclusions

The study represents an extensive analysis of the deformation and failure behaviour of the three commercial PC/ABS blends introduced in Chapter 4. Regarding the uniaxial tensile behaviour, the typical characteristic features of PC/ABS blends regarding the stress-strain and volume strain response were found:

- A small range of elastic deformation of a few percent of overall strain.
- A distinct yield stress that increases with the deformation speed and the PC content of the blend.
- An intrinsic softening upon yield with subsequent progressive rehardening until failure.

- A pronounced plastic dilatancy with a trend to increase with the strain rate and ABS mass fraction of the blends.

As a result of the two-dimensional DIC system, the determination of the volume strain response was based on the assumption of equal transverse in-plane and through-thickness strains. In view of the somewhat anisotropic morphologies of the blends (Sec. 4.3) that could result in an anisotropic dilation behaviour, this assumption might have influenced the results. The progressive rehardening upon large strains was found to be more pronounced for the two PC-rich blends compositions and for lower strain rates. Therefore, it might be attributed to the effect of orientation hardening and a shift towards shear yielding prevailing over distributed crazing as the main mechanism of plastic deformation.

The fracture behaviour was investigated by means of SENT fracture tests. The zone of plastic deformation that develops at a notch or crack tip in the course of loading (including crack propagation) was found to vary experimentally in shape with the blend composition. Particularly in PC/ABS blends with a large amount of the plastically incompressible PC, the crack-tip plastic zone exhibited features such as splitting at the specimen surface which is reminiscent of plastically incompressible materials and likely caused by a through-thickness-slip mechanism. In contrast, in an ABS-rich blend, a single highly elongated plastic zone similar to that in neat ABS [51] was observed. As was to be expected, the peak force in SENT tests increased with an increasing PC mass fraction of the blends and so did the specific work of failure. Qualitatively, these two findings are in agreement with several studies from the literature.

## 7. The impact of the specimen orientation on the material response

---

*In this chapter, a morphology induced anisotropic material behaviour in PC/ABS specimens manufactured from injection-moulded plaques is investigated. Therefore, an experimental study comprising uniaxial tensile tests and SENT fracture tests was conducted where the specimen alignment relative to the direction of the material flow during manufacturing differed. The three materials considered are introduced in detail in Chapter 4 and an extensive study on their composition-dependent deformation and failure behaviour is presented in Chapter 6.*

---

### 7.1. Study outline

In the study presented in Chapter 6, the deformation and failure behaviour of specimens with their tensile axis aligned along the direction of melt flow is investigated. In the study presented here, specimens oriented “perpendicular to flow” were examined (Fig. 5.3). The experimental setup and methods underlying this study remained unchanged over the preceding study and are described in Chapter 5.

### 7.2. Results

The aim of this study was to investigate possible impacts on the material response of the manufacturing induced morphologies found for the three materials (Sec. 4.3). Therefore, the results of the experiments on specimens aligned transversely to the direction of melt flow during injection moulding are compared to those with a parallel orientation.

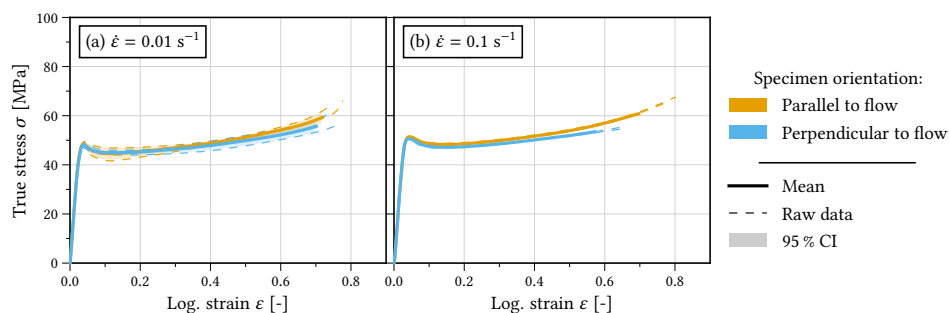


**Figure 7.1.:** True stress-strain behaviour of PC/ABS (45/55) depending on the specimen orientation at a strain rate of (a)  $\dot{\epsilon} = 0.01 \text{ s}^{-1}$  and (b)  $\dot{\epsilon} = 0.1 \text{ s}^{-1}$ .

## 7.2.1. Deformation behaviour - uniaxial tensile tests

### PC/ABS (45/55)

For the two strain rates  $\dot{\epsilon} = 0.01 \text{ s}^{-1}$  and  $\dot{\epsilon} = 0.1 \text{ s}^{-1}$  investigated here, the stress-strain response of PC/ABS (45/55) did not exhibit a pronounced dependency on the specimen orientation (Fig. 7.1). Shown in Fig. 7.1 are the stress-strain curves for both specimen orientations featuring virtually equal yield stresses for both orientations at corresponding strain rates (Tab. B.1). Considering the progressive rehardening behaviour, the specimens oriented parallel to the melt flow reached slightly higher stress levels albeit the difference regarding the lower strain rate was within the margin of error (Fig. 7.1). The failure strain was not significantly impacted by the specimen orientation for the lower strain rate of  $\dot{\epsilon} = 0.01 \text{ s}^{-1}$ . Regarding the higher strain rate of  $\dot{\epsilon} = 0.1 \text{ s}^{-1}$ , the specimens in perpendicular orientation exhibited a trend to fail around  $\epsilon = 0.6$  whilst the ones in parallel orientation exceeded  $\epsilon = 0.7$  (Fig. 7.1). As Fig. 7.2 shows, the specimen alignment relative to the melt flow was not found to impact significantly the volume strain response for the lower strain rate due to the large amount of scatter in the raw data. With respect to the higher strain rate of  $\dot{\epsilon} = 0.1 \text{ s}^{-1}$ , the specimens oriented perpendicular to flow exhibited a greater dilation. This may be an indication that a larger portion of the plastic deformation was caused by distributed crazing (Fig. 7.2). Overall, the specimen orientation had no significant impact on the results for a strain rate of  $\dot{\epsilon} = 0.01 \text{ s}^{-1}$ . Regarding the stress and volume strain response, all differences between the two specimen orientations were within the margin of error (Fig. 7.1 and Tab. B.1).

### PC/ABS (60/40)

For both strain rates investigated, the PC/ABS (60/40) blend exhibited a significantly increased yield stress for specimens featuring a parallel orientation over those with a perpendicular orientation to the melt flow during injection moulding (Fig. 7.3 and Tab. B.1).

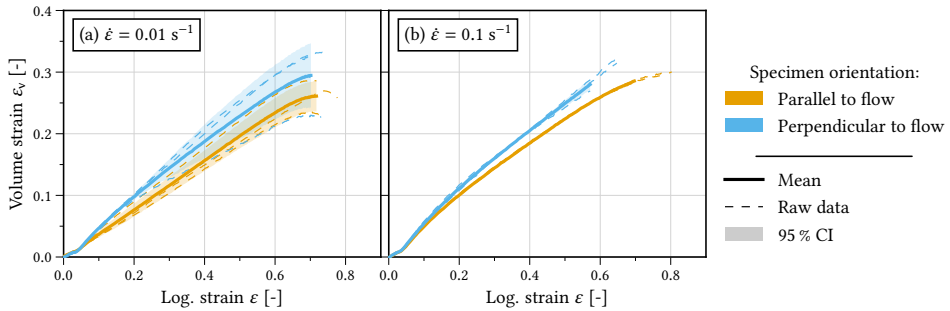


**Figure 7.2.:** Dilation behaviour of PC/ABS (45/55) depending on the specimen orientation at a strain rate of (a)  $\dot{\epsilon} = 0.01 \text{ s}^{-1}$  and (b)  $\dot{\epsilon} = 0.1 \text{ s}^{-1}$ .

Thereby, the increase was more pronounced for the higher strain rate of  $\dot{\epsilon} = 0.1 \text{ s}^{-1}$  (Fig. 7.3b). Considering the rehardening behaviour at the lower strain rate of  $\dot{\epsilon} = 0.01 \text{ s}^{-1}$ , the specimens in parallel orientation exhibited slightly increased stress levels and a more pronounced orientation hardening (Fig. 7.3a). This orientation hardening not only set in earlier but was also more pronounced and persisted over a larger range of deformation in the case of the specimens in parallel orientation. Thus, the specimens aligned along the melt flow exhibited significantly higher failure stresses compared to the specimens in perpendicular orientation at approximately similar failure strains (Fig. 7.3a). For the higher strain rate of  $\dot{\epsilon} = 0.1 \text{ s}^{-1}$ , the rehardening for the specimens in perpendicular orientation set in earlier and was more pronounced such that the stress response for both specimen orientations did not differ significantly for strains between  $\epsilon = 0.3$  to about  $\epsilon = 0.7$  (Fig. 7.3b). For larger strains, the specimens in parallel orientation exhibited a more pronounced rehardening, resulting in a slightly increased failure stress. However, the failure strains did not differ significantly (Fig. 7.3b).

With regard to the higher strain rate of  $\dot{\epsilon} = 0.1 \text{ s}^{-1}$ , the volume strain response of PC/ABS (60/40) did not differ significantly between the two specimen orientations. However, a slightly more pronounced increase in volume strain upon the onset of plastic deformation in the case of the specimens in perpendicular orientation was found (Fig. 7.4b). The increase in the volume strain for the specimens in perpendicular orientation was even more pronounced for the lower strain rate of  $\dot{\epsilon} = 0.01 \text{ s}^{-1}$ . Yet for large plastic deformations, the volume strain responses for both specimen orientations did not differ significantly. However, as illustrated in Fig. 7.4a, the mean volume strain was found to be slightly greater in the case of the specimens aligned transversely to the melt flow. Thus, for the PC/ABS (60/40) blend at both strain rates, the specimen orientation in uniaxial tensile tests had a significant impact on the yield stress and rehardening behaviour prior to failure. The final overall volume strain response exhibited no significant dependence on the specimen orientation, however (Fig. 7.4).

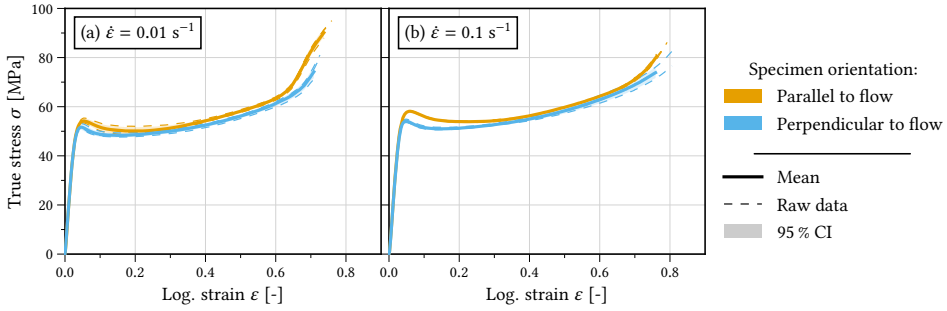


**Figure 7.3.:** True stress-strain behaviour of PC/ABS (60/40) depending on the specimen orientation at a strain rate of (a)  $\dot{\epsilon} = 0.01 \text{ s}^{-1}$  and (b)  $\dot{\epsilon} = 0.1 \text{ s}^{-1}$ .

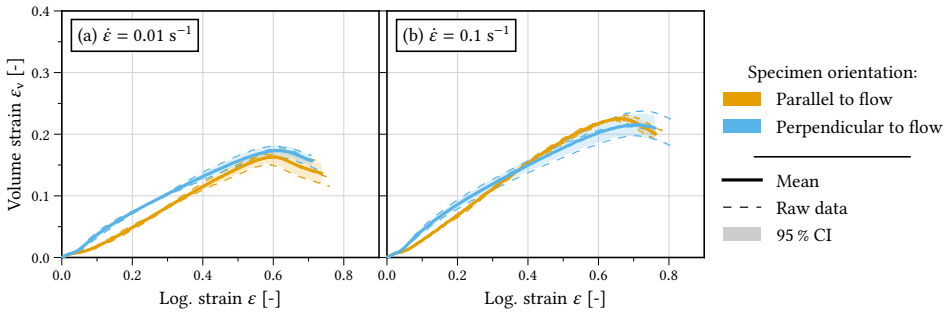


**Figure 7.4.:** Dilation behaviour of PC/ABS (60/40) depending on the specimen orientation at a strain rate of (a)  $\dot{\epsilon} = 0.01 \text{ s}^{-1}$  and (b)  $\dot{\epsilon} = 0.1 \text{ s}^{-1}$ .

### PC/ABS (70/30)

Subjected to uniaxial tension at both strain rates  $\dot{\epsilon} = 0.01 \text{ s}^{-1}$  and  $\dot{\epsilon} = 0.1 \text{ s}^{-1}$ , the PC/ABS (70/30) blend exhibited almost no dependence on the specimen orientation regarding the stress-strain and volume strain response (Figs. 7.5 and 7.6). Similar to the PC/ABS (60/40) blend, orientation hardening was found, yet it was less pronounced for PC/ABS (70/30). In PC/ABS (70/30), the orientation hardening was slightly more pronounced in the case of the lower strain rate and a specimen alignment along the melt flow direction (Fig. 7.5a). Therefore, a higher failure stress was found in this case (Fig. 7.5a).

### 7.2.2. Failure behaviour - SENT tests

#### PC/ABS (45/55)

The SENT fracture tests on PC/ABS (45/55) with the higher test speed exhibited a significant impact of the specimen alignment relative to the melt flow direction (Fig. 7.7b).

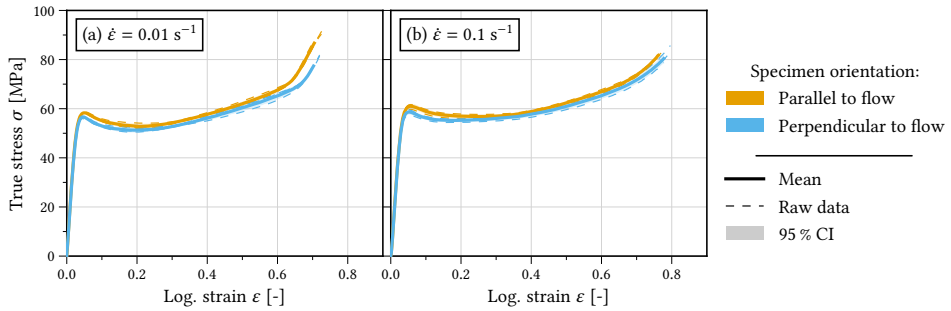


**Figure 7.5.:** True stress-strain behaviour of PC/ABS (70/30) depending on the specimen orientation at a strain rate of (a)  $\dot{\epsilon} = 0.01 \text{ s}^{-1}$  and (b)  $\dot{\epsilon} = 0.1 \text{ s}^{-1}$ .

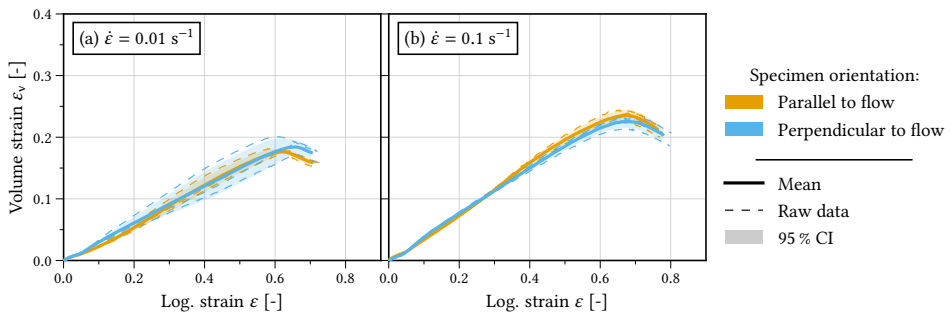


**Figure 7.6.:** Dilation behaviour of PC/ABS (70/30) depending on the specimen orientation at a strain rate of (a)  $\dot{\epsilon} = 0.01 \text{ s}^{-1}$  and (b)  $\dot{\epsilon} = 0.1 \text{ s}^{-1}$ .

An increase regarding the peak force  $F_{\max}$  and corresponding total specimen elongation  $u_{\max}$  for the specimens in parallel orientation was found (Fig. 7.7b, Tab. B.2, and Tab. B.3). Shown in Fig. 7.7a are the results for the lower crosshead speed where a slightly increased mean peak force for the specimens oriented parallel to flow over those in perpendicular orientation was found. However, the difference was within the range of uncertainty (Fig. 7.7 and Tab. A.7). With regard to the specimens aligned transversely to the melt flow direction, increasing the test speed by one magnitude increased neither the peak force nor the corresponding displacement (Fig. 7.7, Tab. B.2, and Tab. B.3). Contrarily, regarding the higher deformation speed, the specimens in parallel orientation not only exhibited an increased peak force by approximately 6 % (Tab. B.2) but also the specimen elongation at failure  $u_{\max}$  rose from less than 3.00 mm to over 3.40 mm (Tab. B.4).

Unlike for the specimens featuring an orientation parallel to the melt flow, the peak force  $F_{\max}$  did not significantly increase with the strain rate regarding the specimens with an orientation perpendicular to flow. Since the specimen orientation did not have a significant impact on the peak force for the lower test speed, a significant impact of the specimen alignment on the force-displacement response of PC/ABS (45/55) was only found in the case of the higher crosshead speed of  $\dot{u} = 6.0 \text{ mm/s}$ . Considering the specific

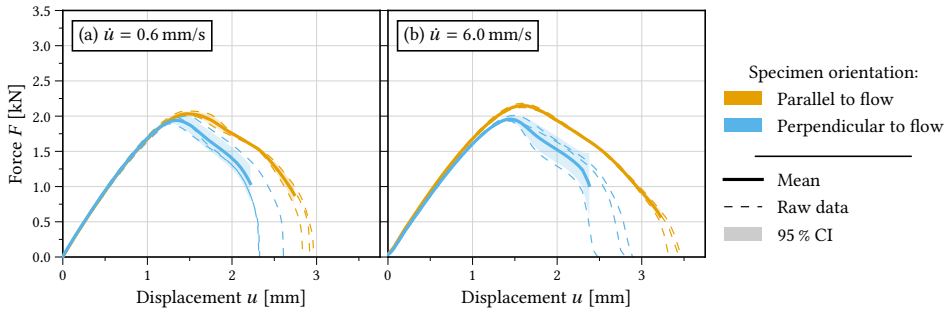


**Figure 7.7.:** Force-displacement curves from SENT tests on PC/ABS (45/55) for two specimen orientations and a test speed of (a)  $\dot{u} = 0.6$  mm/s and (b)  $\dot{u} = 6.0$  mm/s.

work of fracture, the specimen orientation parallel to the melt flow was beneficial for both deformation speeds (Fig. 7.10).

### PC/ABS (60/40)

The PC/ABS (60/40) blend exhibited a significantly increased peak force for the specimens in parallel orientation for both crosshead speeds investigated (Fig. 7.8, Tab. B.2). Considering the lower crosshead speed, the displacement  $u_{\max}$  corresponding to the peak load  $F_{\max}$  was significantly higher for the specimens in parallel orientation (Fig. 7.8a, Tab. B.3). No such impact of the specimen orientation was found regarding the higher strain rate (Fig. 7.8b, Tab. B.3). The total specimen elongation at failure was marginally smaller for the specimens in perpendicular orientation in the case of the lower crosshead speed, but was significantly higher regarding the increased deformation velocity of  $\dot{u} = 6.0$  mm/s (Fig. 7.8a, Tab. B.4).

Regarding the specific work of fracture, the specimen orientation parallel to the direction of melt flow performed better for both deformation speeds (Fig. 7.10). However, the benefit of this specimen orientation regarding the higher crosshead speed was small (Fig. 7.10).

### PC/ABS (70/30)

In the fracture tests on the PC/ABS (70/30) blend with a crosshead speed of  $\dot{u} = 0.6$  mm/s, the specimen orientation relative to the melt flow during manufacturing had no significant impact on both the peak load and the corresponding overall specimen elongation (Fig. 7.9a, Tab. B.2, and Tab. B.3). Yet regarding the displacement at failure, the specimens with their tensile axis aligned along the melt flow direction reached slightly higher values (Tab. B.4). Figure 7.9b shows the results for the higher crosshead speed of  $\dot{u} = 6.0$  mm/s where the mean peak load for the specimen orientation parallel to the melt flow is increased over the perpendicular orientation. However, owing to some scatter in the raw data, the



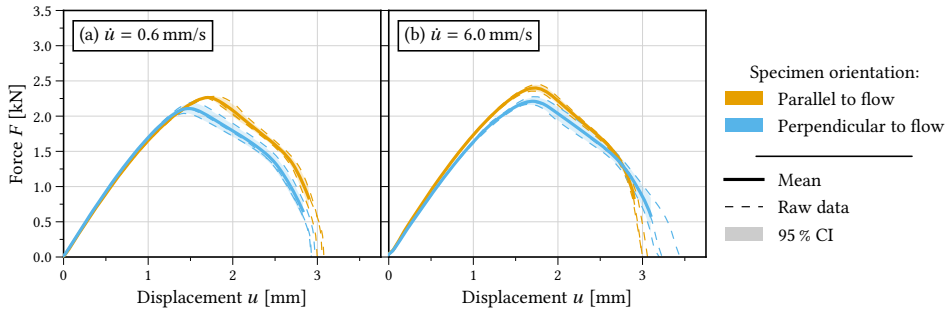


**Figure 7.8.** Force-displacement curves from SENT tests on PC/ABS (60/40) for two specimen orientations and a test speed of (a)  $\dot{u} = 0.6 \text{ mm/s}$  and (b)  $\dot{u} = 6.0 \text{ mm/s}$ .

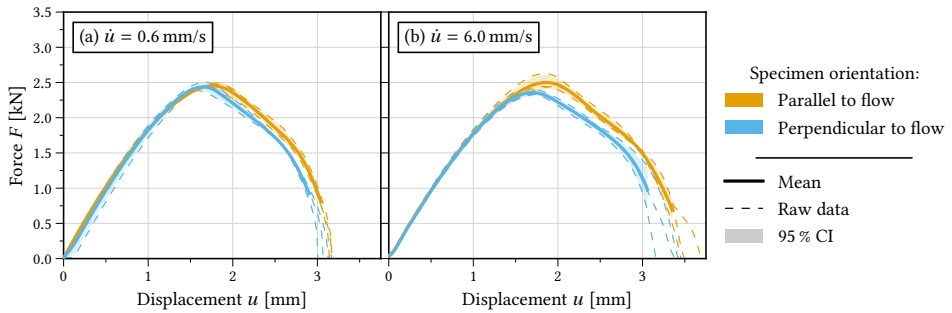


**Figure 7.9.** Force-displacement curves from SENT tests on PC/ABS (70/30) for two specimen orientations and a test speed of (a)  $\dot{u} = 0.6 \text{ mm/s}$  and (b)  $\dot{u} = 6.0 \text{ mm/s}$ .

uncertainty attached is so high that no significant impact of the specimen orientation was found (Tab. B.2). Nonetheless, the overall specimen elongation at the peak load was slightly increased for the specimens in parallel orientation (Fig. 7.9b and B.3). Regardless of the specimen orientation, the displacement at failure in the case of the higher deformation speed showed a considerable amount of scatter which was not the case for the lower crosshead speed (Figs. 7.9 and B.4). Eventually, the specimens aligned along the melt flow direction exhibited a slightly increased mean specimen elongation at the peak force for both test speeds plus an increased mean peak force with respect to the higher crosshead speed (Tabs. B.2 and B.3). Consequently, this orientation yielded a higher specific work of fracture for both deformation speeds (Fig. 7.10).

### 7.3. Discussion and conclusions

The response of the PC/ABS (45/55) blend in uniaxial tensile tests did not exhibit a remarkable dependence on the specimen orientation apart from the failure strain at the higher strain rate (Fig. 7.1, Fig. 7.2, and Tab. B.1). The impact of the specimen orientation

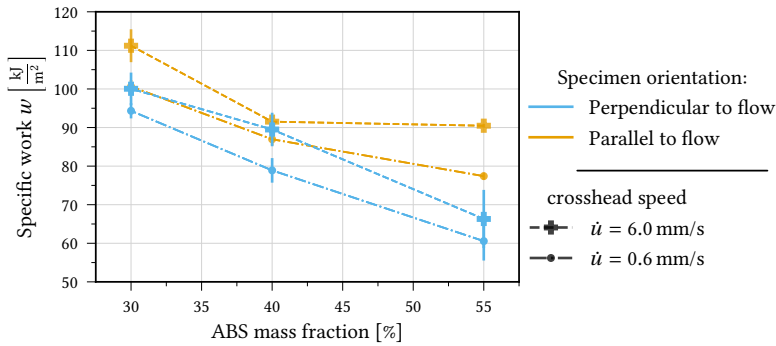


**Figure 7.10.:** Specific work of fracture  $w$  depending on the specimen orientation for all three blends and both deformation speeds investigated.

was even less pronounced regarding the PC/ABS (70/30) blend, where for both specimen orientations similar stress-strain responses were found for the strain rates investigated (Fig. 7.5, Fig. 7.6, and Tab. B.1). However, regarding the PC/ABS (60/40) blend, the yield stress and to a lesser extent the rehardening behaviour was dependent on the orientation of the specimens in the injection-moulded plates (Fig. 7.3, Fig. 7.4, and Tab. B.1). Thereby, a specimen orientation parallel to the melt flow during manufacturing was associated with a higher yield stress. A possible explanation for this behaviour could be a morphology induced promotion of shear yielding at the expense of distributed crazing in the case of the specimens featuring an orientation perpendicular to the melt flow.

As a consequence of the assumption of equal transverse in-plane and through-thickness strains, this finding directly correlates with the different Poisson's ratios that were measured for the different specimen orientations (Fig. 7.11). The higher Poisson's ratios after the onset of plastic deformation with respect to the specimens in parallel orientation caused a greater reduction of the cross section, increasing the true stress in turn. This effect is amplified by the assumption of equal Poisson's ratios in-plane and through-thickness.

However, as shown in Figure 7.12, the reaction force for PC/ABS (60/40) in the uniaxial tensile tests also featured a higher maximum and overall level upon yield in the case of the specimens in parallel orientation to the melt flow regardless of the strain rate. Therefore, the inaccuracies in the measuring method and setup, regarding the Poisson's ratio and thus volume strain, may have amplified the effect of increased stress levels with respect to the specimens in parallel orientation. Yet, they were likely not the fundamental reason of this finding. An investigation using an experimental setup capable of three-dimensional strain measurements would be highly instructive.

In the SENT fracture tests, the response of the PC/ABS (45/55) blend significantly differed for the two specimen orientations at both test speeds. Larger displacements at failure were found for the specimens in parallel orientation (Fig. 7.7 and Tab. B.2). Consequently, the specific work of fracture was also consistently higher for this specimen orientation

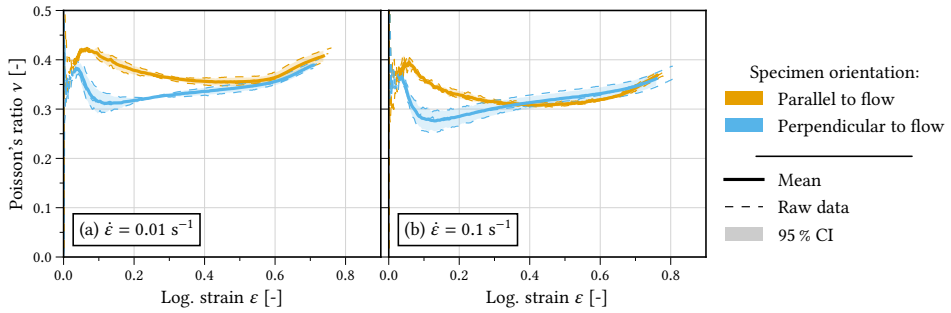


**Figure 7.11.:** Poisson's ratio  $\nu$  of PC/ABS (60/40) for the different specimen orientations at a strain rate of (a)  $\dot{\epsilon} = 0.01 \text{ s}^{-1}$  and (b)  $\dot{\epsilon} = 0.1 \text{ s}^{-1}$ .

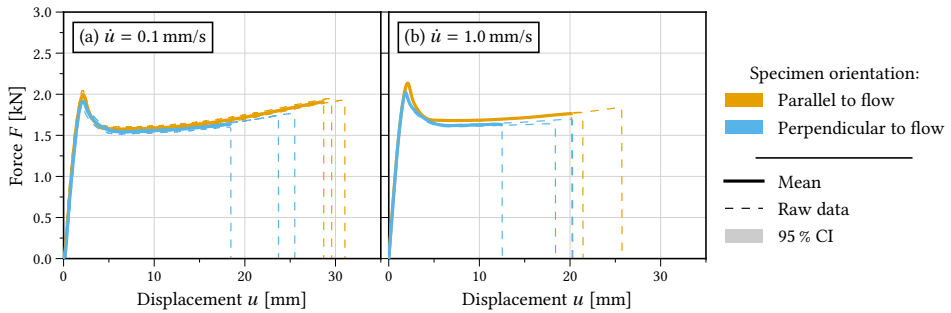


**Figure 7.12.:** Force-displacement response of PC/ABS (60/40) for the different specimen orientations at a crosshead speed of (a)  $\dot{u} = 0.1 \text{ mm/s}$  and (b)  $\dot{u} = 1.0 \text{ mm/s}$ .

(Fig. 7.7 and Tab. B.2). Considering the higher test speed, the specimens aligned along the melt flow also exhibited an increased peak force (Fig. 7.7 and Tab. B.2). Remarkably, increasing the crosshead speed by one magnitude did not significantly impact the peak force considering the SENT specimens transversely to the melt flow. However, a significant impact of the strain rate in uniaxial tensile tests for the same specimen orientation was found (Fig. 7.13).

In SENT tests on PC/ABS (60/40), a variation of the specimen alignment relative to the melt flow from parallel to perpendicular caused a decrease in the maximum force for both test speeds considered (Fig. 7.8 and Tab. B.2). Whereas the fracture displacement did not change in the case of the specimens in parallel orientation for the higher test speed of  $\dot{u} = 6.0 \text{ mm/s}$ , the total specimen elongation at break of the specimens in perpendicular orientation increased considerably (Fig. 7.8 and Tab. B.4). Therefore, the specific work of fracture was found to be virtually equal for both test speeds (Fig. 7.10). In the case of the lower test speed of  $0.6 \text{ mm/s}$ , the specimen orientation parallel to the melt flow proved beneficial. Yet the differences between the two specimen orientations with respect to the specific work of fracture regarding PC/ABS (60/40) were less pronounced than for PC/ABS (45/55) (Fig. 7.10).

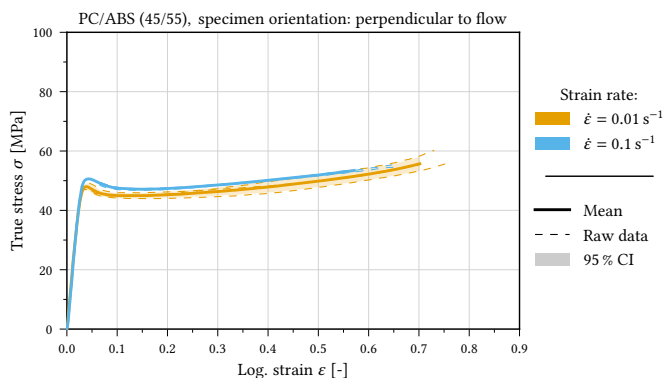


**Figure 7.13.** Uniaxial stress response of PC/ABS (45/55) with a specimen orientation perpendicular to the melt flow during manufacturing for two values of the nominal strain rate  $\dot{\epsilon}$ .

The specific work of fracture for PC/ABS (70/30) was found to decrease when the specimen alignment was altered from parallel to perpendicular relative to the melt flow for both test speeds (Fig. 7.10). Regarding the specific work of fracture for the three different blend compositions investigated, the impact of a variation in the specimen orientation increased with an increasing ABS mass fraction (Fig. 7.10). This finding is somewhat surprising considering the morphologies of the three PC/ABS blends (Sec. 4.3). Out of the three blends investigated, PC/ABS (45/55) featured a microstructure with an orientation depending on the melt flow least clearly. Hence, a less pronounced impact of the specimen alignment for this material was expected. In contrast, the PC-rich blends exhibited a microstructure clearly impacted by the melt flow. Yet regarding the specific work of fracture, the impact of the specimen orientation relative to this anisotropic microstructure was less significant (Sec. 4.3 and Fig. 7.10). A possible reason could be the large PC mass fraction in these two blends such that in the presence of notches the PC phase dominates the failure behaviour and the morphology only plays a secondary role.

## 8. Constitutive modelling

---

*This chapter introduces the constitutive models applied to rubber-toughened polymer blends and glassy amorphous thermoplastics in the numerical studies presented in Chapters 9 and 10. As previously established in Chapter 3, PC, ABS, and PC/ABS blends exhibit different characteristic features that have to be considered when designing or selecting appropriate material models. The scale of the respective modelling approach must also be considered. At first, three models for regarding PC/ABS blends in a homogenised sense are presented in Sec. 8.1, two of which model the plastic dilatancy in a purely phenomenological sense. Subsequently introduced are bespoke material models for the behaviour of the individual phases PC and ABS that are employed in the micromechanical unit cell approach presented in Chapter 10.*

---

### 8.1. Constitutive models to a phenomenological modelling approach

For practical applications involving structural FEA, efficient macroscopic models are needed which quantitatively capture the material behaviour under complex loading states up to failure. In the context of the homogenised approach presented in Chapter 9, the key features of the material response of PC/ABS blends that these models should take into account are:

- the small elastic range,
- the strain rate dependent yield stress (viscoplasticity),
- the intrinsic softening upon yield,
- the large-strain progressive rehardening, and
- the plastic dilatancy.

### 8.1.1. Viscoplastic framework

To appropriately address the prerequisites stated above, the constitutive models used in Chapter 9 all share a common framework that is introduced below. These common features are:

- an elastic-plastic split of the deformation based on the product decomposition of the deformation gradient [68, 73] given by

$$\mathbf{F} = \mathbf{F}^e \cdot \mathbf{F}^p, \quad (8.1)$$

- small-strain linear hypoelasticity,
- large-strain viscoplasticity with an associated flow rule, and
- plastic dilatancy through a yield surface dependent on the hydrostatic stress  $\sigma_m$ .

Formulating the constitutive equations in rate form is convenient regarding the subsequent numerical implementation in form of user material subroutines for Abaqus/Explicit. As a result of the product decomposition of the deformation gradient, the total rate of deformation tensor is additively split into its elastic and viscoplastic part as

$$\mathbf{D} = \mathbf{D}^e + \mathbf{D}^p. \quad (8.2)$$

The elastic part  $\mathbf{D}^e$  enters the hypoelastic relation

$$\overset{\nabla}{\boldsymbol{\sigma}} = \mathbb{C} : (\mathbf{D} - \mathbf{D}^p), \quad (8.3)$$

where  $\overset{\nabla}{\boldsymbol{\sigma}}$  denotes the frame-invariant Jaumann-Zaremba rate of the Cauchy stress tensor (Eq. (2.63)) and  $\mathbb{C}$  is the isotropic fourth-order elasticity tensor given by

$$\mathbb{C} = \frac{E}{1+\nu} \left( \mathbb{I} + \frac{\nu}{1+2\nu} \mathbf{1} \otimes \mathbf{1} \right) \quad (8.4)$$

with Young's modulus  $E$ , Poisson's ratio  $\nu$ , as well as the fourth- and second-order identity tensors  $\mathbb{I}$  and  $\mathbf{1}$ , respectively.

Assuming associated plasticity, the inelastic part of the rate of deformation tensor  $\mathbf{D}^p$  is governed by the normality flow rule

$$\mathbf{D}^p = \dot{\varepsilon}^p \mathbf{N} \quad \text{with} \quad \mathbf{N} = \frac{\partial \Phi / \partial \boldsymbol{\sigma}}{\sqrt{\frac{\partial \Phi}{\partial \boldsymbol{\sigma}} : \frac{\partial \Phi}{\partial \boldsymbol{\sigma}}}}. \quad (8.5)$$

The isotropic yield function in this case is of the general structure

$$\Phi(\boldsymbol{\sigma}, \varepsilon^p) \equiv \tilde{\Phi}(\sigma_e, \sigma_m) - k(\varepsilon^p). \quad (8.6)$$

The yield function is taken to depend on both the equivalent von Mises stress

$$\sigma_e = \sqrt{\frac{3}{2} \boldsymbol{\sigma}' : \boldsymbol{\sigma}'}, \quad (8.7)$$

where  $\boldsymbol{\sigma}'$  denotes the deviatoric part of the stress tensor, and the hydrostatic stress

$$\sigma_m = \frac{1}{3} \boldsymbol{\sigma} : \mathbf{1}. \quad (8.8)$$

Through the dependence of the yield function on the hydrostatic stress in conjunction with the associated flow rule (Eq. (8.5)), the model is capable of reproducing plastic dilatancy to appropriately represent the volume strain behaviour of rubber-toughened polymers (Sec. 3.2.2) and PC/ABS blends in particular (Sec. 6.1.1).

The kinematic hardening of thermoplastic polymers due to molecular alignment [27, 110, 15] is neglected here in view of the essentially monotonic loading situations considered. It should be mentioned that a more sophisticated model for rubber-toughened (porous) glassy polymers (e.g. accounting for kinematic hardening) has been developed in Danielsson, Parks, and Boyce [27]. In this work, the hardening as well as the intrinsic softening (e.g. Fig. 6.5) is modelled in an isotropic fashion through the evolution of the “yield strength”  $k(\varepsilon^p)$  with the accumulated plastic strain

$$\varepsilon^p = \int_{t_0}^t \sqrt{\mathbf{D}^p : \mathbf{D}^p} \, d\tilde{t}. \quad (8.9)$$

This dependence is approximated by the relation

$$k(\varepsilon^p) = \sigma_{\min} + (\sigma_0 - \sigma_{\min}) \exp(-h\varepsilon^p) + h_{\text{hard}} (\varepsilon^p)^q \quad (8.10)$$

with the initial yield stress  $\sigma_0$  and the minimum yield stress  $\sigma_{\min}$  after softening. The parameter  $h$  describes the softening,  $h_{\text{hard}}$  and  $q$  control the progressive rehardening. Therefore, the function specified by Eq. (8.10) enables exponential softening at small plastic strains and subsequent power-law rehardening.

To take into account the rate dependence of the materials, the evolution of the accumulated plastic strain  $\dot{\varepsilon}^p$  is described by an Eyring-type relation

$$\dot{\varepsilon}^p = \dot{\varepsilon}_0 \exp(A\Phi), \quad (8.11)$$

where the pre-exponential factor  $\dot{\varepsilon}_0$  can be interpreted as a reference strain rate that the model is calibrated from. The material parameter  $A$  incorporates the viscous properties and might be taken to depend on temperature. However, Laschütza [71] concluded that an adequately calibrated isothermal approach is also capable of reproducing the material response. Thus, the parameter  $A$  is taken as a constant throughout this work.

### 8.1.2. Three yield surfaces to model plastic dilatancy

Within this isotropic approach, a dependence of the yield function on the hydrostatic stress  $\sigma_m$  in conjunction with the assumed associated flow rule gives rise to isotropic plastic dilatancy. Yield functions to appropriately describe the behaviour of rubber-toughened polymers hence have to consider the hydrostatic stress. Three well established isotropic yield functions fulfilling this prerequisite are considered:

- Drucker-Prager [29]

$$\Phi_{\text{DP}} \equiv \sigma_e + \alpha_{\text{DP}} \sigma_m - k_{\text{DP}}(\varepsilon^{\text{P}}), \quad (8.12)$$

- Raghava [89, 88]

$$\Phi_{\text{R}} \equiv \sqrt{\sigma_e^2 + \alpha_{\text{R}} \sigma_m} - k_{\text{R}}(\varepsilon^{\text{P}}), \quad (8.13)$$

- Green (Gurson-like) [44, 47]

$$\Phi_{\text{G}} \equiv \frac{1}{1-f} \sqrt{\sigma_e^2 + \alpha_{\text{G}} f \sigma_m^2} - k_{\text{G}}(\varepsilon^{\text{P}}). \quad (8.14)$$

The material parameter  $\alpha$  individually controls the dependence of the yield functions on hydrostatic stress. It is assumed to be constant over the whole range of deformation for all models. The interrelation between the von Mises and the hydrostatic stress is linear in the case of the Drucker-Prager (DP) model while it is parabolic regarding the Raghava (R) model. Following Green [44] or slightly simplifying the well-known Gurson model [47], a quadratic dependence on both  $\sigma_e$  and  $\sigma_m$  is considered in the third yield function. In addition, the latter explicitly considers the porosity  $f$ . According to the conservation of mass, the porosity evolves as  $\dot{f} = (1-f) \text{tr}(\mathbf{D}^{\text{P}})$ . Hence, the Drucker-Prager and the Raghava model differ only by the fixed shape of the yield surface, the size of which varies with  $k(\varepsilon^{\text{P}})$ , thus modelling the plastic dilatancy in a purely phenomenological manner. Regarding the Green/Gurson model, the shape and the size of the yield surface change with the evolving microstructural parameter that is the porosity.

## 8.2. Constitutive models for PC

With regard to the unit cell modelling approach to PC/ABS blends presented in Chapter 10, constitutive models to describe the characteristic features of the behaviour of the glassy amorphous thermoplastic PC are required. As presented in detail in Sec. 3.1.2, the material response of PC is ductile if brittle fracture due to crazing can be suppressed. In this case, after overcoming a strain-rate-dependent yield stress, the material exhibits an intrinsic



softening and subsequent kinematic orientation hardening (Fig. 3.3). Since the plastic deformation mechanism in neat PC is shear yielding, in contrast to rubber-toughened polymer blends, the plastic deformation of PC is isochoric. As a consequence, the two models considered solely rely on the deviatoric portion of the stress tensor for the evolution of the plastic deformation. Therefore, the plastic model response is volume-preserving.

### 8.2.1. $J_2$ -plasticity model

The well-known von Mises yield criterion [80] states that the yielding of a material is governed by the second invariant of the deviatoric part of the stress tensor. Recalling Eq. (2.41) and taking into account Eq. (8.7) yields

$$J_2 = \frac{1}{2} \boldsymbol{\sigma}' : \boldsymbol{\sigma}' = \frac{\sigma_e}{\sqrt{3}}. \quad (8.15)$$

Since the Raghava yield criterion is just a variant of the von Mises yield criterion extended to include a dependence of yielding on the hydrostatic portion of the applied stress, the  $J_2$ -plasticity model with all governing equations can easily be obtained by assuming  $\alpha_R = 0$  in Eq. (8.13). Hence, the von Mises or  $J_2$ -yield criterion is given by

$$\Phi_{J_2} \equiv \sigma_e - k(\varepsilon^P). \quad (8.16)$$

In the context of an associated flow rule, the direction of viscoplastic flow reads

$$\mathbf{N} = \frac{\boldsymbol{\sigma}'}{\|\boldsymbol{\sigma}'\|} \quad (8.17)$$

such that the plastic part of the rate of deformation  $\mathbf{D}^P$  is purely deviatoric. By assuming that  $k(\varepsilon^P)$  is specified by Eq. (8.10), the model does not account for kinematic hardening. However, the usage of the model in this work is motivated by the fact that it is well understood and widespread rather than being particularly accurate. Furthermore, the model in a viscoplastic formulation is readily available in the commercial software package Abaqus/Explicit. Also, the model's simple nature allows for calibration of all parameters from uniaxial tensile tests.

### 8.2.2. Boyce model

A model that features kinematic hardening is the widespread constitutive model for glassy amorphous thermoplastics introduced by Boyce, Parks, and Argon [16]. It is based on considerations of the microstructure of thermoplastics consisting of a network of physically entangled macromolecular chains (Sec. 3.1.1). The different physical processes governing the deformation behaviour of these materials resulting from their microstructure can be identified in a rheological sense by a linear elastic spring connected in series with a parallel arrangement of a viscoplastic dashpot and a nonlinear rubber elasticity spring. The linear

elastic spring represents the initial elastic material response. The other two elements represent contributions of two separate mechanisms that a glassy polymer is assumed to need to overcome in order to exhibit large-strain inelastic deformation. The resistance to chain segment rotation in between the macromolecules' entanglements is represented through the viscoplastic dashpot that renders a temperature- and rate-dependent yield stress. Characterised by the nonlinear rubber elasticity spring is the anisotropic resistance to chain alignment that is also referred to as orientation hardening (Sec. 3.1.3).

In the context of this work, the model is employed in isothermal analyses only such that the elastic part of the rate of deformation can be related to the Cauchy stress tensor using Eq. (8.3), the Jaumann-Zaremba stress rate. The plastic part of the rate of deformation  $\mathbf{D}^p$  with its direction  $\mathbf{N}$  is constitutively given by

$$\mathbf{D}^p = \dot{\gamma}^p \mathbf{N}, \quad (8.18)$$

where  $\dot{\gamma}^p$  denotes the plastic shear strain rate. Following an ansatz of Argon [2], the plastic shear strain rate  $\dot{\gamma}^p$  takes into account the isotropic resistance to chain segment rotation as in

$$\dot{\gamma}^p = \dot{\gamma}_0 \exp \left[ -\frac{As}{T} \left( 1 - \frac{\tau}{s} \right)^{5/6} \right]. \quad (8.19)$$

The pre-exponential factor  $\dot{\gamma}_0$  and  $A$  are material parameters,  $T$  is the absolute temperature, and  $\tau$  denotes the applied shear stress. Denoted by  $s$  is the shear resistance to plastic flow and it is assumed to evolve with the accumulated plastic shear strain

$$\gamma^p = \int_{t_0}^t \sqrt{\mathbf{D}^p : \mathbf{D}^p} \, d\tilde{t} \quad (8.20)$$

from an initial value  $s_0$  to a saturation value  $s_s$  as given by

$$s = s_s + (s_0 - s_s) \exp \left( -h \frac{\gamma^p}{s_s} \right) + \alpha \sigma_m, \quad (8.21)$$

where  $h$  denotes the softening slope and  $\alpha$  is the pressure dependence coefficient. The entirely deviatoric direction of the viscoplastic flow  $\mathbf{N}$ , introduced in Eq. (8.18), is taken to be specified by

$$\mathbf{N} = \frac{\bar{\boldsymbol{\sigma}}'}{\sqrt{2}\tau}, \quad (8.22)$$

where  $\bar{\boldsymbol{\sigma}}'$  is the deviatoric part of the driving stress tensor  $\bar{\boldsymbol{\sigma}}$  and  $\tau$  denotes the equivalent shear stress

$$\tau = \sqrt{\frac{1}{2} \bar{\boldsymbol{\sigma}}' : \bar{\boldsymbol{\sigma}}'} \quad (8.23)$$

that is indeed the applied shear stress in Eq. (8.19). The driving stress  $\bar{\boldsymbol{\sigma}}$  of the plastic deformation is taken to be specified by

$$\bar{\boldsymbol{\sigma}} = \boldsymbol{\sigma} - \frac{1}{\det(\mathbf{F}^e)} \mathbf{F}^e \cdot \mathbf{b} \cdot \mathbf{F}^{eT}, \quad (8.24)$$

where the back stress tensor  $\mathbf{b}$  captures the effect of orientation hardening due to molecular alignment and is therefore also referred to as the convected network stress. The deviatoric convected network stress  $\mathbf{b}$  is modelled using the eight-chain model by Arruda and Boyce [4] and is given by

$$\mathbf{b} = C_R \frac{\sqrt{N}}{\lambda_{\text{chain}}} \mathcal{L}^{-1} \left( \frac{\lambda_{\text{chain}}}{\sqrt{N}} \right) [\mathbf{B}^p - \lambda_{\text{chain}}^2 \mathbf{1}] , \quad (8.25)$$

where  $\mathbf{B}^p = \mathbf{F}^p \cdot \mathbf{F}^{pT}$  denotes the plastic left Cauchy-Green deformation tensor,  $\lambda_{\text{chain}}$  is the stretch of each chain in the network, and  $\mathcal{L}$  is the Langevin function defined by  $\mathcal{L}(\beta) = \coth(\beta) - \beta^{-1}$ . The chain stretch is specified by

$$\lambda_{\text{chain}} = \sqrt{\frac{\text{tr}(\mathbf{B}^p)}{3}} . \quad (8.26)$$

The material parameters describing the orientation hardening are the rubber modulus  $C_R$  and the number of chain segments between entanglements  $N$ . This formulation yields a back stress  $\mathbf{b}$  that increases drastically if the chain stretch  $\lambda_{\text{chain}}$  approaches the limit stretch  $\sqrt{N}$ . Therefore, the model reproduces the progressive orientation rehardening as well as the locking of the macromolecular network for large strains.

### 8.3. Continuum micromechanical modelling of ABS

Being a rubber-toughened polymer, ABS is a polymer blend itself and thus not homogeneous (Sec. 3.2). The constitutive models used for modelling ABS in this work all regard the material as homogeneous. Yet, these models feature an inherent dependence on the rubber content due to a continuum micromechanical modelling approach that is introduced below.

Continuum micromechanical modelling approaches use homogenisation methods to model heterogeneous materials in order to treat them as a homogeneous material. The goal of homogenisation schemes is to quantify the impact of heterogeneities on the global material behaviour in the elastic and plastic range based on assumptions made for the distribution, size, and behaviour of the heterogeneities. The heterogeneities with regard to ABS are the rubber particles that are assumed to be of spherical shape, identical size, and uniform distribution. In experimental investigations, the rubber particles in ABS were found to be prone to cavitation upon low hydrostatic stresses effectively giving rise to voids (Sec. 3.2.2). Therefore, the rubber particles in the approach presented here are assumed to form voids after cavitating upon a low hydrostatic stress  $\sigma_{m,\text{cav}}$  within the elastic range of the material response. The constitutive models introduced in this section also make use of the product decomposition of the deformation gradient (Eq. (8.1)) to separate the elastic and plastic portions of the overall deformation.

### 8.3.1. Overall elastic material response

The Mori-Tanaka model is employed to approximate the impact of rubber particle cavitation on the overall elastic response. This elastic response of the homogenised ABS phase is specified in rate formulation by the Jaumann-Zaremba rate of the Cauchy stress tensor  $\overset{\nabla}{\boldsymbol{\sigma}}$  (Eq. (2.63)), governed in this case by the fourth-order effective elasticity tensor  $\mathbb{C}^*$  as specified by

$$\overset{\nabla}{\boldsymbol{\sigma}} = \mathbb{C}^* : (\mathbf{D} - \mathbf{D}^p). \quad (8.27)$$

#### Mori-Tanaka homogenisation model

The Mori-Tanaka approach is a mean-field homogenisation scheme to approximate the overall isotropic elastic stiffness  $\mathbb{C}^*$  of two phased materials [81]. The heterogeneous ABS material is assumed to consist of two isotropic phases: a linear elastic matrix, with bulk and shear moduli  $K_M$  as well as  $G_M$ , and dispersed rubber particles, with bulk and shear moduli  $K_R$  and  $G_R$ , respectively. According to the Mori-Tanaka approach [81], the effective bulk modulus  $K_{MT}^*$  and the effective shear modulus  $G_{MT}^*$  are then specified by

$$K_{MT}^* = K_M \left( 1 + f_R \frac{K_R - K_M}{K_M + \alpha_{MT} (1 - f_R) (K_R - K_M)} \right), \quad (8.28)$$

$$G_{MT}^* = G_M \left( 1 + f_R \frac{G_R - G_M}{G_M + \beta_{MT} (1 - f_R) (G_R - G_M)} \right), \quad (8.29)$$

where  $f_R$  denotes the rubber volume fraction and  $\alpha_{MT}$  as well as  $\beta_{MT}$  are parameters from the Eshelby tensor [45] given by

$$\alpha_{MT} = \frac{3K_M}{3K_M + 4G_M} \quad \text{and} \quad \beta_{MT} = \frac{6(K_M + 2G_M)}{5(3K_M + 4G_M)}.$$

Prior to cavitation, the rubber particles are assumed to have the same bulk modulus as the surrounding matrix ( $K_R = K_M$ ) and no shear resistance ( $G_R = 0$ ). Once cavitated, the rubber particles are treated as voids with  $K_R = 0$ .

### 8.3.2. Microstructural considerations and scaling relations

The approach to take into account the impact of spherical voids on the overall plastic response of the material presented below has initially been introduced by Helbig et al. [51].

The rubber particles in the blend are assumed to have cavitated in the elastic range, such that the initial assumption is a voided material. Since it is assumed that all rubber particles

cavitate, the void volume fraction is equal to the rubber volume fraction  $f_R$ . The fraction of the macroscopic material volume that then can bear load depends on the radius  $r$  of the spherical voids and the rubber or void volume fraction  $f_R$ . Under the assumption of a uniform distribution, these two microstructural parameters determine the initial spacing of the voids

$$b_0 = r \left( \frac{4\pi}{3f_R} \right)^{1/3}. \quad (8.30)$$

Figure 8.1 illustrates in blue the remaining cross section in one unit cell of the material after rubber particle cavitation considering these microstructural parameters. This remaining area fraction of size

$$\frac{b_0^2 - \pi r^2}{b_0^2} \quad (8.31)$$

is assumed to scale both the normal stress  $\bar{\sigma}_n$  as well as the shear stress  $\bar{\sigma}_\tau$ , both acting on the remaining matrix cross section, as given by

$$\bar{\sigma}_n = \frac{\sigma_n}{1 - \pi(r/b_0)^2}, \quad (8.32)$$

$$\bar{\sigma}_\tau = \frac{\sigma_\tau}{1 - \pi(r/b_0)^2}, \quad (8.33)$$

where  $\sigma_n$  and  $\sigma_\tau$  denote the macroscopic stresses in normal and tangential directions relative to the equatorial plane of the unit cell (Fig. 8.1) as given by

$$\sigma_n = \mathbf{n} \cdot \boldsymbol{\sigma} \cdot \mathbf{n}, \quad (8.34)$$

$$\sigma_\tau = |\boldsymbol{\sigma} \cdot \mathbf{n} - \sigma_n \mathbf{n}|, \quad (8.35)$$

where  $\mathbf{n}$  denotes the direction normal to the craze plane.

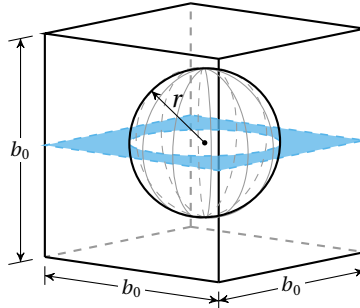


Figure 8.1.: Cubic unit cell of the microstructure with void of radius  $r$  and equatorial plane.

### 8.3.3. Distributed crazing model

The continuum micromechanical model for distributed crazing was introduced by Helbig et al. [51] and is a bespoke material model for rubber-toughened polymer blends. It

attributes all plastic deformation to the mechanism of distributed crazing and neglects a possible coexistence of shear yielding and crazing. Hence, it is referred to as the DC model hereafter. This model uses the continuum micromechanical approach to take into account the impact of the rubber volume fraction presented in Secs. 8.3.1 and 8.3.2, since both were introduced by Helbig et al. [51]. Thus, it is assumed that the rubber particles, present in the initial configuration at time  $t_0$  (Fig. 8.2), cavitate upon a low hydrostatic stress and then form voids that serve as craze initiation sites. The uniform distribution and thus equal spacing of these voids yields an initial spacing  $b_0$  of the crazes in the moment  $t^*$  they are initiated in (Fig. 8.2). Thereby, the craze orientation is determined by the direction  $\mathbf{n}$  of the maximum principal stress exceeding the initial craze resistance  $\sigma_0$ . After craze initiation, the craze widens which is described via the current spacing  $b$  of two neighbouring craze planes (Fig. 8.2). The inelastic part of the rate of deformation  $\mathbf{D}^c$  is introduced following an ansatz of Gearing and Anand [39]. Therein, the effect of distributed crazing is represented in a homogenised sense as specified by

$$\mathbf{D}^c = \frac{1}{b} (\dot{\delta}_n \mathbf{n} \otimes \mathbf{n} + \dot{\delta}_\tau \text{sym}(\boldsymbol{\tau} \otimes \mathbf{n})) , \quad (8.36)$$

where  $\dot{\boldsymbol{\delta}}$  denotes the widening rate vector with its components in the normal direction  $\dot{\delta}_n$  and tangential direction  $\dot{\delta}_\tau$ . The second addend in Eq. (8.36) considers shearing of the representative volume element (RVE) after craze initiation, where  $\boldsymbol{\tau}$  denotes the unit vector tangential to the craze plane given by

$$\boldsymbol{\tau} = \frac{\boldsymbol{\sigma} \cdot \mathbf{n} - \sigma_n \mathbf{n}}{\sigma_\tau} . \quad (8.37)$$

The evolution of the normal and tangential craze widening rates is specified by two Eyring-type relations

$$\dot{\delta}_n = \dot{\delta}_{n0} \exp\left(\frac{A}{T} [\bar{\sigma}_n - \sigma_{n,\text{crit}}(\delta_n)]\right) \quad \text{and} \quad \dot{\delta}_\tau = \dot{\delta}_{\tau0} \exp\left(\frac{A}{T} [\bar{\sigma}_\tau - \sigma_{\tau,\text{crit}}(\delta_n)]\right) , \quad (8.38)$$

where the pre-exponential factors  $\dot{\delta}_{n0}$  and  $\dot{\delta}_{\tau0}$  as well as  $A$  are material parameters and  $T$  is the absolute temperature. The driving stresses of the plastic deformation  $\bar{\sigma}_n$  and  $\bar{\sigma}_\tau$  are the effective stresses acting on remaining matrix cross section of the unit cell that is just the craze plane (Fig. 8.1). The craze resistances corresponding to the effective stresses  $\sigma_{n,\text{crit}}$  and  $\sigma_{\tau,\text{crit}}$  are given by

$$\sigma_{n,\text{crit}}(\delta_n) = \sigma_{\min} + (\sigma_0 - \sigma_{\min}) \exp\left(-h_n \frac{\delta_n}{\delta_{\text{crit}}}\right) + (\sigma_{\text{fail}} - \sigma_{\min}) \left(\frac{\delta_n}{\delta_{\text{crit}}}\right)^q , \quad (8.39)$$

$$\sigma_{\tau,\text{crit}}(\delta_n) = \sigma_{\min} \exp\left(-h_\tau \frac{\delta_n}{\delta_{\text{crit}}}\right) , \quad (8.40)$$

where  $\sigma_{\min}$ ,  $\sigma_0$ ,  $\sigma_{\text{fail}}$ ,  $q$ ,  $h_n$ , and  $h_\tau$  are all material parameters to be calibrated from experimental data. Failure is assumed to take place when the craze opening

$$\delta = \sqrt{\delta_n^2 + \delta_\tau^2} \quad (8.41)$$

reaches the critical value  $\delta_{\text{crit}}$ .

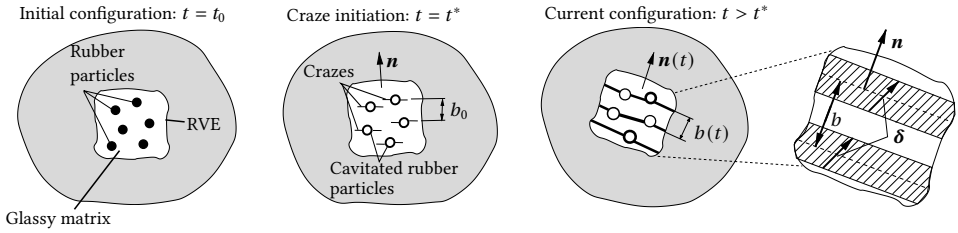


**Figure 8.2.:** Schematic illustration of the deformation stages a representative volume element (RVE) undergoes during crazing (adapted from Helbig et al. [51]).

### 8.3.4. Continuum micromechanical Raghava model

This model is the Raghava model presented in Sec. 8.1, wrapped by the continuum micromechanical approach previously introduced in Secs. 8.3.1 and 8.3.2, to take into account different rubber contents. Hence, the stiffness of the initial elastic response is based on the Mori-Tanaka approach. The driving stress tensor  $\bar{\sigma}$  that enters the Raghava yield surface is assumed to depend on the Cauchy stress tensor  $\sigma$  as given by

$$\bar{\sigma} = \frac{1}{\left(1 - \pi \left(\frac{3}{4\pi} f_R\right)^{2/3}\right)} \sigma. \quad (8.42)$$

Since the failure behaviour is experimentally observed to be dependent on the rubber volume fraction  $f_R$ , the equivalent failure strain  $\varepsilon_{\text{fail}}$  is assumed to feature a dependence on  $f_R$  as specified by

$$\varepsilon_{\text{fail}} = \ln \left( 1 + \beta \left( \frac{3}{4\pi} f_R \right)^{1/3} \right), \quad (8.43)$$

where  $\beta$  denotes a fit parameter to be calibrated for a material of which  $f_R$  is known. Failure then is assumed to take place if  $\varepsilon^p = \varepsilon_{\text{fail}}$ .

### 8.3.5. Combined model for shear yielding and distributed crazing

This model is motivated by the shortcomings of the DC model that are a consequence of attributing all plastic deformation to distributed crazing. As discussed in detail in Sec. 10.4.4, this assumption causes an overestimation of the plastic dilatancy under uniaxial tension (Fig. 10.6). Thus, also Helbig et al. [51] proposed to extend the model to either consider shear yielding or an anisotropic elastic material behaviour after craze initiation.

Another consequence of the fixed direction of inelastic deformation after craze initiation is an overestimation of the load bearing capability in transverse directions. Also, transverse normal stresses do not contribute to a further evolution of the damage in the material after craze initiation. This restriction in the model's kinematics and response to changes in the loading direction restricts its use cases (Secs. 10.4.4 and 10.4.5).

Therefore, the model presented below is an attempt to consider in one constitutive model both shear yielding and distributed crazing, the main mechanisms of plastic deformation in rubber-toughened polymers (Sec. 3.2.2). The groundwork for this constitutive model was laid by Ruge [90]. The DC model introduced in Sec. 8.3.3 serves as one part of the model to which another part is added to take into account shear yielding in form of the  $J_2$ -yield surface (Sec. 8.2.1). The model is therefore referred to as the  $J_2$ -DC model hereafter.

To model the impact of the rubber volume fraction in the case of the  $J_2$ -plasticity model, the continuum micromechanical approach is included in the same straightforward fashion as for the Raghava model presented in Sec. 8.3.4. Thus, the driving stress is computed following Eq. (8.42), and the failure criterion as specified by Eq. (8.43) is employed.

As a consequence of the continuum micromechanical approach to obtain the overall material response, the contributions of both mechanisms are regarded in a smeared manner in each RVE of the material volume, where each mechanism prevails in its corresponding volume fraction. Based on the assumption of each mechanism taking place in its separate volume fraction, the parameter  $\alpha$  is introduced, denoting the volume fraction of shear yielding. Since in each part of the model the multiplicative decomposition of the deformation gradient (Eq. (8.1)) is applied, the same is assumed for the overall model. Following the approach of a volume-averaged macroscopic material response, the plastic part of the rate of deformation  $\mathbf{D}^p$  of the complete model is given by

$$\mathbf{D}^p = \alpha \mathbf{D}_{J_2}^p + (1 - \alpha) \mathbf{D}_{DC}^p, \quad (8.44)$$

where  $\mathbf{D}_{J_2}^p$  and  $\mathbf{D}_{DC}^p$  are the rate of deformation tensors of the  $J_2$  and DC part of the model, respectively. The rate of deformation tensor  $\mathbf{D}$  of the complete model is hence specified by

$$\mathbf{D} = \mathbf{D}^e + \alpha \mathbf{D}_{J_2}^p + (1 - \alpha) \mathbf{D}_{DC}^p \quad (8.45)$$

and the total accumulated plastic strain is given by

$$\varepsilon^p = \alpha \varepsilon_{J_2}^p + (1 - \alpha) \varepsilon_{DC}^p, \quad (8.46)$$

where  $\varepsilon_{DC}^p = \delta_n / \delta_{crit}$ . Following the homogenisation scheme introduced in Sec. 8.3.1, the overall elastic response is formulated in terms of Eq. (8.27).

The evolution of the yield strength  $k(\varepsilon^p)$  is taken to be equal for both mechanisms and approximated by the relation

$$k(\varepsilon^p) = \sigma_{min} + (\sigma_0 - \sigma_{min}) \exp(-h\varepsilon^p) + (\sigma_{fail} - \sigma_{min}) (\varepsilon^p)^q, \quad (8.47)$$

where  $\sigma_{min}$ ,  $\sigma_0$ ,  $\sigma_{fail}$ ,  $q$ , and  $h$  are material parameters to be calibrated from experimental data.

As proposed by Helbig et al. [51], the transition between shear yielding and distributed crazing is assumed to depend on the stress triaxiality

$$\eta = \frac{\sigma_m}{\sigma_e}. \quad (8.48)$$



Therefore, for the parameter describing the mechanisms' volume fractions  $\alpha$ , the following ansatz is made

$$\alpha(\eta) = \begin{cases} 1 - \frac{\eta}{\beta + \eta} & \text{for } \eta > 0 \\ 1 & \text{for } \eta \leq 0, \end{cases} \quad (8.49)$$

where  $\beta$  is a material-specific fit parameter. This approach meets the following prerequisites based on experimental observations:

- No crazing should be initiated in the case of hydrostatic pressure ( $\eta < 0$ ) and stress states with  $\eta = 0$ , i.e.  $\alpha = 1$ .
- For high stress triaxialities ( $\eta \rightarrow \infty$ ), all plastic deformation should result from distributed crazing, hence  $\alpha = 0$ .
- In the case of uniaxial tension ( $\eta = 1/3$ ), the experimentally observed volume strain should be reproduced.

Therefore, the fit parameter  $\beta$  is calibrated from the volume strain response in uniaxial tensile tests. The failure criteria introduced for both parts of the model (Sec. 8.3.3 and Sec. 8.3.4) are assumed to hold also for the overall model in the sense that failure in one of the two mechanisms triggers failure in the overall model.



## 9. Macroscopic modelling approach

---

*In this chapter, a homogenised modelling approach to PC/ABS blends is presented. Three plastically dilatant constitutive models are compared with regard to their ability to capture the large-strain deformation and failure behaviour of the three PC/ABS blends introduced in Chapter 4. Whilst the models are calibrated from uniaxial tensile tests, their capability to reproduce more complex loading conditions is investigated by means of simulations of fracture tests on notched specimens. Special emphasis thereby is devoted to the overall plastically dilatant behaviour and the evolution of the plastic zone.*

---

### 9.1. Constitutive modelling

The three well established yield functions that are compared in this study are: the Drucker-Prager (Eq. (8.12)), the Raghava (Eq. (8.13)), and the Green yield surface (Eq. (8.14)) which structurally resembles the Gurson model. The three yield surfaces as well as the general small-strain elastic finite-strain viscoplastic framework are introduced in detail in Chapter 8.

### 9.2. Parameter calibration

The three constitutive models considered were chosen to be as simple as possible, e.g. each with a constant value of  $\alpha$ . They were calibrated separately for the three materials to match the experimental data of the uniaxial tensile tests, recorded at a nominal strain rate of  $\dot{\epsilon}=0.1\text{ s}^{-1}$  in terms of the true stress-strain response as well as the evolution of volume strain (Figs. 9.1, 9.2, and 9.3).

Figures 9.1, 9.2, and 9.3 show that the uniaxial stress-strain response of the materials is captured quite well by all three models with individual parameter values. Also reasonably well captured is the accompanying evolution of the volume strain. Yet the saturation or even decrease of volume strain between an axial strain of 0.6 and 0.8 is not accounted for by the models.

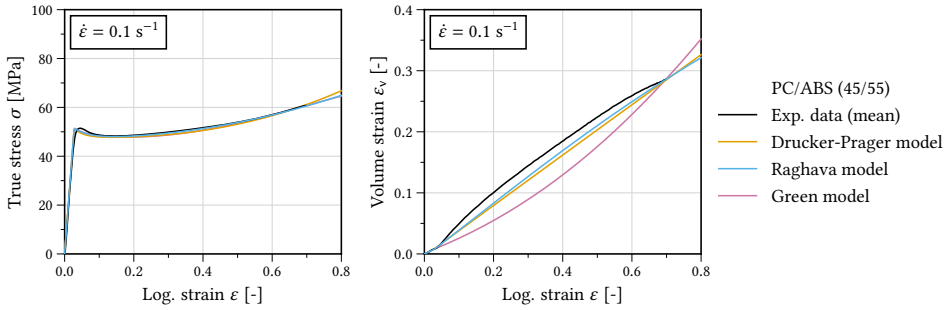


**Figure 9.1.:** Uniaxial stress-strain response and dilation behaviour of all models compared to experimental data for PC/ABS (45/55) and a nominal strain rate of  $\dot{\epsilon} = 0.1 \text{ s}^{-1}$ .

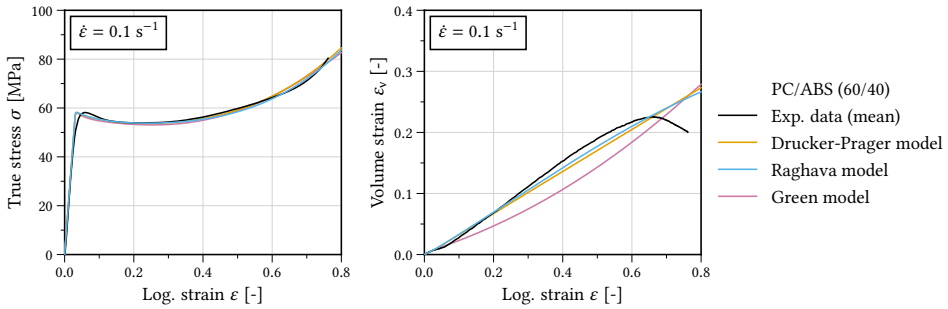


**Figure 9.2.:** Uniaxial stress-strain response and dilation behaviour of all models compared to experimental data for PC/ABS (60/40) and a nominal strain rate of  $\dot{\epsilon} = 0.1 \text{ s}^{-1}$ .

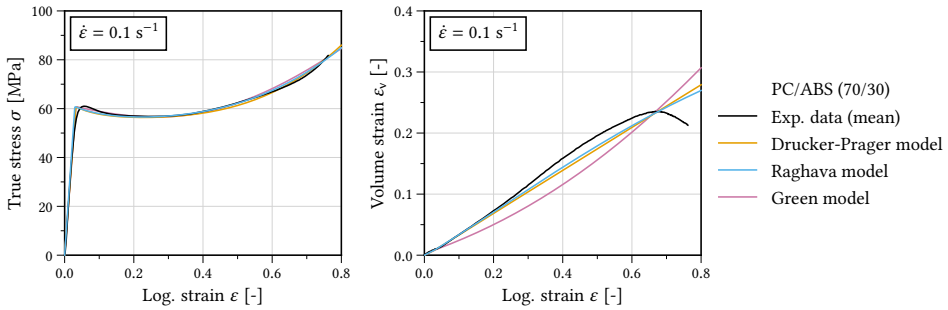


**Figure 9.3.:** Uniaxial stress-strain response and dilation behaviour of all models compared to experimental data for PC/ABS (70/30) and a nominal strain rate of  $\dot{\epsilon} = 0.1 \text{ s}^{-1}$ .

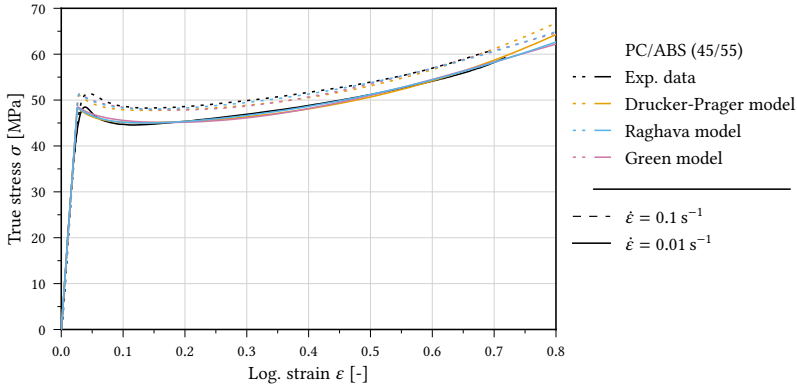


**Figure 9.4.:** Uniaxial stress-strain responses of all models compared to experimental data for PC/ABS (45/55) at two strain rates.

Finally, the experimental data for two strain rates allowed the calibration of the rate dependence of the material models in terms of the parameters  $\dot{\epsilon}_0$  and  $A$  in Eq. (8.11). An example of this in the form of PC/ABS (45/55) is shown in Fig. 9.4. The underlying assumption of modelling the rate dependency within this approach was that only the initial yield stress depends on the strain rate while the actual slope of the stress-strain curve in the plastic range is not impacted by variations of the deformation velocity.

The material parameters for each model and material are given in Tabs. C.1, C.2, and C.3 in Appendix C.

### 9.2.1. Comparison of the initial yield loci

The three material models all capture the mechanical behaviour of PC/ABS blends under uniaxial tension reasonably well. Hence, it is instructive to look at their performance under higher values of the stress triaxiality  $\eta$  (Eq. (8.48)). The yield loci of the three models provide a starting point to assess the impact of the yield surface on the material response in complex loading situations. Figures 9.5, 9.6, and 9.7 show the initial yield loci calibrated from the uniaxial tensile tests. The different slopes of the initial yield surfaces in Figs. 9.5, 9.6, and 9.7 for uniaxial tension correspond to the different slopes of the curves in Figs. 9.1, 9.2, and 9.3 at the onset of yield.

Figure 9.8 depicts the true stress-strain and volumetric strain response of the Drucker-Prager, Raghava, and Green model calibrated for PC/ABS (45/55) with a stress triaxiality under tension of  $\eta = 1$  and  $\eta = 3$ , respectively. For  $\eta = 1$ , the Drucker-Prager and the Raghava model yield almost identical results since at this stress triaxiality the shape (normal direction) of their yield surfaces is quite similar (Figs. 9.5, 9.6, and 9.7).

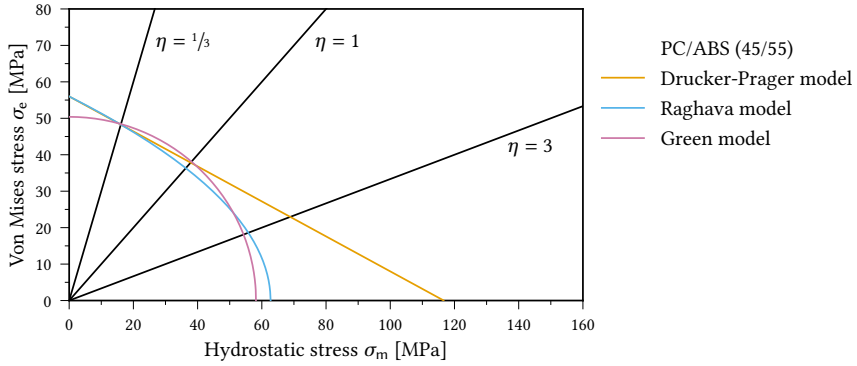


Figure 9.5.: Initial yield loci in  $\sigma_m$ - $\sigma_e$ -plane calibrated for PC/ABS (45/55).

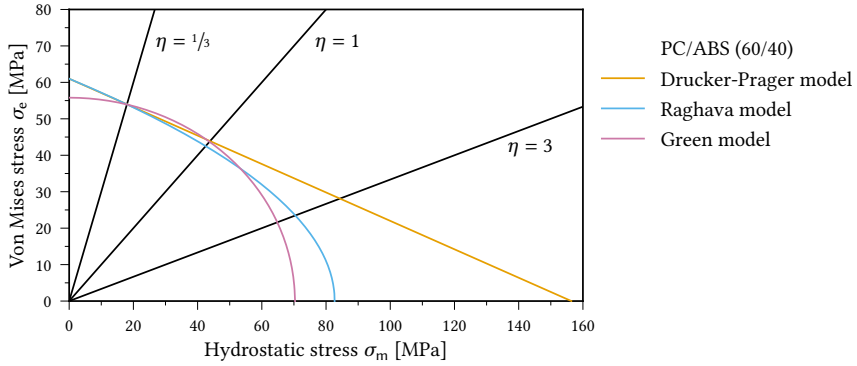


Figure 9.6.: Initial yield loci in  $\sigma_m$ - $\sigma_e$ -plane calibrated for PC/ABS (60/40).

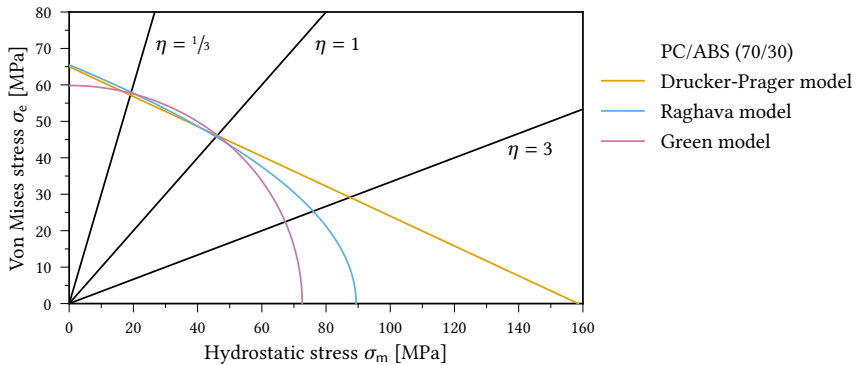
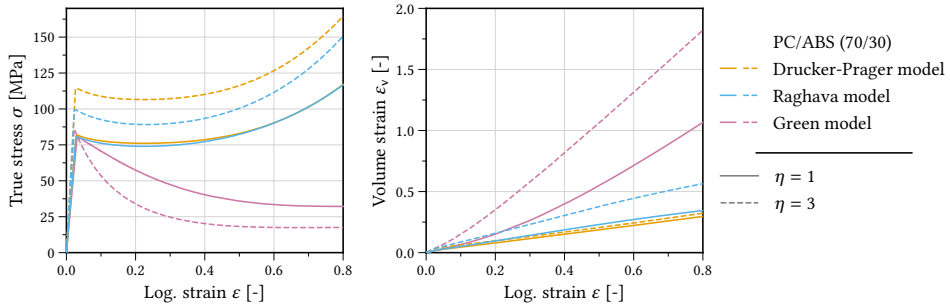


Figure 9.7.: Initial yield loci in  $\sigma_e$ - $\sigma_m$ -plane calibrated for PC/ABS (70/30).



**Figure 9.8.:** Tensile stress-strain response and evolution of volume strain with axial strain of the Drucker-Prager, the Raghava, and the Green model under elevated stress triaxialities.

In Fig. 9.8, significant differences in terms of a reduced stress level and an increased volume strain predicted by the Raghava model in comparison to the Drucker-Prager model only show up at the higher stress triaxiality of  $\eta = 3$ , where the yield loci clearly depart (Figs. 9.5, 9.6, and 9.7). Both the Drucker-Prager and the Raghava model feature a progressive hardening response (Fig. 9.8) even at elevated stress triaxialities. In contrast, the Green model which is governed by the evolving porosity that increases with plastic volume strain and thus causes a shrinkage of the yield surface, exhibits a softening stress-strain response for both elevated stress triaxialities (Fig. 9.8). Hence, in the case of the Green model, the plastic volume strain (increasing porosity) counteracts and dominates strain hardening exhibited under uniaxial tension ( $\eta = 1/3$ ) (Figs. 9.1, 9.2, and 9.3). The effect of the different models' response at elevated stress triaxialities will be discussed further in the following numerical simulations of plastic zones in notched tensile specimens.

## 9.3. Numerical studies

The three regarded material models were implemented as VUMAT user material routines for the FEA software Abaqus/Explicit [28]. Thereby, an efficient semi-implicit time integration of the constitutive equations was employed where only the scalar quantity  $\epsilon^p$  is updated implicitly whereas the tensorial direction of plastic flow is updated in an explicit manner, as suggested in [9].

### 9.3.1. SENT fracture tests

Finite element simulations of the SENT tests presented in Sec. 6.2 were carried out to analyse the performance of the different material models in complex loading situations. Employing symmetry with respect to the centre plane, only half of the SENT specimen was modelled and corresponding boundary conditions of zero normal displacements and zero shear stresses were applied throughout the centre plane. The specimen mesh used,

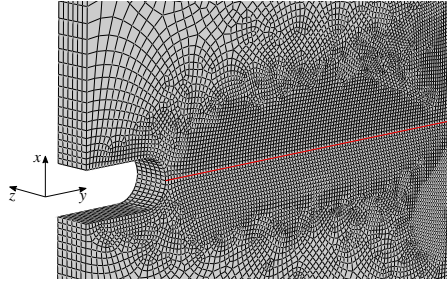


**Figure 9.9.:** FE model of half the SENT specimen exploiting symmetry with respect to centre plane with expected crack path indicated in red.

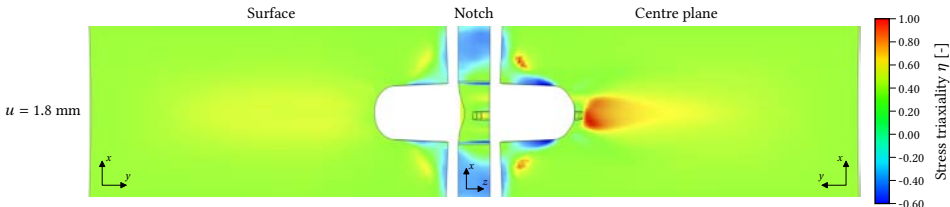


**Figure 9.10.:** Contours of the stress triaxiality  $\eta$  on SENT specimen surface, notch and centre plane at a specimen elongation of  $u = 1.8$  mm (prior to fracture) simulated for PC/ABS (70/30) using the Raghava model.

if not indicated otherwise, consisted of 60540 8-node linear (first-order) displacement brick elements with reduced integration (C3D8R) and is partly shown in Fig. 9.9. The FE model was discretised along the crack path (Fig. 9.9) using 107 elements featuring an approximate characteristic length<sup>1</sup> of 0.175 mm.

The three-dimensionality of the stress state throughout the specimen is illustrated in Fig. 9.10 in terms of the distribution of the stress triaxiality which attains significantly higher values in the specimen centre plane than on the free surface.

### 9.3.2. Plastic zone formation at a notch

The zone of intense inelastic deformation that develops at a notch or crack tip prior to and during fracture is generally of great interest as it is directly related to the amount of energy dissipation and therefore the fracture toughness of a material. Hence, much work has been

<sup>1</sup> As defined by the Abaqus User's Guide [28]: [*The characteristic length*] is a typical length of a line across an element for a first-order element; it is half of the same typical length for a second-order element.



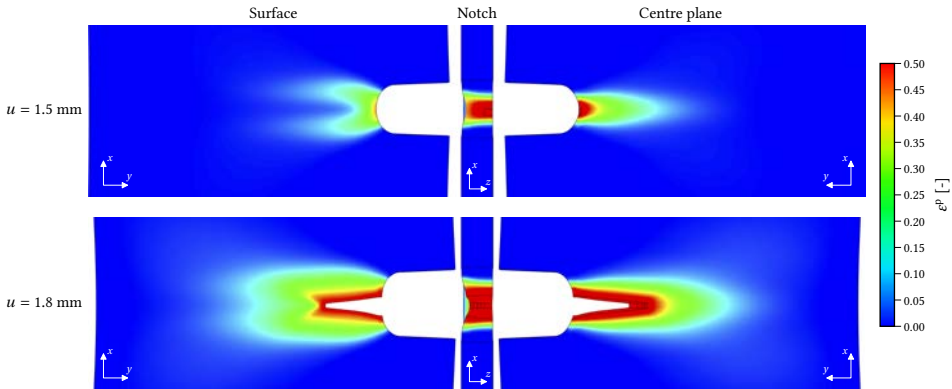


**Figure 9.11.:** Contours of the equivalent plastic strain  $\epsilon^P$  at notch in PC/ABS (45/55) at two different values of specimen elongation simulated using the Drucker-Prager model.

devoted to its numerical analysis with regard to neat [70, 64] as well as rubber-toughened thermoplastics (see, e.g. [110] for a review). For instance, addressing in particular PC/ABS blends, their two-phase microstructure has been explicitly resolved in a two-dimensional plane strain model considering a crack tip under mode I small scale yielding conditions by Seelig and Van der Giessen [93]. Since such a micromechanical (“bottom up”) approach suffers from the lack of knowledge about the individual constituent behaviour on the blend microscale as well as from idealisations in modelling the microstructure, a macroscopic (“top down”) approach towards analysing the plastic zone at a notch was pursued in this study.

Hence, below the evolution of the plastic zone ahead of the notch in simulations of SENT specimens, utilising the different models discussed above, is compared to the experimental findings presented in Sec. 6.2. The plastic zone shapes predicted using the Drucker-Prager and Raghava model are quite similar (e.g. Figs. 9.11 and 9.12). The differences to the distribution of the strain in tensile direction (Figs. 9.13 and 9.14) are minor, validating the assumption made for the strain fields determined through DIC (Figs. 6.16, 6.17, and 6.18).

Thus, for the sake of better comparison with the experimental results at corresponding loading stages, only contours of the strain in tensile direction  $\epsilon_{xx}$  are depicted for the FE simulations of the PC/ABS (60/40) as well as PC/ABS (70/30) blends and models hereafter. Contours of  $\epsilon_{xx}$  at the specimen centre plane and the free surface computed from the Drucker-Prager model are shown for PC/ABS (45/55) in Fig. 9.13, for PC/ABS (60/40) in Fig. 9.15, and for PC/ABS (70/30) in Fig. 9.16, respectively. Similar distributions for each material, computed using the Raghava model, are depicted in Figs. 9.14, 9.17, and 9.18.

An elongated shape of the plastic zone is regarded as typical for rubber-toughened thermoplastics [110]. This feature appears to be reasonably well captured by the simulations for

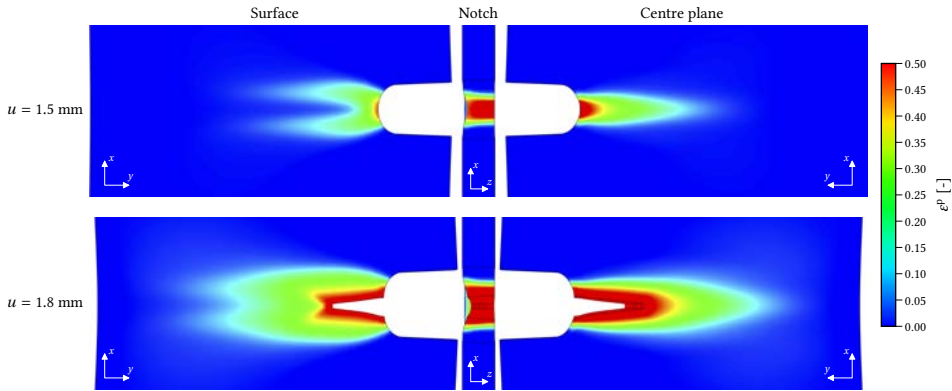


**Figure 9.12.:** Contours of the equivalent plastic strain  $\varepsilon^p$  at notch in PC/ABS (45/55) at two different values of specimen elongation simulated using the Raghava model.

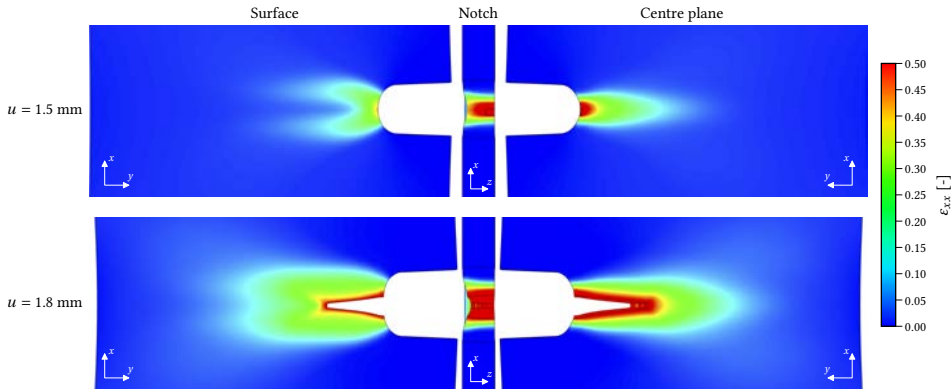


**Figure 9.13.:** Contours of the strain in tensile direction  $\varepsilon_{xx}$  at notch in PC/ABS (45/55) at two different values of specimen elongation simulated using the Drucker-Prager model.

both material models and all three materials. The predicted strain concentrations and thus zones of plastic deformations at the notch of the two models leave a similar impression yet feature subtle differences.

In the stage of crack initiation regarding PC/ABS (45/55) and PC/ABS (70/30), the plastic zone shapes on the surface predicted by the Raghava model tend to split up more clearly and form two slightly longer branches (Figs. 9.14 and 9.18) compared to the predictions by the Drucker-Prager model that feature a plastic zone shape slightly bulkier around the notch and not reaching as far into the specimen's surface (Figs. 9.13 and 9.16). However, in the case of PC/ABS (60/40), the plastic zone shapes predicted are virtually identical (Figs. 9.17 and 9.15).

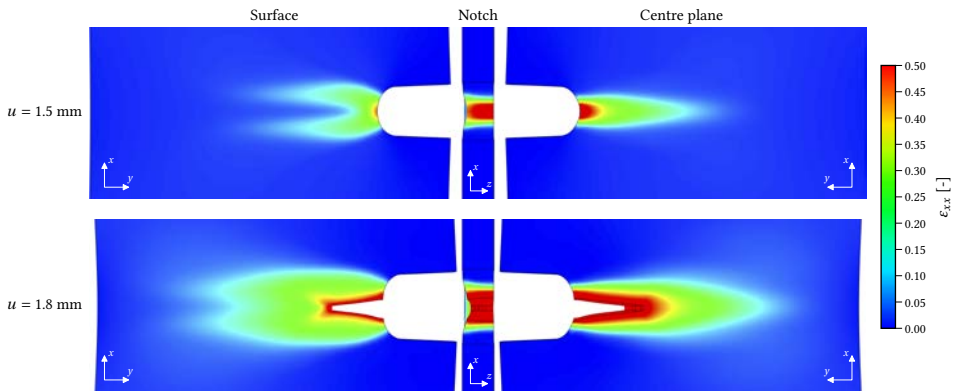


**Figure 9.14.:** Contours of the strain in tensile direction  $\varepsilon_{xx}$  at notch in PC/ABS (45/55) at two different values of specimen elongation simulated using the Raghava model.

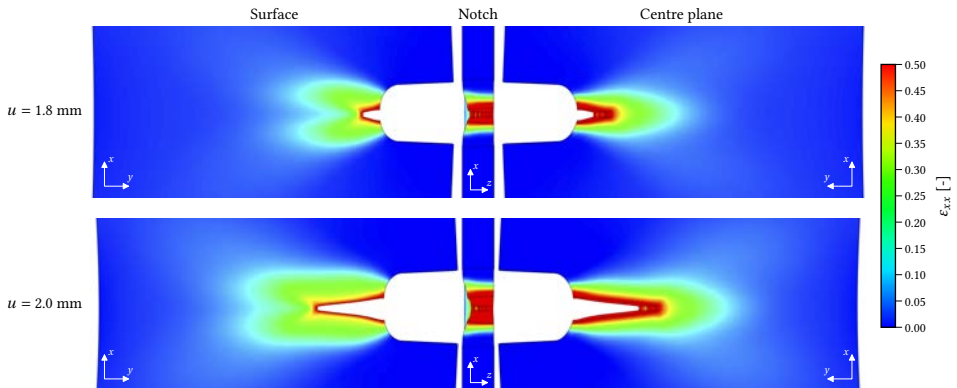


**Figure 9.15.:** Distribution of strain in tensile direction at notch in PC/ABS (60/40) at two different values of specimen elongation simulated using the Drucker-Prager model.

In the later loading stages featuring crack propagation, the trend of the Drucker-Prager model to predict one bulkier plastic zone shape remains for PC/ABS (70/30) and PC/ABS (45/55) (Figs. 9.13 and 9.16). In comparison, the plastic zone shapes obtained with the Raghava model at this loading stage feature two slightly more distinct heads and are not as bulky around the notch (Figs. 9.14 and 9.18). Regarding PC/ABS (60/40), the plastic zone shape at an overall specimen elongation of  $u = 2.0$  mm obtained with the Raghava model is slightly narrower and reaches further into the material than the plastic zone shape computed using the Drucker-Prager model. These subtle differences lead to the conclusion that the Raghava model's predictions are in better agreement with the experimental findings (Figs. 6.16, 6.17, and 6.18).

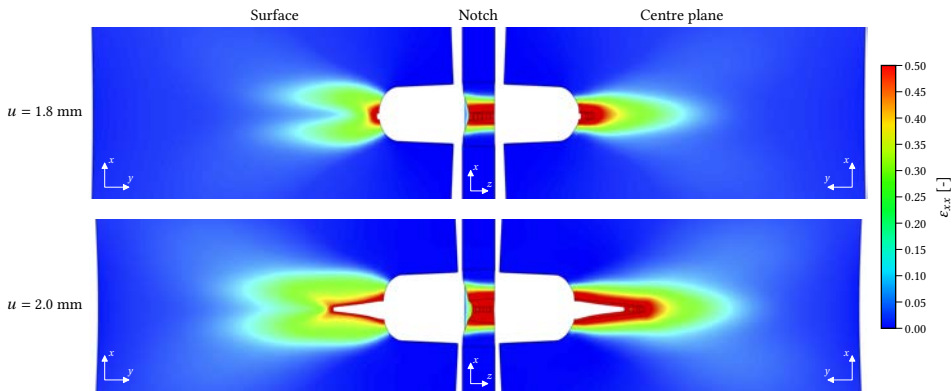


**Figure 9.16.:** Distribution of strain in tensile direction at notch in PC/ABS (70/30) at two different values of specimen elongation simulated using the Drucker-Prager model.

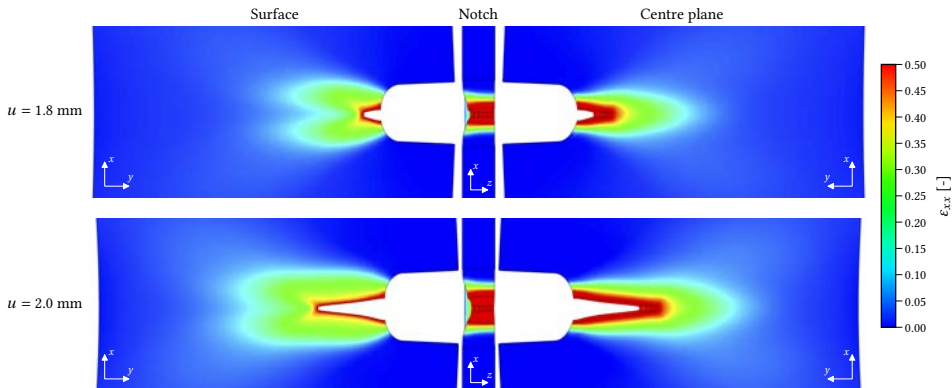


**Figure 9.17.:** Distribution of strain in tensile direction at notch in PC/ABS (60/40) at two different values of specimen elongation simulated using the Raghava model.

Therefore, in the following section, only the Raghava model will be discussed in further detail. The larger extension of the plastic zone shape regarding PC/ABS (45/55) in Fig. 9.14 compared to PC/ABS (60/40) in Fig. 9.17 and PC/ABS (70/30) in Fig. 9.18 corresponds to the experimental findings (Figs. 6.16, 6.17, and 6.18). The view into the notch root (centre of Figs. 9.14, 9.17, and 9.18) indicates necking at the specimen surface which was also observed in the experiments. For all three materials, the simulated plastic zone clearly changes from the interior of the specimen (centre plane) to the free surface, which can be attributed to the differences in hydrostatic stress (Fig. 9.10) that promotes volumetric plastic flow. However, in the case of PC/ABS (45/55), the predicted splitting of the plastic zone at the specimen surface, particularly in the earlier loading stage at an overall displacement of  $u = 1.5$  mm (Fig. 9.14), does not agree with experimental observations (Fig. 6.16). The

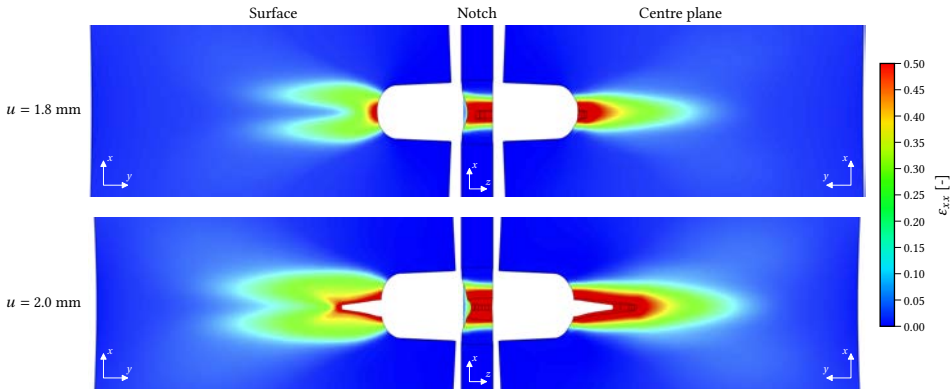


**Figure 9.18.:** Distribution of strain in tensile direction at notch in PC/ABS (70/30) at two different values of specimen elongation simulated using the Drucker-Prager model.

transition from a single localised plastic zone in the specimen interior to two branches at the free surface indicates plastic flow by a through-thickness slip mode. This mechanism of plastic deformation is well known from plastically incompressible materials under plane stress. In the experimental study on PC/ABS (45/55), such a plastic deformation pattern appears to be not present (Fig. 6.16).

Contrarily, in the case of PC/ABS (70/30) and PC/ABS (60/40), the behaviour of which is dominated by a larger amount of the plastically incompressible PC, the computed splitting of the tensile strain distribution at the specimen surface (Figs. 9.18 and 9.17) is also visible in the experiments (Figs. 6.17 and 6.18). This might indicate that the suitability of dilatant plasticity models of the Raghava or Drucker-Prager type to capture the deformation behaviour of PC/ABS blends under complex loading states with an elevated stress triaxiality is limited to grades with only a moderate amount of ABS.

Figure 9.19 shows the plastic zone computed using the Green model in the case of PC/ABS (70/30). Overall similar results are obtained for the other two blend materials using this model.

Analogous to earlier studies [110], these numerical results illustrate that this type of model, which is governed by an evolving porosity, overemphasises the localisation of plastic flow and predicts unrealistically narrow plastic zones at a notch. This is even though the calibrated Green model captures the response of PC/ABS under uniaxial tension including the progressive hardening at large strains (Fig. 9.1). Yet, the questionable behaviour of this model, giving rise to the results in Fig. 9.19, could already be anticipated from its response under elevated stress triaxialities depicted in Fig. 9.8. Owing to the large volume strain predicted by the Green model in such a situation (Fig. 9.8), necking at the specimen surface did not occur in the FE simulation (Fig. 9.19, centre). Because of its incapability

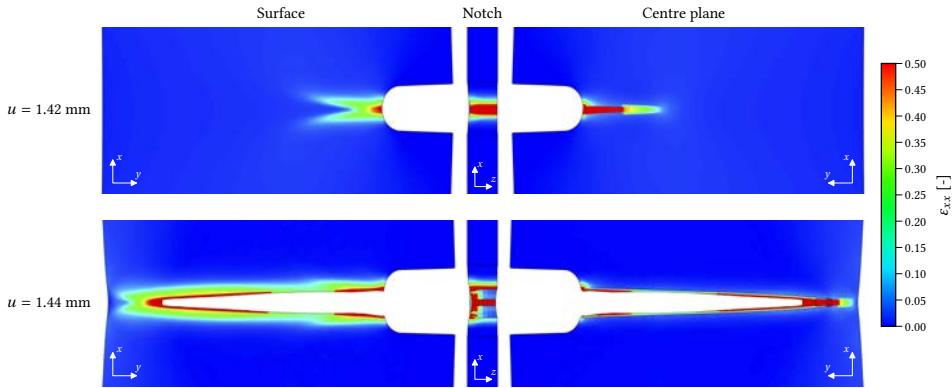


**Figure 9.19.:** Distribution of strain in tensile direction at notch in PC/ABS (70/30) at 1.42 mm and 1.44 mm of specimen elongation simulated using the Green model.

to realistically reproduce the plastic zone at a notch, the Green model is not further considered in the simulation of crack propagation in PC/ABS in Sec. 9.3.3.

The above observations made by comparing the performance of the Raghava, Drucker-Prager, and Green model suggest that an evolving porosity has a much stronger influence on the plastic zone formation at a notch than the shape of the yield surface. This was confirmed by simulations carried out using the Green model with the evolution of the porosity switched off, which led to plastic zone shapes similar to those obtained using the Raghava or the Drucker-Prager model.

The finding that the Drucker-Prager and the Raghava model lead to similar results despite their different yield surface shapes has to be taken with some caution. The specimen geometry considered featured a notch radius comparable to the specimen thickness and the crack growth was modelled by the elimination of not infinitesimally small finite elements (Sec. 9.3.3). As a result, the simulated local stress triaxiality ahead of the crack did not exceed a value of 1.2, for which the response of the two models in terms of their yield surface shape can be assumed to be similar (Figs. 9.5, 9.6, and 9.7). A deviation of the models' responses may be expected for specimens with a significantly sharper notch giving rise to higher local stress triaxialities, however.

### 9.3.3. Simulation of fracture behaviour

To further investigate the performance of the material models to capture the behaviour of PC/ABS blends, the fracture tests reported in Sec. 6.2 were simulated. The Green model was thereby discarded because of its failure to reproduce the plastic zone already prior to fracture (Fig. 9.19). While the Raghava and the Drucker-Prager model yield almost identical results in terms of the plastic zone at the onset of crack, it was of interest whether

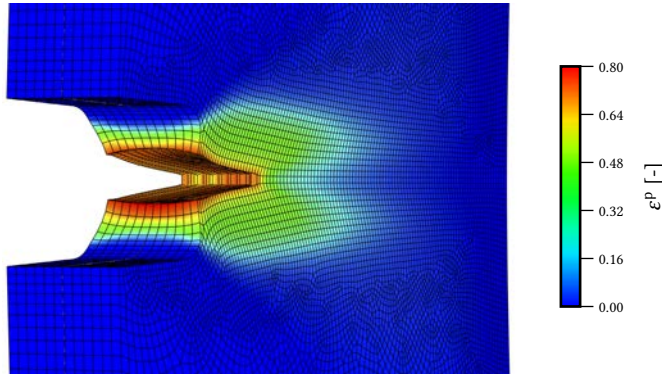


**Figure 9.20.:** Advancing crack in SENT specimen of PC/ABS (70/30) and distribution of accumulated plastic strain computed from Raghava model at specimen elongation of  $u = 2.0$  mm.

the different shape of their yield loci at elevated stress triaxiality (Figs. 9.5, 9.6, and 9.7) would become noticeable in the situation of an advancing crack front being much sharper than the initial notch.

Crack propagation was modelled numerically in a rather coarse manner by the deletion of finite elements upon fulfilment of a local failure criterion (Fig. 9.20). Two common criteria were considered which state that ductile failure takes place at a critical value of accumulated plastic strain

$$\varepsilon^p = \int_{t_0}^t \sqrt{\mathbf{D}^p : \mathbf{D}^p} d\tilde{t} \geq \varepsilon_{crit}^p \quad (9.1)$$

or, alternatively, at a critical value of plastic work per unit volume

$$w^p = \int_{t_0}^t \boldsymbol{\sigma} : \mathbf{D}^p d\tilde{t} \geq w_{crit}^p \quad (9.2)$$

The failure parameters  $\varepsilon_{crit}^p$  or  $w_{crit}^p$  were calibrated from the fracture tests (Tab. 9.1) in order to match the onset of crack propagation which coincides with the peak of the load-displacement curves shown in Figs. 9.21, 9.22, and 9.23. The other material parameters, governing the deformation behaviour, were taken fixed as calibrated from the uniaxial tensile tests (Tabs. C.1, C.2, and C.3). The local failure strains using Eq. (9.1) were in good agreement with those measured in the uniaxial tensile tests from which the deformation behaviour had been calibrated (Tab. 9.1 and Sec. 9.2).

As depicted in Figs. 9.21, 9.22, and 9.23, both the Raghava and the Drucker-Prager model once calibrated to the uniaxial tensile tests reproduce the elastic range very well. However, using either of the two failure criteria Eq. (9.1) or Eq. (9.2), they overestimate the reaction force from the SENT fracture experiments for PC/ABS (45/55), PC/ABS (60/40), and

Material	PC/ABS (45/55)		PC/ABS (60/40)		PC/ABS (70/30)	
Model	DP	R	DP	R	DP	R
$w_{crit}^p$ [MPa]	34.50	38.00	39.50	40.00	46.00	48.50
$\epsilon_{crit}^p$ [-]	0.68	0.74	0.68	0.70	0.74	0.78

**Table 9.1.:** Failure parameters calibrated for fine mesh (SENT specimen), see Tab. 9.2 and Fig. 9.24.

FE mesh	fine	coarse
No. of elements [-]	60528	20167
Characteristic length [mm]	0.175	0.277

**Table 9.2.:** Variation of the FE mesh parameters.

PC/ABS (70/30). Also, after the onset of failure, the crack propagates too rapidly. Yet, the displacements corresponding with the onset of crack as well as total failure are reasonably well reproduced by both models.

However, the observations regarding the simulated specimen response in the crack propagation regime (Figs. 9.21, 9.22, and 9.23) should be taken with caution since the results might be affected by the coarse numerical modelling of crack advance as discussed below.

Since crack propagation was modelled through the elimination of finite elements upon a local failure criterion, the issue of mesh dependence deserves special attention. In Figure 9.24, the simulated force-displacement curves obtained for two differently fine meshes are compared. What is referred to as the “fine” mesh was the standard mesh with 60528 elements (Tab. 9.2) used throughout the numerical studies underlying Figs. 9.21, 9.22, and 9.23. The “coarse” mesh for comparison consisted of 20167 finite elements. Figure 9.24 clearly shows that the crack propagation is mesh-dependent. If the value for the failure parameter is fixed, a coarser mesh leads to a delayed overall specimen failure. Nevertheless, the moment of crack initiation is almost identical for the two meshes such that the peak forces also don not significantly differ.

Since only the crack propagation stage, setting on at a displacement of about 1.8 mm, suffers from mesh dependence this effect could be overcome by calibrating the parameters  $\epsilon_{crit}^p$  or  $w_{crit}^p$  controlling local failure to the size of the finite elements. Consequently, the overestimation of the peak force in the simulations (Figs. 9.21, 9.22, and 9.23) is an indication that both the Drucker-Prager and the Raghava yield surface underestimate the PC/ABS materials’ susceptibility to elevated stress triaxialities.



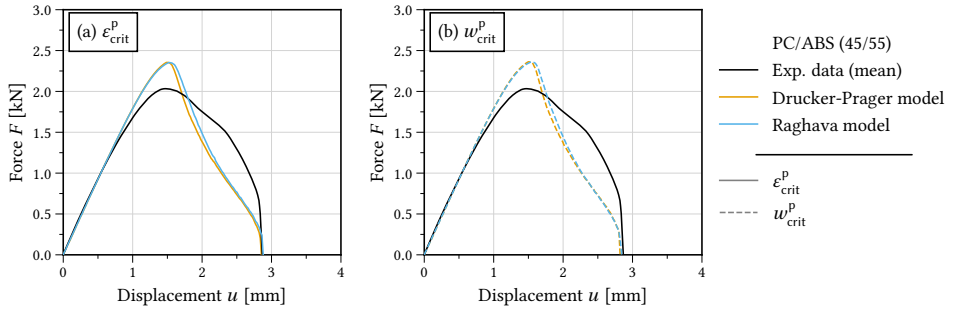


**Figure 9.21.:** Force-displacement curve of PC/ABS (45/55) from SENT fracture test compared to simulations using the Drucker-Prager or Raghava model and a failure criterion based on (a)  $\epsilon_{crit}^p$  and (b)  $w_{crit}^p$ .

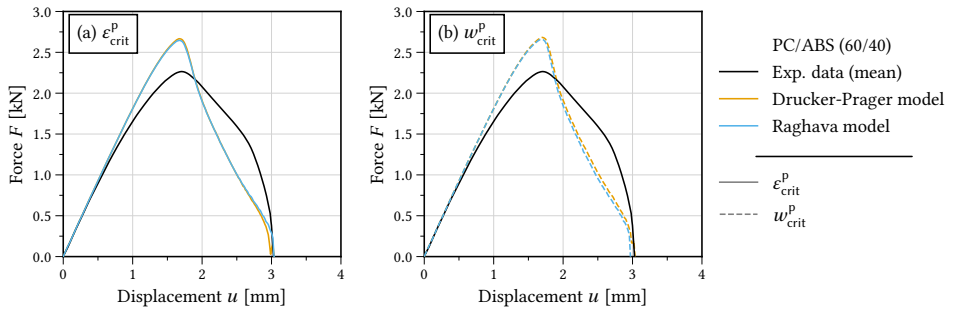


**Figure 9.22.:** Force-displacement curve of PC/ABS (60/40) from SENT fracture test compared to simulations using the Drucker-Prager or Raghava model and a failure criterion based on (a)  $\epsilon_{crit}^p$  and (b)  $w_{crit}^p$ .

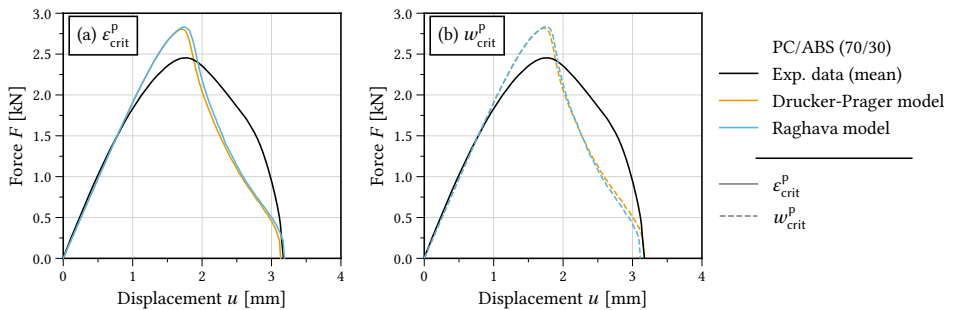


**Figure 9.23.:** Force-displacement curve of PC/ABS (70/30) from SENT fracture test compared to simulations using the Drucker-Prager or Raghava model and a failure criterion based on (a)  $\epsilon_{crit}^p$  and (b)  $w_{crit}^p$ .

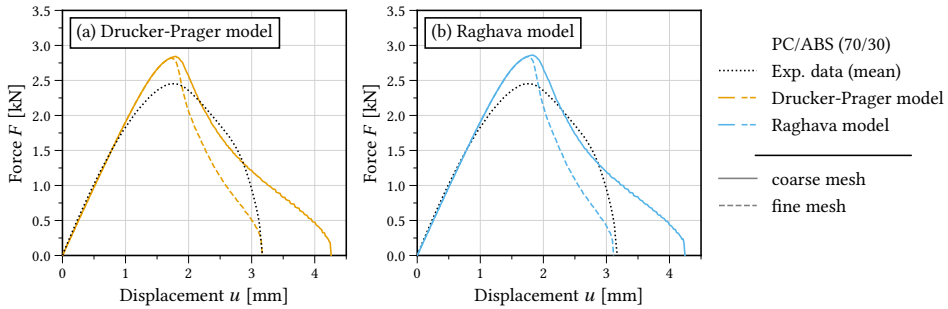


**Figure 9.24.** Force-displacement curve of PC/ABS (70/30) from SENT fracture test compared to simulations using (a) the Drucker-Prager model and (b) the Raghava model with  $w_{crit}^p$  failure criterion calibrated to the fine mesh.

## 9.4. Conclusions

In this investigation different material models – all featuring a plastically dilatant behaviour under tension – were systematically analysed with regard to their ability to describe the mechanical response of three PC/ABS materials with different compositions. These models were chosen since they are widespread and kept as simple as possible to be useful for practical applications such as structural FEA of technical components. The focus thereby was not on a perfect fit but rather on the investigation of the effect of basic features such as yield surface shape and porosity evolution. The experimental results on three commercial PC/ABS blends with different compositions show a clear influence of the composition on the deformation and fracture behaviour, which is in line with various earlier studies in the literature. However, the latter are typically less complete in presenting data on the true stress-strain response along with the accompanying evolution of volume strain, which are both needed for an adequate calibration of constitutive models. The three “classical” isotropic constitutive models investigated in this study were the Drucker–Prager and the Raghava model, which differ only by the shape of the yield surface, and the Green model, which additionally displays a dependence of the yield surface on the evolving porosity, representing microscale damage mechanisms. These models all proved to capture the true stress-strain response as well as the evolution of volume strain of the three PC/ABS blends in uniaxial tensile tests. Yet, they exhibited a rather ambivalent performance in FE simulations of the SENT fracture tests. Key findings and conclusions from this study are:

- In simulations of the SENT fracture tests on all three materials, the Green (Gurson-like) model, which accounts for an increasing porosity and thus features a shrinkage of the yield surface under high stress triaxiality as prevailing at a notch, severely overestimated the localisation of plastic strain. Hence, this model is not suited to describe the behaviour of PC/ABS blends. This corresponds to findings from other studies applying such a type of model to rubber-toughened polymers [110].

- In contrast, plastically dilatant material models which do not feature a shrinkage of the yield surface with plastic volume strain, such as the Drucker–Prager and the Raghava model, appeared to be more successful in simulations of the overall response of PC/ABS in SENT fracture tests.
- A closer inspection indicates that the suitability of the simple isotropic models of Drucker–Prager or Raghava type is limited to PC-rich PC/ABS grades. Regarding the ABS-rich PC/ABS (45/55) blend, these models showed larger deficiencies in reproducing the plastic zone shape. Therefore, the complex behaviour of ABS, such as its overall anisotropy due to the effect of distributed crazing [51], needs to be also accounted for in modelling the mechanical behaviour of ABS-rich PC/ABS blends.
- The finding that the models overestimate the reaction force in simulations of the SENT fracture tests indicates that both the Drucker–Prager and the Raghava yield surface do not sufficiently account for the materials' susceptibility to stress states with an elevated triaxiality.
- Through these findings, the present study provides some indication of the range of applicability of established (i.e. easy-to-use) material models for numerical structural analyses of technical components made of PC/ABS – which is of practical value.
- On the other hand, the revealed limitations of the above discussed models indicate needs for further fundamental research on the improved constitutive modelling of PC/ABS, possibly supported by multiscale modelling.



# 10. Unit cell modelling approach

---

*In the following chapter, a unit cell modelling approach to PC/ABS blends is presented. In Sec. 3.3, several studies on composition-dependent fracture toughness of PC/ABS blends in the literature are discussed. The contradictory nature of these studies' results indicates a basic need for further understanding that can only partly be met by the homogenised phenomenological approach presented in Chapter 9. Therefore, the aim of this computational study was to gain a better understanding of the impact of the key microstructural parameters on blend behaviour and fracture toughness. In FE simulations, unit cell models of PC/ABS blends, varying with regard to their PC/ABS ratios and the rubber contents in ABS, were subjected to loading conditions of different complexities. Thereby, the characteristic material response of each main constituent was modelled using bespoke constitutive models. Eventually, a novel material model introduced in Sec. 8.3.5, combining the micromechanical failure mechanisms of distributed crazing and shear yielding, was employed in the ABS phase and compared to existing micromechanical and phenomenological material models.*

---

## 10.1. Unit cell models

The smallest periodic unit in a periodic structure is commonly referred to as a unit cell. On the atomic scale, unit cells are employed to describe the arrangement of atoms or molecules in crystalline materials. Applied to continuum micromechanics, unit cell arrays can be used to approximate the arrangement of at least two distinct constituents of a morphology. Common three-dimensional structures to represent two different species or constituents are body-centred cubic (BCC), face-centred cubic (FCC), or stacked hexagonal arrays (SHA) [98, 109].

The advantage of approximating the complex morphologies of PC/ABS blends via a unit cell approach in this study is the lower computational effort when compared to more elaborate representations of the microstructure, such as representative volume elements (RVE).

## 10.2. Blend morphology and unit cell geometry

In Sec. 4.3, the blend microstructures of three commercial PC/ABS materials were found to be dependent on the PC/ABS ratio as well as processing parameters such as melt flow. These findings mirror those in the literature presented in Sec. 3.4. The ternary nature of the microstructure of PC/ABS blends, where the ABS phase is a binary rubber-toughened polymer itself, is seen in micrographs (Sec. 4.3). Yet for the sake of simplicity, PC/ABS blends were regarded as a binary system of the two main constituents PC and ABS in this study. Similar to the investigation presented by Seelig and Van der Giessen [93], the heterogeneous nature of ABS was neglected. Hence, ABS was modelled in a homogenised sense. Furthermore, the impact of processing parameters such as the flow direction during injection moulding causing, for instance, an anisotropic morphology, was neglected. Modelling PC/ABS blends as a binary system, the PC/ABS ratio becomes the key parameter determining the unit cell geometry, i.e. arrangement of the phases.

The PC/ABS ratio is commonly given in terms of mass fractions. As unit cell models represent the phases' volume fractions, the mass densities of the individual phases were used for conversion (Tab. 10.1). To convert the PC/ABS mass ratios into PC/ABS volume ratios, a mass density for ABS of  $\rho_{\text{ABS}} = 1030 \text{ kg/m}^3$  and a mass density for PC of  $\rho_{\text{PC}} = 1200 \text{ kg/m}^3$  was assumed (Sec. 4.3.4). These assumptions yield equal volume fractions for a PC/ABS mass ratio of (54/46) (Tab. 10.1).

Mass fractions (PC/ABS) [%]	90/10	80/20	70/30	64/36	60/40	54/46	50/50	44/56	40/60	30/70	20/80	10/90
Vol. fractions (PC/ABS) [%]	89/11	77/23	67/33	60/40	56/44	50/50	46/54	40/60	36/64	27/73	18/82	9/91

**Table 10.1:** Conversion of PC/ABS mass ratios to PC/ABS volume ratios.

Blends featuring a composition rich in PC or ABS that were cooled sufficiently slowly, exhibit a matrix particle morphology [106, 74, 76]. With an increasing ABS content, a transition occurs from a dispersed to a continuous ABS-phase for an ABS mass fraction between 35 % and 45 % [57]. A similar transition to an ABS matrix occurs for ABS mass fractions of approximately 60 % (Secs. 3.4 and 4.3). To reflect these transitions regarding the morphology, the unit cell arrangement was changed accordingly. For ABS volume fractions between 40 % and 60 % or ABS mass fractions from 36 % to 56 %, respectively, a co-continuous microstructure was used. Blend compositions rich in one of the two main constituents were approximated through unit cells either with a PC matrix and evenly dispersed spherical ABS particles or an ABS matrix with embedded PC inclusions.

### PC/ABS blends rich in one of the two main constituents

For a given PC/ABS ratio, all inclusions were assumed to be of the same size, i.e. feature the same volume. As an implication of the underlying assumption of periodicity, the particle centre points were uniformly distributed, i.e. were equidistant from each other.

To represent spherically shaped particles, a three-dimensional cell geometry is required. Moreover, in most two-dimensional unit cell approaches, not only the geometrical representation of the microstructure is restricted to two dimensions but also the loading conditions can only be two-dimensional, i.e. plane strain, as a consequence. Axisymmetric approaches, such as SHA unit cells, may provide the opportunity to investigate effects of triaxial loading conditions. Nonetheless, SHA unit cells suffer from the highly non-uniform distribution of the second phase along the principal loading axis especially in loading conditions of higher stress triaxialities [98]. The investigations of Seelig and Van der Giessen [94] highlighted that SHAs, approximated through an axisymmetric unit cell, exhibit artefacts in reproducing the deformation behaviour of rubber-toughened polymers. Therefore, a three-dimensional unit cell approach is presented here.

Taking into account the unit cell geometry requirements and the previously made assumptions, the particles were arranged on a regular BCC lattice. A cubic lattice also proves beneficial to avoid meshing issues mentioned in Danielsson, Parks, and Boyce [26], where a more elaborate Voronoi BCC unit cell was employed. The BCC unit cells allowed for automatic spatial discretisation using hexahedral elements for all PC/ABS ratios regarded (Sec. 10.3). Assuming that the unit cell faces remain plane throughout the deformation enabled further exploitation of the symmetries in the BCC arrangement. Consequently, only one eighth of the complete BCC cell was modelled (Fig. 10.1a).

### PC/ABS blends with a co-continuous microstructure

The unit cell models to approximate PC/ABS blends with an ABS mass fraction from 36 % to 55 % featured two interpenetrating phases (IPP). The arrangement of phases chosen reflected the assumption of an isotropic morphology (Fig. 10.1b).

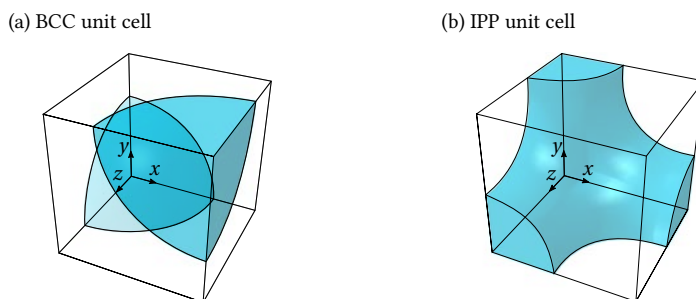


**Figure 10.1.:** Schematic representation of unit cells with (a) BCC and (b) co-continuous phase arrangement.

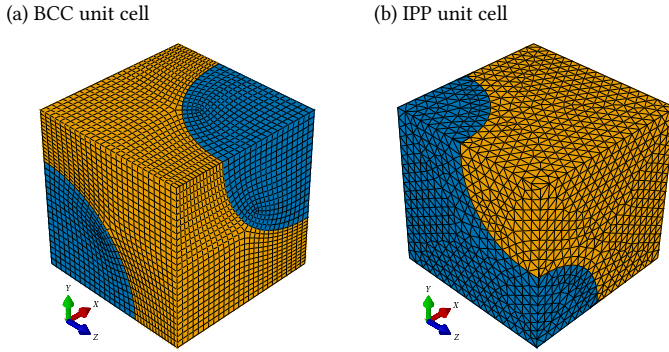


Figure 10.2.: Meshed unit cells with (a) BCC and (b) co-continuous phase arrangement.

## 10.3. Finite element modelling

The simulations were conducted using the commercial FEA software Abaqus/Explicit [28]. The creation and meshing of the FE models, representing different compositions subjected to different loadings, was automated using the software's Python interface.

### 10.3.1. Meshing and local failure

The unit cells representing a BCC arrangement used a hexahedral mesh of fully integrated first order elements (C3D8). The IPP unit cell models featured a tetrahedral mesh with 4-node linear tetrahedron elements (C3D4) (Fig. 10.2). In both cases, element erosion was employed to model local failure. During meshing, it was ensured that elements on the phase boundaries of BCC and IPP unit cells featured the same edge length for all PC/ABS ratios considered. Hence, regardless of the phase volume ratio, the edge length and volume of elements around a particle (BCC) or on the phase boundary (IPP) remained constant. Thus, in the event of element deletion, an equal amount of energy was dissipated.

### 10.3.2. Boundary conditions and load cases

In order to gain insight into the dependency of fracture toughness on blend composition, three different load cases were considered. Besides uniaxial tension, two load cases inducing stress states of higher triaxialities were chosen. The load cases causing higher stress triaxialities were considered to investigate the effectiveness of rubber-toughening and possible synergistic effects regarding fracture toughness (Sec. 3.5). The loadings and the overall response of the unit cell were specified in terms of macroscopic stress and strain quantities denoted by surrounding brackets  $\langle \rangle$ .



## Uniaxial tension

The stress state of uniaxial tension is characterised by a macroscopic stress triaxiality of

$$\langle \eta \rangle = \frac{\langle \sigma_m \rangle}{\langle \sigma_e \rangle} = \frac{1}{3}. \quad (10.1)$$

The unit cell models' uniaxial tensile response was investigated to assess the modelling approach's abilities in terms of qualitatively reproducing the macroscopic stress-strain response in comparison to the experimental results presented in Sec. 6.1.1.

## Load cases of higher strain (and stress) triaxiality

The two other load cases investigated should provide insights into the unit cells' behaviour in loading situations resembling impact scenarios and fracture tests typically employed to determine fracture toughness. The load cases were characterised through their macroscopic triaxiality in the strain space  $\langle \eta_\epsilon \rangle$ , defined as the ratio of the volume strain  $\langle \epsilon_v \rangle$  to the strain in the deviatoric plane  $\langle \epsilon_d \rangle$  as given by

$$\langle \eta_\epsilon \rangle = \frac{\langle \epsilon_v \rangle}{\langle \epsilon_d \rangle}, \quad (10.2)$$

where

$$\langle \epsilon_d \rangle = \sqrt{\frac{2}{3}} \left\| \langle \epsilon \rangle - \frac{1}{3} \langle \epsilon_v \rangle \mathbf{1} \right\|. \quad (10.3)$$

The considered load cases featured strain ratios of  $\langle \eta_\epsilon \rangle = 2/3$  and  $\langle \eta_\epsilon \rangle = 1$  (Fig. 10.3).

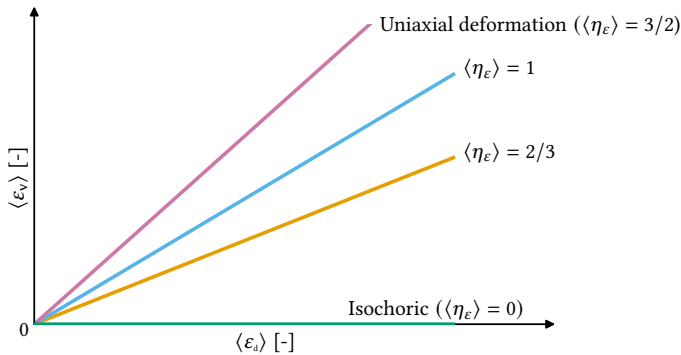
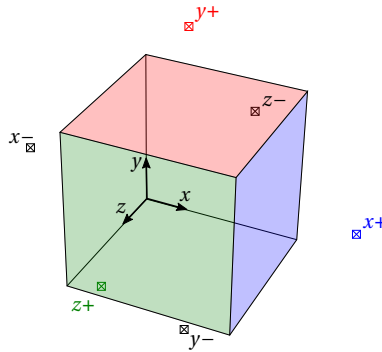


Figure 10.3.: Load cases characterised by  $\langle \eta_\epsilon \rangle$  represented in the  $\langle \epsilon_v \rangle$ - $\langle \epsilon_d \rangle$  strain space.

### Issues prescribing the stress triaxiality

The macroscopic strain triaxiality  $\langle \eta_\varepsilon \rangle$  was used because of problems encountered employing the macroscopic stress triaxiality  $\langle \eta \rangle$  in explicit FE simulations. Prescribing the necessary stress boundary conditions while using Abaqus/Explicit as the solver led to high-frequency oscillations during plastic deformation. However, the issue did not occur using Abaqus/Standard relying on identical code to control the boundary conditions. Unfortunately, Abaqus/Standard does not offer the functionality to model local failure via element erosion based on a user-defined criterion. Since the reason for the behaviour could not be identified, deformation boundary conditions prescribing  $\langle \eta_\varepsilon \rangle$  were used.

### Deformation controlled boundary conditions



**Figure 10.4.:** Schematic representation of the FE model with each reference point  $\boxtimes$  controlling the degrees of freedom (DOF) of the corresponding face of the hexahedral unit cell.

The prerequisite to only model one eighth of the complete BCC unit cell was the assumption that all its faces remain plane and parallel to the principal axes of the model  $\{x, y, z\}$  throughout the loading history. To retain compatibility with the deformation field and periodicity, symmetry boundary conditions to the  $\{x^-, y^-, z^-\}$ -faces were applied whereas normal displacements on the corresponding three “+”-faces were prescribed. To control the deformation on each face of the unit cell hexahedron, a corresponding reference point was introduced (Fig. 10.4). Each reference point was bound to the nodes of its corresponding face via equation constraints [28].

The three principal main stretches  $\lambda_x$ ,  $\lambda_y$ , and  $\lambda_z$  denote the macroscopic stretches of the unit cell in the principal directions  $\{x, y, z\}$ . Thereby, the  $y$ - and  $z$ -directions were considered equal such that  $\lambda_z = \lambda_y$  held. As a consequence,  $\lambda_y$  could be expressed as a function of  $\langle \eta_\varepsilon \rangle$  and  $\lambda_x$  as given by

$$\lambda_y = \lambda_x^\Gamma \quad \text{with} \quad \Gamma = \frac{\langle \eta_\varepsilon \rangle - \frac{3}{2}}{3 + \langle \eta_\varepsilon \rangle}. \quad (10.4)$$

The macroscopic deformation was controlled by prescribing the displacement  $u_x$  and therefore  $\lambda_x$  while computing the stretches and subsequently the displacements applied in the  $y$ - and  $z$ -directions. This was done by means of a user-defined amplitude subroutine (VUAMP) in each time step.

In the case of uniaxial tension, only  $\lambda_x$ , or  $u_x$ , respectively, were prescribed in conjunction with zero stress boundary conditions applied to the  $y^+$ - and  $z^+$ -faces. Volume forces were not considered.

## 10.4. Impact of the key microstructural parameters

The PC/ABS ratio and the rubber content in ABS can be singled out as the blend parameters most decisive for a PC/ABS material's mechanical response (Sec. 3.5). To gauge both parameters' impact on the unit cell response, they were varied systematically over a broad range.

The ABS mass fraction was varied in steps of 10 % beginning with neat PC and stopping at 100 % ABS. Additionally, for comparison with the experimental results, PC/ABS (45/55) was considered as well. Since PC/ABS blends were regarded as a binary system, a variation of the rubber content in ABS had no implications on the unit cell geometry. Thus, a variation of the rubber volume fraction  $f_R$  in ABS was reflected solely through a different material parameter and response of the ABS phase (Secs. 10.4.1 and 10.4.3). According to Seelig and Van der Giessen [94], the common upper limit for the rubber content in ABS is a volume fraction of 40 %. The lower bound of the spectrum of rubber volume fractions typically used for toughening glassy polymers is 5 % [98]. Using these bounds, the following five different rubber volume fractions in ABS were considered if not stated otherwise:  $f_R = \{5, 10, 20, 30, 40\}$  %.

### 10.4.1. Constitutive modelling

For each phase within the unit cell model, a bespoke material model was chosen to represent the characteristic features of either PC or ABS. The models are presented in detail in Chapter 8 and only introduced briefly here with particular emphasis on the parameter calibration process.

#### Polycarbonate (PC)

To reproduce the plastically incompressible behaviour of the PC-phase, the common  $J_2$  viscoplasticity model was used (Sec. 8.2.1). Local failure was modelled as induced by crazing through a criterion based on a critical hydrostatic stress of  $\sigma_m^{\text{crit}} = 90$  MPa [83, 107].

## Acrylonitrile-butadiene-styrene (ABS)

To model the binary polymer blend ABS, two different material models were investigated and compared to each other regarding their ability to reproduce the stress response and plastic dilatancy. These models were:

- the Raghava model wrapped by a continuum mechanical approach to take into account different rubber volume fractions (Sec. 8.3.4) and
- the continuum micromechanical model for distributed crazing in rubber-toughened polymers by Helbig et al. [51] (Sec. 8.3.3).

The distributed crazing (DC) model attributes all plastic dilatancy to the damage mechanism of distributed crazing whereas the Raghava (R) model takes the plastic dilatancy into account in a phenomenological sense. Both models, however, take into consideration the impact of different rubber contents assuming rubber particle cavitation in the elastic range such that upon yield a voided material is considered (Sec. 8.3.1). Local failure in the case of the Raghava model is assessed on a critical accumulated plastic strain. In the DC model, failure is triggered upon a critical craze width. The resulting two variants regarding the material model assignment to the respective phases of the unit cell models are referred to as PC/ABS ( $J_2/R$ ) and PC/ABS ( $J_2/DC$ ) hereafter.

### 10.4.2. Material parameter calibration

While the behaviour of the main constituents as bulk materials might be well known from experiments, their response as constituents of a blend remains unknown. Also, the response of a material on the macroscopic scale may significantly differ from the same material's response on the microscale due to phenomena like the size-effect [97].

As a consequence, the response of a material present as a constituent of a microstructure might be significantly different compared to the material's macroscopically observed behaviour in bulk form. As the difference between the two states remains unknown, similar bulk and phase material behaviour were assumed throughout the study presented.

Blending materials together introduces an interface at the phase boundaries with a particular behaviour on the microscale also impacting the blend's macroscopic response. One strategy to deal with the interface is to introduce it as a third phase with its own constitutive model. Knowledge about the mechanical interface behaviour of PC and ABS is contradictory (Sec. 3.3). In the approach presented, any impact of the interface between the PC and ABS phase on the blend behaviour was neglected. Hence, perfect adherence of the two phases was assumed.

Based on the assumption of similar bulk and phase material behaviour, the constitutive models for each phase were calibrated from the corresponding bulk material's uniaxial tensile response. The yield curves at different strain rates of PC and ABS under uniaxial tension are approximately self-similar (Secs. 3.1 and 3.2). Therefore, an impact of the strain

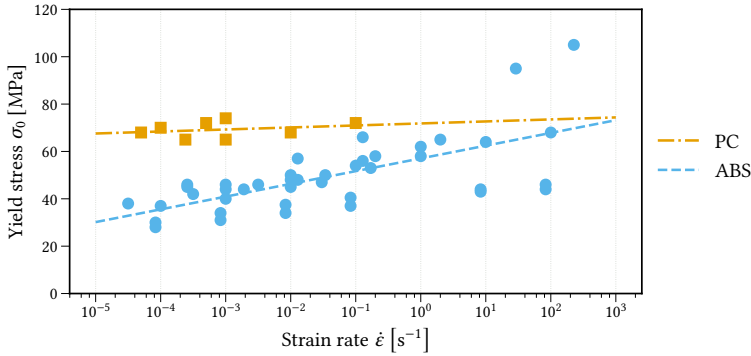


**Figure 10.5.:** Strain rate dependency of the initial yield stress for PC and ABS based on averaging experimental results compiled from literature sources [77, 87, 117, 119, 20, 120, 22, 38, 82, 53].

rate on the characteristic features and slope of the hardening curves, i.e. the constitutive models' parameters describing hardening, was neglected in this study.

The material parameters determining the initial softening and progressive rehardening behaviour, i.e. the slope of the yield stress, were fitted from G'Sell et al. [38] in the case of PC and Helbig et al. [51] with regard to ABS. In both cases, the experimental data of the smallest strain rate available was used and taken as the reference strain rate  $\dot{\epsilon}_0$ . Regarding the ABS phase, the rubber volume fraction  $f_R$  was assumed to not impact the slope of the stress response during plastic deformation.

The viscoplastic nature of the materials modelled was accounted for by a strain rate dependency of the initial yield stress. For their good availability and the straightforward calibration procedure, the yield stress was calibrated from uniaxial tensile tests. To robustly model viscoplastic behaviour, a wide range of strain rates was considered. Moreover, the yield stress may be highly dependent on the composition of a material. Hence, calibrating the viscoplastic properties of a constitutive model relying on a single literature source may not be accurate.

Therefore, yield stresses measured over a wide range of strain rates originating from various sources<sup>1,2</sup> were approximated by means of linear regression as depicted in Fig. 10.5. Since the bulk behaviour of the main constituents remained unknown, this fitting method was chosen to consider a common strain rate dependence with regard to the initial yield stress.

Regarding ABS, the dependence of the yield stress on composition, i.e the rubber content  $f_R$ , had to be addressed. The rubber contents of the materials investigated in the

<sup>1</sup> Data for ABS compiled from Louche et al. [77], Park et al. [87], Xu and Xu [117], Yin and Wang [119], Castellani et al. [20], Yokouchi, Seto, and Kobayashi [120], and Chen and Sauer [22].

<sup>2</sup> Data for PC compiled from G'Sell et al. [38], Mulliken and Boyce [82], Yin and Wang [119], and Hempel [53].

forementioned literature sources used for calibration of the initial yield stress were mostly unknown. Therefore, an intermediate rubber content within the typical range of  $f_R = 20\%$  [18, 99] was assumed for what was defined as the standard ABS for which the other material parameters were calibrated. The material parameters of the calibrated Raghava and DC material models are listed in Tabs. D.1 and D.2, respectively.

### 10.4.3. Calibrated phase material behaviour

Owing to a greater variety of possible compositions, the range of reported yield strengths for the same strain rate is broader in the case of ABS (Fig. 10.5). Whereas PC generally exhibits a high yield stress, relatively speaking, the reported yield stresses for ABS double over the range of reported strain rates between  $10^{-5} \text{ s}^{-1}$  and  $10^2 \text{ s}^{-1}$ . The calibration method outlined above reflects this through a more pronounced strain rate dependency for ABS. Thus, for a strain rate of about  $1.8 \cdot 10^3 \text{ s}^{-1}$  the approach predicts an identical initial yield stress of  $\sigma_0 = 74.59 \text{ MPa}$  for both main constituents.

The stress-strain response of the  $J_2$ -plasticity model as employed in the PC phase of the unit cell models is shown in Fig. 10.8. The strain rate dependency of the calibrated constitutive model for PC is far less pronounced than that of the constitutive models in the ABS phase (Figs. 10.6 and 10.7).

The material parameter  $\alpha$  in the Raghava model, describing the materials' sensitivity to hydrostatic stress, allows for calibration of the volume strain response from the experimental data (Fig. 10.7). Regarding the DC model, its micromechanical nature and the assumption of all inelastic deformation resulting from distributed crazing leads to an overestimation of the volume strain response (Fig. 10.6).

Figures 10.9 and 10.10 illustrate the dependence of the failure strain and the overall stress response on the rubber content as introduced in Sec. 8.3. As a consequence of this micromechanical approach to take into account the rubber content, both models qualitatively reproduce the experimentally observed features, i.e. with a decreasing rubber content, the failure strain decreases whereas the yield stress and elastic stiffness increase (Sec. 3.2.2).

### 10.4.4. Results - uniaxial tension

Simulations of overall uniaxial tension were carried out at a macroscopic strain rate of  $\langle \dot{\epsilon} \rangle = 0.1 \text{ s}^{-1}$  for comparison with the experimental results (Sec. 6.1.1). Based on estimates from the micrographs, rubber volume fractions of  $f_R = 20\%$  and  $f_R = 30\%$  were considered for this load case.

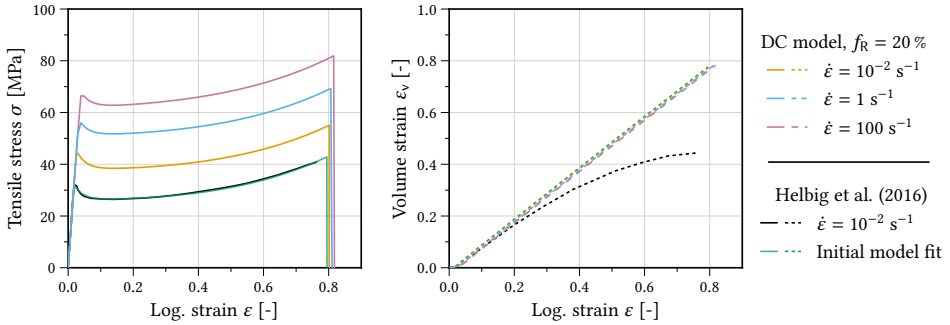


**Figure 10.6.:** Stress-strain and volume strain response under uniaxial tension of the DC model ( $f_R = 20\%$ ) with the initial fit from Helbig et al. [51] and the final fit from the literature for three values of the strain rate.

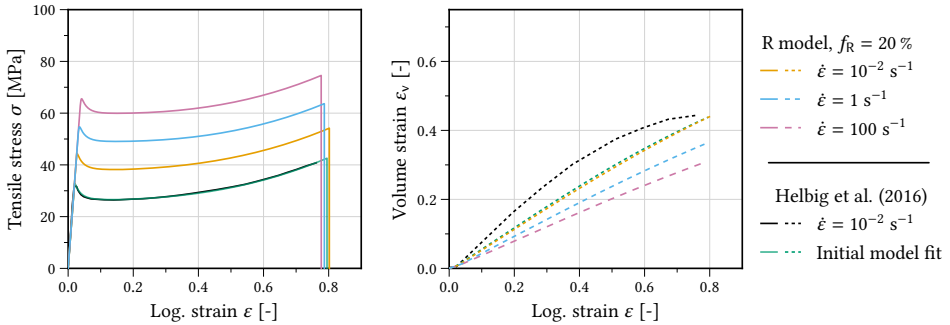
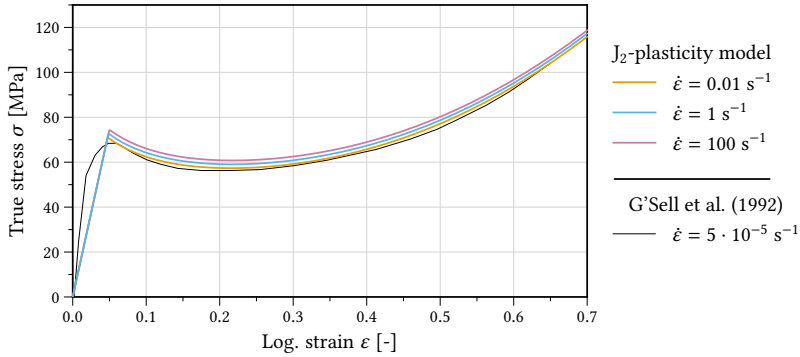


**Figure 10.7.:** Stress-strain and volume strain response under uniaxial tension of the Raghava model ( $f_R = 20\%$ ) with the initial fit from Helbig et al. [51] and the final fit from the literature for three values of the strain rate.

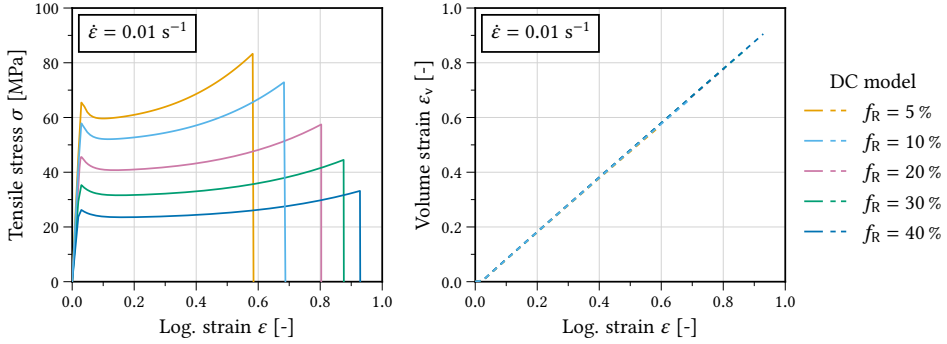
#### 10.4.4.1. PC/ABS (70/30)

Figure 10.11 shows the overall true stress and volume strain responses of the PC/ABS (70/30) BCC unit cells with the DC model in the ABS phase. In the case of a rubber content of 20 %, the initial yield stress was accurately predicted (Fig. 10.11). The unit cells' stress-strain curves also feature a partially accurate amount of softening as illustrated in Fig. 10.11. However, the rehardening for larger strains was overestimated. This overestimation can partly be attributed to the unit cell modelling approach because the assumption of periodicity does not allow modelling of distributed phenomena such as neck propagation. Regarding the volume strain response of the PC/ABS ( $J_2$ /DC) unit cells, the general trend was well captured for both rubber contents (Fig. 10.11). Yet, the unit cell model with a rubber content of 20 % in the ABS phase yielded a better prediction of the experimental results (Fig. 10.11).

In the case of the PC/ABS ( $J_2$ /R) unit cells (Fig. 10.12), the yield stress for both rubber contents was underestimated. Similar to the PC/ABS ( $J_2$ /DC) unit cells, the progressive



**Figure 10.8.:** Response under uniaxial tension of the calibrated  $J_2$  plasticity model for three values of the strain rate.



**Figure 10.9.:** Stress-strain and volume strain response under uniaxial tension of the DC model for five values of the rubber volume fraction  $f_R$ .

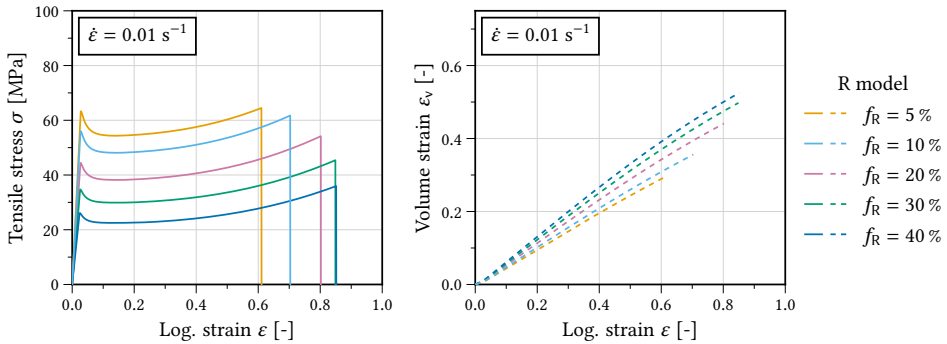


**Figure 10.10.:** Stress-strain and volume strain response under uniaxial tension of the Raghava model for five values of the rubber volume fraction  $f_R$ .



rehardening was overestimated (Fig. 10.12). Regarding the dilation behaviour, the unit cells with the Raghava model in the ABS phase yielded an underestimation of the overall amount of volume strain in comparison to the experiments (Fig. 10.12).

The PC/ABS ( $J_2/DC$ ) unit cell models underestimated the overall failure strain and failed at  $\langle \epsilon \rangle \approx 0.6$  (Fig. 10.11). In contrast, the PC/ABS ( $J_2/R$ ) unit cell models passed through two stages of failure. The failure of the ABS particles and PC matrix took place separately (Fig. 10.12). Regarding a rubber content of 20 %, the response of the then porous PC unit cell featured a greatly overestimated amount of rehardening and failure strain. The different failure behaviours found for the two material models in the ABS phase can be attributed to the respective model's behaviour under higher stress triaxialities and kinematics. The DC model attributes all plastic deformation to its eponymous deformation mechanism. Thereby, the craze normal direction is based on the maximum principal stress and is fixed after initiation. However, loadings not in the craze normal direction do not contribute to damage propagation. This can be illustrated with the axial stress-strain response of the DC model for higher stress triaxialities which are identical to those under uniaxial tension (Fig. 10.13).

In the case of macroscopic uniaxial tension, the local craze normal direction in all elements coincided with the tensile direction (Fig. 10.15a). Consequently, the material response in the craze plane remained purely elastic throughout all stages of deformation. Therefore, the DC model caused a high hydrostatic stress in the PC matrix around the particle perpendicular to the macroscopic tensile direction (Fig. 10.16a). Eventually, matrix failure was triggered when the hydrostatic stress exceeded the local failure criterion (Fig. 10.17a). Regarding the Raghava model, the hydrostatic stress in the matrix around the particle was lower since the plastic response of the material model takes into account the triaxiality of the stress state (Figs. 10.16b and 10.14). Failure started in the equatorial plane of the particle causing the drop in the macroscopic stress response (Fig. 10.12). Delamination of the matrix particle interface followed. Yet, the matrix still carried load, and an overall larger deformation was enabled (Fig. 10.17b).

The increased amount of overall volume strain found for the PC/ABS ( $J_2/DC$ ) unit cells compared to the PC/ABS ( $J_2/R$ ) unit cells is a consequence of the DC model's capability to bear unlimited loading in all directions normal to the craze normal direction. However, in the case of overall uniaxial tension, this behaviour led to a better approximation of the experimental results regarding both the stress-strain and volume strain response (Figs. 10.11 and 10.12).

#### 10.4.4.2. PC/ABS (60/40)

The uniaxial stress-strain response for the PC/ABS (60/40) blend, approximated using the IPP arrangement, exposed the flawed kinematics of the DC model even more (Fig. 10.18). The purely elastic response in all directions in the craze plane resulted in a high hydrostatic stress in the PC phase and large stress gradients at the interface. Eventually, this led

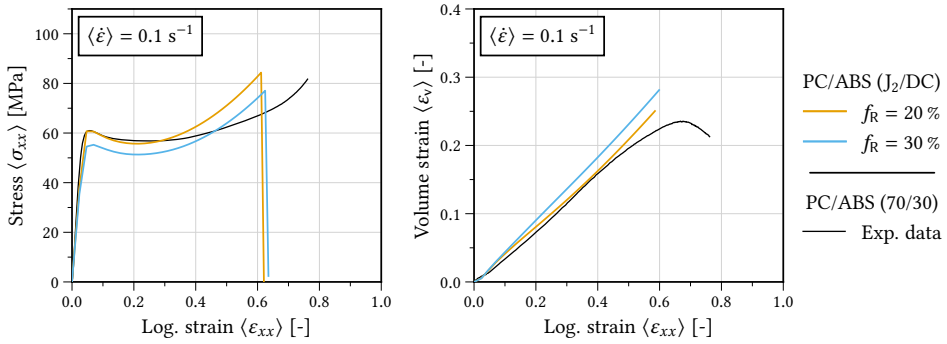


**Figure 10.11.:** Uniaxial stress-strain and volume strain response of PC/ABS (70/30) unit cell models with the DC model in the ABS phase at a macroscopic strain rate  $\langle \dot{\epsilon} \rangle = 0.1 \text{ s}^{-1}$ .

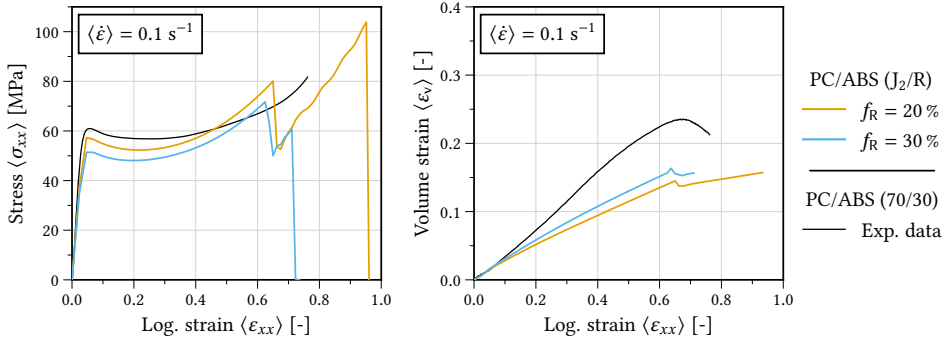


**Figure 10.12.:** Uniaxial stress-strain and volume strain response of PC/ABS (70/30) unit cell models with the Raghava model in the ABS phase at a macroscopic strain rate  $\langle \dot{\epsilon} \rangle = 0.1 \text{ s}^{-1}$ .

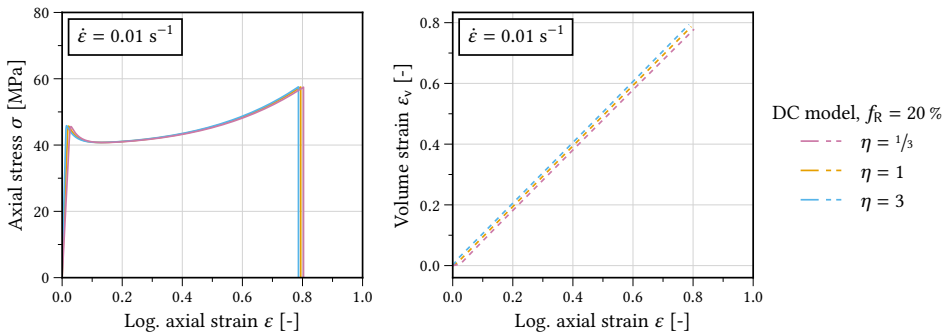


**Figure 10.13.:** Impact of the stress triaxiality  $\eta$  on the stress-strain and volume strain response of the DC model.

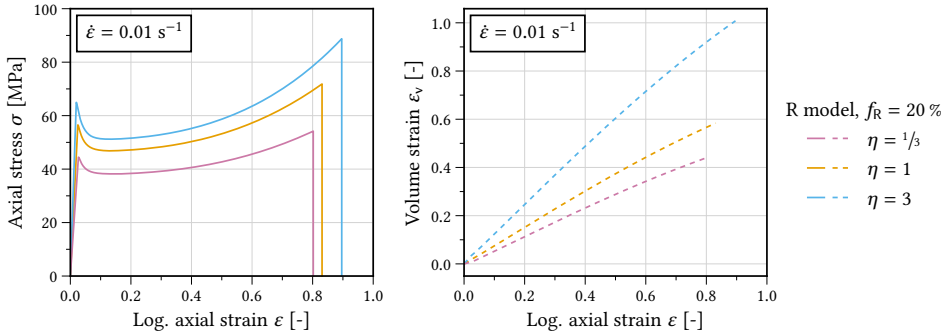


**Figure 10.14.:** Impact of the stress triaxiality  $\eta$  on the stress-strain and volume strain response of the Raghava model.

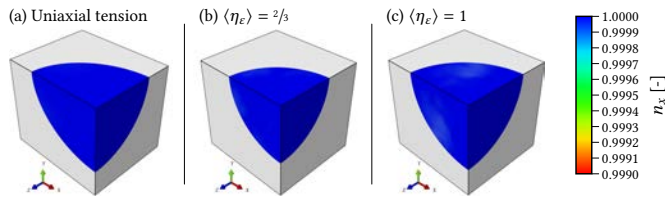


**Figure 10.15.:** Component  $n_x$  of the unit craze normal vector  $\mathbf{n}$  for (a) uniaxial tension, (b)  $\langle \eta_\epsilon \rangle = 2/3$ , and (c)  $\langle \eta_\epsilon \rangle = 1$  in the PC/ABS (70/30) unit cell model with a rubber volume fraction  $f_R = 20\%$ .

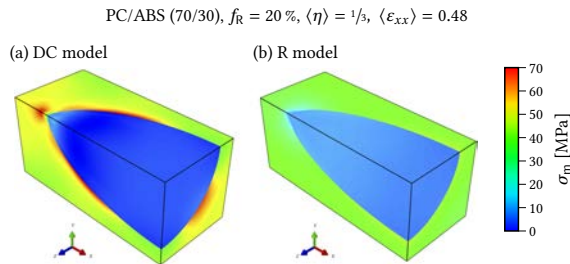


**Figure 10.16.:** Contours of the hydrostatic stress  $\sigma_m$  on PC/ABS (70/30) unit cell with (a) the DC model and (b) the Raghava model in the ABS phase subjected to uniaxial tension.

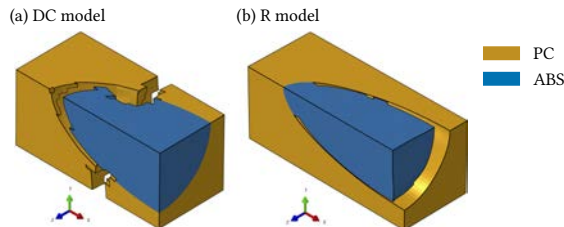


**Figure 10.17.:** PC/ABS (70/30) unit cell failure behaviour under uniaxial tension for  $f_R = 20\%$  with (a) DC model and (b) Raghava model in the ABS phase.

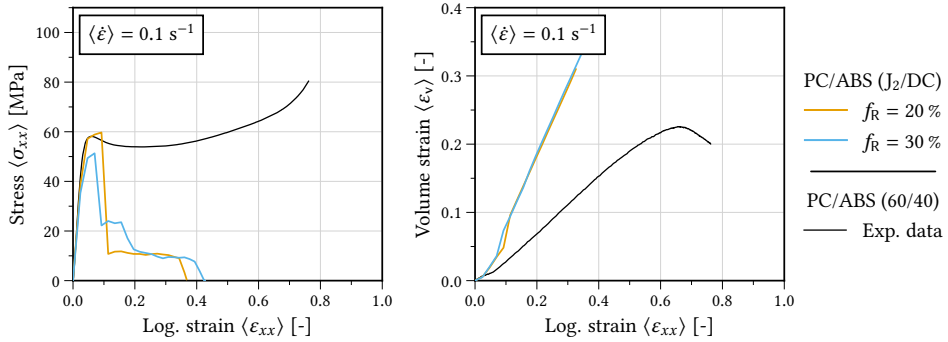


**Figure 10.18.:** Uniaxial stress-strain and volume strain response of PC/ABS (60/40) unit cell model with the DC model in the ABS phase for two values of the rubber volume fraction  $f_R$  and a macroscopic strain rate of  $\langle \dot{\epsilon} \rangle = 0.1 \text{ s}^{-1}$ .

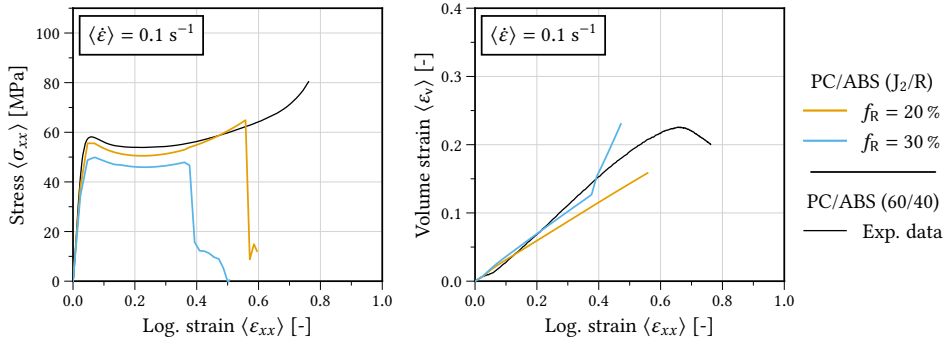


**Figure 10.19.:** Uniaxial stress-strain and volume strain response of PC/ABS (60/40) unit cell model with the Raghava model in the ABS phase for two values of the rubber volume fraction  $f_R$  and a macroscopic strain rate of  $\langle \dot{\epsilon} \rangle = 0.1 \text{ s}^{-1}$ .

to early local failure in the PC phase (Figs. 10.20a and 10.21). Further phase separation at the interface left behind only a fraction of the original cross section for load bearing (Fig. 10.21). Yet, due to the co-continuous phase arrangement, the overall plastic dilation was strongly overestimated (Fig. 10.18).

The Raghava model proved to be better suited to reproduce the overall behaviour in the IPP unit cell. Regarding a rubber content in the ABS phase of 20 %, both the yield stress and the softening upon yield were well approximated (Fig. 10.19). The overall volume strain was underestimated for this rubber content, though. Regarding  $f_R = 30\%$ , the overall stress level was lower and the overall dilation higher (Fig. 10.19).

Failure for both rubber contents considered was predicted to occur earlier than in the experimental results. Once more, this shows the limitations of the unit cell model approach which cannot account for distributed processes such as neck propagation resulting in a

more distinct rehardening. Also, critical strains at failure might locally be higher than experimentally measured in a macroscopic sense. Therefore, the failure parameters used here, calibrated from uniaxial tension, might underestimate the actual local material strength within the micromechanical approach.

Yet, the unit cell model approach presented, endowed with the Raghava model in the ABS phase, proved to be capable of qualitatively reproducing the stress-strain and volume strain behaviour of PC/ABS (60/40).

#### 10.4.4.3. PC/ABS (45/55)

The PC/ABS (45/55) blend was also modelled using the IPP unit cell. Hence, the DC model again was not suited to reproduce the experimental behaviour as was the case for the PC/ABS (60/40) blend (Fig. 10.24). The PC phase of the model failed early as a result of a hydrostatic stress concentration induced by the ABS phase (Figs. 10.24, 10.22a, and 10.23a). Since delamination also took place, the load bearing cross section was greatly reduced resulting in a sudden decrease regarding the stress response (Figs. 10.23 and 10.24). As a result of the delamination, the overestimation of the volume strain became even more severe (Fig. 10.24).

Regarding the PC/ABS (45/55) unit cell with the Raghava model in the ABS phase, both the stress-strain and volume strain behaviour were qualitatively reproduced up to an earlier failure than in the experimental results (Fig. 10.25). For both rubber contents, the extent of softening was well reproduced. With regard to a rubber content of 20 %, the yield stress was approximately predicted by the unit cell simulation (Fig. 10.25).

Final failure locally arose in the PC phase and subsequently caused failure of the ABS phase (Fig. 10.23b). Regarding the distribution of hydrostatic stress before failure, the Raghava model in the ABS phase did not cause as severe stress gradients at the interface as the DC model (Fig. 10.22b).

#### 10.4.4.4. Concluding remarks

The distributed crazing material model exhibited limitations due to its assumption that all plastic deformation is caused by distributed crazing such that only loadings in the craze normal direction drive the plastic deformation. As a consequence, it was not allowing a reasonable material response when employed in a co-continuous phase or as a matrix. The Raghava model proved to be a better choice in modelling the overall uniaxial tensile response within the unit cell model approach presented.

The comparison of the simulation results with the experimental data shows the capabilities of the approach with material parameters calibrated from averaged macroscopic experimental data. In this regard, the unit cell approach presented yielded a reasonable approximation of the experimental data in terms of the deformation behaviour. However,

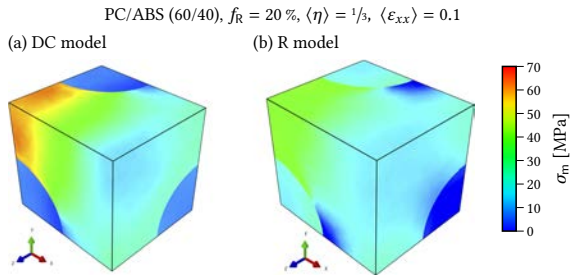


**Figure 10.20.:** Contours of the hydrostatic stress  $\sigma_m$  on PC/ABS (60/40) unit cell with (a) the DC model and (b) the Raghava model in the ABS phase subjected to uniaxial tension.

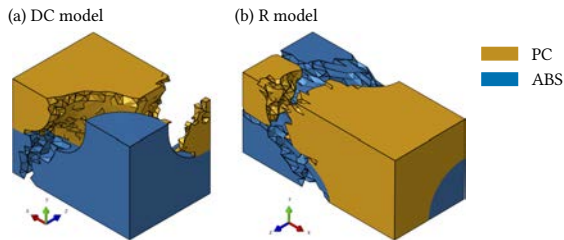


**Figure 10.21.:** PC/ABS (60/40) unit cell failure behaviour under uniaxial tension for  $f_R = 20\%$  with (a) DC model and (b) Raghava model in the ABS phase.

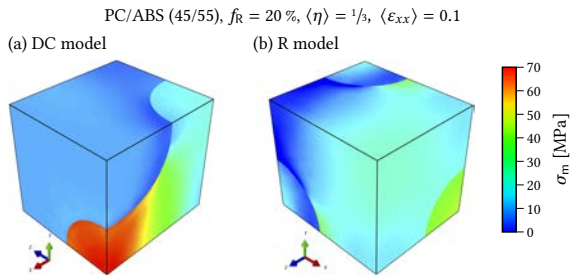


**Figure 10.22.:** Contours of the hydrostatic stress  $\sigma_m$  on PC/ABS (45/55) unit cell with (a) the DC model and (b) the Raghava model in the ABS phase subjected to uniaxial tension.

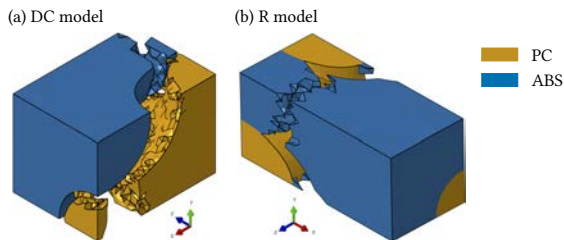


**Figure 10.23.:** PC/ABS (45/55) unit cell failure behaviour under uniaxial tension for  $f_R = 20\%$  with (a) DC model and (b) Raghava model in the ABS phase.

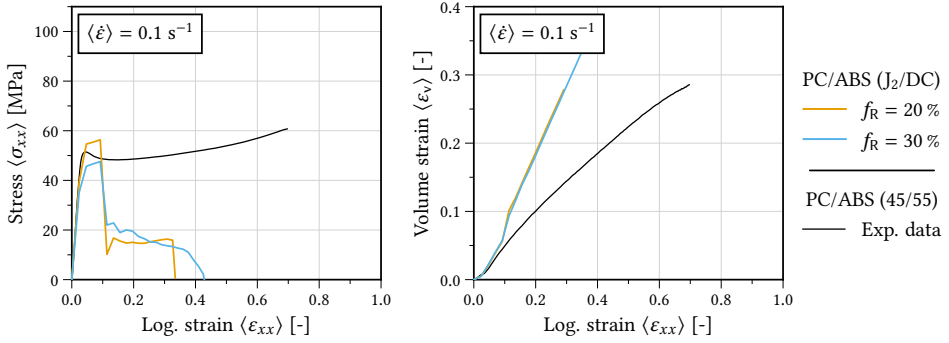


**Figure 10.24.** Uniaxial stress-strain and volume strain response of PC/ABS (45/55) unit cell models with the DC model in the ABS phase at a macroscopic strain rate  $\langle \dot{\epsilon} \rangle = 0.1 \text{ s}^{-1}$ .

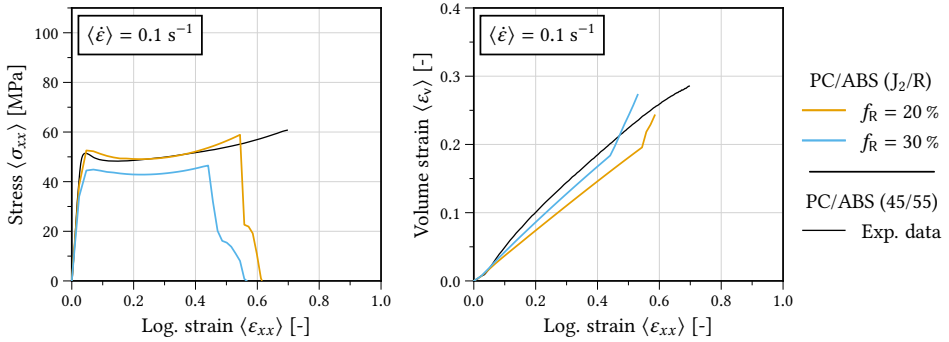


**Figure 10.25.** Uniaxial stress-strain and volume strain response of PC/ABS (45/55) unit cell models with the Raghava model in the ABS phase at a macroscopic strain rate  $\langle \dot{\epsilon} \rangle = 0.1 \text{ s}^{-1}$ .

the prediction of the failure behaviour was found to lack accuracy. This can be attributed to the inherent inability of the approach to account for distributed processes that impact the macroscopic plastic material response. Furthermore, the material response on the microscale, in particular when the failure behaviour is concerned, may significantly differ from the macroscopic behaviour. Thus, the assumption of equal bulk and phase behaviour represents another uncertainty and possible source of error.

### 10.4.5. Results - specific work of fracture

To investigate the unit cell models' response in load cases causing a higher stress triaxiality, simulations constrained as outlined in Sec. 10.3.2 were carried out. The resulting macroscopic stress states proved to be of a higher stress triaxiality. Figure 10.26 shows the overall stress triaxiality for a BCC unit cell using the DC model for ABS whereas Fig. 10.27 illustrates the same for the Raghava model in the ABS phase.

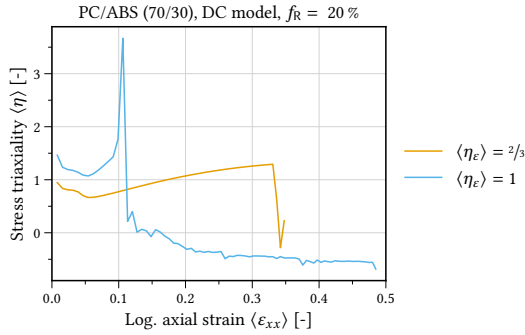


**Figure 10.26.:** Macroscopic stress triaxiality  $\eta$  for two values of the overall strain triaxiality  $\langle\eta_\epsilon\rangle$  of PC/ABS (70/30) BCC unit cell model using the DC model with a rubber content of  $f_R = 20\%$  in the ABS phase.

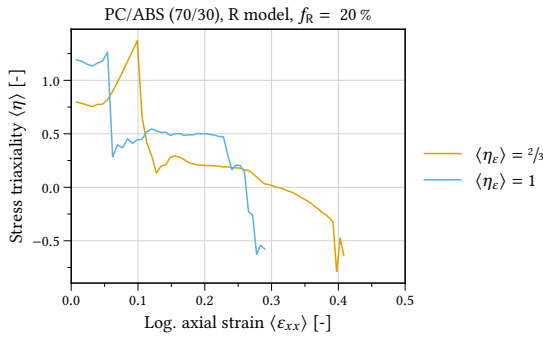


**Figure 10.27.:** Macroscopic stress triaxiality  $\eta$  for two values of the overall strain triaxiality  $\langle\eta_\epsilon\rangle$  of PC/ABS (70/30) BCC unit cell model using the Raghava model with a rubber content of  $f_R = 20\%$  in the ABS phase.

Since the loading situations specified by  $\langle\eta_\epsilon\rangle$  were selected with impact scenarios in mind, the macroscopic strain rate was set to  $\langle\dot{\epsilon}\rangle = 1000 \text{ s}^{-1}$ . Through the systematic variation of the key blend parameters (Sec. 10.4), their impact on the work of fracture and possible synergistic effects as well as optimum compositions were the aim of this numerical study. The specific work of fracture was of particular interest as a measure to qualitatively assess the dependence of the materials' toughness on composition and thus enable a comparison with results reported in the literature (Sec. 3.3).

The total work of external forces  $W^{\text{ext}}$  done on a unit cell over the course of a deformation is given by

$$W^{\text{ext}} = \int_{t_0}^{t_1} \left( \iint_{\partial V_t} \mathbf{t} \cdot \dot{\mathbf{u}} \, da \right) dt \quad (10.5)$$



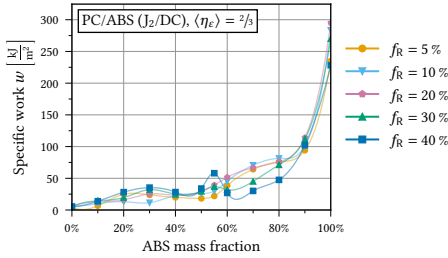


**Figure 10.28.:** Specific work of fracture for PC/ABS ( $J_2/DC$ ) unit cell models subjected to  $\langle \eta_\varepsilon \rangle = 2/3$  depending on the ABS mass fraction for five values of the rubber volume fraction  $f_R$ .

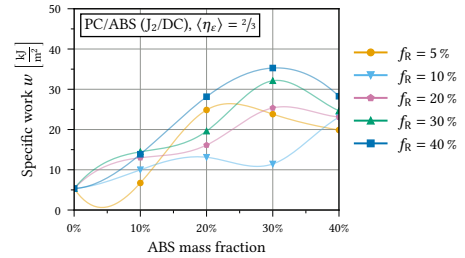


**Figure 10.29.:** Specific work of fracture for PC/ABS ( $J_2/DC$ ) unit cell models subjected to  $\langle \eta_\varepsilon \rangle = 2/3$  for ABS mass fractions up to 40% and five values of the rubber volume fraction  $f_R$ .

where  $t_0$  and  $t_1$  denote the beginning and end of the deformation, respectively,  $\partial V_t$  is the time-dependent unit cell surface,  $\mathbf{t}$  is the (macroscopic) stress vector, and  $\dot{\mathbf{u}} = (\dot{u}_x, \dot{u}_y, \dot{u}_z)^T$  are the velocities of the plane unit cell surfaces (Fig. 10.4). The specific work of fracture  $w$  is obtained by relating the total work of external forces (Eq. (10.5)) to the initial cross section  $A_0$  in the  $yz$ -plane perpendicular to the main loading direction as given by

$$w = \frac{W^{\text{ext}}}{A_0}. \quad (10.6)$$

#### 10.4.5.1. Load case $\langle \eta_\varepsilon \rangle = 2/3$

Figure 10.28 shows the dependency of the specific work of fracture on blend composition for the PC/ABS ( $J_2/DC$ ) unit cell models subjected to a macroscopic loading characterised by  $\langle \eta_\varepsilon \rangle = 2/3$ . Despite the higher overall stress triaxiality, the principal stress direction at craze initiation, i.e. the craze normal direction, was found to coincide with the  $x$ -direction throughout the whole ABS phase (Fig. 10.15). Considering the limited kinematics of the DC model (Sec. 10.4.4), the specific work obtained for all unit cell models where ABS acted as a co-continuous or matrix phase is excluded from the analysis below. Only those compositions where PC acted as a matrix with ABS particles embedded are considered (Fig. 10.29). In these cases, regarding the PC/ABS ( $J_2/DC$ ) unit cell models, the highest rubber content considered ( $f_R = 40\%$ ) yielded the overall highest specific work of fracture (Fig. 10.29).

This is a consequence of the DC model's decreasing yield stress for higher rubber contents (Fig. 10.9) which, in conjunction with the elastic response in directions perpendicular to the craze normal direction, led to a lower hydrostatic stress in the matrix. Thus, final failure took place at higher macroscopic overall strains simultaneously resulting in a higher specific work of fracture. Yet, it was not generally the case that with an increasing rubber volume fraction the specific work of fracture increased as well. Regarding the PC/ABS (80/20) blend, a rubber content of 5% resulted in the second highest work of fracture (Fig. 10.29).

The initial yield stress for the calibrated DC model with a rubber content of 5 % amounted to 72.7 MPa and therefore just exceeded the initial yield stress of the PC phase of  $\sigma_{0,PC} = 72.2$  MPa in this case. Regarding the PC/ABS (80/20) blend, this initiated failure in the matrix around the particles' equator plane (Fig. 10.37a). The other rubber volume fractions, for which the ABS phase entered the plastic domain before the PC phase, exhibited different failure patterns (Fig. 10.37b and Fig. 10.37c). The failure pattern shown in Fig. 10.37b was characteristic of PC/ABS ( $J_2/DC$ ) BCC unit cell models featuring rubber volume fractions between 10 % and 30 % and comprising of one crack through the unit cell's  $yz$ -centre plane as well as subsequent matrix particle delamination.

Since the distribution of craze normal direction was identical to that under macroscopic uniaxial tension, the DC model's response was also identical. Hence, the same implications apply for the material response in the  $yz$ -plane, being elastic over the whole course of the deformation, as in the case of uniaxial tension. The highest rubber volume fraction of 40 % caused critical hydrostatic stress states in the PC matrix only for deformations larger than the stiffer ABS grades with lower rubber contents (Fig. 10.37). Therefore, for a rubber content of 40 %, the failure patterns deviated from those obtained with the other rubber contents and tended to exhibit also intra-particle failure rather than just delamination. The reduced proneness towards delamination, i.e. better compatibility between the two phases, seems key for the overall higher values for the specific work of fracture found for a rubber volume fraction of 40 %.

The PC/ABS ( $J_2/R$ ) unit cell models yielded lower values for the specific work of fracture than the PC/ABS ( $J_2/DC$ ) unit cells (Fig. 10.31). Yet, the PC/ABS ( $J_2/R$ ) BCC unit cells with an ABS matrix also exhibited the highest specific work of fracture (Fig. 10.31). This finding does not reflect those in the literature regarding the composition dependence of fracture toughness (Sec. 3.3). Therefore, the Raghava model possibly underestimates the susceptibility of ABS to higher stress triaxialities. This finding is similar to what was found for the applicability of this model to PC/ABS (Sec. 9.4). Also, the transition to the IPP unit cell model from both bounds regarding the ABS mass fraction led to a significant drop in fracture toughness for all rubber contents (Fig. 10.31). This observation indicates that the change of the specific work in these cases depends rather on the transition from the BCC to the IPP unit cell model than the different compositions. Failure in all IPP unit cell models was found to begin in the PC phase with subsequent delamination. The remaining intact ABS phase afterwards failed at, or close to, its smallest  $yz$ -cross section (Fig. 10.30).

As a consequence, also for the PC/ABS ( $J_2/R$ ) unit cell models, only ABS mass fractions up to 40 % and thus BCC unit cells where PC acted as the matrix are regarded hereafter (Fig. 10.32). For corresponding rubber volume fractions, the specific work of fracture obtained with the Raghava model in the ABS phase was consistently lower than with the DC model (Figs. 10.32 and 10.29). Only for a rubber volume fraction of 10 % were the values for the specific work for both models approximately similar. Restricting the analysis to just the PC/ABS ( $J_2/R$ ) unit cell models and rubber contents greater than 10 %,

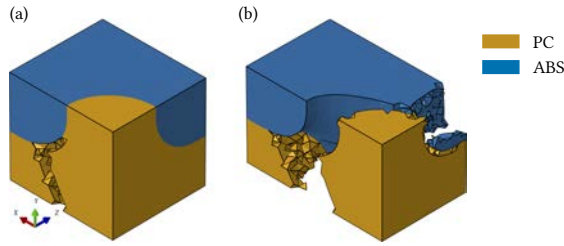


**Figure 10.30.** Failure pattern of PC/ABS (45/55) unit cell with the Raghava model in the ABS phase ( $f_R = 30\%$ ) subjected to  $\langle \eta_e \rangle = 2/3$  in the stages of (a) failure initiation and (b) final failure.

the general trend was an increase in specific work with an increasing ABS mass fraction (Fig. 10.32).

With regard to a rubber content of 5%, even a slight decrease in specific work was found for the ABS mass fractions of 10% and 20%. The failure pattern of all PC/ABS ( $J_2/R$ ) BCC unit cells with a rubber volume fraction of 5% was similar in the sense that delamination and matrix failure in the  $yz$ -centre plane emerged virtually simultaneously (Fig. 10.38a). Regarding PC/ABS (80/20) with  $f_R = 40\%$ , failure began in the matrix with subsequent intra-particle failure (Fig. 10.38c). The same was found for the other PC/ABS ratios with a PC matrix and ABS particles. A crack path through the particle as opposed to just along the phase boundary was also found in the case of a rubber volume fraction of 20% (Fig. 10.38c). For lower rubber volume fractions this did not occur.

Apart from the rubber volume fraction of 10%, the PC/ABS ( $J_2/R$ ) unit cell models exhibited a local maximum with regard to the specific work for an ABS mass fraction of 30%. Disregarding  $f_R = 5\%$ , it was only the case for PC/ABS (70/30) where noteworthy differences were found for a variation of  $f_R$  between 10% and 30% (Fig. 10.32). In contrast to the findings for the PC/ABS ( $J_2/DC$ ) unit cells, a rubber volume fraction of 40% only consistently outperformed a rubber volume fraction of 5% with respect to the specific work in the PC/ABS ( $J_2/R$ ) unit cells (Fig. 10.32). Solely for the PC/ABS (70/30) blend, a rubber volume fraction of  $f_R = 10\%$  yielded worse results than  $f_R = 40\%$ . Based on these findings, the optimum rubber volume fraction can be assumed to be in the intermediate range between 20% and 30%.

In the case of the PC/ABS (70/30) composition and hence overall for the range considered, the optimum rubber volume fraction maximising the specific work amounted to 30% resulting in roughly twice the specific work than  $f_R = 5\%$  (Fig. 10.32). Regarding the impact of an increase of the rubber content in the ABS phase with the Raghava model, generally a higher rubber content resulted in a larger displacement until failure initiation in the matrix due to its lower yield stress and overall stress response. Therefore, final failure was delayed due to the failure strain also increasing with the rubber content (Fig. 10.10). Hence, the failure characteristic with an increasing rubber content transitioned from brittle to more ductile. However, a larger overall deformation did not consistently yield a higher specific work of fracture. This can be attributed to the load bearing capacity of

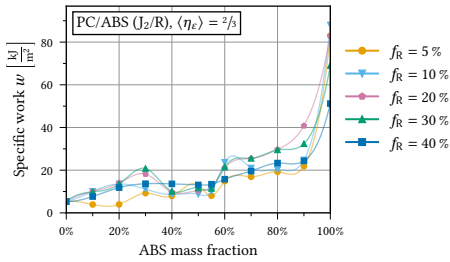


**Figure 10.31.:** Specific work of fracture for PC/ABS ( $J_2/R$ ) unit cell models subjected to  $\langle \eta_\epsilon \rangle = 2/3$  depending on the ABS mass fraction for five values of the rubber volume fraction  $f_R$ .

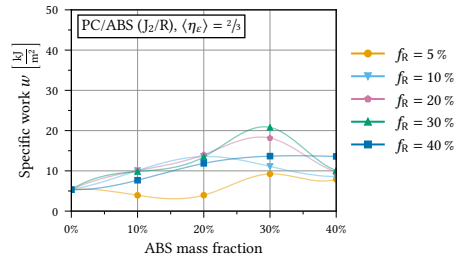


**Figure 10.32.:** Specific work of fracture for PC/ABS ( $J_2/R$ ) unit cell models subjected to  $\langle \eta_\epsilon \rangle = 2/3$  for ABS mass fractions up to 40% and five values of the rubber volume fraction  $f_R$ .

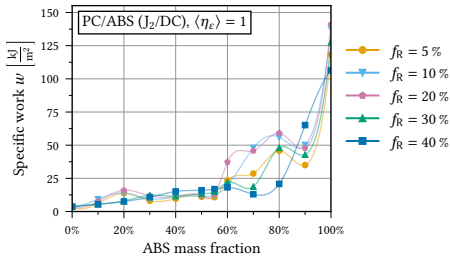


**Figure 10.33.:** Specific work of fracture for PC/ABS ( $J_2/DC$ ) unit cell models subjected to  $\langle \eta_\epsilon \rangle = 1$  depending on the ABS mass fraction for five values of the rubber volume fraction  $f_R$ .

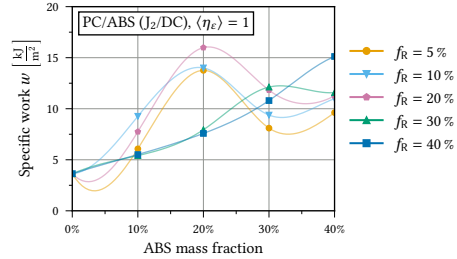


**Figure 10.34.:** Specific work of fracture for PC/ABS ( $J_2/DC$ ) unit cell models subjected to  $\langle \eta_\epsilon \rangle = 1$  for ABS mass fractions up to 40% and five values of the rubber volume fraction  $f_R$ .

ABS decreasing for an increasing rubber volume fraction (Fig. 10.10). With an increasing particle volume fraction, i.e. higher ABS mass fraction, the impact of the rubber content on the failure behaviour of the particles gains importance. Consequently, considering PC/ABS (70/30), a rubber volume fraction of  $f_R = 30\%$  represents the optimum between a large failure strain and load bearing capacity (Fig. 10.32).

With regard to the PC/ABS (80/20) and PC/ABS (90/10) blends, a certain compatibility between the matrix and particle seems beneficial, i.e. the particle yield stress should not exceed that of the matrix as is the case for  $f_R = 5\%$  (Fig. 10.32). If this prerequisite is met, the overall failure behaviour and specific work appears to be dominated by the failure of the PC matrix. Hence, a variation of the rubber volume fraction in ABS did not have a great impact on the macroscopic specific work (Fig. 10.32).

#### 10.4.6. Loading with $\langle \eta_\epsilon \rangle = 1$

The loading characterised by  $\langle \eta_\epsilon \rangle = 1$  generally led to a quicker rise of the hydrostatic stress in the whole unit cell. Therefore, the failure in the PC phase set in earlier, resulting

in lower values for the specific work of fracture compared to the load case of  $\langle \eta_\epsilon \rangle = 2/3$  (Figs. 10.33, 10.28, 10.35, and 10.31).

Comparing the two different constitutive models in the ABS phase with respect to the specific work, the DC model yielded higher results throughout the whole range of compositions considered (Figs. 10.33 and 10.35). This is once more a consequence of the material response to loadings perpendicular to the craze normal direction (Sec. 10.4.4). Regarding the loading characterised by  $\langle \eta_\epsilon \rangle = 1$ , the craze normal direction also coincided with the main macroscopic loading direction (Fig. 10.15). Thus, for the same reasons as for uniaxial tension and  $\langle \eta_\epsilon \rangle = 2/3$ , the following analysis is restricted to compositions with a PC matrix and ABS particles (Figs. 10.34 and 10.36).

Regarding the PC/ABS ( $J_2$ /DC) unit cells in the range of ABS mass fractions less than or equal to 30 %, a PC/ABS ratio of (80/20) was found most beneficial for rubber volume fractions up to 20 % (Fig. 10.34). For rubber volume fractions from 30 % up to 40 %, a virtually linear increase in specific work with an increasing ABS mass fraction was found (Fig. 10.34).

With the matrix properties being independent of a change in the rubber volume fraction, the overall high hydrostatic stress led to matrix failure for all compositions and thus also for the PC/ABS (80/20) blend (Fig. 10.40). For rubber volume fractions up to 10 %, the failure subsequently advanced along the phase boundary (Fig. 10.40a). With regard to greater rubber volume fractions, the particles exhibited better adherence to the matrix (Fig. 10.40b). Therefore, a more ductile response of the unit cells featuring intra-particle failure was found (Fig. 10.40b). Whereas first cracks formed in the equatorial planes of the particles for rubber volume fractions less than 20 %, they originated more towards the centre of the whole arrangement in the case of the rubber volume fractions of 30 % and 40 %. Therefore, a larger volume of remaining matrix material between the particles in the case of the lower rubber contents allowed for further load bearing while at the same time the overall hydrostatic stress was reduced.

Considering the PC/ABS (90/10) compositions, the onset of failure was found to be similar to that shown in Fig. 10.40a. Yet, for all rubber volume fractions, failure of the matrix in the equatorial plane of the matrix led to subsequent failure of the particle in the same plane. This result suggests that a particle volume fraction of 10 % is too little to significantly impact the failure behaviour of the surrounding matrix. In the case of the PC/ABS (70/30) blends, the unit cells generally cracked towards the unit cell  $yz$ -centre plane (Fig. 10.40c).

Regarding the specific work, PC/ABS ( $J_2$ /R) unit cells subjected to a macroscopic load characterised by  $\langle \eta_\epsilon \rangle = 1$  yielded similar results to the load case  $\langle \eta_\epsilon \rangle = 2/3$  in the sense that a rubber volume fraction of 5 % consistently performed worst (Fig. 10.36). Yet, the differences for an ABS mass fraction up to 20 % for all rubber contents were small and the overall results not remarkably better than neat PC (Fig. 10.36). Only for the PC/ABS (70/30) blend was a significant increase in specific work and differences between the different rubber volume fractions found (Fig. 10.36).

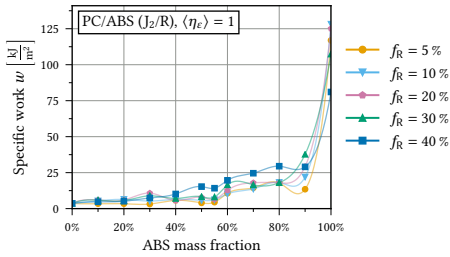


**Figure 10.35.:** Specific work of fracture for PC/ABS ( $J_2/R$ ) unit cell models subjected to  $\langle \eta_\varepsilon \rangle = 1$  depending on the ABS mass fraction for five values of the rubber volume fraction  $f_R$ .

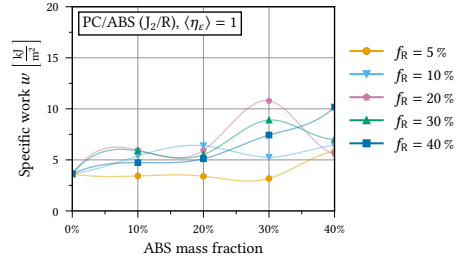


**Figure 10.36.:** Specific work of fracture for PC/ABS ( $J_2/R$ ) unit cell models subjected to  $\langle \eta_\varepsilon \rangle = 1$  for ABS mass fractions up to 40% and five values of the rubber volume fraction  $f_R$ .

An ABS mass fraction of 30% optimised the specific work in the case of the PC/ABS ( $J_2/R$ ) unit cells and  $\langle \eta_\varepsilon \rangle = 1$  (Fig. 10.36). The same was found with respect to  $\langle \eta_\varepsilon \rangle = 2/3$  (Fig. 10.32). Not considering a rubber volume fraction of 5%, this PC/ABS ratio also represented the only one where the rubber content had a significant impact (Fig. 10.36). Consequently, a rubber content of 20% resulted in the best performance regarding fracture toughness (Fig. 10.36). Whereas the unit cell models cracked in their  $yz$ -centre plane for rubber volume fractions of 5% and 10%, the onset of failure was located towards the equatorial plane of the particles for higher rubber contents (Fig. 10.41). Analogous to the PC/ABS ( $J_2/DC$ ) unit cells, this failure pattern proved to be more beneficial regarding the specific work. Once the unit cell models did not just crack in their centre planes, the load bearing capabilities of the ABS phase seemed crucial for the specific work. Therefore, a rubber volume fraction of 20% was found to be optimal, providing the greatest load bearing capability while simultaneously ensuring that overall failure did not originate in the unit cell's  $yz$ -centre plane.

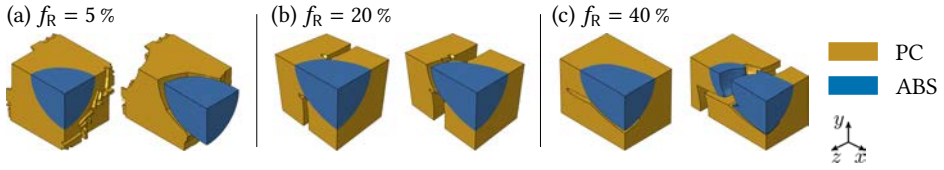


**Figure 10.37.:** Crack initiation and failure pattern of PC/ABS (80/20) BCC unit cell models subjected to  $\langle \eta_\epsilon \rangle = 2/3$  using the DC model in the ABS phase for three values of the rubber volume fraction  $f_R$ .

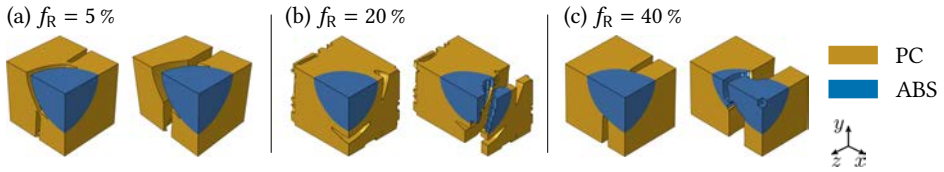


**Figure 10.38.:** Crack initiation and failure pattern of PC/ABS (80/20) BCC unit cell models subjected to  $\langle \eta_\epsilon \rangle = 2/3$  using the Raghava model in the ABS phase for three values of the rubber volume fraction  $f_R$ .

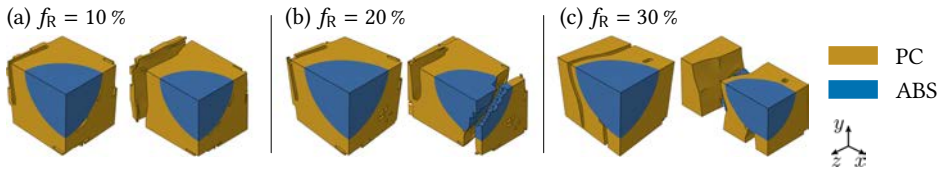


**Figure 10.39.:** Crack initiation and failure pattern of PC/ABS (70/30) BCC unit cell models subjected to  $\langle \eta_\epsilon \rangle = 2/3$  using the Raghava model in the ABS phase for three values of the rubber volume fraction  $f_R$ .

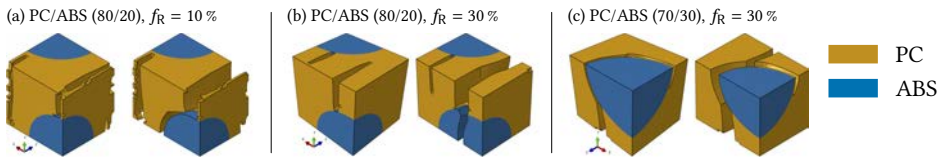


**Figure 10.40.:** Crack initiation and failure pattern of BCC unit cell models subjected to  $\langle \eta_\epsilon \rangle = 1$  using the DC model in the ABS phase for three values of the rubber volume fraction  $f_R$ .

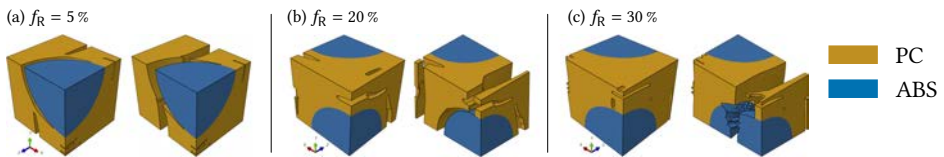


**Figure 10.41.:** Crack initiation and failure pattern of PC/ABS (70/30) BCC unit cell models subjected to  $\langle \eta_\epsilon \rangle = 1$  using the Raghava model in the ABS phase for three values of the rubber volume fraction  $f_R$ .

### 10.4.7. Conclusions

In simulations of uniaxial tensile tests, the DC model was found to only yield a qualitatively appropriate response in blends with ABS particles in a PC matrix due to its restricted kinematics (Sec. 10.4.4). For the two load cases of higher overall strain triaxiality, the local maximum principal stress direction at craze initiation, i.e. the craze normal direction, also coincided with the  $x$ -direction, as was the case for uniaxial tension (Fig. 10.15). Therefore, the material response of the particles with the DC model did not change for the different global loading situations (Fig. 10.13). This can be considered the main reason for the significantly higher overall values regarding the specific work of fracture with the DC model over those obtained using the Raghava model. As such, the unit cell response using the DC model must be questioned as a whole.

If the Raghava model was used in the ABS phase, the PC/ABS (70/30) blend with a rubber volume fraction of 30 % in the ABS phase proved to be most beneficial regarding the specific work of fracture for a loading characterised by  $\langle \eta_\epsilon \rangle = 2/3$  (Fig. 10.32). The same PC/ABS ratio proved the most beneficial in the case of  $\langle \eta_\epsilon \rangle = 1$ , but a rubber content of 20 % resulted in the highest specific work (Fig. 10.36). These findings are in qualitative agreement with the experimental studies of Greco [42] and Lombardo, Keskkula, and Paul [76] (Sec. 3.3). The non-monotonic dependence of the failure behaviour on the PC/ABS ratio and the rubber volume fraction in the ABS phase was qualitatively captured in the regarded range of ABS mass fraction with this BCC unit cell approach.

Whereas the PC/ABS ( $J_2/R$ ) IPP unit cell models subjected to uniaxial tension were found to reasonably well approximate the experiments, this arrangement's ability to reproduce the material response under higher strain and stress triaxialities has to be questioned. The transition to the IPP unit cell from both boundaries with respect to the ABS mass fraction resulted in approximately equally low values for the specific work for all compositions in the case of  $\langle \eta_\epsilon \rangle = 2/3$  (Fig. 10.31). Regarding this finding, it is in approximate agreement with experimental findings from Greco [42] for certain rubber volume fractions. However, taking into account that simulations with all rubber volume fractions performed badly, this unit cell arrangement with the models used appears not suited to reproduce the experimental results. Furthermore, for all models and load cases in the approach presented, the neat ABS material and unit cell models with ABS acting as the matrix phase consistently outperformed the other phase arrangements. This finding is in stark contrast to the studies found in the literature (Sec. 3.3). Therefore, not only the DC model overestimates the specific work but also the Raghava model may not sufficiently take into account the impact of a higher stress triaxiality on the model response.

The approach presented underlines the non-monotonic impact of the key blend parameters on the specific work of fracture. A variation of the rubber volume fraction for identical PC/ABS ratios was found to significantly alter the failure behaviour of the complete unit cell. As a result, optimum rubber volume fractions for a fixed PC/ABS ratio were found that roughly doubled the specific work in some cases over the compositions with the least beneficial rubber contents. However, particularly with regard to the DC model, the



shortcomings of this constitutive model to appropriately take into account the impact of the stress triaxiality on the material response became obvious.

## 10.5. Impact of plastic deformation mechanisms

The results analysed in Sec. 10.4 illustrate the shortcomings of the DC model when applied to ABS in triaxial loading situations. These shortcomings are a result of attributing all plastic deformation to distributed crazing and simultaneously neglecting the damaging impact of loadings perpendicular to the craze normal direction (Sec. 10.4.4). In an attempt to overcome these disadvantages, in Sec. 8.3.5 the  $J_2$ -DC model is introduced. This model considers the plastic deformation mechanisms of shear yielding and distributed crazing. In the following, the behaviour of this model is analysed with emphasis on its impact on the unit cell response when being employed in the ABS phase. Previously, a study of the model's behaviour with regard to the reproduction of the plastic zone shape in SENT tests on ABS was carried out by Ruge [90].

### 10.5.1. $J_2$ -DC model calibration

The  $J_2$ -DC model was calibrated using the same data and procedure that was used in the case of the DC and Raghava models (Sec. 10.4.2). As introduced in Eq. (8.49), the ratio of shear yielding to distributed crazing  $\alpha$  is taken to depend on the stress triaxiality  $\eta$  and a fit parameter  $\beta$ . The fit parameter  $\beta$  is calibrated such that under uniaxial tension the volume strain response is reproduced (Fig. 10.43). The complete set of material parameters to the material model is listed in Tab. D.3. Figure 10.42 shows the resulting  $\alpha$  as a function of the stress triaxiality  $\eta$ . Subjected to uniaxial tension, the calibrated model attributes 28 % of the total plastic deformation to shear yielding (Fig. 10.42). Similar to the DC model, the  $J_2$ -DC model's stress response varies for different rubber volume fractions (Fig. 10.44). Because of the addition of the  $J_2$  mechanism, the volume strain response also exhibits a slight dependency on the rubber content (Fig. 10.44).

Considering higher stress triaxialities, the stress response in the tensile direction only varies regarding the failure strain (Fig. 10.45). However, the volume strain responses for the higher stress triaxialities  $\eta = 1$  and  $\eta = 3$  significantly differ from the dilation under uniaxial tension (Fig. 10.45). Yet, for both elevated stress triaxialities regarded, the model's volume strain response is almost identical (Fig. 10.45). This is a consequence of the ansatz made for  $\alpha$ . This ansatz predicts almost equal values of  $\alpha$  for both  $\eta = 1$  and  $\eta = 3$ , attributing virtually all plastic deformation to distributed crazing (Fig. 10.42). Additional experimental data with a known stress triaxiality would allow for a more sophisticated ansatz and improved description of the transition from shear yielding to distributed crazing depending on the stress triaxiality. However, this approach is limited to data from uniaxial tensile tests and should be understood to be an initial guess.

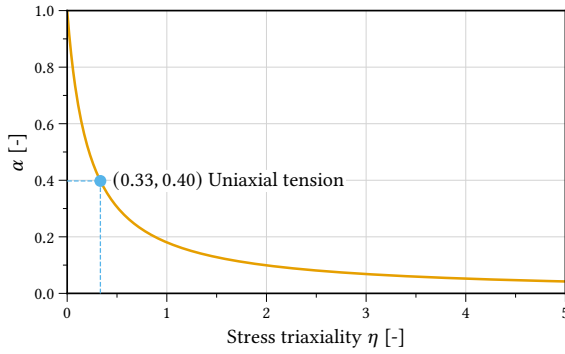


**Figure 10.42.:** Dependence of the deformation mechanism ratio  $\alpha$  on the stress triaxiality  $\eta$

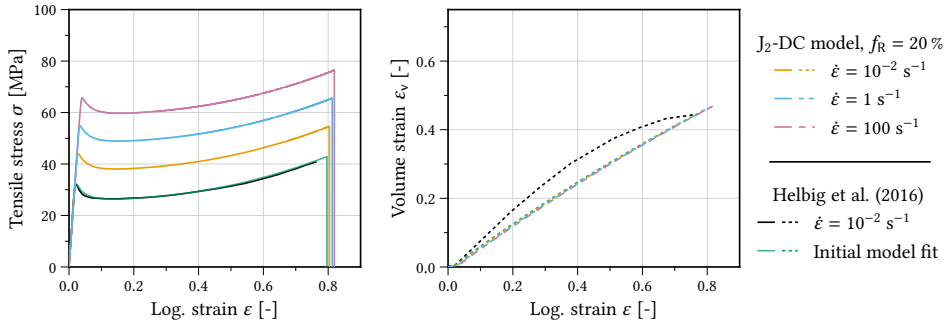


**Figure 10.43.:** Stress-strain and volume strain response of the  $J_2$ -DC model ( $f_R = 20\%$ ) subjected to uniaxial tension for three values of the strain rate with the initial fit for the hardening behaviour from Helbig et al. [51] and the final fit considering the strain rate dependency (Sec. 10.4.2).

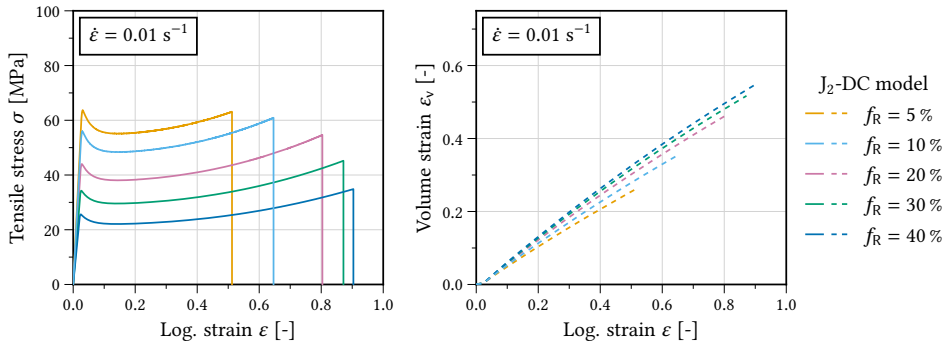


**Figure 10.44.:** Stress-strain and volume strain response under uniaxial tension of the  $J_2$ -DC model for five values of the rubber volume fraction  $f_R$ .

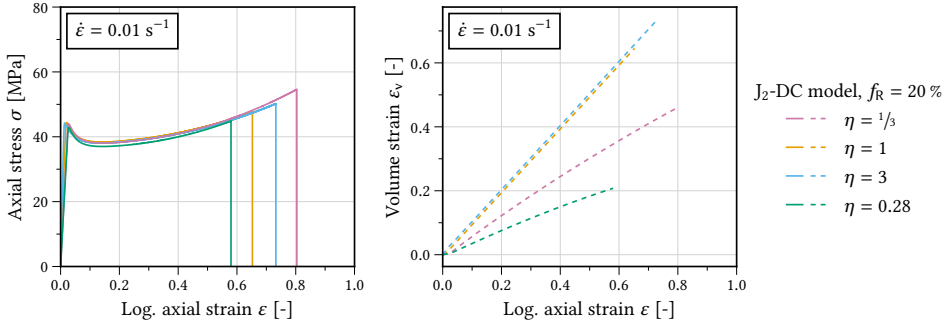


**Figure 10.45.:** Stress-strain and volume strain response of the  $J_2$ -DC model ( $f_R = 20\%$ ) for three different values of the stress triaxiality  $\eta$ .

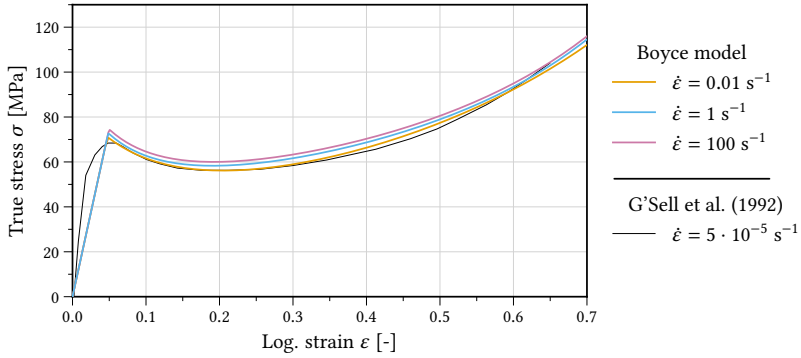


**Figure 10.46.:** Uniaxial tensile response of the calibrated Boyce plasticity model for three values of the strain rate.

## 10.5.2. Numerical study - deformation behaviour

During the simulations in this study, the ABS phase was modelled using the  $J_2$ -DC model. Regarding the PC phase, two different models were considered with different objectives. To gain insight into the impact of the  $J_2$ -DC model on the unit cell response, and for comparison with the results previously presented in Sec. 10.4, the  $J_2$ -plasticity was selected. Following the assignment of the constitutive models to the phases, these unit cells are referred to as PC/ABS ( $J_2/J_2$ -DC).

With the aim of improving the representation of the material response of the PC phase, i.e. by taking into account kinematic hardening, the Boyce model (Sec. 8.2.2) was used in an approach referred to as PC/ABS (Boyce/ $J_2$ -DC). The Boyce model was also calibrated following the procedure outlined in Sec. 10.4.2. The resulting set of material parameters is given in Tab. D.4. The calibrated model's response to uniaxial tension is shown in Fig. 10.46.

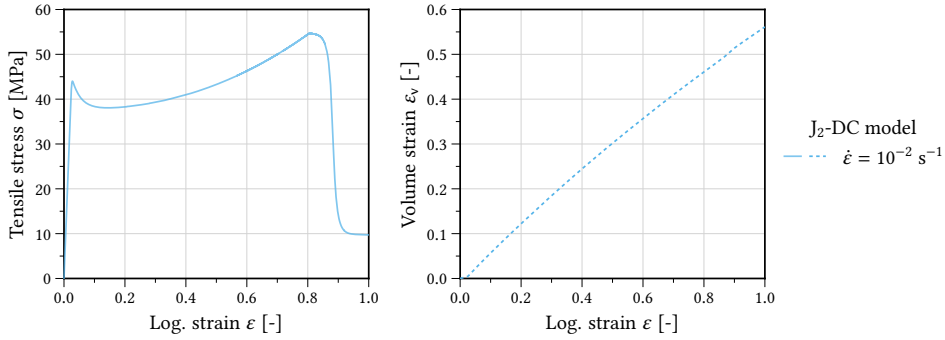


**Figure 10.47.:** Stress-strain and volume strain response under uniaxial tension of the J<sub>2</sub>-DC model ( $f_R = 20\%$ ) with failure behaviour modelled using the logistic function.

### 10.5.2.1. Numerical issues

Initially, local failure in the ABS phase was modelled using element deletion. However, in unit cell simulations with Abaqus/Explicit the J<sub>2</sub>-DC material model proved to be sensitive to element erosion causing an abortion of the simulations due to distorted elements. The reasons for this behaviour could not be ascertained since the independent J<sub>2</sub> and DC plasticity models did not suffer from numerical instabilities.

In order to model a pseudo-failure behaviour through a stress drop, the logistic function

$$\ell(x) = \frac{1}{1 - \exp(-x)} \quad (10.7)$$

was used to describe the yield stress after failure  $\hat{k}$  as specified by

$$\hat{k}(\epsilon^P) = -k(\epsilon_{crit}^P) \ell(-c_1(\epsilon^P - c_0)) \quad \forall \quad \epsilon^P > \epsilon_{crit}^P, \quad (10.8)$$

where  $\epsilon_{crit}^P$  denotes the “failure” strain,  $c_1$  represents the logistic decrease rate, and  $c_0$  is the resulting curve’s midpoint (Fig. 10.47). However, a certain load bearing capacity remains using this approach (Fig. 10.47). Therefore, the analyses with the J<sub>2</sub>-DC model were confined to BCC unit cell models with PC matrix phase under uniaxial tension to at least assess the model’s impact on the unit cells’ deformation behaviour. Analogous to the results presented in Sec. 10.4.4, only rubber volume fractions of 20 % and 30 % were considered.

## 10.5.3. Results - PC/ABS (J<sub>2</sub>/J<sub>2</sub>-DC)

### 10.5.3.1. PC/ABS (70/30)

The macroscopic stress and volume strain response of the PC/ABS (70/30) BCC unit cell models up to final failure of the PC matrix is shown in Fig. 10.48. For both rubber

volume fractions, the PC/ABS ( $J_2/J_2$ -DC) unit cells captured the stress-strain behaviour in a qualitative sense, neglecting the overestimation of the final failure strain (Fig. 10.48). This overestimation of the failure strain in the case of the PC/ABS ( $J_2/J_2$ -DC) unit cells is a result of the residual, i.e. post failure, load bearing capacities of the ABS particles (Fig. 10.48).

For a rubber volume fraction of 20 %, the onset of yield and thus also the stress level during the softening afterwards was only slightly underestimated (Fig. 10.48). Regarding a rubber content of 30 %, the overall stress level was lower because of the generally lower stress response of the  $J_2$ -DC model (Fig. 10.44).

Considering the overall volume strain, the PC/ABS ( $J_2/J_2$ -DC) unit cell models predicted a far lower volume strain response than what was found in the corresponding experiments (Fig. 10.48). In this regard, the overall response using the DC model in the ABS phase approximated the experimental data more accurately (Fig. 10.11). Comparing the PC/ABS ( $J_2/J_2$ -DC) unit cells to those using the Raghava model in the ABS phase, the stress response up to failure of the particles (represented by the stress drop during rehardening) was quite similar (Fig. 10.12). However, the particles in the PC/ABS ( $J_2/J_2$ -DC) arrangement failed at a lower overall axial strain of  $\epsilon \approx 0.5$  (Fig. 10.48). As a result, the rehardening behaviour was not as severely overestimated by the PC/ABS ( $J_2/J_2$ -DC) unit cells.

Despite calibrating the volume strain response of the  $J_2$ -DC model from the experimental results, the volume strain response of the PC/ABS ( $J_2/J_2$ -DC) unit cells yielded the worst approximation of the overall volume strain response of the three models regarded (Figs. 10.48, 10.11, and 10.12). Figure 10.51 shows contours of the stress triaxiality  $\eta$  and the distribution of the model parameter  $\alpha$  on the PC/ABS (70/30) unit cell featuring a rubber volume fraction of 20 %. Since the stress triaxiality in the particles in this case was found to be virtually homogeneous, the same applied to the distribution of  $\alpha$  (Fig. 10.51). With the stress triaxiality of  $\eta \approx 0.27$  being lower than under uniaxial tension, the model attributed a greater fraction of the plastic deformation to shear yielding ( $\alpha \approx 0.44$ ). Hence, for a stress triaxiality of  $\eta = 0.28$ , the volume strain of the  $J_2$ -DC model is considerably lower than under uniaxial tension (Fig. 10.45). The DC model's overestimation of the volume strain under uniaxial tension yields a good reproduction of the overall volume strain in the case of the PC/ABS ( $J_2/DC$ ) unit cell models of PC/ABS (70/30) (Fig. 10.48). The reduced volume strain of the  $J_2$ -DC model due to the lower stress triaxiality hence yields a significant underestimation of the dilation regarding the PC/ABS (70/30) BCC unit cell model.

### 10.5.3.2. PC/ABS (60/40)

Figure 10.49 shows the macroscopic stress and volume strain response of the PC/ABS (60/40) IPP unit cell models in comparison to the experimental data. The simulation results are shown until final failure of both phases where failure of the ABS phase using the  $J_2$ -DC

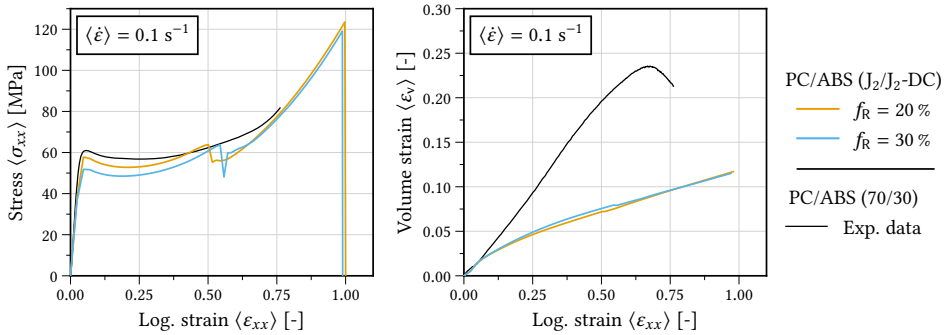


**Figure 10.48.:** Uniaxial stress-strain and volume strain response of PC/ABS (70/30) unit cell models with the  $J_2$ -DC model in the ABS phase at a macroscopic strain rate of  $\langle \dot{\epsilon} \rangle = 0.1 \text{ s}^{-1}$ .

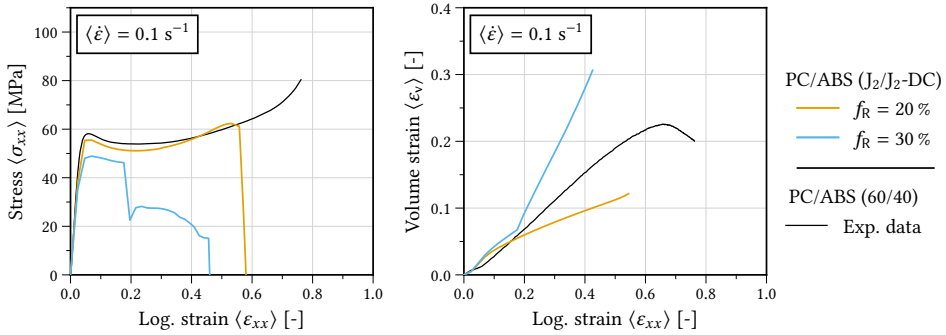


**Figure 10.49.:** Uniaxial stress-strain and volume strain response of PC/ABS (60/40) unit cell models with the  $J_2$ -DC model in the ABS phase at a macroscopic strain rate  $\langle \dot{\epsilon} \rangle = 0.1 \text{ s}^{-1}$ .

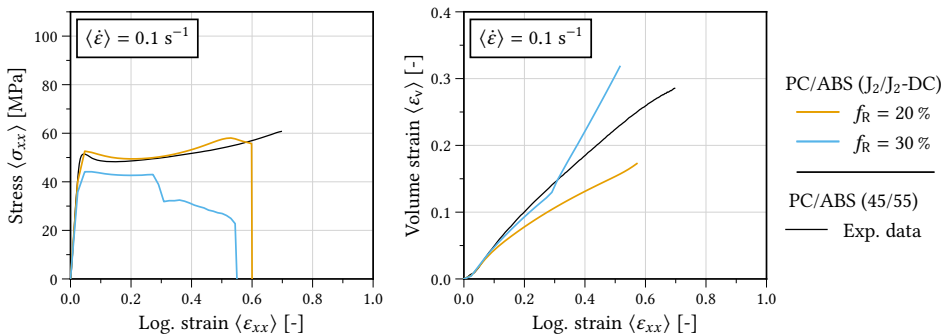


**Figure 10.50.:** Uniaxial stress-strain and volume strain response of PC/ABS (45/55) unit cell models with the  $J_2$ -DC model in the ABS phase at a macroscopic strain rate  $\langle \dot{\epsilon} \rangle = 0.1 \text{ s}^{-1}$ .

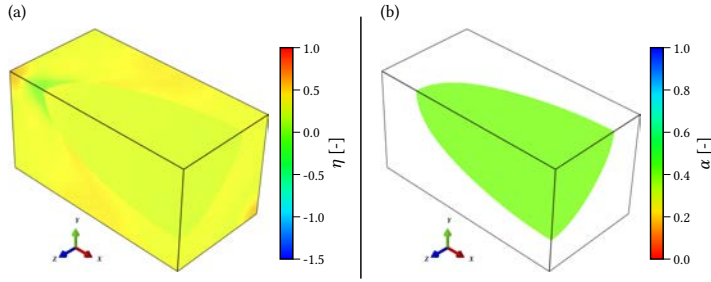


**Figure 10.51.:** Contours of (a) the stress triaxiality  $\eta$  and (b) the model quantity  $\alpha$  on PC/ABS (70/30) unit cell ( $f_R = 20\%$ ).

model was defined as the state where the yield stress had dropped over the entire cross section of this phase.

For a rubber volume fraction of 20 %, the stress-strain response was qualitatively and quantitatively well reproduced regarding the onset of yield and the early stages of the progressive rehardening (Fig. 10.49). Local failure arose in the ABS phase, represented in the overall stress response through the decline upon  $\varepsilon \approx 0.5$ . The subsequent brittle failure of the PC phase denoted final failure of the model.

The unit cell model with a rubber volume fraction of 30 % rubber in the ABS phase underestimated the initial yield stress compared to the experiments and failed even before the stress response reached the stage of progressive rehardening (Fig. 10.49). As opposed to the unit cell model with  $f_R = 20\%$ , failure began in the PC phase causing the stress drop at  $\varepsilon \approx 0.2$ . Afterwards, the remaining cross section of the ABS phase passed through the stages of rehardening and then failure. The differences in the stress-strain response between the two simulations, only differing regarding their rubber volume fraction in ABS, once more emphasises the impact of this blend parameter on the overall material response.

The volume strain response of both PC/ABS (60/40) IPP unit cell models is shown in Fig. 10.49 and is not in good agreement with the experimental findings. For a rubber volume fraction of 20 % in the ABS phase, the dilation was slightly overestimated for values of the overall axial strain up to approximately 0.15 (Fig. 10.49). Afterwards, the volume increase predicted by the unit cell models was considerably lower than the experimental findings (Fig. 10.49).

The declining slope of the volume strain for both rubber contents is a result of the dilation behaviour of the  $J_2$ -DC model being sensitive towards changes of  $\alpha$  and the stress triaxiality  $\eta$ , respectively (Figs. 10.45 and 10.42). The contours of  $\alpha$  for an overall strain of  $\langle \varepsilon_{xx} \rangle = 0.07$  and  $\langle \varepsilon_{xx} \rangle = 0.29$  are shown in Fig. 10.52. The transition towards higher values of  $\alpha$  is associated with a higher fraction of the plastically incompressible deformation mechanism of shear yielding and thus a lower overall volume strain of the model.

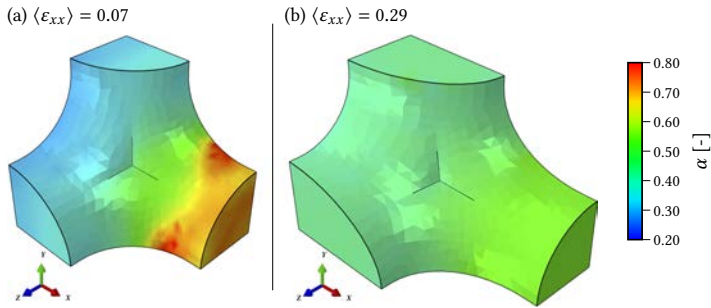


**Figure 10.52.:** Contours of  $\alpha$  in the ABS phase of the PC/ABS (60/40) unit cell model  $f_R = 20\%$  for overall strains of (a)  $\langle \epsilon_{xx} \rangle = 0.07$  and (b)  $\langle \epsilon_{xx} \rangle = 0.29$  where the PC phase has been removed for better visibility.

For the higher rubber volume fraction of 30%, an overestimation of the volume strain was found until the onset of failure. Yet, after the early failure of the PC phase, the post critical behaviour of the  $J_2$ -DC model (Fig. 10.47) caused an unrealistically pronounced increase in volume strain in conjunction with the delamination (Fig. 10.49).

Overall, the PC/ABS ( $J_2/J_2$ -DC) IPP unit cell with a rubber volume fraction of 20% in the ABS phase blend yielded a qualitatively reasonable approximation of the stress-strain and volume strain response of the experimentally investigated PC/ABS (60/40) blend. Considering the stress response only, the initial yield stress and the subsequent plastic deformation was also quantitatively well reproduced taking into account the uncertainties not only with regard to the modelling approach but also the experimental results (Sec. 6.1.1). Nonetheless, the Raghava model equally well approximated the uniaxial stress response and better reproduced the experimentally observed volume strain (Sec. 10.4.4 and Fig. 10.19).

### 10.5.3.3. PC/ABS (45/55)

The deformation behaviour of the PC/ABS (45/55) IPP unit cell models with the  $J_2$ -DC model in the ABS phase for rubber volume fractions of 20% and 30% is shown in Fig. 10.50. The observations for the PC/ABS (60/40) IPP unit cells with the same constitutive models also apply to the PC/ABS (45/55) unit cell models. Similarly, the Raghava model yielded quite similar results regarding the stress response while performing better with respect to the dilation behaviour (Figs. 10.50 and 10.25).

## 10.5.4. Results - PC/ABS (Boyce/ $J_2$ -DC)

To assess the impact of the material modelling of the PC phase, unit cell model simulations with the Boyce model employed in this phase were carried out with the  $J_2$ -DC model being used in the ABS phase. Figures 10.53, 10.54, and 10.55 show the PC/ABS (Boyce/ $J_2$ -DC)



unit cells' responses for the three different PC/ABS fractions and two different rubber contents.

Regarding the PC/ABS (70/30) blends, the behaviour of all unit cells until the failure of the particles was virtually identical (Figs. 10.48 and 10.53). However, the PC/ABS (Boyce/ $J_2$ -DC) unit cells exhibited a smaller overall failure strain. Note that both the  $J_2$  and the Boyce model were calibrated from the same experimental data for strains up to  $\varepsilon = 0.7$ . Thus, the response of both models is virtually equal regarding this range (Figs. 10.8 and 10.46). However, for larger strains, the Boyce model predicts a more progressive rehardening (Fig. 10.56). As a consequence, the local critical hydrostatic stress was exceeded for lower values of the macroscopic strain in the PC/ABS (Boyce/ $J_2$ -DC) unit cell models.

In the case of the IPP unit cell models, the Boyce model in the PC phase in conjunction with a rubber content of 20 % yielded results like the PC/ABS ( $J_2$ / $J_2$ -DC) unit cell models. Differences occurred regarding the higher rubber volume fraction of 30 %. The Boyce model in the PC phase led to an earlier onset of failure rendering the results worse than with the  $J_2$  model and a rubber volume fraction of 30 % in the ABS phase. This may also be attributed to the slightly more pronounced progressive rehardening triggering local failure for lower overall strains.

As a consequence, the Boyce model did not yield a beneficial approximation of the deformation behaviour, and, for the parameters used, resulted in a worse prediction of the overall failure behaviour for higher rubber contents in comparison to the simple  $J_2$ -plasticity model.

### 10.5.5. Conclusions

The PC/ABS (70/30) unit cell models with the  $J_2$ -DC model underestimated the overall volume strain response (Fig. 10.48). Therefore, the ansatz for  $\alpha$  may underestimate the contribution of distributed crazing to the overall plastic deformation for lower stress triaxialities. Other plastically dilatant mechanisms not considered by the model could have an impact and should be considered. Furthermore, the unit cell approach with its simple approximation of the morphology might not be able to reproduce the actual stress states in the material such that the contribution of distributed crazing to the overall material response is underestimated.

If the  $J_2$ -DC material model was to be developed further, the numerical instabilities regarding the failure behaviour have to be addressed. In its current state the model is only suited to deformation analysis.

The unit cell models with the  $J_2$ -DC constitutive model employed in the ABS phase indicate that variations in the evolution of the volume strain, also observed during the experiments (Sec. 6.1.1), may be the result of changes in the plastic deformation mechanisms. In comparison with the PC/ABS ( $J_2$ /DC) unit cell models, the consideration of shear yielding in the PC/ABS ( $J_2$ / $J_2$ -DC) unit cell models improved the stress and volume strain response

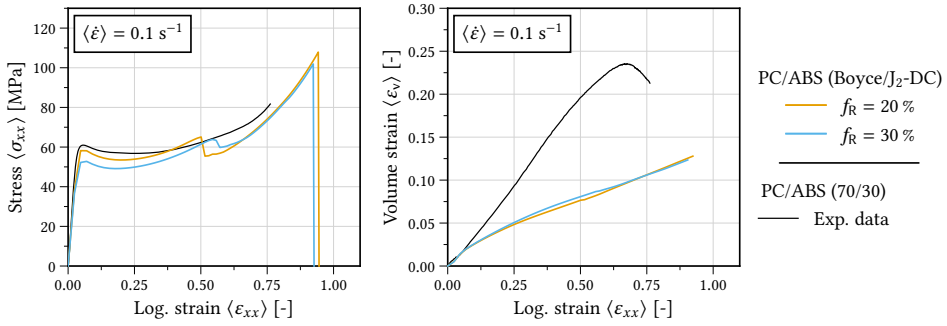


**Figure 10.53.:** Uniaxial stress-strain and volume strain response of PC/ABS (70/30) unit cell models with the J<sub>2</sub>-DC model in the ABS phase and the Boyce model in the PC phase at a macroscopic strain rate  $\langle \dot{\epsilon} \rangle = 0.1 \text{ s}^{-1}$ .

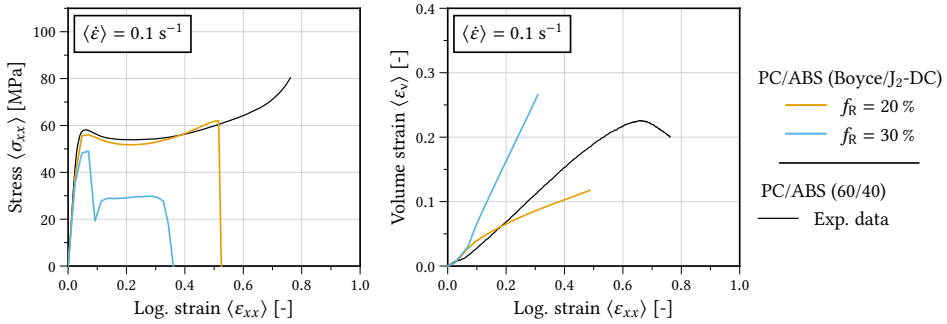


**Figure 10.54.:** Uniaxial stress-strain and volume strain response of PC/ABS (60/40) unit cell models with the J<sub>2</sub>-DC model in the ABS phase and the Boyce model in the PC phase at a macroscopic strain rate  $\langle \dot{\epsilon} \rangle = 0.1 \text{ s}^{-1}$ .

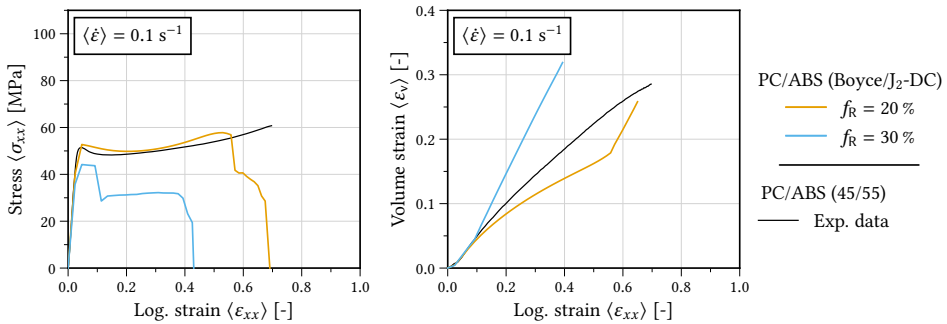


**Figure 10.55.:** Uniaxial stress-strain and volume strain response of PC/ABS (45/55) unit cell models with the J<sub>2</sub>-DC model in the ABS phase and the Boyce model in the PC phase at a macroscopic strain rate  $\langle \dot{\epsilon} \rangle = 0.1 \text{ s}^{-1}$ .

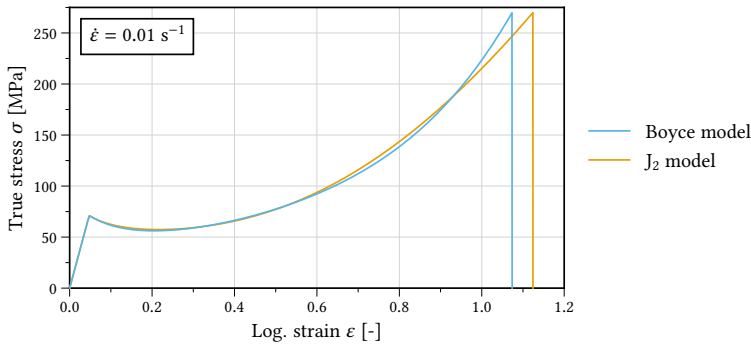


**Figure 10.56.:** Uniaxial tensile response up to failure for the  $J_2$  and Boyce material models used for PC.

regarding an approximation of the experimental results (e.g. Figs. 10.49 and 10.18). In this regard, the approach taken with the  $J_2$ -DC model can be seen as a successful step in the development of improved continuum micromechanical constitutive models for rubber-toughened polymers. However, in comparison to the PC/ABS ( $J_2$ /R) unit cell models, the phenomenological approach with the Raghava model still resulted in better approximations of the experimental data (e.g. Figs. 10.50 and 10.25). It remains an open question as to whether this is an issue of the simple nature of the ansatz made for  $\alpha$  being inaccurate.

## 10.6. Conclusions

The study presented shows that both the PC/ABS ratio and the rubber volume fraction in ABS have a significant impact on the mechanical properties of PC/ABS blends. The deformation behaviour was found to be reasonably well captured by the PC/ABS ( $J_2$ /R) unit cell models with a rubber volume fraction of 20 % in the ABS phase for all three experimentally investigated compositions. In failure tests, the fracture toughness was found to be non-monotonic in both blend parameters as well. Unit cell simulations featuring complex macroscopic stress states were able to reproduce the non-monotonic nature of the dependence of fracture toughness on composition observed in experiments to a certain extent. An explanation for the vastly improved specific work for certain compositions may be a change in the failure behaviour from brittle to ductile as well as a good compatibility of the deformation behaviour of the two phases. Yet, the flaws in the material modelling as well as the crude approximation of the actual microstructure have to be considered such that quantitative conclusions are not feasible. The unit cell approach exposes the limitations in the kinematics of the distributed crazing model that renders it inapt to serve as a matrix or a co-continuous phase. Therefore, the results obtained with the PC/ABS ( $J_2$ /DC) unit cell models highlight the need for a more elaborate modelling approach to ABS rather than credibly capturing the material response.

The unit cell approach presented did not account for interface properties apart from assuming perfect cohesion. This assumption might be valid in the case of certain compositions but likely does not represent an appropriate general approach to this crucial property in the failure behaviour of PC/ABS blends [59, 57, 42]. Similarly, regarding ABS in a homogenised sense neglects the variety in rubber particle shape, size, and distribution that impacts the experimentally observed failure behaviour of both ABS and PC/ABS blends (Secs. 3.2.2, 3.4, and 3.3).

With regard to the failure behaviour, the impact of the unit cell arrangement also has to be reviewed critically. In the approach presented, the transformation from the BCC arrangement to the IPP arrangement is accompanied by a general drop of the specific work in the case of the PC/ABS ( $J_2/R$ ) unit cell models. This observation casts doubts on the comparability of the results with respect to the specific work between the different unit cell arrangements. However, restricting the analysis to the PC/ABS ( $J_2/R$ ) unit cell models, the BCC arrangement yielded a qualitatively reasonable approximation of the experimentally observed non-monotonic failure behaviour.

The deformation of PC/ABS blends mostly takes place uniformly throughout the whole material volume, enabling appropriate studies of the deformation behaviour within the unit cell approach. But failure does usually initiate in sub-volumes, i.e. more locally and in a non-uniform manner. In terms of a unit cell model approach, localisation means that the assumption of a periodic microstructure is no longer valid. Furthermore, the localisation of failure results in an unevenly distributed energy dissipation. A small unit cell model is limited in its ability to reproduce this process and thus overestimates the energy dissipation in the material volume as a consequence. To counteract this effect, a larger sub-volume of the material may be modelled. In real materials, the probability for material inhomogeneities acting as triggers for failure initiation increases with increasing specimen size, i.e. material volume. Thus, a larger unit cell model or representative volume element including a perturbation in the shape of a material inhomogeneity should be better suited to investigate the failure process.

In conclusion, both the constitutive modelling of the ABS phase and the representation of the microstructure of PC/ABS blends prove to be challenging. The study presented exhibits issues in both regards. Yet it provides valuable insights into the complex deformation and failure behaviour of PC/ABS blends. On the basis of the findings of this study, the complex issue of PC/ABS blends should be further investigated using more elaborate material models as well as ternary approximations of the microstructure, possibly in the shape of representative volume elements.

# 11. Conclusions and outlook

## 11.1. Conclusions

The present work is dedicated to a better understanding of the mechanical response of PC/ABS blends. With an emphasis on the large-strain deformation and failure behaviour, PC/ABS blends of different compositions were investigated from an experimental and modelling perspective. Experimental studies on three commercial PC/ABS blends were conducted to study the impact of a variation in composition and of a manufacturing-induced anisotropic microstructure on the stress-strain and volume strain response as well as failure behaviour. Furthermore, modelling approaches at two different scales were presented. In a macroscopic modelling approach, the abilities of three plastically dilatant constitutive models in their application to PC/ABS blends were assessed. In addition, numerical studies using a micromechanical unit cell approach were carried out. The goal was to gain insight into the non-monotonic composition dependence of the fracture toughness of PC/ABS blends and the impact of different plastic deformation mechanisms on the overall material response.

The subject of the experimental work was three commercial PC/ABS blends featuring PC/ABS ratios of (70/30), (60/40), and (45/55). For the purpose of investigating the composition-dependent large-strain deformation and failure behaviour, uniaxial tensile tests and fracture tests on notched specimens were conducted. By means of digital image correlation (DIC), the local deformation behaviour on the specimen surface was measured. This allowed the composition-dependent volume strain response to be investigated and in combination with the global force-displacement response, the true stress-strain response under uniaxial tension was determined. A general trend to a higher yield stress and overall stress response with an increasing PC content of the blends was found. Regarding the deformation behaviour of the three blends investigated, the greatest dilation was found for PC/ABS (45/55). Contrary to the general finding that a greater share of the plastically dilatant ABS results in a greater overall plastic dilatancy, the PC/ABS (60/40) blend exhibited the least pronounced volume strain response. However, it could not be ruled out that the restriction of the DIC system to two dimensions impacted the results in this case. Possibly, the blends actually feature an anisotropic volume strain response that could not be determined by the setup used. The fracture tests were carried out on single-edge-notch-tension (SENT) specimens. Of paramount interest in these experiments was the size and shape of the plastic zone. The size of the plastic zone is linked to the amount of dissipated energy during the fracture process and was found to increase in size

with an increasing PC content of the blends. Accordingly, the specific work of fracture increased with a rising PC content of the blends as well. Regarding the shape of the plastic zone, the finding of an elongated plastic zone is typical for rubber-toughened polymers. Consequently, the blend with the highest ABS content exhibited the most elongated plastic zone shape.

The materials were provided in the form of injection-moulded rectangular plates. In micrographs, all three blends exhibited a morphology with the direction of the melt flow during manufacturing being apparent. In order to study the impact of the anisotropic microstructure on the material response, uniaxial tensile tests and fracture tests were carried out on specimens in perpendicular and parallel orientation to the direction of melt flow. In the uniaxial tensile tests, the specimens in parallel orientation exhibited an increased yield stress for all blend compositions. The dilation behaviour was found to slightly differ for the two specimen orientations as well. This finding points towards an anisotropic dilation behaviour that should be considered the subject of further investigations using an appropriate test setup.

In the SENT fracture tests, the specific work was increased for an orientation parallel to the melt flow. The PC/ABS (45/55) blend, which featured the least apparent orientation of the microstructure of the materials investigated, exhibited the greatest differences between the two specimen orientations.

With the goal of providing a powerful yet simple-to-calibrate tool for FEA of complex parts, three plastically dilatant constitutive models were compared in their abilities to capture the behaviour of the three experimentally investigated PC/ABS blends. The three yield functions, namely the Drucker-Prager, Raghava, and Green yield function, were calibrated from the uniaxial tensile tests and proved capable of capturing the uniaxial tensile response in terms of stress and volume strain. Regarding the behaviour in more complex loading situations such as around a notch in SENT tests, the Green model with an evolving porosity was found unsuited to reproduce the plastic zone shape due to localisation of the failure. However, both the Drucker-Prager and the Raghava model, representing fully phenomenological approaches to modelling plastic dilatancy, were capable of reproducing the experimentally observed plastic zone shape for the PC-rich blend compositions PC/ABS (60/40) and PC/ABS (70/30). Endowed with a failure criterion based on specific work or accumulated plastic strain calibrated towards the onset of failure, both models overestimated the peak force in simulations of the SENT tests. Hence, the yield surfaces investigated might not sufficiently account for the susceptibility of PC/ABS blends to higher stress triaxialities. Yet, the straightforward calibration procedure from a limited set of experimental data still yielded admissible results and important indications of the applicability of these established material models to PC/ABS blends. As such, the size and shape of the plastic zone in the simulations were found to qualitatively agree with the experimental findings.

As part of the material modelling in this work, a micromechanical unit cell approach to PC/ABS blends has been presented as well. To better understand the composition-dependent fracture behaviour, two key blend parameters in form of the PC/ABS ratio and

the rubber content in ABS were systematically varied. Within this unit cell approach, the PC phase and the ABS phase were modelled discretely. The rubber content was considered through a continuum micromechanical approach being part of the constitutive models employed in the ABS phase. Unit cell models using a thus extended Raghava model in the ABS phase and the  $J_2$ -plasticity model in the PC phase, proved to be capable of reproducing the macroscopic uniaxial tensile behaviour, granted an optimum rubber content was specified. Furthermore, this approach proved capable of qualitatively capturing the non-monotonic dependence of the fracture toughness on composition and, in doing so, emphasised the importance of the rubber content in ABS on the blend response. The continuum mechanical model for distributed crazing was also considered and found to be unsuited to reproduce the deformation behaviour of ABS in three-dimensional loading situations. The unit cell approach exhibited kinematic restrictions in the model's plastic response, in the sense that loadings perpendicular to the direction of the principal stress at craze initiation do not contribute to the evolution of plastic deformation. This finding illustrated the need for a better understanding of the micromechanisms involved in the plastic deformation of ABS that must also be considered in the constitutive modelling. Consequently, a material model that combines the aforementioned model for distributed crazing with the  $J_2$ -plasticity model representing shear yielding was introduced. Within this model, the interrelationship between the contribution of the two plastic deformation mechanisms to the plastic response and the loading was assumed to solely depend on the stress triaxiality. As such, the model was calibrated from uniaxial tensile tests so that both the stress-strain and volume strain response were captured. When used in the unit cells' ABS phase, the model represented a clear improvement over the model that only considers distributed crazing. However, the Raghava model endowed with a continuum micromechanical approach to take into account the rubber volume fraction in ABS still proved to be superior. Yet, the newly introduced model showed potential such that further development seems instructive to gain more insight into the micromechanisms that govern the plastic response of ABS.

The results gathered during the extensive numerical unit cell studies highlighted the importance of the rubber content not only on the material response of ABS, but also on the fracture toughness of PC/ABS blends and, in doing so, are in qualitative agreement with experimental evidence. Yet, the unit cell models did not enable a quantitative analysis since the assumption of periodicity proved to be a limitation regarding the modelling of localised failure processes. However, capturing the fundamental deformation and failure behaviour provides a basis for further investigations with more elaborate approaches.

Overall, from both the experimental and modelling perspective the present work represents a comprehensive approach to investigating PC/ABS blends. Yet, its limitations illustrate a continued lack of reliable experimental data as well as a need for further research regarding the complex interrelationship of blend response and composition that govern the characteristic features of these materials.

## 11.2. Outlook

The uniaxial tensile tests on specimens featuring different orientations relative to the direction of melt flow during injection moulding revealed an impact on the in-plane Poisson's ratios and thus the extent of volume strain. The assumption of equal transverse in-plane and through-thickness strains, means that the through-thickness Poisson's ratio changes accordingly. Considering the different Poisson's ratios in-plane, an independent Poisson's ratio through-thickness and a therefore anisotropic dilation behaviour seems likely. Thus, the limitation of the test setup to in-plane measurements introduces an error into the results. Therefore, future work should comprise more experimental investigations into the interrelationship between the anisotropic morphology and volume strain response using a three-dimensional measuring setup. The SENT fracture tests exhibited that the anisotropic microstructure also impacts the failure behaviour of the blends. The modelling approaches presented do not account for any anisotropy, neither with respect to the deformation behaviour nor regarding the failure behaviour. Macroscopic models that feature an orientation-dependent failure criterion in conjunction with mould filling simulations could be an approach to more precise predictions of the local failure behaviour. Improved micromechanical models in the form of more elaborate unit cell approaches or representative volume elements should also geometrically consider the anisotropic blend morphologies to gain further insight into the mechanisms determining the anisotropic failure behaviour. In terms of the material modelling, a further development of the micromechanical modelling regarding the deformation mechanisms with an appropriate failure criterion also offers the potential to improve the understanding and prediction of the material response on different scales. To improve the material modelling, particularly regarding situations featuring high deformation speeds, the impact of temperature and self-heating should be considered as well.



# A. Appendix to Chapter 6

## A.1. Tables to the uniaxial tensile tests

Material	$E$ [MPa]	$\sigma_0$ [MPa]	$\epsilon_0$ [-]	$\sigma_{\min}$ [MPa]	$\epsilon_{\min}$ [-]
PC/ABS (45/55)	$2011 \pm 0$	$51.46 \pm 0.24$	$0.046 \pm 0.001$	$48.24 \pm 0.39$	$0.141 \pm 0.003$
PC/ABS (60/40)	$2030 \pm 0$	$58.15 \pm 0.14$	$0.059 \pm 0.000$	$53.84 \pm 0.28$	$0.223 \pm 0.024$
PC/ABS (70/30)	$2147 \pm 0$	$60.98 \pm 1.01$	$0.056 \pm 0.001$	$56.78 \pm 0.79$	$0.250 \pm 0.008$

**Table A.1.:** Modulus  $E$  of the elastic deformation, initial yield stress  $\sigma_0$ , and (minimum) yield stress  $\sigma_{\min}$  after softening with corresponding strains  $\epsilon_0$  and  $\epsilon_{\min}$  for the three materials at a strain rate of  $\dot{\epsilon} = 0.1 \text{ s}^{-1}$ .

Material	$F_{\max}$ [kN]	$u_{\text{fail}}$ [mm]
PC/ABS (45/55)	$1.93 \pm 0.01$	$10.49 \pm 1.84$
PC/ABS (60/40)	$2.14 \pm 0.01$	$22.46 \pm 2.68$
PC/ABS (70/30)	$2.27 \pm 0.03$	$18.41 \pm 1.42$

**Table A.2.:** Peak force  $F_{\max}$  in uniaxial tensile tests and total specimen elongation at failure  $u_{\text{fail}}$  for the three materials at a crosshead speed of  $\dot{u} = 1.0 \text{ mm/s}$ .

Material	$\sigma_{\text{fail}}$ [MPa]	$\epsilon_{\text{fail}}$ [-]
PC/ABS (45/55)	$64.48 \pm 3.75$	$0.762 \pm 0.053$
PC/ABS (60/40)	$83.30 \pm 2.35$	$0.776 \pm 0.014$
PC/ABS (70/30)	$81.97 \pm 0.34$	$0.765 \pm 0.004$

**Table A.3.:** Uniaxial stress at failure  $\sigma_{\text{fail}}$  and corresponding failure strain  $\epsilon_{\text{fail}}$  for all three materials at a strain rate of  $\dot{\epsilon} = 0.1 \text{ s}^{-1}$ .

Material	$F_{\max}$ [kN]	$u_{\text{fail}}$ [mm]
PC/ABS (45/55)	$1.81 \pm 0.02$	$16.03 \pm 5.03$
PC/ABS (60/40)	$2.01 \pm 0.03$	$29.77 \pm 1.08$
PC/ABS (70/30)	$2.17 \pm 0.02$	$26.88 \pm 1.19$

**Table A.4.:** Peak force  $F_{\max}$  and total specimen elongation at failure  $u_{\text{fail}}$  for the three materials at a crosshead speed of  $\dot{u} = 0.1 \text{ mm/s}$ .

Material	$\sigma_0$ [MPa]	$\varepsilon_0$ [-]	$\sigma_{\min}$ [MPa]	$\varepsilon_{\min}$ [-]
PC/ABS (45/55)	$48.60 \pm 0.70$	$0.038 \pm 0.002$	$44.54 \pm 2.47$	$0.117 \pm 0.009$
PC/ABS (60/40)	$54.21 \pm 0.96$	$0.054 \pm 0.011$	$50.00 \pm 1.59$	$0.204 \pm 0.011$
PC/ABS (70/30)	$58.33 \pm 0.47$	$0.051 \pm 0.002$	$52.77 \pm 1.08$	$0.213 \pm 0.015$

**Table A.5.:** Initial yield stress  $\sigma_0$  and (minimum) yield stress  $\sigma_{\min}$  with corresponding strains  $\varepsilon_0$  and  $\varepsilon_{\min}$  for the three materials at a strain rate of  $\dot{\varepsilon} = 0.01 \text{ s}^{-1}$ .

Material	$\nu_{\max}$ [-]	$\varepsilon_{\nu_{\max}}$ [-]	$\nu_{\min}$ [-]	$\varepsilon_{\nu_{\min}}$ [-]
PC/ABS (45/55)	$0.37 \pm 0.00$	$0.034 \pm 0.002$	$0.24 \pm 0.00$	$0.135 \pm 0.005$
PC/ABS (60/40)	$0.40 \pm 0.01$	$0.047 \pm 0.007$	$0.31 \pm 0.00$	$0.405 \pm 0.021$
PC/ABS (70/30)	$0.37 \pm 0.00$	$0.044 \pm 0.005$	$0.30 \pm 0.01$	$0.414 \pm 0.022$

**Table A.6.:** Maximum and minimum Poisson's ratios with corresponding axial strains for the three materials for log. strains  $\varepsilon > 0.03$  at a strain rate of  $\dot{\varepsilon} = 0.1 \text{ s}^{-1}$ .

## A.2. Tables to the SENT fracture tests

Material	$\dot{u}$ [mm/s]	$F_{\max}$ [kN]	$u_{\max}$ [mm]	$u_{\text{fail}}$ [mm]
PC/ABS (45/55)	0.6	$2.03 \pm 0.03$	$1.47 \pm 0.02$	$2.91 \pm 0.06$
	6.0	$2.15 \pm 0.03$	$1.59 \pm 0.03$	$3.42 \pm 0.08$
PC/ABS (60/40)	0.6	$2.27 \pm 0.01$	$1.81 \pm 0.11$	$3.04 \pm 0.04$
	6.0	$2.40 \pm 0.04$	$1.73 \pm 0.01$	$3.02 \pm 0.03$
PC/ABS (70/30)	0.6	$2.46 \pm 0.03$	$1.77 \pm 0.08$	$3.16 \pm 0.02$
	6.0	$2.51 \pm 0.10$	$1.86 \pm 0.05$	$3.55 \pm 0.12$

**Table A.7.:** Peak force  $F_{\max}$ , corresponding overall specimen elongation  $u_{\max}$ , and specimen elongation at complete specimen failure  $u_{\text{fail}}$  of the three materials for two values of the crosshead speed  $\dot{u}$ .

## B. Appendix to Chapter 7

### B.1. Tables to the uniaxial tensile tests

Specimen orientation	$\sigma_0(\dot{\epsilon} = 0.01 \text{ s}^{-1})$ [MPa]		$\sigma_0(\dot{\epsilon} = 0.1 \text{ s}^{-1})$ [MPa]	
	$\perp$	$\parallel$	$\perp$	$\parallel$
PC/ABS (45/55)	$48.05 \pm 1.05$	$48.60 \pm 0.70$	$50.63 \pm 0.10$	$51.46 \pm 0.24$
PC/ABS (60/40)	$51.50 \pm 1.15$	$54.21 \pm 0.96$	$54.14 \pm 0.58$	$58.15 \pm 0.14$
PC/ABS (70/30)	$58.12 \pm 2.56$	$58.33 \pm 0.47$	$59.96 \pm 2.59$	$60.98 \pm 1.01$

**Table B.1.:** Initial yield stress  $\sigma_0$  of the three materials subjected to uniaxial tension for both specimen orientations investigated and two values the nominal strain rate  $\dot{\epsilon}$ .

### B.2. Tables to the SENT fracture tests

Specimen orientation	$F_{\max}(\dot{u} = 0.6 \text{ mm/s})$ [kN]		$F_{\max}(\dot{u} = 6.0 \text{ mm/s})$ [kN]	
	$\perp$	$\parallel$	$\perp$	$\parallel$
PC/ABS (45/55)	$1.96 \pm 0.06$	$2.03 \pm 0.03$	$1.96 \pm 0.04$	$2.15 \pm 0.03$
PC/ABS (60/40)	$2.11 \pm 0.07$	$2.27 \pm 0.01$	$2.21 \pm 0.05$	$2.40 \pm 0.04$
PC/ABS (70/30)	$2.44 \pm 0.05$	$2.46 \pm 0.03$	$2.36 \pm 0.05$	$2.51 \pm 0.10$

**Table B.2.:** Peak force  $F_{\max}$  of the three materials in SENT fracture tests for two specimen orientations and two values of the crosshead speed  $\dot{u}$ .

Specimen orientation	$u_{\max}(\dot{u} = 0.6 \text{ mm/s})$ [mm]		$u_{\max}(\dot{u} = 6.0 \text{ mm/s})$ [mm]	
	$\perp$	$\parallel$	$\perp$	$\parallel$
PC/ABS (45/55)	$1.34 \pm 0.10$	$1.47 \pm 0.02$	$1.46 \pm 0.05$	$1.59 \pm 0.03$
PC/ABS (60/40)	$1.46 \pm 0.05$	$1.81 \pm 0.11$	$1.70 \pm 0.06$	$1.73 \pm 0.01$
PC/ABS (70/30)	$1.65 \pm 0.06$	$1.77 \pm 0.08$	$1.71 \pm 0.07$	$1.86 \pm 0.05$

**Table B.3.:** Total specimen elongation  $u_{\max}$  corresponding to  $F_{\max}$  of the three materials in SENT fracture tests for two specimen orientations and two values of the crosshead speed  $\dot{u}$ .

Specimen orientation	$u_{\text{fail}}(\dot{u} = 0.6 \text{ mm/s})$ [mm]		$u_{\text{fail}}(\dot{u} = 6.0 \text{ mm/s})$ [mm]	
	$\perp$	$\parallel$	$\perp$	$\parallel$
PC/ABS (45/55)	$2.42 \pm 0.15$	$2.91 \pm 0.06$	$2.72 \pm 0.18$	$3.42 \pm 0.08$
PC/ABS (60/40)	$2.94 \pm 0.03$	$3.04 \pm 0.04$	$3.29 \pm 0.12$	$3.02 \pm 0.03$
PC/ABS (70/30)	$3.06 \pm 0.06$	$3.16 \pm 0.02$	$3.32 \pm 0.13$	$3.55 \pm 0.12$

**Table B.4.** Total specimen elongation at failure  $u_{\text{fail}}$  of the three materials in SENT fracture tests for two specimen orientations and two values of the crosshead speed  $\dot{u}$ .

# C. Appendix to Chapter 9

## C.1. Material parameters to the constitutive models

In the macroscopic modelling approach presented in Chapter 9, the material parameters specified in Tabs. C.1, C.2, and C.3 have been used. The Drucker-Prager, the Raghava, and the Green (Gurson-like) yield surface are introduced in Sec. 8.1. All models were implemented in the form of VUMAT subroutines for the commercial FEA software Abaqus/Explicit [28].

Parameter		Drucker-Prager	Raghava	Green (Gurson-like)
$E$	[MPa]	1900	1900	2300
$\nu$	[-]	0.36	0.37	0.38
$\dot{\epsilon}_0$	[s <sup>-1</sup> ]	0.01	0.01	0.01
$A$	[MPa <sup>-1</sup> ]	0.675	0.72775	0.38
$\alpha$		0.48	50 MPa	7.5
$\sigma_0$	[MPa]	56	56	56
$\sigma_{\min}$	[MPa]	52	52	53.5
$h$	[-]	31	22	30
$h_{\text{hard}}$	[MPa]	36	27	90
$q$	[-]	2.5	2	2.3
$f_0$	[-]	-	-	0.1

**Table C.1.:** Material parameters calibrated for PC/ABS (45/55).

Parameter		Drucker-Prager	Raghava	Green (Gurson-like)
$E$	[MPa]	1900	1900	2300
$\nu$	[-]	0.36	0.36	0.38
$\dot{\epsilon}_0$	[s <sup>-1</sup> ]	0.01	0.01	0.01
$A$	[MPa <sup>-1</sup> ]	0.44	0.52	0.21
$\alpha$		0.39	45 MPa	6.3
$\sigma_0$	[MPa]	61	61	62
$\sigma_{\min}$	[MPa]	55.5	56	59
$h$	[-]	10	12	30
$h_{\text{hard}}$	[MPa]	65	60	120
$q$	[-]	3.3	3.5	3.1
$f_0$	[-]	-	-	0.1

**Table C.2.:** Material parameters calibrated for PC/ABS (60/40).

Parameter		Drucker-Prager	Raghava	Green (Gurson-like)
$E$	[MPa]	2000	2000	2400
$\nu$	[-]	0.36	0.36	0.38
$\dot{\epsilon}_0$	[s <sup>-1</sup> ]	0.01	0.01	0.01
$A$	[MPa <sup>-1</sup> ]	0.55	0.48	0.30
$\alpha$		0.41	48 MPa	6.8
$\sigma_0$	[MPa]	65	65.5	66.5
$\sigma_{\min}$	[MPa]	60	60.5	63.5
$h$	[-]	13	10	4
$h_{\text{hard}}$	[MPa]	65	50	130
$q$	[-]	3.5	3.	2.9
$f_0$	[-]	-	-	0.1

**Table C.3.:** Material parameters calibrated for PC/ABS (70/30).

# D. Appendix to Chapter 10

## D.1. Material parameters to the constitutive models

In the unit cell modelling approach, the ABS phase was modelled either using the Raghava, DC, or  $J_2$ -DC material model. In the PC-phase, either the  $J_2$ -plasticity model of Abaqus (Sec. D.2.3) or the Boyce model was used. All of the aforementioned material models are introduced in detail in Chapter 8 and have been implemented in the form of VUMAT subroutines for Abaqus/Explicit [28]. In the simulations presented in Chapter 10, the material parameters specified in Tabs. D.1, D.2, D.3, and D.4 have been used.

Parameter		R model (ABS)
$E$	[MPa]	2550.00
$\nu$	[-]	0.38
$\alpha$	[MPa]	73.50
$\dot{\epsilon}_0$	[s <sup>-1</sup> ]	0.01
$\sigma_0$	[MPa]	87.00
$\sigma_{\min}$	[MPa]	76.00
$h$	[-]	40.00
$h_{\text{hard}}$	[-]	34.00
$q$	[-]	2.50
$A$	[MPa <sup>-1</sup> ]	53.00
$f_{\text{R}}$	[-]	0.20
$\beta$	[-]	2.60

**Table D.1.:** Material parameters for the Raghava model in the ABS phase.

Parameter		DC model (ABS)
$E$	[MPa]	2550.00
$\nu$	[-]	0.38
$\dot{\epsilon}_0$	[s <sup>-1</sup> ]	$1 \times 10^{-4}$
$A$	[MPa <sup>-1</sup> ]	73.00
$\sigma_{\text{m,cav}}$	[MPa]	10.00
$\sigma_0$	[MPa]	61.00
$\sigma_{\min}$	[MPa]	51.00
$\sigma_{\text{fail}}$	[MPa]	79.00
$h_n$	[-]	38.00
$h_\tau$	[-]	1.00
$q$	[-]	2.00
$\delta_{\text{crit}}$	[-]	0.64
$r$	[-]	0.20
$f_{\text{R}}$	[-]	0.20

**Table D.2.:** Material parameters for the DC model in the ABS phase.

Parameter	J <sub>2</sub> -DC model (ABS)	
$E$	[MPa]	2550.00
$\nu$	[-]	0.38
$\dot{\epsilon}_0$	[s <sup>-1</sup> ]	$1 \times 10^{-4}$
$A$	[MPa <sup>-1</sup> ]	73.00
$\sigma_{m,cav}$	[MPa]	15.00
$\sigma_0$	[MPa]	58.00
$\sigma_{min}$	[MPa]	46.00
$\sigma_{fail}$	[MPa]	90.00
$h$	[-]	30.00
$q$	[-]	2.20
$\delta_{crit}$	[-]	0.65
$r$	[-]	0.20
$f_R$	[-]	0.20
$\beta$	[-]	0.22
$c_1$	[-]	70.00
$c_0$	[-]	0.10

**Table D.3.:** Material parameters for the J<sub>2</sub>-DC model in the ABS phase.

Parameter	Boyce model (PC)	
$E$	[MPa]	2550.00
$\nu$	[-]	0.38
$\dot{\gamma}_0$	[s <sup>-1</sup> ]	$1 \times 10^{14}$
$A$	[K·MPa <sup>-1</sup> ]	545.00
$s_0$	[MPa]	82.00
$s_s$	[MPa]	49.00
$C_R$	[MPa]	18.00
$\sqrt{N}$	[-]	1.8
$h$	[MPa]	300.00
$\alpha$	[-]	0.06
$\sigma_{m,fail}$	[-]	90.00

**Table D.4.:** Material parameters for the Boyce model.

## D.2. Implementation details

### D.2.1. Time scaling in simulations of viscous materials

In the case of the simulations presented in Chapter 10, a time scaling method from Gruben, Hopperstad, and Børvik [46] was used. Through multiplying the overall strain rate  $\dot{\epsilon}$  and the reference strain rate  $\dot{\epsilon}_0$  by the same time scaling factor  $\alpha_t$ , the ratio between the two stays constant. Therefore, the viscous material response is not affected but the simulated time span is reduced by  $\alpha_t$ . Obviously, as a consequence of a higher loading rate, the kinetic energy of the whole model increases. To prevent the time scaling from significantly altering the results, the kinetic energy has to remain negligible in comparison to the external work done on the whole model.

### D.2.2. Coordinate systems in Abaqus VUMAT user subroutines

Abaqus/Explicit [28] passes over stresses `stressOld` and strain increments `strainInc` in the orientation of the material axes to a VUMAT user subroutine. The material axes are defined by a co-rotational coordinate system  $\{\hat{e}_i\}$  rotating with the material. The stresses `stressNew` defined in a VUMAT subroutine have to be returned in this local material coordinate system.



The deformation gradients `defGradOld` and `defGradNew` are passed over from Abaqus/Explicit to VUMATs as components of the global basis  $\{\mathbf{e}_i\}$ . However, the components of the right stretch tensors `stretchOld` and `stretchNew` are passed over in the co-rotational coordinate system  $\{\hat{\mathbf{e}}_i\}$ . A rotation of a second-order tensor  $\mathbf{A}$  in the global basis  $\{\mathbf{e}_i\}$  with the orthogonal rotation tensor  $\mathbf{R}$  to the co-rotational system  $\{\hat{\mathbf{e}}_i\}$  is given by

$$\hat{\mathbf{A}} = \mathbf{R}^T \cdot \mathbf{A} \cdot \mathbf{R}. \quad (\text{D.1})$$

### D.2.3. The $J_2$ -plasticity model in Abaqus/Explicit

Since the  $J_2$  yield criterion is widespread and frequently used in metal plasticity it is readily implemented in Abaqus/Explicit [28]. It allows the reference yield curve to be specified in tabular form where the uniaxial yield stress has to be given as a function of the equivalent accumulated plastic strain which in Abaqus/Explicit is defined as

$$\varepsilon^p = \int_{t_0}^{t_1} \sqrt{\frac{2}{3} \dot{\varepsilon}^p : \dot{\varepsilon}^p} dt. \quad (\text{D.2})$$

In addition to specifying the yield stress under quasi-static loading or at a certain strain rate, a rate dependency can be entered as well. Assuming that the rate dependency of the modelled material only changes the onset of yield but not the hardening behaviour, the ratio of the yield stress  $\sigma_1^y$  at a certain strain rate  $\dot{\varepsilon}_1$  to the yield stress  $\sigma_0^y$  at the reference strain rate  $\dot{\varepsilon}_0$  can be specified (*Suboptions*→*Rate Dependent*→*Yield Ratio*). The first row of the table represents the ratio of the given stress-strain data to the behaviour at the reference loading rate. All of the above mentioned options can also be entered using the “Edit Keywords” option of the graphical user interface or be written into the input file directly, e.g. by a script. An example with material parameters for a material called `J2_PLASTICITY` calibrated to PC as described in Sec. 10.4.2 is given in Listing D.1. In Listing D.1, `<yield stress in MPa>` and `<equivalent accumulated plastic strain>` denote pairs of values representing the yield stress  $k$  in MPa at corresponding values of the equivalent plastic strain  $\varepsilon^p$  (Eq. (D.2)). A failure criterion based on the hydrostatic stress  $\sigma_m$  triggering element deletion in Abaqus 2019 can be invoked via editing the keywords (in the graphical user interface) or the input file as in Listing D.2. Therein, `<hydrostatic failure stress in MPa>` represents  $\sigma_{m,\text{fail}}$ .

```
**  
** MATERIALS  
**  
*Material, name=J2_PLASTICITY  
*Density  
1e-09,  
*Elastic  
1500., 0.38  
*Plastic  
<yield stress in MPa>, <equivalent accumulated plastic strain>  
*Rate Dependent, type=YIELD RATIO  
1., 0.  
1.0433, 1.  
1.056, 10.  
1.068, 100.  
1.08, 1000.
```

**Listing D.1:** Abaqus input file MATERIALS keyword section

```
*TENSILE FAILURE, ELEMENT DELETION=YES  
<hydrostatic failure stress in MPa>
```

**Listing D.2:** Abaqus input file TENSILE FAILURE keyword section

# Publications and talks

## Journal papers

- J. Hund, J. Naumann, and T. Seelig. ‘An Experimental and Constitutive Modeling Study on the Large Strain Deformation and Fracture Behavior of PC/ABS Blends’. In: *Mechanics of Materials* 124 (2018), pp. 132–142. DOI: 10.1016/j.mechmat.2018.06.003.
- J. Hund et al. ‘Stress-Strain Characterization and Damage Modeling of Glass-Fiber-Reinforced Polymer Composites with Vinylester Matrix.’ in: *Journal of Composite Materials* (2016). DOI: 10.1177/0021998316648227.

## Conference proceedings

- J. Hund, J. Naumann, and T. Seelig. ‘Comparison of Dilatant Plasticity Models in Application to Rubber-Toughened Polymers’. In: *PAMM* 16.1 (2016), pp. 349–350. DOI: 10.1002/pamm.201610163.
- J. Hund and T. Seelig. ‘Multiscale Modeling of Thermoplastic PC/ABS Blends’. In: *PAMM* 17.1 (2017), pp. 417–418. DOI: 10.1002/pamm.201710178.
- J. Hund and T. Seelig. ‘Application of Different Plasticity Models to PC/ABS Blends within Micromechanical Approaches’. In: *PAMM* 19.1 (2019), e201900093. DOI: 10.1002/pamm.201900093.

## Conference talks

- J. Hund and T. Seelig. ‘Computational study of morphological effects on the deformation and fracture behavior of PC/ABS blends’. 29th International Workshop on Computational Mechanics of Materials (IWCMM29), Dubrovnik, Sep. 15-18, 2019
- J. Hund and T. Seelig. ‘Application of different plasticity models to PC/ABS blends within a micromechanical unit cell approach’. 90th Annual Meeting of the International Association of Applied Mathematics and Mechanics (GAMM), Vienna, Austria, Feb. 18-22, 2019

- J. Hund and T. Seelig. 'Micromechanical analysis of composition dependent failure in thermoplastic PC/ABS blends at high strain rates'. 28th International Workshop on Computational Mechanics of Materials (IWCMM28), Glasgow, UK, Sep. 10-12, 2018
- J. Hund and T. Seelig. 'Micromechanical analysis of failure in thermoplastic PC/ABS blends'. European Mechanics of Materials Conference (EMMC16), Nantes, France, Mar. 26-28, 2018
- J. Hund and T. Seelig. 'Multiscale modeling of failure in thermoplastic PC/ABS blends'. 27th International Workshop on Computational Mechanics of Materials (IWCMM27), Leuven, Belgium, Sep. 20-22, 2017
- J. Hund and T. Seelig. 'Multiscale modeling of fracture in thermoplastic PC/ABS-blends'. 5th International Conference on Computational Modeling of Fracture and Failure of Materials and Structures (CFRAC), Nantes, France, Jun. 14-16, 2017
- J. Hund and T. Seelig. 'Multiscale modeling of thermoplastic PC/ABS-blends'. 88th Annual Meeting of the International Association of Applied Mathematics and Mechanics (GAMM), Weimar, Germany, Mar. 6-10, 2017
- J. Hund and T. Seelig. 'Modeling of rubber-toughened polymers using dilatant plasticity models'. European Mechanics of Materials Conference (EMMC15), Brussels, Belgium, Sep. 7-9, 2016
- J. Hund, J. Naumann, and T. Seelig. 'Comparison of dilatant plasticity models in application to rubber-toughened polymers'. 87th Annual Meeting of the International Association of Applied Mathematics and Mechanics (GAMM), Braunschweig, Germany, Mar. 7-11, 2016

# Nomenclature

## General notation and operators

$\mathbb{E}^3$	three-dimensional Euclidean space
$(x, y, z)$ or $(x_1, x_2, x_3)$	Cartesian coordinates
$\{\mathbf{e}_x, \mathbf{e}_y, \mathbf{e}_z\}$ or $\{\mathbf{e}_1, \mathbf{e}_2, \mathbf{e}_3\}$	Cartesian basis
$\mathbf{1}$	second-order identity tensor
$\mathbb{I}$	fourth-order identity tensor
$\mathbf{Z}^T$	transpose of tensor $\mathbf{Z}$
$\mathbf{Z}^{-1}$	inverse of tensor $\mathbf{Z}$
$\mathbf{Z}'$	deviatoric part of tensor $\mathbf{Z}$
$\text{tr}(\mathbf{Z})$	trace of tensor $\mathbf{Z}$
$\ \mathbf{Z}\ $	Frobenius norm of tensor $\mathbf{Z}$
$\text{sym}(\mathbf{Z})$	symmetric part of tensor $\mathbf{Z}$
$\text{skw}(\mathbf{Z})$	skew part of tensor $\mathbf{Z}$
$\det(\mathbf{Z})$	determinant of tensor $\mathbf{Z}$
$\text{div}(\mathbf{Z})$	divergence of tensor $\mathbf{Z}$
$\text{grad}(\cdot)$	gradient operator with respect to the spatial coordinates
$\text{Grad}(\cdot)$	gradient operator with respect to the material coordinates
$\cup$	assembly operator
$\hat{(\cdot)}$	material (Lagrangian) representation of a quantity
$\bar{(\cdot)}$	spatial (Eulerian) representation of a quantity
$(\cdot)_0$	quantity in the initial configuration
$\dot{(\cdot)}$	material time derivative of a quantity
$(\cdot)^*$	quantity from the view of a second observer
$(\cdot)_h, (\cdot)^h$	approximation of a quantity
$(\cdot)_n$	physical quantity at time $t_n$
$(\cdot)_{n+1}$	physical quantity at time $t_{n+1}$
$(\cdot)_{\text{fail}}$	quantity at failure

$\langle \cdot \rangle$  macroscopic quantity

## Greek Letters

$\alpha$	pressure coefficient
$\alpha$	volume share of shear yielding
$\alpha_t$	time scaling factor
$\alpha_{MT}, \beta_{MT}$	parameters from the Eshelby tensor in the Mori-Tanaka homogenisation scheme
$\beta$	fit parameter
$\gamma^P$	accumulated plastic shear strain
$\dot{\gamma}_0$	reference shear strain rate
$\delta$	craze opening
$\boldsymbol{\delta}$	craze widening vector
$\delta_n$	component of $\boldsymbol{\delta}$ in craze normal direction
$\delta_\tau$	component of $\boldsymbol{\delta}$ in craze tangential direction
$\dot{\delta}_{n0}, \dot{\delta}_{\tau0}$	reference widening rate in craze normal and tangential direction
$\delta_{crit}$	critical craze widening
$\delta \mathbf{u}$	test function or virtual displacement
$\delta W$	virtual work
$\Delta t$	time increment
$\partial V$	domain boundary (surface) of $\mathcal{B}$ in the current configuration
$\varepsilon$	normal strain
$\boldsymbol{\varepsilon}$	logarithmic strain tensor
$\varepsilon^P$	accumulated plastic strain
$\varepsilon_v$	volumetric strain
$\varepsilon_d$	strain in the deviatoric plane
$\varepsilon_{min}$	logarithmic strain at $\sigma_{min}$
$\varepsilon_{tr}$	transverse strain
$\varepsilon_0$	logarithmic strain at $\sigma_0$
$\dot{\varepsilon}$	strain rate
$\dot{\varepsilon}_0$	reference strain rate
$\boldsymbol{\epsilon}$	Levi-Civita tensor
$\eta$	stress triaxiality
$\eta_\varepsilon$	strain triaxiality
$\lambda$	stretch

$\lambda_a$	principal stretches ( $a = 1, 2, 3$ )
$\lambda_{\text{chain}}$	macromolecular chain stretch
$\xi, \eta$	subset shape functions
$\rho_0, \rho$	volumetric mass density in the reference and current configuration, respectively
$\sigma$	stress
$\boldsymbol{\sigma}$	Cauchy stress tensor
$\sigma_a$	principal stresses ( $a = 1, 2, 3$ )
$\sigma_e$	von Mises stress
$\sigma_m$	hydrostatic stress
$\sigma_{m,\text{cav}}$	hydrostatic stress upon which rubber particle cavitation occurs
$\sigma_0$	initial yield stress
$\sigma_{\text{min}}$	minimum yield stress
$\sigma_n$	stress normal to craze plane
$\sigma_\tau$	stress tangential to craze plane
$\sigma_{n,\text{crit}}, \sigma_{\tau,\text{crit}}$	craze resistance in craze normal and tangential direction
$\bar{\boldsymbol{\sigma}}$	driving stress tensor
$\bar{\sigma}_n$	portion of the driving stress in craze normal direction
$\bar{\sigma}_\tau$	portion of the driving stress tangential to the craze
$\overset{\nabla}{\boldsymbol{\sigma}}$	Jaumann-Zaremba rate of Cauchy stress
$\dot{\boldsymbol{\sigma}}$	Green-Naghdi rate of Cauchy stress
$\tau$	applied shear stress
$\boldsymbol{\tau}$	portion of stress in the craze tangential direction
$\Phi$	yield function
$\chi$	motion
$\chi_t$	time-dependent current configuration
$\chi_{t_0}$	initial configuration at time $t = 0$
$\psi, \boldsymbol{\Psi}$	volume specific scalar- and vector-valued physical quantity
$\Omega_\square$	isoparametric reference element

## Latin Letters

$\mathbf{a}$	acceleration
$A$	cross section
$A$	material parameter accounting for viscous properties

$\mathbf{A}$	Euler-Almansi strain tensor
$b$	rubber particle spacing
$\mathbf{b}$	volume force density per unit mass
$\mathbf{b}$	back stress tensor
$\mathbf{B}$	left Cauchy-Green tensor
$\mathbf{B}^p$	plastic part of the left Cauchy-Green deformation tensor
$\mathbf{B}_{0i}$	matrices specifying the symmetric part of the spatial gradient of the shape functions $N_i$
$\mathcal{B}$	material body
$c_0$	midpoint of logistic curve
$c_1$	logistic decrease rate
$c_d$	dilatational wave speed
$C_R$	rubber modulus
$\mathbf{C}$	right Cauchy-Green tensor
$\mathbb{C}$	isotropic fourth-order elasticity tensor
$\bar{d}$	mean particle size
$d\mathbf{x}, d\mathbf{X}$	line element with respect to the spatial and material configuration, respectively
$d\mathbf{a}, d\mathbf{A}$	surface elements with respect to the spatial and material configuration, respectively
$d\nu, dV$	volume elements with respect to the spatial and material configuration, respectively
$d\mathbf{f}_o$	infinitesimal surface force
$\mathbf{D}$	rate of deformation tensor
$\mathbf{D}^e, \mathbf{D}^p$	elastic and inelastic part of the rate of deformation tensor
$\mathbf{D}^c$	part of the rate of deformation tensor associated with crazing
$E$	Young's modulus
$\mathbf{E}$	Green-Lagrange strain tensor
$\dot{\mathbf{E}}$	Green-Lagrange strain rate tensor
$\mathbf{E}^k, \mathbf{e}^k$	generalised strain tensor in material (Lagrangian) and spatial (Eulerian) description as a function of $k \in \mathbb{R} \setminus 0$
$\mathbf{E}^H, \mathbf{e}^H$	Hencky strain tensor in material (Lagrangian) and spatial (Eulerian) description
$f$	porosity
$f_R$	rubber content in ABS



---

$\mathbf{f}$	resultant force
$\mathbf{f}^{\text{int}}$	vector of internal forces
$\mathbf{f}^{\text{ext}}$	total applied external forces
$F$	reaction force
$F_{\text{max}}$	peak load
$\mathbf{F}$	deformation gradient
$\mathbf{F}^e, \mathbf{F}^p$	elastic and inelastic part of the deformation gradient
$G$	shear modulus
$G_M$	matrix shear modulus
$G_R$	rubber particle shear modulus
$G^*$	effective shear modulus
$h$	softening slope
$h_n, h_\tau$	softening slope in craze normal and tangential direction
$h_{\text{hard}}$	hardening modulus
$\mathbf{H}$	rotational momentum
$I_a$	principal invariants of the Cauchy stress $\boldsymbol{\sigma}$ ( $a = 1, 2, 3$ )
$\mathbf{I}$	linear momentum
$J$	volume ratio
$J_a$	principal invariants of the stress deviator ( $a = 1, 2, 3$ )
$k$	yield strength as a function of $\varepsilon^p$
$\hat{k}$	yield stress after “failure”
$K$	bulk modulus
$K_M$	matrix bulk modulus
$K_R$	rubber particle bulk modulus
$K^*$	effective bulk modulus
$l_{\text{min}}$	smallest characteristic finite element length
$\ell$	logistic function
$\mathbf{L}$	spatial velocity gradient
$\mathcal{L}$	Langevin function
$\mathcal{L}(\boldsymbol{\sigma})$	Oldroyd rate of Cauchy stress
$m$	mass
$M_0$	molecular weight of a single repeat unit
$M_n$	number-average molecular weight
$\mathbf{M}$	mass matrix

$\mathbf{M}$	resultant torque
$\nu$	Poisson's ratio
$n$	particle count
$n_{\text{el}}$	number of finite elements
$n_{\Gamma}$	number of finite elements on the traction boundary
$N$	sample size
$N$	number of chain segments between entanglements
$N_i$	shape functions defined in the reference element $\Omega_{\square}$
$\mathbf{n}$	craze normal direction
$\mathbf{N}$	direction of $\mathbf{D}^{\text{P}}$
$\mathbf{N}, \mathbf{n}$	surface unit normal in the reference and current configuration
$\mathbf{N}_a, \mathbf{n}_a$	principal material and spatial directions ( $a = 1, 2, 3$ )
$p_{\psi}, \mathbf{p}_{\psi}$	production of $\psi$ and $\boldsymbol{\psi}$ , respectively
$P$	centre point of the subset in the reference image
$\tilde{P}$	centre point of the subset in the target image
$\mathbf{P}$	1st Piola-Kirchhoff stress tensor
$\mathcal{P}$	material point of $\mathcal{B}$
$q$	hardening exponent
$\mathbf{q}_{\psi}$	vector of non-convective flow of $\psi$
$\tilde{Q}$	point in the subset in the target image
$\mathbf{Q}_{\psi}$	second-order tensor of non-convective flow of $\boldsymbol{\psi}$
$r$	void radius
$\mathbf{r}$	position vector
$R$	residual
$\mathbf{R}$	rotation
$\mathbf{R}$	reference configuration
$s$	shear resistance to plastic flow
$s_0$	initial resistance to plastic flow
$s_s$	saturation value of the shear resistance to plastic flow
$s_{\psi}, \mathbf{s}_{\psi}$	supply of $\psi$ and $\boldsymbol{\psi}$ , respectively
$s_{\bar{y}}$	standard error of the sample mean
$s_N$	sample standard deviation
$t$	time
$t$	specimen thickness

---

$\mathbf{t}, T$	traction vector related to material surface elements in the spatial and material configuration
$\bar{\mathbf{t}}$	prescribed traction vector
$T$	absolute temperature
$\mathbb{T}_{\mathbf{X}}, \mathbb{T}_{\mathbf{x}}$	tangent spaces formed by $\mathbf{X}$ and $\mathbf{x}$
$u$	displacement
$\dot{u}$	crosshead speed
$u_{\max}$	specimen elongation at $F_{\max}$
$\mathbf{u}$	displacement vector
$\bar{\mathbf{u}}$	prescribed displacement
$\mathbf{U}$	right stretch tensor
$v$	displacement
$\mathbf{v}$	velocity
$V_0, V$	volume of $\mathcal{B}$ in the reference and current configuration, respectively
$V_0^e$	volume of one finite element in the reference configuration
$\mathbf{V}$	left stretch tensor
$w$	specific work of fracture
$w^p$	plastic work per unit volume
$W$	work
$W^{\text{ext}}$	work of external forces
$\mathbf{W}$	spin tensor
$X_n$	degree of polymerisation
$\mathbf{X}, \mathbf{x}$	material and spatial coordinates

## Acronyms

ABS	acrylonitrile-butadiene-styrene
AN	acrylonitrile
BCC	body-centred cubic
CCD	charge-coupled device
CI	confidence interval
$CL_{U/L}$	upper/lower confidence limit
DC	distributed crazing
DIC	digital image correlation
DP	Drucker-Prager

FCC	face-centred cubic
FE	finite element
FEA	finite element analysis
FEM	finite element method
IBVP	initial boundary value problem
IPP	interpenetrating phases
MSE	standard error of the sample mean
PC	polycarbonate
R	Raghava
ROI	region of interest
RVE	representative volume element
SAN	styrene-acrylonitrile
SENT	single-edge-notch-tesion
SHA	stacked hexagonal array
TEM	transmission electron microscopy
VUAMP	user-defined amplitude subroutine for Abaqus/Explicit
VUMAT	user-defined material subroutine for Abaqus/Explicit

# Bibliography

- [1] J. Aranda-Ruiz, K. Ravi-Chandar, and J. Loya. ‘On the Double Transition in the Failure Mode of Polycarbonate’. In: *Mechanics of Materials* 140 (2020), p. 103242. DOI: 10.1016/j.mechmat.2019.103242.
- [2] A. S. Argon. ‘A Theory for the Low-Temperature Plastic Deformation of Glassy Polymers’. In: *The Philosophical Magazine: A Journal of Theoretical Experimental and Applied Physics* 28.4 (1973), pp. 839–865. DOI: 10.1080/14786437308220987.
- [3] A. S. Argon and M. Salama. ‘The Mechanism of Fracture in Glassy Materials Capable of Some Inelastic Deformation’. In: *Materials Science and Engineering. The Second International Conference on Rapidly Quenched Metals* 23.2 (1976), pp. 219–230. DOI: 10.1016/0025-5416(76)90198-1.
- [4] E. M. Arruda and M. C. Boyce. ‘A Three-Dimensional Constitutive Model for the Large Stretch Behavior of Rubber Elastic Materials’. In: *Journal of the Mechanics and Physics of Solids* 41.2 (1993), pp. 389–412. DOI: 10.1016/0022-5096(93)90013-6.
- [5] S. Balakrishnan and N. R. Neelakantan. ‘Mechanical Properties of Blends of Polycarbonate with Unmodified and Maleic Anhydride Grafted ABS’. In: *Polymer International* 45.4 (1998), pp. 347–352. DOI: 10.1002/(SICI)1097-0126(199804)45:4<347::AID-PI940>3.0.CO;2-R.
- [6] S. Bärwinkel et al. ‘Morphology Formation in PC/ABS Blends during Thermal Processing and the Effect of the Viscosity Ratio of Blend Partners’. In: *Materials* 9.8 (2016), p. 659. DOI: 10.3390/ma9080659.
- [7] P. Beardmore and S. Rabinowitz. ‘Craze Formation and Growth in Anisotropic Polymers’. In: *Journal of Materials Science* 10.10 (1975), pp. 1763–1770. DOI: 10.1007/BF00554938.
- [8] F. Becker. ‘Entwicklung einer Beschreibungsmethodik für das mechanische Verhalten unverstärkter Thermoplaste bei hohen Deformationsgeschwindigkeiten’. Doctoral Thesis. Universitäts- und Landesbibliothek Sachsen-Anhalt, 2009.
- [9] T. Belytschko et al. *Nonlinear Finite Elements for Continua and Structures*. Wiley, 2013.
- [10] S. Berg et al. ‘Ilastik: Interactive Machine Learning for (Bio)Image Analysis’. In: *Nature Methods* 16.12 (2019), pp. 1226–1232. DOI: 10.1038/s41592-019-0582-9.

- [11] C. R. Bernal et al. 'Microstructure, Deformation, and Fracture Behavior of Commercial ABS Resins'. In: *Journal of Applied Polymer Science* 58.1 (1995), pp. 1–10. doi: 10.1002/app.1995.070580101.
- [12] A. Bertram. *Elasticity and Plasticity of Large Deformations*. Springer, 2012.
- [13] J. Bonet and R. D. Wood. *Nonlinear Continuum Mechanics for Finite Element Analysis*. Cambridge university press, 1997.
- [14] A. F. Bower. *Applied Mechanics of Solids*. CRC press, 2009.
- [15] M. C. Boyce and E. M. Arruda. 'An Experimental and Analytical Investigation of the Large Strain Compressive and Tensile Response of Glassy Polymers'. In: *Polymer Engineering & Science* 30.20 (1990), pp. 1288–1298. doi: 10.1002/pen.760302005.
- [16] M. C. Boyce, D. M. Parks, and A. S. Argon. 'Large Inelastic Deformation of Glassy Polymers. Part I: Rate Dependent Constitutive Model'. In: *Mechanics of Materials* 7.1 (1988), pp. 15–33. doi: 10.1016/0167-6636(88)90003-8.
- [17] R. A. Bubeck et al. 'Modes of Deformation in Rubber-Modified Thermoplastics during Tensile Impact'. In: *J. Mat. Sci.* 26.23 (1991), pp. 6249–6259. doi: 10.1007/BF02387801.
- [18] C. Bucknall. *Toughened Plastics*. Materials Science Series. Springer Netherlands, 1977. doi: 10.1007/978-94-017-5349-4.
- [19] T. A. Callaghan et al. 'Polycarbonate-SAN Copolymer Interaction'. In: *Polymer* 34.18 (1993), pp. 3796–3808. doi: 10.1016/0032-3861(93)90503-3.
- [20] L. Castellani et al. 'Rate and Temperature Dependence of Fracture Toughness in ABS Resins in Relation to Dispersed-Phase Structure'. In: *Polymer* 37.8 (1996), pp. 1329–1338. doi: 10.1016/0032-3861(96)81129-3.
- [21] B. I. Chaudhry, E. Hage, and L. A. Pessan. 'Effects of Processing Conditions on the Phase Morphology of PC/ABS Polymer Blends'. In: *Journal of Applied Polymer Science* 67.9 (1998), pp. 1605–1613. doi: 10.1002/(SICI)1097-4628(19980228)67:9<1605::AID-APP12>3.0.CO;2-T.
- [22] C. C. Chen and J. A. Sauer. 'Yield and Fracture Mechanisms in ABS'. In: *Journal of Applied Polymer Science* 40.3-4 (1990), pp. 503–521. doi: 10.1002/app.1990.070400317.
- [23] W.-Y. Chiang and D.-S. Hwung. 'Properties of Polycarbonate/Acrylonitrile-Butadiene-Styrene Blends'. In: *Pol. Eng. Sci.* 27.9 (1987), pp. 632–639. doi: 10.1002/pen.760270906.
- [24] K. Cho et al. 'Toughening of Polycarbonate: Effect of Particle Size and Rubber Phase Contents of the Core-Shell Impact Modifier'. In: *Journal of Applied Polymer Science* 95.3 (2005), pp. 748–755. doi: 10.1002/app.21252.
- [25] J.-H. Chun, K.-S. Maeng, and K. S. Suh. 'Miscibility and Synergistic Effect of Impact Strength in Polycarbonate/ABS Blends'. In: *Journal of Materials Science* 26.19 (1991), pp. 5347–5352. doi: 10.1007/BF01143232.

- [26] M. Danielsson, D. Parks, and M. Boyce. 'Three-Dimensional Micromechanical Modeling of Voided Polymeric Materials'. In: *Journal of the Mechanics and Physics of Solids* 50.2 (2002), pp. 351–379. doi: 10.1016/S0022-5096(01)00060-6.
- [27] M. Danielsson, D. M. Parks, and M. C. Boyce. 'Micromechanics, Macromechanics and Constitutive Modeling of the Elasto-Viscoplastic Deformation of Rubber-Toughened Glassy Polymers'. In: *Journal of the Mechanics and Physics of Solids* 55.3 (2007), pp. 533–561. doi: 10.1016/j.jmps.2006.08.006.
- [28] Dassault Systèmes Simulia Corp. *Abaqus 2019*. Dassault Systèmes Simulia Corp. 2018.
- [29] E. A. De Souza Neto, D. Peric, and D. R. J. Owen. *Computational Methods for Plasticity: Theory and Applications*. Wiley, 2011.
- [30] M. A. Delesse. 'Procédé mécanique pour déterminer la composition des roches.' In: *CR Acad. Sci. Paris* 25 (1847), pp. 544–545.
- [31] A. M. Donald and E. J. Kramer. 'The Competition between Shear Deformation and Crazing in Glassy Polymers'. In: *Journal of Materials Science* 17.7 (1982), pp. 1871–1879. doi: 10.1007/BF00540402.
- [32] L. Dong, R. Greco, and G. Orsello. 'Polycarbonate/acrylonitrile-Butadiene-Styrene Blends: 1. Complementary Etching Techniques for Morphology Observations'. In: *POLYMER* 34.7 (1993), pp. 1375–1382.
- [33] T. Ebeling, A. Hiltner, and E. Baer. 'Effect of Acrylonitrile Content on the Delamination Toughness of PC/SAN Microlayers'. In: *Polymer* 40.8 (1999), pp. 1985–1992. doi: 10.1016/S0032-3861(98)00416-9.
- [34] G. W. Ehrenstein. *Polymer Werkstoffe: Struktur – Eigenschaften – Anwendung*. Third. München: Carl Hanser Verlag GmbH & Co. KG, 2011. doi: 10.3139/9783446429673.
- [35] Q.-Z. Fang et al. 'Rate-Dependent Large Deformation Behavior of PC/ABS'. In: *Polymer* 50.1 (2009), pp. 296–304. doi: 10.1016/j.polymer.2008.10.042.
- [36] S. Fellahi, B. D. Favis, and B. Fisa. 'Morphological Stability in Injection-Moulded High-Density Polyethylene/Polyamide-6 Blends'. In: *Polymer* 37.13 (1996), pp. 2615–2626. doi: 10.1016/0032-3861(96)87620-8.
- [37] K. Finlayson. *Advances in Polymer Blends and Alloys Technology*. Vol. 5. CRC Press, 1994.
- [38] C. G'Sell et al. 'Video-Controlled Tensile Testing of Polymers and Metals beyond the Necking Point'. In: *Journal of Materials Science* 27.18 (1992), pp. 5031–5039. doi: 10.1007/BF01105270.
- [39] B. Gearing and L. Anand. 'On Modeling the Deformation and Fracture Response of Glassy Polymers Due to Shear-Yielding and Crazing'. In: *International Journal of Solids and Structures* 41.11 (2004), pp. 3125–3150. doi: 10.1016/j.ijso1str.2004.01.017.

- [40] G. F. Giacconi et al. 'Development of Toughness in ABS Resins'. In: *Polymer* 39.25 (1998), pp. 6315–6324. DOI: 10.1016/S0032-3861(97)10256-7.
- [41] R. Greco. 'Polycarbonate Toughening by ABS.' In: *Martuscelli, E. et al. (Eds), Advanced Routes for Polymer Toughening*. Elsevier, 1996, pp. 469–526.
- [42] R. Greco. "'Natural" Polymer Alloys: PC/ABS Systems'. In: *Polymer Blends and Alloys*. Ed. by G. O. Shonaike and G. P. Simon. First. CRC Press, 1999, pp. 289–330.
- [43] R. Greco et al. 'Polycarbonate/ABS Blends: Processability, Thermal Properties, and Mechanical and Impact Behavior'. In: *Advances in Polymer Technology* 13.4 (1994), pp. 259–274. DOI: 10.1002/adv.1994.060130402.
- [44] R. J. Green. 'A Plasticity Theory for Porous Solids'. In: *Int. J. Mech. Sci.* 14.4 (1972), pp. 215–224. DOI: 10.1016/0020-7403(72)90063-X.
- [45] D. Gross and T. Seelig. *Fracture Mechanics: With an Introduction to Micromechanics*. Springer, 2017. DOI: 10.1007/978-3-319-71090-7.
- [46] G. Gruben, O. S. Hopperstad, and T. Børvik. 'Simulation of Ductile Crack Propagation in Dual-Phase Steel'. In: *International Journal of Fracture* 180.1 (2013), pp. 1–22. DOI: 10.1007/s10704-012-9791-2; 10.1007/s10704-012-9791-2.
- [47] A. L. Gurson. 'Continuum Theory of Ductile Rupture by Void Nucleation and Growth'. In: *J. Eng. Mat. Technol.* 99 (1977), pp. 2–15.
- [48] A. Hassan and W. Y. Jwu. 'Mechanical Properties of High Impact ABS/PC Blends – Effect of Blend Ratio'. In: *Polymer Symposium, Kebangsaan Ke-V, Malaysia*. 2005.
- [49] P. Haupt. *Continuum Mechanics and Theory of Materials*. Second. Springer-Verlag Berlin Heidelberg, 2002.
- [50] R. N. Haward, ed. *The Physics of Glassy Polymers*. Second. Springer Netherlands, 1997. DOI: 10.1007/978-94-011-5850-3.
- [51] M. Helbig et al. 'Continuum-Micromechanical Modeling of Distributed Crazing in Rubber-Toughened Polymers'. In: *Eur. J. Mech. A/Solids* 57 (2016), pp. 108–120. DOI: 10.1016/j.euromechsol.2015.11.007.
- [52] M. Helbig. 'Mehrskalenmodellierung von Schädigung in gummimodifizierten thermoplastischen Kunststoffen'. Doctoral Thesis. Karlsruher Institut für Technologie (KIT), 2016. DOI: 10.5445/IR/1000059308.
- [53] P. Hempel. 'Constitutive Modeling of Amorphous Thermoplastic Polymers with Special Emphasis on Manufacturing Processes'. Doctoral Thesis. Karlsruher Institut für Technologie (KIT), 2016. DOI: 10.5445/KSP/1000056493.
- [54] S. Hiermaier and F. Huberth. 'Volume Dilatation in a Polycarbonate Blend at Varying Strain Rates'. In: *The European Physical Journal Special Topics* 206.1 (2012), pp. 173–181. DOI: 10.1140/epjst/e2012-01598-x.
- [55] G. A. Holzapfel. *Nonlinear Solid Mechanics: A Continuum Approach for Engineering*. Repr. Chichester ; Weinheim [u.a.]: Wiley, 2010.



- [56] J.-C. Huang and M.-S. Wang. 'Recent Advances in ABS/PC Blends'. In: *Advances in Polymer Technology* 9.4 (1989), pp. 293–299. DOI: 10.1002/adv.1989.060090403.
- [57] J. P. F. Inberg and R. J. Gaymans. 'Co-Continuous Polycarbonate/ABS Blends'. In: *Polymer* 43.8 (2002), pp. 2425–2434. DOI: 10.1016/S0032-3861(01)00813-8.
- [58] J. P. F. Inberg and R. J. Gaymans. 'Polycarbonate and Co-Continuous Polycarbonate/ABS Blends: Influence of Notch Radius'. In: *Polymer* 43.15 (2002), pp. 4197–4205. DOI: 10.1016/S0032-3861(02)00220-3.
- [59] J. P. F. Inberg. 'Fracture of Polycarbonate/ABS Blends.' In: *PhD thesis, University of Twente* (2001).
- [60] M. Ishikawa. 'Stability of Plastic Deformation and Toughness of Polycarbonate Blended with Poly(Acrylonitrile-Butadiene-Styrene) Copolymer'. In: *Polymer* 36.11 (1995), pp. 2203–2210. DOI: 10.1016/0032-3861(95)95297-E.
- [61] P.-Y. B. Jar et al. 'Rubber Particle Cavitation on Toughness Enhancement of SMI-Modified Poly(Acrylonitrile-Butadiene-Styrene)'. In: *Journal of Polymer Science Part B: Polymer Physics* 37.14 (1999), pp. 1739–1748. DOI: 10.1002/(SICI)1099-0488(19990715)37:14<1739::AID-POLB16>3.0.CO;2-Z.
- [62] P.-Y. B. Jar et al. 'Mechanical Properties and Deformation Mechanisms in High Thermal Resistant Poly(Acrylonitrile-Butadiene-Styrene) under Static Tension and Izod Impact'. In: *Journal of Applied Polymer Science* 85.1 (2002), pp. 17–24. DOI: 10.1002/app.10522.
- [63] R. P. Kambour. 'A Review of Crazeing and Fracture in Thermoplastics'. In: *Journal of Polymer Science: Macromolecular Reviews* 7.1 (1973), pp. 1–154. DOI: 10.1002/pol.1973.230070101.
- [64] B. Kattakola, A. Ranjan, and S. Basu. 'Three Dimensional Finite Element Investigations into the Effects of Thickness and Notch Radius on the Fracture Toughness of Polycarbonate'. In: *International Journal of Fracture* 181.1 (2013), pp. 1–12. DOI: 10.1007/s10704-013-9808-5.
- [65] H. H. Kausch, ed. *Crazeing in Polymers Vol. 2*. Advances in Polymer Science, Adv Polymer Science Kausch, H.H. (Ed): Crazeing Polymers. Berlin Heidelberg: Springer-Verlag, 1990. DOI: 10.1007/BFb0018017.
- [66] M. M. K. Khan et al. 'Rheological and Mechanical Properties of ABS/PC Blends'. In: *Korea-Australia Rheology Journal* 17.1 (2005), pp. 1–7.
- [67] R. Krache and I. Debah. 'Some Mechanical and Thermal Properties of PC/ABS Blends'. In: *Materials Sciences and Applications* 2.5 (2011), pp. 404–410.
- [68] E. Kröner. 'Allgemeine Kontinuumstheorie der Versetzungen und Eigenspannungen'. In: *Archive for Rational Mechanics and Analysis* 4.1 (1959), p. 273. DOI: 10.1007/BF00281393.
- [69] T. Kurauchi and T. Ohta. 'Energy Absorption in Blends of Polycarbonate with ABS and SAN'. In: *Journal of Materials Science* 19.5 (1984), pp. 1699–1709. DOI: 10.1007/BF00563068.

- [70] J. Lai and E. Van der Giessen. 'A Numerical Study of Crack-Tip Plasticity in Glassy Polymers'. In: *Mech. Mater.* 25 (1997), pp. 183–197.
- [71] T. Laschütza. 'Numerical Study of Adiabatic Temperature Effects during Fracture of Thermoplastic Polymers'. Master's Thesis. Karlsruhe Institut für Technologie (KIT), 2018.
- [72] A. Lazzeri and C. B. Bucknall. 'Dilatational Bands in Rubber-Toughened Polymers'. In: *Journal of Materials Science* 28.24 (1993), pp. 6799–6808. DOI: 10.1007/BF00356433.
- [73] E. H. Lee. 'Elastic-Plastic Deformation at Finite Strains'. In: *Journal of Applied Mechanics* 36.1 (1969), pp. 1–6. DOI: 10.1115/1.3564580.
- [74] M. -P. Lee, A. Hiltner, and E. Baer. 'Phase Morphology of Injection-Moulded Polycarbonate/Acrylonitrile-Butadiene-Styrene Blends'. In: *Polymer* 33.4 (1992), pp. 685–697. DOI: 10.1016/0032-3861(92)90323-0.
- [75] M.-P. Lee, A. Hiltner, and E. Baer. 'Formation and Break-up of a Bead-and-String Structure during Injection Moulding of a Polycarbonate/Acrylonitrile-Butadiene-Styrene Blend'. In: *Polymer* 33.4 (1992), pp. 675–684. DOI: 10.1016/0032-3861(92)90322-N.
- [76] B. S. Lombardo, H. Keskkula, and D. R. Paul. 'Influence of ABS Type on Morphology and Mechanical Properties of PC/ABS Blends'. In: *J. Appl. Pol. Sci.* 54.11 (1994), pp. 1697–1720. DOI: 10.1002/app.1994.070541113.
- [77] H. Louche et al. 'An Experimental and Modeling Study of the Thermomechanical Behavior of an {ABS Polymer Structural Component during an Impact Test'. In: *International Journal of Impact Engineering* 36.6 (2009), pp. 847–861. DOI: 10.1016/j.ijimpeng.2008.09.007.
- [78] J. Lu and K. Ravi-Chandar. 'Inelastic Deformation and Localization in Polycarbonate under Tension'. In: *International Journal of Solids and Structures* 36.3 (1999), pp. 391–425. DOI: 10.1016/S0020-7683(98)00004-3.
- [79] M. Ma et al. 'Shear Yielding Modes of Polycarbonate'. In: *Journal of Materials Science* 24.8 (1989), pp. 2687–2696. DOI: 10.1007/BF02385612.
- [80] R. v Mises. 'Mechanik der festen Körper im plastisch- deformablen Zustand'. In: *Nachrichten von der Gesellschaft der Wissenschaften zu Göttingen, Mathematisch-Physikalische Klasse* 1913 (1913), pp. 582–592.
- [81] T. Mori and K. Tanaka. 'Average Stress in Matrix and Average Elastic Energy of Materials with Misfitting Inclusions'. In: *Acta Metallurgica* 21.5 (1973), pp. 571–574. DOI: 10.1016/0001-6160(73)90064-3.
- [82] A. D. Mulliken and M. C. Boyce. 'Mechanics of the Rate-Dependent Elastic-Plastic Deformation of Glassy Polymers from Low to High Strain Rates'. In: *International Journal of Solids and Structures* 43.5 (2006), pp. 1331–1356. DOI: 10.1016/j.ijsolstr.2005.04.016.

- [83] I. Narisawa and A. Yee. 'Materials Science and Technology: A Comprehensive Treatment'. In: *Structure and Properties of Polymers*. Vol. 12. VCH Publishers Inc. New York, 1993, pp. 699–765.
- [84] J. Naumann. 'Bruchmechanische Experimente an Kunststoffen unter optischer Verformungsanalyse mittels digitaler Bildkorrelation'. Bachelor Thesis. Karlsruher Institut für Technologie (KIT), 2015.
- [85] B. Ni, J. Li, and V. Berry. 'Plastic Zone in Front of a Mode I Crack in Acrylonitrile-Butadiene-Styrene Polymers'. In: *Polymer* 32.15 (1991), pp. 2766–2770. DOI: 10.1016/0032-3861(91)90106-5.
- [86] I. Nigam, D. Nigam, and G. N. Mathur. 'Effect of Rubber Content in ABS on Properties of PC/ABS Blends'. In: *Pol.-Plast. Tech. Eng.* 44 (2005), pp. 815–832.
- [87] C. Park et al. 'Determination of True Stress–True Strain Curves of Polymers at Various Strain Rates Using Force Equilibrium Grid Method'. In: *Journal of Composite Materials* 46.17 (2012), pp. 2065–2077. DOI: 10.1177/0021998311429882.
- [88] M. Polanco-Loria et al. 'Constitutive Model for Thermoplastics with Structural Applications'. In: *Int. J. Impact Eng.* 37.12 (2010), pp. 1207–1219. DOI: 10.1016/j.ijimpeng.2010.06.006.
- [89] R. Raghava, R. M. Caddell, and G. S. Y. Yeh. 'The Macroscopic Yield Behaviour of Polymers'. In: *Journal of Materials Science* 8.2 (1973), pp. 225–232. DOI: 10.1007/BF00550671.
- [90] J. Ruge. 'Entwicklung eines viskoplastischen Werkstoffmodells für gummi-modifizierte thermoplastische Kunststoffe'. Master's Thesis. Karlsruher Institut für Technologie (KIT), 2017.
- [91] H. W. Schreier and R. Lichtenberger. 'Kombination von Stereoskopie Und Digitalen Korrelationsverfahren Zur Messung von Kontur, Verformung Und Dehnung'. In: *3D Tag Oldenburg*. 2003.
- [92] T. Seelig and E. Van der Giessen. 'Localized Plastic Deformation in Ternary Polymer Blends'. In: *International Journal of Solids and Structures* 39.13 (2002), pp. 3505–3522. DOI: 10.1016/S0020-7683(02)00161-0.
- [93] T. Seelig and E. Van der Giessen. 'Effects of Microstructure on Crack Tip Fields and Fracture Toughness in PC/ABS Polymer Blends'. In: *Int. J. Frac.* 145 (2007), pp. 205–222. DOI: 10.1007/s10704-007-9117-y.
- [94] T. Seelig and E. Van der Giessen. 'A Cell Model Study of Crazing and Matrix Plasticity in Rubber-Toughened Glassy Polymers'. In: *Computational Materials Science* 45.3 (2009), pp. 725–728. DOI: 10.1016/j.commatsci.2008.05.024.
- [95] S. Seidler and W. Grellmann. 'Fracture Behaviour and Morphology of PC/ABS Blends'. In: *J. Mat. Sci.* 28.15 (1993), pp. 4078–4084. DOI: 10.1007/BF00351236.
- [96] B. R. Seth. *Generalized Strain Measure with Applications to Physical Problems*. Tech. rep. WISCONSIN UNIV-MADISON MATHEMATICS RESEARCH CENTER, 1961.

- [97] R. J. M. Smit, W. A. M. Brekelmans, and H. E. H. Meijer. 'Predictive Modelling of the Properties and Toughness of Polymeric Materials Part I Why Is Polystyrene Brittle and Polycarbonate Tough?' In: *Journal of Materials Science* 35.11 (2000), pp. 2855–2867. DOI: 10.1023/A:1004711622159.
- [98] S. Socrate and M. C. Boyce. 'Micromechanics of Toughened Polycarbonate'. In: *Journal of the Mechanics and Physics of Solids* 48.2 (2000), pp. 233–273. DOI: 10.1016/S0022-5096(99)00037-X.
- [99] A. C. Steenbrink, E. Van Der Giessen, and P. D. Wu. 'Void Growth in Glassy Polymers'. In: *Journal of the Mechanics and Physics of Solids* 45.3 (1997), pp. 405–437. DOI: 10.1016/S0022-5096(96)00093-2.
- [100] A. C. Steenbrink, E. Van Der Giessen, and P. D. Wu. 'Studies on the Growth of Voids in Amorphous Glassy Polymers'. In: *Journal of Materials Science* 33.12 (1998), pp. 3163–3175. DOI: 10.1023/A:1004356108870.
- [101] V. K. Stokes. *Introduction to Plastics Engineering*. Wiley-ASME Press Series. John Wiley & Sons, 2020.
- [102] V. K. Stokes and W. C. Bushko. 'On the Phenomenology of Yield in Bisphenol-a Polycarbonate'. In: *Polymer Engineering & Science* 35.4 (1995), pp. 291–303. DOI: 10.1002/pen.760350403.
- [103] H. Suarez, J. W. Barlow, and D. R. Paul. 'Mechanical Properties of ABS/Polycarbonate Blends'. In: *J. Appl. Pol. Sci.* 29.11 (1984), pp. 3253–3259. DOI: 10.1002/app.1984.070291104.
- [104] M. A. Sutton et al. 'The Effect of Out-of-Plane Motion on 2D and 3D Digital Image Correlation Measurements'. In: *Optics and Lasers in Engineering* 46.10 (2008), pp. 746–757. DOI: 10.1016/j.optlaseng.2008.05.005.
- [105] Z. Tadmor. 'Molecular Orientation in Injection Molding'. In: *Journal of Applied Polymer Science* 18.6 (1974), pp. 1753–1772. DOI: 10.1002/app.1974.070180614.
- [106] Z. Y. Tan et al. 'Influence of Rubber Content in ABS in Wide Range on the Mechanical Properties and Morphology of PC/ABS Blends with Different Composition'. In: *Pol. Eng. Sci.* 46.10 (2006), pp. 1476–1484. DOI: 10.1002/pen.20584.
- [107] T. A. Tervoort and L. E. Govaert. 'Strain-Hardening Behavior of Polycarbonate in the Glassy State'. In: *Journal of Rheology* 44.6 (2000), pp. 1263–1277. DOI: 10.1122/1.1319175.
- [108] M. G. A. Tijssens, E. Van der Giessen, and L. J. Sluys. 'Modeling of Crazeing Using a Cohesive Surface Methodology'. In: *Mechanics of Materials* 32.1 (2000), pp. 19–35. DOI: 10.1016/S0167-6636(99)00044-7.
- [109] V. Tvergaard. 'On Localization in Ductile Materials Containing Spherical Voids'. In: *International Journal of Fracture* 18.4 (1982), pp. 237–252. DOI: 10.1007/BF00015686.

- [110] E. Van der Giessen and T. Seelig. 'Computational Modeling of Rubber-Toughening in Amorphous Thermoplastic Polymers: A Review'. In: *Int. J. Frac.* 196.1 (2015), pp. 207–222. DOI: 10.1007/s10704-015-0066-6.
- [111] M. C. M. van der Sanden, J. M. M. de Kok, and H. E. H. Meijer. 'Deformation and Toughness of Polymeric Systems: 7. Influence of Dispersed Rubbery Phase'. In: *Polymer* 35.14 (1994), pp. 2995–3004. DOI: 10.1016/0032-3861(94)90412-X.
- [112] H. Wang et al. 'Experimental Investigation and Modeling of the Mechanical Behavior of PC/ABS during Monotonic and Cyclic Loading'. In: *Polymer Testing* 50 (2016), pp. 216–223. DOI: 10.1016/j.polymertesting.2015.12.010.
- [113] G. Weber and J. Schoeps. 'Morphologie und technologische Eigenschaften von Polycarbonat/ABS-Mischungen'. In: *Die Angewandte Makromolekulare Chemie* 136.1 (1985), pp. 45–64. DOI: 10.1002/apmc.1985.051360104.
- [114] G. Wildes, H. Keskkula, and D. R. Paul. 'Fracture Characterization of PC/ABS Blends: Effect of Reactive Compatibilization, ABS Type and Rubber Concentration'. In: *Polymer* 40.25 (1999), pp. 7089–7107. DOI: 10.1016/S0032-3861(98)00865-9.
- [115] P. Wriggers. *Nonlinear Finite Element Methods*. Berlin: Springer, 2008.
- [116] J.-S. Wu, S.-C. Shen, and F.-C. Chang. 'Effect of Polycarbonate Molecular Weight on Polymer Blends of Polycarbonate and ABS'. In: *Journal of Applied Polymer Science* 50.8 (1993), pp. 1379–1389. DOI: 10.1002/app.1993.070500809.
- [117] X. Xu and X. Xu. 'Mechanical Properties and Deformation Behaviors of Acrylonitrile-Butadiene-Styrene under Izod Impact Test and Uniaxial Tension at Various Strain Rates'. In: *Polymer Engineering & Science* 51.5 (2011), pp. 902–907. DOI: 10.1002/pen.21908.
- [118] K. Yang, S.-H. Lee, and J.-M. Oh. 'Effects of Viscosity Ratio and Compatibilizers on the Morphology and Mechanical Properties of Polycarbonate/Acrylonitrile-Butadiene-Styrene Blends'. In: *Polymer Engineering & Science* 39.9 (1999), pp. 1667–1677. DOI: 10.1002/pen.11561.
- [119] Z.-n. Yin and T.-j. Wang. 'Investigation of Tensile Deformation Behavior of PC, ABS, and PC/ABS Blends from Low to High Strain Rates'. In: *Applied Mathematics and Mechanics* 33.4 (2012), pp. 455–464. DOI: 10.1007/s10483-012-1563-x.
- [120] M. Yokouchi, S. Seto, and Y. Kobayashi. 'Comparison of Polystyrene, Poly(Styrene/Acrylonitrile), High-Impact Polystyrene, and Poly(Acrylonitrile/Butadiene/Styrene) with Respect to Tensile and Impact Properties'. In: *Journal of Applied Polymer Science* 28.7 (1983), pp. 2209–2216. DOI: 10.1002/app.1983.070280707.
- [121] B. Zhao et al. 'Effect of Methyl Methacrylate Graft Acrylonitrile-Butadiene-Styrene on Morphology and Properties of Polycarbonate/Acrylonitrile-Butadiene-Styrene Blend'. In: *Journal of Macromolecular Science, Part B* 51.11 (2012), pp. 2276–2283. DOI: 10.1080/00222348.2012.672839.
- [122] G.-J. Zhong and Z.-M. Li. 'Injection Molding-Induced Morphology of Thermoplastic Polymer Blends'. In: *Polymer Engineering & Science* 45.12 (2005), pp. 1655–1665. DOI: 10.1002/pen.20448.



# List of figures

3.1.	Network of entangled macromolecules of a thermoplastic. . . . .	33
3.2.	Deformed network of entangled macromolecules of a thermoplastic. . . . .	33
3.3.	Uniaxial stress-strain response of PC for different nominal strain rates [38].	34
3.4.	Schematic illustration of the stages of the necking process in a PC specimen under uniaxial tension (adapted from Stokes and Bushko [102]). . . . .	35
3.5.	Schematic visualisation of the craze propagation through the meniscus instability process (adapted from Stokes [101]). . . . .	36
3.6.	Micrograph of an ABS blend with homogeneous rubber particles [40]. . . . .	37
3.7.	Micrograph of an ABS blend featuring rubber particles with SAN subinclusions (“salami” structure) [40]. . . . .	38
3.8.	Uniaxial stress-strain response and volume strain response of ABS for different nominal strain rates [52]. . . . .	40
3.9.	Impact strength of PC/ABS blends in Izod test setup (adapted from Greco [42]).	41
3.10.	Standard notch and sharp notch Izod impact strength of PC/ABS blends (adapted from Lombardo, Keskkula, and Paul [76]). . . . .	41
3.11.	Izod impact strength of PC/ABS blends (adapted from Suarez, Barlow, and Paul [103]). . . . .	41
3.12.	Micrograph of a PC/ABS (70/30) blend with homogeneous rubber particles [114].	43
3.13.	Micrographs from Dong, Greco, and Orsello [32] of PC/ABS (60/40) and PC/ABS (40/60). . . . .	44
4.1.	The morphology at the surface of the three PC/ABS blends investigated. . . . .	51
4.2.	Detail of the morphology at the surface of the three PC/ABS blends investigated.	51
4.3.	The morphology in the skin layer of the three PC/ABS blends investigated.	52
4.4.	Detail of the morphology in the skin layer of (a) PC/ABS (70/30) and (b) PC/ABS (45/55). . . . .	52
4.5.	The morphology in the core region of the three PC/ABS blends investigated.	53
4.6.	Detail of the morphology in the core region of the three PC/ABS blends investigated. . . . .	53
5.1.	Geometry of tensile test specimen (thickness $t = (3.22 \pm 0.01)$ mm). . . . .	58
5.2.	Geometry of SENT fracture test specimen (thickness $t = (3.22 \pm 0.01)$ mm).	59
5.3.	Specimen orientations relative to material flow during injection moulding. . . . .	59
5.4.	Example specimens showing speckle pattern for (a) the uniaxial tensile tests and (b) the SENT fracture tests. . . . .	60

---

5.5.	Displacement and deformation of the reference square subset with centre point $P(x_0, y_0)$ . . . . .	61
5.6.	Transverse strain $\epsilon_{tr}$ measured using DIC in the $xy$ -plane and $xz$ -plane of the specimen surface and corresponding true stress-strain curves. . . . .	63
5.7.	Transverse logarithmic strains in the $xy$ -plane and $xz$ -plane of the specimen surface and corresponding true stress-strain curves from FE simulations. . . . .	64
6.1.	Force-displacement behaviour depending on PC/ABS composition at a crosshead speed of $\dot{u} = 1.0$ mm/s. . . . .	68
6.2.	Distribution of the axial strain $\epsilon_{xx}$ on the specimen surface of PC/ABS (45/55) belonging to curve (A). . . . .	69
6.3.	Distribution of the axial strain $\epsilon_{xx}$ on the specimen surface of PC/ABS (60/40) belonging to curve (B). . . . .	69
6.4.	Distribution of the axial strain $\epsilon_{xx}$ on the specimen surface of PC/ABS (70/30) belonging to curve (C). . . . .	69
6.5.	True stress-strain behaviour depending on PC/ABS composition at a strain rate of $\dot{\epsilon} = 0.1$ s <sup>-1</sup> . . . . .	70
6.6.	True stress-strain behaviour of the three PC/ABS blends for a log. axial strain up to $\epsilon = 0.1$ at a strain rate of $\dot{\epsilon} = 0.1$ s <sup>-1</sup> . . . . .	70
6.7.	Dilation behaviour depending on PC/ABS composition at a strain rate of $\dot{\epsilon} = 0.1$ s <sup>-1</sup> . . . . .	70
6.8.	Poisson's ratio depending on PC/ABS composition at a strain rate of $\dot{\epsilon} = 0.1$ s <sup>-1</sup> . . . . .	72
6.9.	Force-displacement behaviour depending on PC/ABS composition at a crosshead speed of $\dot{u} = 0.1$ mm/s; the DIC strain fields belonging to experiments (A), (B), and (C) are shown in Figs. 6.10, 6.11, and 6.12. . . . .	73
6.10.	Distribution of the axial strain $\epsilon_{xx}$ on the specimen surface of PC/ABS (45/55) belonging to curve (A). . . . .	74
6.11.	Distribution of the axial strain $\epsilon_{xx}$ on the specimen surface of PC/ABS (60/40) belonging to curve (B). . . . .	74
6.12.	Distribution of the axial strain $\epsilon_{xx}$ on the specimen surface of PC/ABS (70/30) belonging to curve (C). . . . .	74
6.13.	True stress-strain behaviour depending on PC/ABS composition at a strain rate of $\dot{\epsilon} = 0.01$ s <sup>-1</sup> . . . . .	75
6.14.	Dilation behaviour depending on PC/ABS composition at a strain rate of $\dot{\epsilon} = 0.01$ s <sup>-1</sup> . . . . .	75
6.15.	Poisson's ratio depending on PC/ABS composition at a strain rate of $\dot{\epsilon} = 0.01$ s <sup>-1</sup> . . . . .	75
6.16.	Contours of the strain $\epsilon_{xx}$ in tensile direction on SENT specimen for PC/ABS (45/55) at a crosshead speed of $\dot{u} = 0.6$ mm/s. . . . .	77
6.17.	Contours of the strain $\epsilon_{xx}$ in tensile direction on SENT specimen for PC/ABS (60/40) at a crosshead speed of $\dot{u} = 0.6$ mm/s. . . . .	77
6.18.	Contours of the strain $\epsilon_{xx}$ in tensile direction on SENT specimen for PC/ABS (70/30) at a crosshead speed of $\dot{u} = 0.6$ mm/s. . . . .	77
6.19.	Contours of the strain $\epsilon_{xx}$ in tensile direction on SENT specimen for PC/ABS (45/55) at a crosshead speed of $\dot{u} = 6.0$ mm/s. . . . .	78



6.20.	Contours of the strain $\epsilon_{xx}$ in tensile direction on SENT specimen for PC/ABS (60/40) at a crosshead speed of $\dot{u} = 6.0$ mm/s. . . . .	78
6.21.	Contours of the strain $\epsilon_{xx}$ in tensile direction on SENT specimen for PC/ABS (70/30) at a crosshead speed of $\dot{u} = 6.0$ mm/s. . . . .	78
6.22.	Force-displacement curves from SENT tests on PC/ABS blends at a crosshead speed of $\dot{u} = 0.6$ mm/s. . . . .	80
6.23.	Force-displacement curves from SENT tests on PC/ABS blends at a crosshead speed of $\dot{u} = 6.0$ mm/s. . . . .	80
6.24.	Specific work of fracture $w$ depending on composition for both crosshead speeds investigated. . . . .	80
6.25.	Stress response of PC/ABS (45/55) to uniaxial tension for two values of the nominal strain rate $\dot{\epsilon}$ . . . . .	83
6.26.	Stress response of PC/ABS (60/40) to uniaxial tension for two values of the nominal strain rate $\dot{\epsilon}$ . . . . .	83
6.27.	Stress response of PC/ABS (70/30) to uniaxial tension for two values of the nominal strain rate $\dot{\epsilon}$ . . . . .	83
6.28.	Volume strain response of PC/ABS (45/55) in uniaxial tensile tests for two values of the nominal strain rate $\dot{\epsilon}$ . . . . .	84
6.29.	Volume strain response of PC/ABS (60/40) in uniaxial tensile tests for two values of the nominal strain rate $\dot{\epsilon}$ . . . . .	84
6.30.	Volume strain response of PC/ABS (70/30) in uniaxial tensile tests for two values of the nominal strain rate $\dot{\epsilon}$ . . . . .	84
6.31.	Force-displacement curves of PC/ABS (45/55) from SENT fracture tests for two values of the test speed $\dot{u}$ . . . . .	86
6.32.	Force-displacement curves of PC/ABS (60/40) from SENT fracture tests for two values of the test speed $\dot{u}$ . . . . .	86
6.33.	Force-displacement curves of PC/ABS (70/30) from SENT fracture tests for two values of the test speed $\dot{u}$ . . . . .	86
7.1.	True stress-strain behaviour of PC/ABS (45/55) depending on the specimen orientation at a strain rate of (a) $\dot{\epsilon} = 0.01$ s <sup>-1</sup> and (b) $\dot{\epsilon} = 0.1$ s <sup>-1</sup> . . . . .	90
7.2.	Dilation behaviour of PC/ABS (45/55) depending on the specimen orientation at a strain rate of (a) $\dot{\epsilon} = 0.01$ s <sup>-1</sup> and (b) $\dot{\epsilon} = 0.1$ s <sup>-1</sup> . . . . .	91
7.3.	True stress-strain behaviour of PC/ABS (60/40) depending on the specimen orientation at a strain rate of (a) $\dot{\epsilon} = 0.01$ s <sup>-1</sup> and (b) $\dot{\epsilon} = 0.1$ s <sup>-1</sup> . . . . .	92
7.4.	Dilation behaviour of PC/ABS (60/40) depending on the specimen orientation at a strain rate of (a) $\dot{\epsilon} = 0.01$ s <sup>-1</sup> and (b) $\dot{\epsilon} = 0.1$ s <sup>-1</sup> . . . . .	92
7.5.	True stress-strain behaviour of PC/ABS (70/30) depending on the specimen orientation at a strain rate of (a) $\dot{\epsilon} = 0.01$ s <sup>-1</sup> and (b) $\dot{\epsilon} = 0.1$ s <sup>-1</sup> . . . . .	93
7.6.	Dilation behaviour of PC/ABS (70/30) depending on the specimen orientation at a strain rate of (a) $\dot{\epsilon} = 0.01$ s <sup>-1</sup> and (b) $\dot{\epsilon} = 0.1$ s <sup>-1</sup> . . . . .	93
7.7.	Force-displacement curves from SENT tests on PC/ABS (45/55) for two specimen orientations and a test speed of (a) $\dot{u} = 0.6$ mm/s and (b) $\dot{u} = 6.0$ mm/s. . . . .	94

7.8.	Force-displacement curves from SENT tests on PC/ABS (60/40) for two specimen orientations and a test speed of (a) $\dot{u} = 0.6$ mm/s and (b) $\dot{u} = 6.0$ mm/s.	95
7.9.	Force-displacement curves from SENT tests on PC/ABS (70/30) for two specimen orientations and a test speed of (a) $\dot{u} = 0.6$ mm/s and (b) $\dot{u} = 6.0$ mm/s.	95
7.10.	Specific work of fracture $w$ depending on the specimen orientation for all three blends and both deformation speeds investigated. . . . .	96
7.11.	Poisson's ratio $\nu$ of PC/ABS (60/40) for the different specimen orientations at a strain rate of (a) $\dot{\epsilon} = 0.01$ s <sup>-1</sup> and (b) $\dot{\epsilon} = 0.1$ s <sup>-1</sup> . . . . .	97
7.12.	Force-displacement response of PC/ABS (60/40) for the different specimen orientations and crosshead speeds. . . . .	97
7.13.	Uniaxial stress response of PC/ABS (45/55) with a specimen orientation perpendicular to the melt flow during manufacturing for two values of the nominal strain rate $\dot{\epsilon}$ . . . . .	98
8.1.	Cubic unit cell of the microstructure with void of radius $r$ and equatorial plane.	107
8.2.	Schematic illustration of the deformation stages a representative volume element (RVE) undergoes during crazing (adapted from Helbig et al. [51]). .	109
9.1.	Uniaxial stress-strain response and dilation behaviour of all models compared to experimental data for PC/ABS (45/55) and a nominal strain rate of $\dot{\epsilon} = 0.1$ s <sup>-1</sup> .	114
9.2.	Uniaxial stress-strain response and dilation behaviour of all models compared to experimental data for PC/ABS (60/40) and a nominal strain rate of $\dot{\epsilon} = 0.1$ s <sup>-1</sup> .	114
9.3.	Uniaxial stress-strain response and dilation behaviour of all models compared to experimental data for PC/ABS (70/30) and a nominal strain rate of $\dot{\epsilon} = 0.1$ s <sup>-1</sup> .	114
9.4.	Uniaxial stress-strain responses of all models compared to experimental data for PC/ABS (45/55) at two strain rates. . . . .	115
9.5.	Initial yield loci in $\sigma_m$ - $\sigma_e$ -plane calibrated for PC/ABS (45/55). . . . .	116
9.6.	Initial yield loci in $\sigma_m$ - $\sigma_e$ -plane calibrated for PC/ABS (60/40). . . . .	116
9.7.	Initial yield loci in $\sigma_e$ - $\sigma_m$ -plane calibrated for PC/ABS (70/30). . . . .	116
9.8.	Tensile stress-strain response and evolution of volume strain with axial strain of the Drucker-Prager, the Raghava, and the Green model under elevated stress triaxialities. . . . .	117
9.9.	FE model of half the SENT specimen exploiting symmetry with respect to centre plane with expected crack path indicated in red. . . . .	118
9.10.	Contours of the stress triaxiality $\eta$ on SENT specimen surface, notch and centre plane at a specimen elongation of $u = 1.8$ mm (prior to fracture) simulated for PC/ABS (70/30) using the Raghava model. . . . .	118
9.11.	Contours of the equivalent plastic strain $\epsilon^p$ at notch in PC/ABS (45/55) at two different values of specimen elongation simulated using the Drucker-Prager model. . . . .	119
9.12.	Contours of the equivalent plastic strain $\epsilon^p$ at notch in PC/ABS (45/55) at two different values of specimen elongation simulated using the Raghava model.	120

9.13.	Contours of the strain in tensile direction $\epsilon_{xx}$ at notch in PC/ABS (45/55) at two different values of specimen elongation simulated using the Drucker-Prager model. . . . .	120
9.14.	Contours of the strain in tensile direction $\epsilon_{xx}$ at notch in PC/ABS (45/55) at two different values of specimen elongation simulated using the Raghava model. . . . .	121
9.15.	Distribution of strain in tensile direction at notch in PC/ABS (60/40) at two different values of specimen elongation simulated using the Drucker-Prager model. . . . .	121
9.16.	Distribution of strain in tensile direction at notch in PC/ABS (70/30) at two different values of specimen elongation simulated using the Drucker-Prager model. . . . .	122
9.17.	Distribution of strain in tensile direction at notch in PC/ABS (60/40) at two different values of specimen elongation simulated using the Raghava model. . . . .	122
9.18.	Distribution of strain in tensile direction at notch in PC/ABS (70/30) at two different values of specimen elongation simulated using the Drucker-Prager model. . . . .	123
9.19.	Distribution of strain in tensile direction at notch in PC/ABS (70/30) simulated using the Green model. . . . .	124
9.20.	Advancing crack in SENT specimen of PC/ABS (70/30) and distribution of accumulated plastic strain computed from Raghava model at specimen elongation of $u = 2.0$ mm. . . . .	125
9.21.	Force-displacement curve of PC/ABS (45/55) from SENT fracture test compared to simulations using the Drucker-Prager or Raghava model and a failure criterion based on (a) $\epsilon_{crit}^p$ and (b) $w_{crit}^p$ . . . . .	127
9.22.	Force-displacement curve of PC/ABS (60/40) from SENT fracture test compared to simulations using the Drucker-Prager or Raghava model and a failure criterion based on (a) $\epsilon_{crit}^p$ and (b) $w_{crit}^p$ . . . . .	127
9.23.	Force-displacement curve of PC/ABS (70/30) from SENT fracture test compared to simulations using the Drucker-Prager or Raghava model and a failure criterion based on (a) $\epsilon_{crit}^p$ and (b) $w_{crit}^p$ . . . . .	127
9.24.	Force-displacement curve of PC/ABS (70/30) from SENT fracture test compared to simulations using (a) the Drucker-Prager model and (b) the Raghava model with $w_{crit}^p$ failure criterion calibrated to the fine mesh. . . . .	128
10.1.	Schematic representation of unit cells with (a) BCC and (b) co-continuous phase arrangement. . . . .	133
10.2.	Meshed unit cells with (a) BCC and (b) co-continuous phase arrangement. . . . .	134
10.3.	Load cases characterised by $\langle \eta_\epsilon \rangle$ represented in the $\langle \epsilon_v \rangle$ - $\langle \epsilon_d \rangle$ strain space. . . . .	135
10.4.	Schematic representation of the FE model with each reference point $\boxtimes$ controlling the degrees of freedom (DOF) of the corresponding face of the hexahedral unit cell. . . . .	136

10.5. Strain rate dependency of the initial yield stress for PC and ABS based on averaging experimental results compiled from literature sources [77, 87, 117, 119, 20, 120, 22, 38, 82, 53]. . . . .	139
10.6. Stress-strain and volume strain response under uniaxial tension of the DC model ( $f_R = 20\%$ ) with the initial fit from Helbig et al. [51] and the final fit from the literature for three values of the strain rate. . . . .	141
10.7. Stress-strain and volume strain response under uniaxial tension of the Raghava model ( $f_R = 20\%$ ) with the initial fit from Helbig et al. [51] and the final fit from the literature for three values of the strain rate. . . . .	141
10.8. Response under uniaxial tension of the calibrated $J_2$ plasticity model for three values of the strain rate. . . . .	142
10.9. Stress-strain and volume strain response under uniaxial tension of the DC model for five values of the rubber volume fraction $f_R$ . . . . .	142
10.10. Stress-strain and volume strain response under uniaxial tension of the Raghava model for five values of the rubber volume fraction $f_R$ . . . . .	142
10.11. Uniaxial stress-strain and volume strain response of PC/ABS (70/30) unit cell models with the DC model in the ABS phase at a macroscopic strain rate $\langle \dot{\epsilon} \rangle = 0.1 \text{ s}^{-1}$ . . . . .	144
10.12. Uniaxial stress-strain and volume strain response of PC/ABS (70/30) unit cell models with the Raghava model in the ABS phase at a macroscopic strain rate $\langle \dot{\epsilon} \rangle = 0.1 \text{ s}^{-1}$ . . . . .	144
10.13. Impact of the stress triaxiality $\eta$ on the stress-strain and volume strain response of the DC model. . . . .	144
10.14. Impact of the stress triaxiality $\eta$ on the stress-strain and volume strain response of the Raghava model. . . . .	145
10.15. Component $n_x$ of the unit craze normal vector $\mathbf{n}$ for (a) uniaxial tension, (b) $\langle \eta_\epsilon \rangle = 2/3$ , and (c) $\langle \eta_\epsilon \rangle = 1$ in the PC/ABS (70/30) unit cell model with a rubber volume fraction $f_R = 20\%$ . . . . .	145
10.16. Contours of the hydrostatic stress $\sigma_m$ on PC/ABS (70/30) unit cell with (a) the DC model and (b) the Raghava model in the ABS phase subjected to uniaxial tension. . . . .	145
10.17. PC/ABS (70/30) unit cell failure behaviour under uniaxial tension for $f_R = 20\%$ with (a) DC model and (b) Raghava model in the ABS phase. . . . .	145
10.18. Uniaxial stress-strain and volume strain response of PC/ABS (60/40) unit cell model with the DC model in the ABS phase for two values of the rubber volume fraction $f_R$ and a macroscopic strain rate of $\langle \dot{\epsilon} \rangle = 0.1 \text{ s}^{-1}$ . . . . .	146
10.19. Uniaxial stress-strain and volume strain response of PC/ABS (60/40) unit cell model with the Raghava model in the ABS phase for two values of the rubber volume fraction $f_R$ and a macroscopic strain rate of $\langle \dot{\epsilon} \rangle = 0.1 \text{ s}^{-1}$ . . . . .	146
10.20. Contours of the hydrostatic stress $\sigma_m$ on PC/ABS (60/40) unit cell with (a) the DC model and (b) the Raghava model in the ABS phase subjected to uniaxial tension. . . . .	148
10.21. PC/ABS (60/40) unit cell failure behaviour under uniaxial tension for $f_R = 20\%$ with (a) DC model and (b) Raghava model in the ABS phase. . . . .	148

10.22. Contours of the hydrostatic stress $\sigma_m$ on PC/ABS (45/55) unit cell with (a) the DC model and (b) the Raghava model in the ABS phase subjected to uniaxial tension. . . . .	148
10.23. PC/ABS (45/55) unit cell failure behaviour under uniaxial tension for $f_R = 20\%$ with (a) DC model and (b) Raghava model in the ABS phase. . . . .	148
10.24. Uniaxial stress-strain and volume strain response of PC/ABS (45/55) unit cell models with the DC model in the ABS phase at a macroscopic strain rate $\langle \dot{\epsilon} \rangle = 0.1 \text{ s}^{-1}$ . . . . .	149
10.25. Uniaxial stress-strain and volume strain response of PC/ABS (45/55) unit cell models with the Raghava model in the ABS phase at a macroscopic strain rate $\langle \dot{\epsilon} \rangle = 0.1 \text{ s}^{-1}$ . . . . .	149
10.26. Macroscopic stress triaxiality $\eta$ for two values of the overall strain triaxiality $\langle \eta_\epsilon \rangle$ of PC/ABS (70/30) BCC unit cell model using the DC model with a rubber content of $f_R = 20\%$ in the ABS phase. . . . .	150
10.27. Macroscopic stress triaxiality $\eta$ for two values of the overall strain triaxiality $\langle \eta_\epsilon \rangle$ of PC/ABS (70/30) BCC unit cell model using the Raghava model with a rubber content of $f_R = 20\%$ in the ABS phase. . . . .	150
10.28. Specific work of fracture for PC/ABS ( $J_2$ /DC) unit cell models subjected to $\langle \eta_\epsilon \rangle = 2/3$ depending on the ABS mass fraction for five values of the rubber volume fraction $f_R$ . . . . .	151
10.29. Specific work of fracture for PC/ABS ( $J_2$ /DC) unit cell models subjected to $\langle \eta_\epsilon \rangle = 2/3$ for ABS mass fractions up to 40% and five values of the rubber volume fraction $f_R$ . . . . .	151
10.30. Failure pattern of PC/ABS (45/55) unit cell with the Raghava model in the ABS phase ( $f_R = 30\%$ ) subjected to $\langle \eta_\epsilon \rangle = 2/3$ in the stages of (a) failure initiation and (b) final failure. . . . .	153
10.31. Specific work of fracture for PC/ABS ( $J_2$ /R) unit cell models subjected to $\langle \eta_\epsilon \rangle = 2/3$ depending on the ABS mass fraction for five values of the rubber volume fraction $f_R$ . . . . .	154
10.32. Specific work of fracture for PC/ABS ( $J_2$ /R) unit cell models subjected to $\langle \eta_\epsilon \rangle = 2/3$ for ABS mass fractions up to 40% and five values of the rubber volume fraction $f_R$ . . . . .	154
10.33. Specific work of fracture for PC/ABS ( $J_2$ /DC) unit cell models subjected to $\langle \eta_\epsilon \rangle = 1$ depending on the ABS mass fraction for five values of the rubber volume fraction $f_R$ . . . . .	154
10.34. Specific work of fracture for PC/ABS ( $J_2$ /DC) unit cell models subjected to $\langle \eta_\epsilon \rangle = 1$ for ABS mass fractions up to 40% and five values of the rubber volume fraction $f_R$ . . . . .	154
10.35. Specific work of fracture for PC/ABS ( $J_2$ /R) unit cell models subjected to $\langle \eta_\epsilon \rangle = 1$ depending on the ABS mass fraction for five values of the rubber volume fraction $f_R$ . . . . .	156
10.36. Specific work of fracture for PC/ABS ( $J_2$ /R) unit cell models subjected to $\langle \eta_\epsilon \rangle = 1$ for ABS mass fractions up to 40% and five values of the rubber volume fraction $f_R$ . . . . .	156

10.37. Crack initiation and failure pattern of PC/ABS (80/20) BCC unit cell models subjected to $\langle \eta_\epsilon \rangle = 2/3$ using the DC model in the ABS phase for three values of the rubber volume fraction $f_R$ . . . . .	157
10.38. Crack initiation and failure pattern of PC/ABS (80/20) BCC unit cell models subjected to $\langle \eta_\epsilon \rangle = 2/3$ using the Raghava model in the ABS phase for three values of the rubber volume fraction $f_R$ . . . . .	157
10.39. Crack initiation and failure pattern of PC/ABS (70/30) BCC unit cell models subjected to $\langle \eta_\epsilon \rangle = 2/3$ using the Raghava model in the ABS phase for three values of the rubber volume fraction $f_R$ . . . . .	157
10.40. Crack initiation and failure pattern of BCC unit cell models subjected to $\langle \eta_\epsilon \rangle = 1$ using the DC model in the ABS phase for three values of the rubber volume fraction $f_R$ . . . . .	157
10.41. Crack initiation and failure pattern of PC/ABS (70/30) BCC unit cell models subjected to $\langle \eta_\epsilon \rangle = 1$ using the Raghava model in the ABS phase for three values of the rubber volume fraction $f_R$ . . . . .	157
10.42. Dependence of the deformation mechanism ratio $\alpha$ on the stress triaxiality $\eta$	160
10.43. Stress-strain and volume strain response of the $J_2$ -DC model subjected to uniaxial tension for three values of the strain rate. . . . .	160
10.44. Stress-strain and volume strain response under uniaxial tension of the $J_2$ -DC model for five values of the rubber volume fraction $f_R$ . . . . .	160
10.45. Stress-strain and volume strain response of the $J_2$ -DC model ( $f_R = 20\%$ ) for three different values of the stress triaxiality $\eta$ . . . . .	161
10.46. Uniaxial tensile response of the calibrated Boyce plasticity model for three values of the strain rate. . . . .	161
10.47. Stress-strain and volume strain response under uniaxial tension of the $J_2$ -DC model with failure behaviour modelled using the logistic function. . . . .	162
10.48. Uniaxial stress-strain and volume strain response of PC/ABS (70/30) unit cell models with the $J_2$ -DC model in the ABS phase at a macroscopic strain rate of $\langle \dot{\epsilon} \rangle = 0.1 \text{ s}^{-1}$ . . . . .	164
10.49. Uniaxial stress-strain and volume strain response of PC/ABS (60/40) unit cell models with the $J_2$ -DC model in the ABS phase at a macroscopic strain rate $\langle \dot{\epsilon} \rangle = 0.1 \text{ s}^{-1}$ . . . . .	164
10.50. Uniaxial stress-strain and volume strain response of PC/ABS (45/55) unit cell models with the $J_2$ -DC model in the ABS phase at a macroscopic strain rate $\langle \dot{\epsilon} \rangle = 0.1 \text{ s}^{-1}$ . . . . .	164
10.51. Contours of (a) the stress triaxiality $\eta$ and (b) the model quantity $\alpha$ on PC/ABS (70/30) unit cell ( $f_R = 20\%$ ). . . . .	165
10.52. Contours of $\alpha$ in the ABS phase of the PC/ABS (60/40) unit cell model $f_R = 20\%$ for overall strains of (a) $\langle \epsilon_{xx} \rangle = 0.07$ and (b) $\langle \epsilon_{xx} \rangle = 0.29$ where the PC phase has been removed for better visibility. . . . .	166
10.53. Uniaxial stress-strain and volume strain response of PC/ABS (70/30) unit cell models with the $J_2$ -DC model in the ABS phase and the Boyce model in the PC phase at a macroscopic strain rate $\langle \dot{\epsilon} \rangle = 0.1 \text{ s}^{-1}$ . . . . .	168

---

10.54. Uniaxial stress-strain and volume strain response of PC/ABS (60/40) unit cell models with the $J_2$ -DC model in the ABS phase and the Boyce model in the PC phase at a macroscopic strain rate $\langle \dot{\epsilon} \rangle = 0.1 \text{ s}^{-1}$ . . . . .	168
10.55. Uniaxial stress-strain and volume strain response of PC/ABS (45/55) unit cell models with the $J_2$ -DC model in the ABS phase and the Boyce model in the PC phase at a macroscopic strain rate $\langle \dot{\epsilon} \rangle = 0.1 \text{ s}^{-1}$ . . . . .	168
10.56. Uniaxial tensile response up to failure for the $J_2$ and Boyce material models used for PC. . . . .	169





# List of tables

4.1.	PC/ABS volume fractions, overall blend mass density and estimated mass density of the ABS phase for all three PC/ABS blends investigated. . . . .	51
4.2.	Mean particle size $\bar{d}$ with 95 % confidence interval (CI) for all three materials. . . . .	55
5.1.	Machining parameters for each stage of the specimen manufacturing process. . . . .	59
9.1.	Failure parameters calibrated for fine mesh (SENT specimen). . . . .	126
9.2.	Variation of the FE mesh parameters. . . . .	126
10.1.	Conversion of PC/ABS mass ratios to PC/ABS volume ratios. . . . .	132
A.1.	Modulus $E$ of the elastic deformation, initial yield stress $\sigma_0$ , and (minimum) yield stress $\sigma_{\min}$ after softening with corresponding strains $\varepsilon_0$ and $\varepsilon_{\min}$ for the three materials at a strain rate of $\dot{\varepsilon} = 0.1 \text{ s}^{-1}$ . . . . .	175
A.2.	Peak force $F_{\max}$ in uniaxial tensile tests and total specimen elongation at failure $u_{\text{fail}}$ for the three materials at a crosshead speed of $\dot{u} = 1.0 \text{ mm/s}$ . . . . .	175
A.3.	Uniaxial stress at failure $\sigma_{\text{fail}}$ and corresponding failure strain $\varepsilon_{\text{fail}}$ for all three materials at a strain rate of $\dot{\varepsilon} = 0.1 \text{ s}^{-1}$ . . . . .	175
A.4.	Peak force $F_{\max}$ and total specimen elongation at failure $u_{\text{fail}}$ for the three materials at a crosshead speed of $\dot{u} = 0.1 \text{ mm/s}$ . . . . .	175
A.5.	Initial yield stress $\sigma_0$ and (minimum) yield stress $\sigma_{\min}$ with corresponding strains $\varepsilon_0$ and $\varepsilon_{\min}$ for the three materials at a strain rate of $\dot{\varepsilon} = 0.01 \text{ s}^{-1}$ . . . . .	176
A.6.	Maximum and minimum Poisson's ratios with corresponding axial strains for the three materials for log. strains $\varepsilon > 0.03$ at a strain rate of $\dot{\varepsilon} = 0.1 \text{ s}^{-1}$ . . . . .	176
A.7.	Peak force $F_{\max}$ , corresponding overall specimen elongation $u_{\max}$ , and specimen elongation at complete specimen failure $u_{\text{fail}}$ of the three materials for two values of the crosshead speed $\dot{u}$ . . . . .	176
B.1.	Initial yield stress $\sigma_0$ of the three materials subjected to uniaxial tension for both specimen orientations investigated and two values the nominal strain rate $\dot{\varepsilon}$ . . . . .	177
B.2.	Peak force $F_{\max}$ of the three materials in SENT fracture tests for two specimen orientations and two values of the crosshead speed $\dot{u}$ . . . . .	177
B.3.	Total specimen elongation $u_{\max}$ corresponding to $F_{\max}$ of the three materials in SENT fracture tests for two specimen orientations and two values of the crosshead speed $\dot{u}$ . . . . .	177

B.4.	Total specimen elongation at failure $u_{fail}$ of the three materials in SENT fracture tests for two specimen orientations and two values of the crosshead speed $\dot{u}$ . . . . .	178
C.1.	Material parameters calibrated for PC/ABS (45/55). . . . .	179
C.2.	Material parameters calibrated for PC/ABS (60/40). . . . .	179
C.3.	Material parameters calibrated for PC/ABS (70/30). . . . .	180
D.1.	Material parameters for the Raghava model in the ABS phase. . . . .	181
D.2.	Material parameters for the DC model in the ABS phase. . . . .	181
D.3.	Material parameters for the $J_2$ -DC model in the ABS phase. . . . .	182
D.4.	Material parameters for the Boyce model. . . . .	182





# Schriftenreihe des Instituts für Mechanik

## ISSN 2363-4936

---

- Band 1    Marlon Franke  
**Discretisation techniques for large deformation computational contact elastodynamics.**  
ISBN 978-3-7315-0278-4
- Band 2    Philipp Hempel  
**Constitutive modeling of amorphous thermoplastic polymers with special emphasis on manufacturing processes.**  
ISBN 978-3-7315-0550-1
- Band 3    Martin Helbig  
**Mehrskalenmodellierung von Schädigung in gummimodifizierten thermoplastischen Kunststoffen.**  
ISBN 978-3-7315-0571-6
- Band 4    Maik Dittmann  
**Isogeometric analysis and hierarchical refinement for multi-field contact problems.**  
ISBN 978-3-7315-0616-4
- Band 5    Yinping Yang  
**Numerical methods for the inverse dynamics simulation of underactuated mechanical systems.**  
ISBN 978-3-7315-0626-3
- Band 6    Alexander Janz  
**Structure-preserving space-time discretization in a mixed framework for multi-field problems in large strain elasticity.**  
ISBN 978-3-7315-0926-4
- Band 7    Mark Georg Schiebl  
**Thermodynamically consistent space-time discretization of non-isothermal mechanical systems in the framework of GENERIC.**  
ISBN 978-3-7315-1117-5
- Band 8    Jonas Hund  
**Characterisation and modelling of PC/ABS blends.**  
ISBN 978-3-7315-1157-1

# Band 8

Schriftenreihe des Instituts für Mechanik  
Karlsruher Institut für Technologie (KIT)

HERAUSGEBER

Prof. Dr.-Ing. habil. Peter Betsch

Prof. Dr.-Ing. habil. Thomas Seelig



ISSN 2363-4936  
ISBN 978-3-7315-1157-1